



Universitat Autònoma de Barcelona

**ADVERTIMENT.** L'accés als continguts d'aquesta tesi queda condicionat a l'acceptació de les condicions d'ús establertes per la següent llicència Creative Commons:  [http://cat.creativecommons.org/?page\\_id=184](http://cat.creativecommons.org/?page_id=184)

**ADVERTENCIA.** El acceso a los contenidos de esta tesis queda condicionado a la aceptación de las condiciones de uso establecidas por la siguiente licencia Creative Commons:  <http://es.creativecommons.org/blog/licencias/>

**WARNING.** The access to the contents of this doctoral thesis it is limited to the acceptance of the use conditions set by the following Creative Commons license:  <https://creativecommons.org/licenses/?lang=en>



**Universitat Autònoma de Barcelona**

Escola d'Enginyeria

Departament d'Enginyeria Química, Biològica i Ambiental

Programa de Doctorat en Biotecnologia

# **Characterization and purification of HIV-1 based virus-like particles**

Irene González Domínguez

Advisors

Dr Francesc Gòdia Casablanca

Dr Laura Cervera Gràcia

**Title** Characterization and purification of HIV-1 based virus-like particles

**Keywords** HEK 293, virus-like particles, EVs, Cryo-EM, super-resolution, AFM, flow virometry, NTA.

**Author** Irene González Domínguez

**Supervisors** Prof. Francesc Gòdia Casablanca and PhD Laura Cervera Gràcia

**Cover Design** Evan ReeceWalker

PhD program in Biotechnology

Departament d'Enginyeria Química, Biològica i Ambiental

Escola d'Enginyeria

Universitat Autònoma de Barcelona

July 2020

El Dr. Francesc Gòdia Casablanças, Catedràtic d'Enginyeria, i la Dra. Laura Cervera i Gràcia, investigadora post-doctoral del Departament d'Enginyeria Química, Biològica i Ambiental de la Universitat Autònoma de Barcelona

Certifiquem:

Que la graduada en Biotecnologia Irene González Domínguez ha dut a terme al Departament d'Enginyeria Química, Biològica i Ambiental de la Universitat Autònoma de Barcelona i amb la nostra direcció, la tesi doctoral titulada “**Characterization and purification of HIV-1 based virus-like particles**”. La mateixa, es presenta en aquesta memòria i constitueix el manuscrit per optar al Grau de Doctor en Biotecnologia per la Universitat Autònoma de Barcelona.

I per tal que se'n prengui coneixement i consti als efectes oportuns, signem aquest certificat a Bellaterra, a juliol de 2020.

Irene González Domínguez


(autor)


Laura Cervera Gràcia


(co-director)

Francesc Gòdia Casablanças

(co-director)

**ADVERTIMENT.** L'accés als continguts d'aquesta tesi queda condicionat a l'acceptació de les condicions d'ús establertes per la següent llicència Creative Commons:  [http://cat.creativecommons.org/?page\\_id=184](http://cat.creativecommons.org/?page_id=184)

**ADVERTENCIA.** El acceso a los contenidos de esta tesis queda condicionado a la aceptación de las condiciones de uso establecidas por la siguiente licencia Creative Commons:  <http://es.creativecommons.org/blog/licencias/>

**WARNING.** The access to the contents of this doctoral thesis it is limited to the acceptance of the use conditions set by the following Creative Commons license:  <https://creativecommons.org/licenses/?lang=en>

---

## Table of contents

<b>Resum</b> .....	11
<b>Resumen</b> .....	15
<b>Summary</b> .....	19
<b>Introduction</b> .....	23
<b>Objectives</b> .....	75
<b>Results</b> .....	77
<b>Chapter 1</b> – Impact of physicochemical properties of DNA/PEI complexes on transient transfection of mammalian cells .....	79
<b>Chapter 2</b> – Rational design of the DNA/PEI complex physicochemical properties for DNA delivery in mammalian cells .....	109
<b>Chapter 3</b> – Quantitative colocalization analysis of DNA delivery by PEI-mediated cationic polymers in mammalian cells .....	151
<b>Chapter 4</b> – Quantification of the HIV-1 virus-like particle production process by super-resolution imaging: from VLP budding to nanoparticle analysis.....	177
<b>Chapter 5</b> – Identification of Human Immunodeficiency Virus Type 1 (HIV-1) Based Virus-Like Particles by Multifrequency Atomic Force Microscopy .....	219
<b>Chapter 6</b> – Quality assessment of virus-like particles at single particle level: a comparative study.....	237
<b>Chapter 7</b> – A four-step purification process for HIV-1 Gag VLPs: from cell culture supernatant to lyophilization .....	277

---

<b>General Discussion .....</b>	<b>315</b>
<b>Conclusions .....</b>	<b>329</b>
<b>Curriculum Vitae .....</b>	<b>333</b>

---

## Abbreviations

3D	three-dimensional
AB	Alcian Blue
AAV	Adeno-Associated Virus
AcMNPV	<i>Autographa californica</i> multiple nucleopolyhedrovirus
AFM	Atomic Force Microscopy
AM-FM	Amplitude Modulation-Frequency Modulation
BacMaM	Baculovirus gene transfer into mammalian cells
BEVS	Baculovirus Expression Vector System
BSA	Bovine Serum Albumin
BV	Baculovirus
CAR-T	Chimeric Antigen Receptor -T cells
CCD	central composite design
Cl	Chloride
CLSM	Confocal Laser Scanning Microscopy
CQA	Critical Quality Attributes
CPZ	Chlorpromazine
CPP	Critical Process Parameters
Cryo-TEM	Cryogenic Transmission Electron Microscopy
DBC	Dynamic Binding Capacity
dCR	derived count rate
DLS	Dynamic Light Scattering
DoE	Design of Experiments
dsDNA	double stranded DNA
DSP	Down-Stream Process
EDS	Energy Dispersive X-ray Spectroscopy
EGE	Extended Gene Expression
eGFP	enhanced Green Fluorescence Protein
EIPA	5(N-ethyl-N-isopropyl) amiloride
EM	Electron Microscopy
ESCRT	Endosomal Sorting Complexes Required for Transport
EV	Extracellular Vesicle
FreeStyle	FreeStyle™ cell culture medium



---

FU	Fluorescence Units
FWHM	Full Width at Half Maximum
FTIR	Fourier-transform infrared spectroscopy
GOI	Gene of Interest
HCD	host-cell DNA
HCP	host-cell protein
HIV	human immunodeficiency virus
Hpi	hours post infection
Hpt	Hours Post Transfection
HPV	Human Papilloma Virus
IEX	Ion-Exchange Chromatography
Inc.Time	incubation time
JACoP	Just Another Co-localization Plug-in
Kcps	Kilo counts per second
LOD	Limit of Detection
LM	Lipid Membrane
MF AFM	Multifrequency Atomic Force Microscopy
Min	Minute
MOI	Multiplicity of Infection
M-PMV	Mason-Pfizer Monkey Virus
MVB	Multivesicular Body
N/P ratio	Nitrogen to Phosphate ratio
Na	Sodium
NS	Negative Staining
NTA	Nanoparticle Tracking Analysis
Nys	Nystatin
OD	Overall Desirability
ODV	Occlusion-Derived Baculovirus
P	Phosphorus
PAT	Process Analytical Technologies
PBS	Phosphate Buffer Saline
PDI	Polydispersity Index
PEI	Polyethylenimine
PSD	Particle Size Distribution
PSF	Point Spread Function
PTM	Post-Translational Modification
QbD	Quality by Design

---

rBV	relaxed-form of Baculovirus
RI	Refractive Index
RFU	Relative Fluorescence Units
ROI	Regions of Interest
RT	Room Temperature
SD	Standard Deviation
SEC	Size Exclusion Chromatography
SEM	Scanning Electron Microscopy
SIM	Structured Illumination
SIV	Simian Immunodeficiency Virus
SRFM	Super-Resolution Fluorescence Microscopy
STED	Stimulated Emission Depletion
STORM	Stochastic Optical Reconstruction Microscopy
TEM	Transmission Electron Microscopy
TGE	Transient Gene Expression
TFF	Tangential Flow Filtration
TRPS	Tunable Resistive Pulse Sensing
U	Uranium
VLP	Virus-like particle
V-SSC	Violet Side Scatter



**Resum**

---

Les *virus-like particles* (VLPs) de VIH han sorgit com una prometedora alternativa per al desenvolupament de nous candidats vacunals, i per al disseny de teràpies avançades en el camp de la nanomedicina. En els últims anys, s'han desenvolupat diferents estratègies d'optimització per la producció de VLPs de VIH en cultius de cèl·lules animals. Malgrat aquests avanços, la manca d'informació sobre el procés de producció de les VLPs a nivell intracel·lular, la necessitat de mètodes analítics adients per la quantificació de les VLPs de VIH i la seua diferenciació d'altres estructures vesiculars, conegudes com *extracellular vesicles* (EVs), conjuntament amb la falta de mètodes de purificació, han limitat l'ús d'aquestes nanopartícules a la clínica. Per aquesta raó, la motivació d'aquesta tesis doctoral és aprofundir en els diferents paràmetres que participen en la generació de VLPs de VIH, així com el desenvolupament de nous mètodes d'anàlisi i purificació amb l'objectiu d'establir una plataforma de producció per la seua aplicació en l'àmbit de la biotecnologia.

En primer lloc, es va estudiar el procés de producció de les VLPs de VIH mitjançant l'expressió transitòria en la línia cel·lular HEK 293 emprant la polietilenimina (PEI) com agent transfectant. Quan el PEI es mescla amb un plasmidi d'ADN que codifica per la proteïna d'interès, es produeix la condensació de l'ADN generant complexos d'ADN/PEI en el rang dels nanòmetres. Durant la incubació d'aquests complexos en solucions salines, com és el propi medi de cultiu, els complexos sofreixen un procés d'agregació en el qual, estructures d'ADN/PEI en el rang dels micròmetres són obtingudes. Aquesta segona població de complexos, resulta necessària per maximitzar la producció de transfecció transitòria en cèl·lules de mamífer. L'aplicació de metodologies de disseny d'experiments ha permès modelitzar l'efecte de la concentració de ions de clorur de sodi (NaCl), el pH i el temps de incubació en el procés de formació d'aquests complexos d'ADN/PEI. D'aquests estudis es va determinar la participació dels ions juntament amb el temps de incubació com els paràmetres clau responsables de l'agregació de l'ADN/PEI. Finalment, el comportament dels complexos a nivell intracel·lular es va investigar mitjançant eines de col·localització amb microscòpia confocal. L'alliberació del plasmidi d'ADN dintre de les cèl·lules fou observat entre les 2 i les 10 hores, on el coeficient de col·localització de Manders fou identificat com el millor

per la monitorització d'aquestes nanopartícules. Tanmateix, la presència de complexos micromètrics en les proximitats del nucli cel·lular a les 24 hores post transfecció va ser observat. Tot plegat, aquests resultats senyalen la contribució dels agregats d'ADN/PEI per a una correcta execució dels processos de transfecció transitòria en cèl·lules de mamífer.

El procés d'acoblament de les VLPs de VIH a la membrana cel·lular fou també caracteritzat emprant la microscòpia de super-resolució. La plataforma de producció HEK 293 prèviament estudiada es va comparar amb el sistema de producció basat en la infecció amb baculovirus en les línies cel·lulars *High Five* i Sf9. La comparativa d'aquestes estratègies va permetre identificar la producció de proteïna no acoblada i la presència de EVs i baculovirus, com a dos grans fonts de contaminació en el procés de producció de VLPs de VIH.

En tercer lloc, es va valorar l'ús de diferents eines per la caracterització i quantificació de les VLPs de VIH. Tècniques avançades de microscòpia electrònica, microscòpia de força atòmica, microscòpia de super-resolució, *nanoparticle tracking analysis* (NTA) i la citometria de nanopartícules han sigut emprades en aquesta tesis. De totes elles, la microscòpia de força atòmica va determinar les propietats nanomecàniques de les VLPs de VIH, mentre que la microscòpia electrònica de criogènia va permetre l'estudi de l'organització de la proteïna estructural Gag a l'interior de les VLPs. D'altra banda, la quantificació i diferenciació de VLPs VIH es va assolir amb tècniques d'alt rendiment, com ara un mètode de quantificació desenvolupat basat en microscòpia de super-resolució, l'NTA i la citometria de nanopartícules.

Per últim, l'estabilitat, purificació i conservació de les VLPs de VIH fou estudiat. El desenvolupament d'un sistema de purificació es va basar en quatre unitats d'operació definides com clarificació, cromatografia d'intercanvi iònic, cromatografia d'exclusió per grandària i liofilització. La separació de les VLPs i els EVs, així com la seua purificació d'altres contaminants derivats del procés de producció, com son proteïna o ADN intracel·lulars, van ser assolits al final del procés. Vials amb una concentració de  $2.2 \cdot 10^9$  VLPs y 24  $\mu\text{g}$  d'antigen del VIH van ser preservats durant dos mesos a temperatura ambient.

Els resultats de la present tesis doctoral, combinats amb diferents estratègies de producció permetran l'obtenció d'una plataforma per a la generació de nous candidats terapèutics en el camp de la biotecnologia i la nanomedicina. Les eines i protocols desenvolupats en aquest treball, són també de interès en l'estudi d'altres nanopartícules biològiques, com ara virus amb embolcall o els mateixos EVs produïts en cultius animals.

## Resumen

---



Las *virus-like particles* (VLPs) derivadas del VIH han surgido como una potente alternativa para el desarrollo de nuevos candidatos vacunales, pero también para el diseño de terapias avanzadas en el campo de la nanomedicina. En los últimos años, se han optimizado diferentes estrategias para la producción de estas VLPs en cultivos de células animales. No obstante, el desconocimiento acerca de los diferentes pasos que acontecen a su producción a nivel intracelular, y que afectan al rendimiento de producción, la falta de métodos analíticos para su correcta caracterización y cuantificación, así como de su diferenciación de otras estructuras vesiculares, conocidas como *extracelular vesicles* (EVs), y la carencia de métodos de purificación adecuados dificultan su aplicación en la clínica. Por todo ello, el objetivo de la presente tesis es investigar en el proceso de producción de VLPs de VIH, así como desarrollar nuevos métodos analíticos y de purificación con el objetivo de establecer una plataforma de producción de estas nanopartículas para su uso en aplicaciones biotecnológicas.

En primer lugar, se estudió el proceso de producción de las VLPs de VIH mediante expresión transitoria en la línea celular HEK 293 usando polietilenimina (PEI) como agente de transfección. Cuando el PEI se une con el plásmido de ADN que codifica para la proteína de interés, se produce la condensación del ADN en complejos de ADN/PEI con un tamaño medio de 300 nm. Mediante la incubación de estos complejos en soluciones salinas, como es el propio medio de cultivo, se produce la agregación de estos complejos generando partículas en el rango de los micrómetros. Esta segunda población de partículas resulta necesaria para la maximización de la transfección. La aplicación de metodologías de diseño de experimentos ha permitido modelizar el efecto de la concentración de iones de cloruro de sodio (NaCl), el pH y el tiempo de incubación en el proceso de formación de los complejos de ADN/PEI y su posterior relación con su eficiencia de transfección. Estos estudios permitieron identificar la concentración de iones y el tiempo de incubación como los parámetros clave para controlar el proceso de agregación de los complejos de ADN/PEI. Finalmente, el comportamiento de estos complejos a nivel intracelular se estudió empleando técnicas de colocalización en microscopía confocal. La liberación del plásmido de ADN a nivel intracelular se monitorizó mediante el coeficiente de colocalización de Manders,

donde la presencia de complejos de ADN/PEI con tamaño micrométrico fueron observados en los alrededores del núcleo de las células a las 24 horas post transfección. En conjunto, estos estudios señalan la contribución de los complejos micrométricos para la correcta producción de VLPs de VIH mediante transfección transitoria en células de mamífero.

Los análisis a nivel intracelular también se emplearon para estudiar el proceso de ensamblaje de las VLPs de VIH en el interior de la membrana celular. El uso de la microscopía de super-resolución permitió caracterizar el proceso de ensamblaje de las VLPs de forma individual en tres líneas celulares animales. La plataforma HEK 293 previamente estudiada, se comparó con el sistema de producción basado en la infección con baculovirus en las líneas celulares *High Five* y Sf9. La comparativa entre estas plataformas permitió también la identificación de proteína no ensamblada y la presencia de EVs así como de baculovirus, como dos grandes fuentes de contaminación en la producción de VLPs de VIH.

En tercer lugar, se determinaron diferentes técnicas analíticas para la caracterización y cuantificación de VLPs de VIH. Técnicas avanzadas de microscopía electrónica, microscopía de fuerza atómica, microscopía de super-resolución, *nanoparticle tracking analysis* (NTA) y citometría de nanopartículas fueron empleadas. Entre todas ellas, destacaron el uso de la microscopía de fuerza atómica para estudiar las propiedades nanomecánicas de las VLPs de VIH y el uso de la microscopía electrónica de criogenia para el estudio de la organización de la proteína estructural Gag dentro de la VLP. Por otro lado, la cuantificación y diferenciación de VLPs se obtuvo mediante tecnologías de alto rendimiento como el desarrollo de un método basado en microscopía de super-resolución, el NTA y la citometría de nanopartículas.

Finalmente, se estudió la estabilidad, purificación y conservación de estas partículas para su uso a nivel industrial. Se desarrolló un método de purificación basado en cuatro unidades de operación tales como clarificación, cromatografía de intercambio iónico, cromatografía por exclusión de tamaño y liofilización. La separación de VLPs de VIH de los EVs, así como su purificación de otros componentes presentes en la muestra inicial derivados de los cultivos celulares fueron

reportados. Viales de VLPs purificadas y liofilizadas con una concentración  $2.2 \cdot 10^9$  VLPs y 24  $\mu$ g de antígeno del VIH fueron conservados durante dos meses a temperatura ambiente.

Los resultados de la presente tesis, combinados con diferentes plataformas de producción de VLPs de VIH, permitirán la obtención de una plataforma de producción de estas partículas para el desarrollo de nuevos candidatos terapéuticos en el campo de la biotecnología y la nanomedicina.

Los métodos desarrollados en esta tesis son también de interés para el estudio de otras nanopartículas biológicas con las cuales comparten propiedades bioquímicas y fisicoquímicas con las VLPs, como son los virus con envuelta o los propios EVs producidos naturalmente en cultivos animales.

## Summary

---

HIV-1 virus-like particles (VLPs) have emerged as an interesting alternative for the development of novel vaccine candidates and delivery strategies of different cargos into different cells and tissues. Great efforts have been undertaken to optimize the generation of these nanoparticles in animal cell cultures. However, the limited understanding of its production at intracellular level, the need for analytical tools allowing its specific quantification over extracellular vesicles (EVs), and the few purification processes available hamper their clinical application. The aim of this thesis is to gain insight into the process parameters affecting HIV-1 Gag VLP production, and the development of analytical and purification methods to establish a complete platform for its clinical-grade production.

First, a PEI-mediated transient gene expression (TGE) platform in the mammalian HEK 293 cell line has been characterized in a physicochemical manner and at intracellular level. Nanometric DNA/PEI complexes are formed upon the mixture of the PEI with the coding DNA plasmid. Their incubation in ionic solutions, i.e. cell culture medium, causes a heterogeneous aggregation process, where the transfection of mammalian cells benefits from the presence of micrometric aggregates in the complexing solution. To deepen into the factors governing this process, a Design of Experiments (DoE) approach has been used to rationally study the interactions between NaCl ions, pH and incubation time in PEI-mediated transfections. This DoE has identified ion concentration and incubation time as the driving forces in DNA/PEI aggregation. The fate of these complexes within cells has been further studied with quantitative colocalization in confocal laser scanning microscopy (CLSM). The use Manders' Overlap coefficient is selected as the best method to evaluate their disassembly in living cells. These analyses show DNA/PEI complex aggregates in the nuclear envelope surroundings at 24 hours post transfection; altogether, supporting the contribution of micrometric complexes in DNA delivery strategies of mammalian cells.

Second, intracellular characterization has been also applied to better understand the VLP assembly in living cells. Upon the expression of the structural Gag polyprotein from the HIV-1, Gag accumulates underneath the plasma membrane and through a budding process these

enveloped VLPs are released to the extracellular space. Super Resolution Fluorescence Microscopy (SRFM) has been applied to the HEK 293 platform, but also to Baculovirus Expression Vector System (BEVS) in High Five and Sf9 cells. From 500 to 3000 individual VLP assembly sites per cell are quantified in the different systems. This characterization has also revealed the presence of free Gag monomer and other contaminant nanoparticles, like EVs and baculovirus in BEVS, as a significant source of contamination in the production of HIV-1 Gag VLPs.

Thirdly, novel methodologies are assessed for the characterization and quantification of HIV-1 Gag VLPs. Fluorimetry, Transmission (TEM), Scanning (SEM) and cryogenic Electron Microscopy (cryo-EM), Atomic Force Microscopy (AFM), SRFM, NTA and flow virometry have been studied in this thesis. Advanced AFM and cryo-EM unveil the nanomechanical properties and ultrastructure of VLPs, whereas, a novel SRFM-developed quantification method, NTA and flow virometry enable the high throughput quantification of HIV-1 Gag VLPs and its differentiation from EVs.

In the last chapter, the stability, purification and preservation of these nanoparticles is investigated. A nimble purification consisting of clarification, ion-exchange (IEX) chromatography, size-exclusion chromatography (SEC) and lyophilization has been developed. The separation of HIV-1 Gag VLPs from EVs is obtained in the final purified samples, where Gag polyprotein represented more than the 95% of total protein, although the overall yields obtained in these first attempts are still low. Lyophilized vials containing  $2.2 \cdot 10^9$  VLPs and 24  $\mu\text{g}$  of Gag polyprotein were stored at room temperature for up to two months.

Overall, the findings on product characterization and purification presented in this thesis could be further combined with previously optimized platforms, for the development of novel chimeric HIV-1 Gag VLP candidates, but also for other biological enveloped structures sharing similar biochemical and physicochemical properties with VLPs, like enveloped viruses or EVs.



## Introduction

---





## 1. Virus-based products

The production of virus-based products to prevent infectious diseases has been used to protect human health for more than three centuries. At the end of the 18<sup>th</sup> century, Edward Jenner introduced the concept of vaccination by using animal pox virus to prevent smallpox [1]. From that time on, interest in virus-based products, as well as, virus-related technologies and manufacturing capacities have evolved, and novel applications, such as recombinants vaccines, gene therapy or cancer immunotherapy are now on the spotlight (Figure 1) [2,3].

Advances in genetic engineering, molecular biology and cell culture technologies have brought out the design of non-replicative viral vectors for gene transfer approaches, such as adeno-associated viruses (AAVs) or lentiviruses. In the last years, several products have received the approval from the EMA or the FDA for their clinical use in humans, namely Glybera®, Luxturna® and Zolgensma® for *in-vivo* application, or the promising *ex-vivo* Chimeric Antigen Receptor (CAR)-T cells such as Kymirah® or Yescarta®, among others [4]. Furthermore, alternative use of replicative viral vectors, like adenoviruses or herpes viruses, are now being explored to fight several cancers [5]. Of note, H101®, IMLYGIC®, Rigvir®, and Rexin-G® products have been approved against advanced head and neck cancer or advanced melanoma among others, by different health agencies [4,5]. As a consequence of this success, a remarkable number of clinical trials are nowadays on-going on these topics (Figure 1B-D), specially CAR-T cells cope the great majority of the on-going *ex-vivo* clinical trials in gene therapy approaches.

## 2. Vaccines

Vaccine development was the firstborn application of virus-based products to prevent infectious diseases, and still today maintains a sustained interest [3,6]. In Figure 2, a timeline of the approved vaccines, since 18<sup>th</sup> century is depicted. Up to now, there are more than 60 licensed vaccines by the FDA (Table 1) and more than 300 on-going clinical trials (Figure 1D) against novel infectious diseases, such as Malaria, Zika or Coronavirus, among others. The occurrence of devastating pandemics like the current COVID19 (coronavirus disease 2019) made evident the fragility of globalized societies to the spread of new emerging infectious diseases and how critical are

vaccines to protect the health of World’s population. The preparedness of modern societies to react rapidly on similar future emergencies depends heavily on their potential to rapidly develop new vaccines, having manufacturing capacities and enabling their distribution everywhere to guarantee the right to universal vaccination.

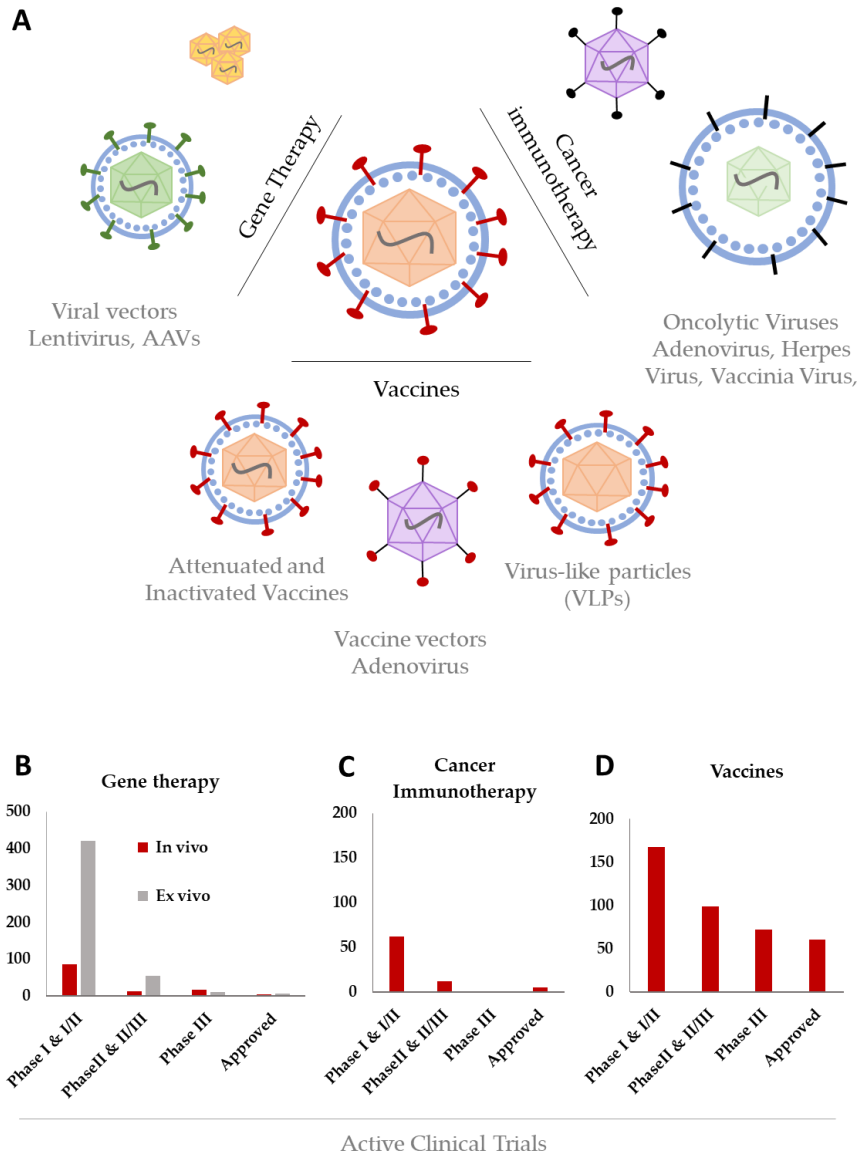


**Figure 1:Virus-based products. (A) Applications of virus-based products adapted from [7]. (B-D) Active clinical trials and approved products of virus-based products into Gene Therapy (B), Cancer Immunotherapy (C) and Vaccines (D) fields. Data obtained from [clinicaltrials.gov](https://clinicaltrials.gov) (Accessed March 2020). AAVs: adeno-associated vectors; VLP: virus-like particles.**

Mass vaccination campaigns have been one of the biggest medical interventions that have proved capital to protect human beings. In the 19<sup>th</sup> century, Pasteur and colleagues developed the concept of attenuated vaccines that followed by the appearance of first inactivated vaccines contributed to

extend the human life span up to 30 years in the next century (Figure 2) [1,3]. Live-attenuated vaccines efficiently induce a potent immune response, since they perfectly mimic the natural infection. They are obtained by several cell culture passages, where the virus loses its infectivity in humans while acquiring the ability to grow in cell cultures *in vitro*, like Varicella or Yellow fever vaccines, among others [1]. Inactivated vaccines consist on the application of heat or chemical treatments to kill the virus upon production. This second-generation vaccine offers a safer alternative to live-attenuated candidates, although being less immunogenic, requiring adjuvation [3].

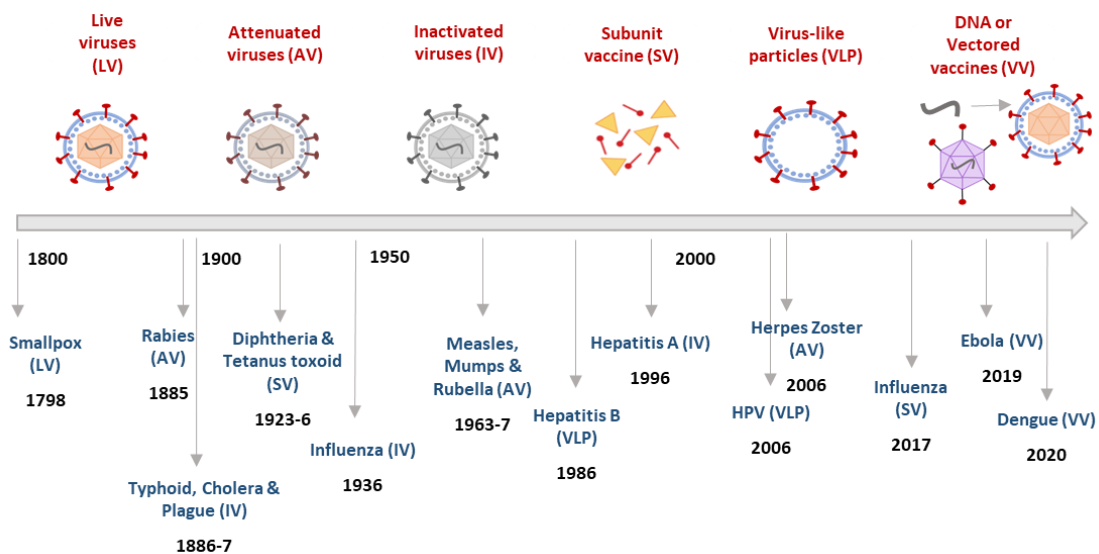


Figure 2: Timeline of first-time approved human vaccines, figure adapted from [1,8] and updated with data obtained from FDA ; (Accessed March 2020). HPV: Human Papilloma Virus.

Both types of vaccines are still being used nowadays, where technological advancements have been implemented into the already established production processes, like the use of new producer cell lines [6]. Nonetheless, the production of these vaccines requires the manipulation of live viruses that have the low but real risk to become virulent. With views to facilitate the production of new vaccines and avoid the risk of infection, alternative third-generation vaccines have been investigated in the last decades (Table 1).

Among the different third-generation vaccines, subunit vaccines have been claimed as one of the most promising alternatives, particularly against bacterial infections with a high number of licensed toxoids and polysaccharides-based vaccines [3,9]. Moreover, two successful cases have

been recently licensed by the FDA against flu and shingles diseases (Table 1). DNA vaccines, consisting on the introduction of a nucleic acid sequence coding for viral antigens, have been proven in the veterinary field. Nonetheless, a poor cell-based immunogenicity has been observed in human clinical trials, where the use of novel adjuvants are being investigated to overcome this problem [10,11]. The use of vectored vaccines, where a non-replicative or attenuated virus is used as a scaffold to present the antigens of a desired virus, has been also approved against Dengue and Ebola diseases (Table 1). However, a strong immunity against the vector itself has limited their effectiveness in some applications [11,12]. Virus-like particles (VLPs), which are defined as nanometric particles that mimic the native viral conformation in the absence of the viral genome, offer great promise to overcome some of the mentioned limitations of other vaccine types. Up to now, Hepatitis B and Human Papilloma Virus (HPV) vaccines have been developed using that technology, firstly approved in 1986 and 2006, respectively (Table 1). VLP vaccines against Hepatitis E (Hecolin®, Inovax) in China, or Malaria (RTS,S/AS01 vaccine) in Europe have also recently received approval.

**Table 1: Viral-based Vaccines Licensed for Use in the United States. Data obtained from FDA ( Accessed March 2020).**

Type of Vaccine	Disease	Commercial Name
<b>Live Attenuated Virus Vaccine</b>	Anthrax	Biothrax
	Influenza	FluMist
	Measles, Mumps, Rubella	M-M-R II, ProQuad
	Rotavirus	ROTARIX, RotaTeq
	Smallpox	JYNEEOS
	Varicella	Varivax
	Yellow Fever	YF-Vax
	Herpes Zoster (Shingles)	Zostavax
Adenovirus Type 4 and 7	No trade name	
<b>Inactivated Virus Vaccine</b>	Polio	Poliovax
	Polio *	Pediarix, KINRIX, Quadracel, VAXELIS, Pentacel
	Hepatitis A	Havrix, VAQTA and Twinrix**
	Influenza	AUDENZ, FLUAD, AFLURIA, Flucelvax, Afluria, FluLaval, Fluarix, Fluvirin, Agriflu, Fluzone, Flucelvax,
Japanese Encephalitis	Ixaro	
<b>Vectored Vaccine</b>	Dengue	DENGVAXIA (vectored in Yellow Fever)
	Ebola	ERVEBO (vectored in Vesicular Stomatitis Virus)
	Smallpox	ACAM2000 (vectored in Vaccinia Virus)
<b>Subunit Vaccine</b>	Influenza	Flublok
	Herpes Zoster (Shingles)	SHINGRIX
<b>Virus-like particles</b>	Hepatitis B	Recombivax HB, Engerix-B, HEPLISAV-B
	Human Papilloma Virus infection	Gardasil, Gardasil 9, Cervarix

\*Combined Virus-based with toxoid and subunit vaccine\*\* Combined with Hepatitis B VLP Vaccine

### 3. Virus-like particles

VLPs resemble the viral native conformation by the recombinant expression of their structural proteins. Their highly organized and repetitive structure has proven to generate a potent immunogenic response activating both the cellular and humoral pathways [13,14]. Wild-type VLPs can be classified in non-enveloped and enveloped structures (Figure 3). Within this general classification, there is a large diversity of VLP configurations: from the simplest non-enveloped single-protein composition, as in the Hepatitis B candidates, to multilayered protein configurations [15]. The ease of production, safety and their efficient recognition and cellular uptake, has expanded the interest on the possible applications of these structures in the last decade. VLPs can be further improved by encapsulation, chemical conjugation and genetic manipulation (Figure 3). Bioengineering has been applied to strengthen their stability and immunostimulatory properties and to generate novel engineered VLPs, as well as, vectors for DNA and drug delivery strategies [16–20].

Depending on the complexity of the final structure, there are several production platforms available (Figure 3). The more simple VLP types could be produced in prokaryotes and assembled in cell-free environments, referred as virosomes in some works [21,22]. The bacteria *Escherichia coli* or the yeast *Pichia pastoris* have been described as the most productive platforms with bulk concentrations up to 4.38 mg/mL [23] and 400 mg/mL[24], respectively, however post-translational modification (PTMs) may limit their application into the production of complex VLPs [8,15,19]. Transgenic plants such as Potato or Tobacco [15,19,25] and baculovirus-vector expression system (BEVS) with High Five or Sf9 insect cell lines are also used to produce VLPs. Despite PTMs suffer from alterations [25,26], several licensed and phase III clinical trials are ongoing with VLPs produced in these systems [17,22]. Finally, the mammalian CHO and HEK 293 cell lines, which present better glycosylation patterns, are preferred for the expression of highly complex VLP candidates.

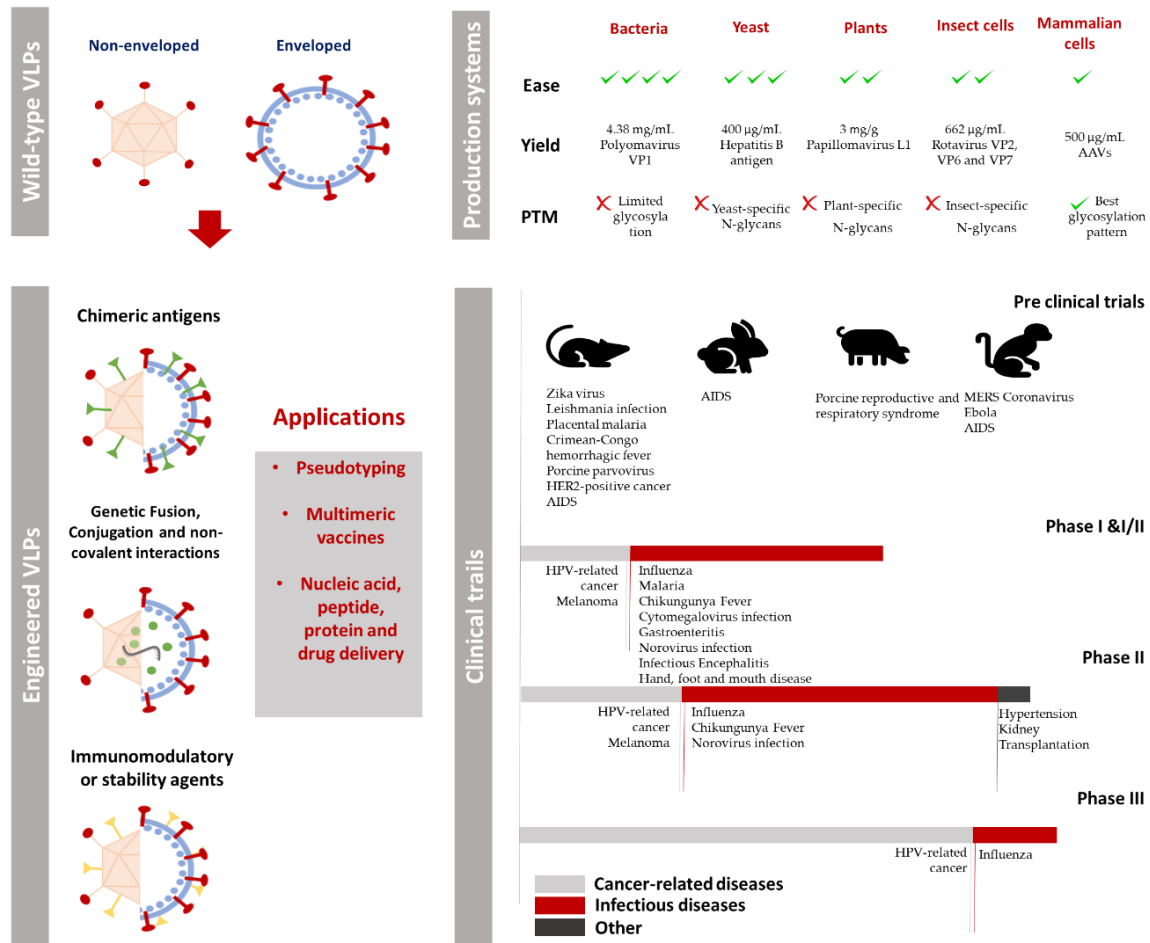


**Figure 3: Virus-like particles state-of-the-art. Wild-type VLPs:** VLPs can be classified in non-enveloped and enveloped structures depending on the nature of the wild-type virus. For both types single or multilayered protein can be found (adapted from [15]). **Engineered VLPs:** synthetic biology tools are applied to wide VLP applications. By the addition of chimeric antigens, multimeric vaccines or pseudotyping of different VLP scaffold are proposed. Furthermore, surface modification and cell-specific targeting molecules are also described in the literature for the controlled release of nucleic acids or drug, increase the immune response or improve the stability of the VLP candidates (adapted from [15,16,18]). **Production systems:** bacteria, yeast, plants, baculovirus-infected insect cells and mammalian cells are used for the production of different VLP candidates (adapted from [8,15,26,27]). **Clinical trials:** VLPs are currently tested against several diseases in pre-clinical studies in several animal models (mouse, rabbit, pig or rhesus macaque). Currently there are more than 100 clinical trials (on-going and completed) based on VLPs mainly targeting cancer and infectious diseases; data obtained from [clinicaltrials.gov](https://clinicaltrials.gov) (Accessed March 2020) and [17,28]. AAV: adeno-associated virus; AIDS: acquired immunodeficiency syndrome; HPV: human papilloma virus; MERS: middle east respiratory syndrome.

Up to date, 140 on-going or completed clinical trials have tested VLPs as vaccine candidates (Figure 3). From them, two main applications can be highlighted: infectious viral diseases and cancer [16], being Influenza and HPV-cancer related the ones in more advanced phases. Of note, many diseases such as Malaria or Chikungunya Fever are being tested in Phase I, while new VLP

vaccine candidates against Ebola, Zika, MERS (Middle East Respiratory Syndrome) coronavirus or AIDS (acquired immune deficiency syndrome) have been investigated in pre-clinical trials, among others [17].

#### 4. HIV-1 Gag VLPs

The human immunodeficiency virus (HIV), known to be the etiological agent of AIDS, was first diagnosed in 1981. Since that time on, the generation of a protective vaccine has been a major challenge worldwide. HIV-1 and HIV-2 are the two well-defined serotypes of the HIV. While HIV-1 accounts for the 95% of all AIDS infections worldwide, HIV-2 is shown to be less aggressive and has a more restricted geographic spread [29]. HIV-1 contains two copies of single stranded RNA (ssRNA) genome composed of nine open reading frames (ORF), with three main structural genes: *gag*, *pol* and *env*, two regulatory proteins (*tat* and *rev*) and four accessory genes (*nef*, *vif*, *vpu* and *vpr*) (Figure 4A). From the three main genes, *gag* codes for the structural polyprotein, encompassing the nucleocapsid (NC), capsid (CA) and matrix (MA), while *pol* and *env* encode for the main enzymes (PR, RT and IN) and the receptor binding proteins (gp120 and gp41), respectively (Figure 4B). At the end of 20<sup>th</sup> century, Göttlinger described the capacity of the Gag polyprotein to generate non-infectious viral particles on its own [30]. Once produced in the cytoplasm of a host-cell, myristoylation of the N-terminal is produced, increasing its affinity for the cell membrane and with the aid of the ESCRT (endosomal sorting complexes required for transport) machinery, immature particles are secreted to the extracellular space taking part of the cell membrane through a budding process [31]. The ability of Gag to assemble VLPs has been also exploited in other retroviruses and, as with the simian immunodeficiency virus (SIV) [32]. The first application of VLPs consisted on the generation of HIV-1 vaccine candidates by expressing the native Env glycoprotein on its surface. However, this strategy was shown to be very inefficient and the following approaches moved toward using recombinant-truncated and conserved Env fragments [28,32]. Although the increased knowledge on HIV-1 VLPs, no candidate has reached clinical trials to date. Advances in prime boost immunization regimens, mucosal immunizations or the addition of novel adjuvants in the formulation have reported



positive results in preclinical studies in mice, rabbit or rhesus macaque models, and offer great promise for the development of future candidates (Table 2) [28,29,33].

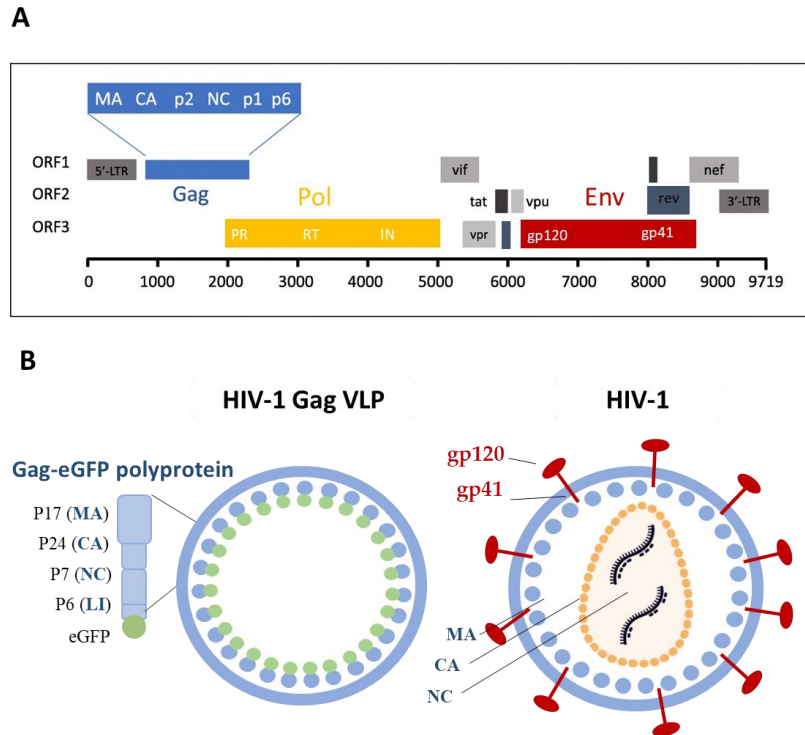


**Figure 4: Structure of HIV-1 Gag VLP and mature HIV-1. (A) Schematic representation of HIV-1 genome with its 9 coding genes. The genome is composed of 3 structural genes (*gag*, *pol* and *env*) 4 accessory genes in grey and 2 regulatory genes located throughout the 3 ORFs. Gag is further processed into 6 protein domains known as matrix (MA or p17), capsid (CA or p24), spacer peptide 1 (SP1 or p2), nucleocapsid (NC or p7), spacer peptide 2 (SP2 or p1) and p6 (Adapted from “Landmarks of the HIV genome”). (B) Morphological structure of Gag VLP and wildtype HIV-1. Wild type HIV-1 is composed of the cleavage products of three major viral polyproteins: Gag, Pol and Env. The sole expression of Gag polyprotein gives rise to the generation of Gag virus-like particles, which are basically immature HIV-1 particles carrying uncleaved Gag capsids surrounded by a host cell lipid layer, (adapted from [28] with editorial permission).**

Interest in Gag VLPs has not been limited to HIV-1 vaccines; the development of chimeric VLPs against different diseases or for delivery strategies has been also described in the literature. In Table 2, different applications entailing the use of Gag VLPs are listed. Several authors have exploited the Gag polyprotein for antigen presentation of Influenza, Dengue, West Nile Virus, HPV, Equine Herpes Virus and Pseudorabies immunogens (Table 2). Furthermore, genetic modifications into the Gag sequence have been explored for the delivery of nucleic acids, enzymes or drugs. Vorácková and coworkers used M-PMV (mason-pfizer monkey virus) Gag VLPs, as nanocages, producing the recombinant Gag subunits in *E.coli* and performing their

assembly *ex vivo* loading small interference RNA (siRNA) inside the nanoparticles [41]. Kaczmarczyk et al. generated in fusion Gag proteins with several prodrugs and enzymes and demonstrated its directed delivery *in vitro* [42]. The immunogenicity of VLPs has been also studied in cancer research [47]: functionalized Gag VLPs were proposed as therapeutic vaccines to counterattack pancreatic cancer (Table 2).

## 5. Production of HIV-1 Gag VLPs

HIV-1 Gag VLP production has been achieved in several cellular platforms [28], but most of the research is performed with animal cell cultures, as shown in Table 2. A summary on the state-of-the-art of this technology is depicted in Figure 5. Animal cell technology could be broadly divided into three main topics: cell culture technologies, cell line and vector engineering and production strategies.

Cell culture conditions, entailing adherent or suspension cell lines could be used for the obtention of bioproducts. Production titers have been increased from micrograms to grams by in recombinant protein production by several strategies [48]. Media optimization have moved towards serum-free, animal-component free and chemically-defined media to improve their regulatory profile and reduce testing costs [49,50]. The production of HIV-1 Gag VLPs has been achieved in chemically defined cell culture media, with supplementation strategies targeting cell growth [51] and production yields [51]. Their obtention at bioreactor scale has been also proven in recent years [52–54]. Process intensification towards continuous manufacturing, and the optimization of process parameters could enhance the final production in viral-based products [55].

**Table 2: Summary of different applications of Gag VLPs.**

Application	Target	Gag sequence	Antigen/cargo	Strategy	Cell line	Animal Model	Reference
HIV-1 Vaccines		HIV-1 pr55, SIVmac239, dGag	Env Variants gp120, gp140, gp41, gp145	BEVS and TGE	Sf9, HEK 293F, HEK 293 T, COS, S2 cells	BALB/c mice, C57BL/6 J, Rabbit, Guinea Pig, Rhesus macaque, Chacma baboon	Cervera, et.al. 2019 (review) [28]
	Influenza	HIV-1 pr55	HA and NA (H1N1)	TGE +SGE	HEK 293 SF cells	BALB/c mice	Venereo-Sanchez, et. al. 2016 [34]
Pseudotyped Vaccines	Influenza	HIV-1	HA and NA (H1N1 & H5N1)	TGE	HEK 293T cells	BALB/c mice	Giles, et al. 2011[35] and Carter, et al. 2016 [36]
	Dengue	HIV-1 pr55	DIII-DENV <sup>1</sup> _RigE	BEVS	Sf9 cells	BALB/c mice	Chua, et al. 2013 [37]
	West Nile Virus		DIII-WNV <sup>Kun</sup> _RigE				
	HPV	HIV-1	HPV-16 E7 and VSV-G	TGE+ Packaging cell	gag-pol 293 GPR packaging cells	C57BL/6 mice	Di Bonito, et al. 2009 [38]
	Equine Herpes Virus	HIV-1 b-p55	Truncated gp14	BEVS	High Five	BALB/c mice	Osterrieder, et al. 1995 [39]
	Pseudorabies	HIV-1 pr55	gD	BEVS	Sf9 cells		Garnier, et al. 1995[40]
Delivery Strategies	Nucleic Acid delivery	M-PMV ΔProCa-NC	AKR-targeted siRNA	Transformation	<i>e.Coli</i> BL21 (DE3)		Voráčková, et al. 2014 [41]
	Protein Delivery	RSV Pr76gag	Gag-cre recombinase, Gag-Fcy::Fur, and Gag-human caspase-8, VSV-G, truncated NA and HA, NA-IFN-γ	TGE	HEK 293T cells		Kaczmarczyk, et al. 2011[42]
	Protein Delivery	HIV-1 Pr55	Vpr1 and Vpx-2 in fusion with SN, SN* and CAT	TGE	HeLa cells		Wu, et al. 1995 [43]
	Drug Delivery	RSV gag-577	calcein-AM and doxorubicin	Bacmid injection	Silkworm	BALB/c mice	Deo, et al. 2015 [44]
Therapeutic Vaccines	Pancreatic Cancer	SIVmac239 gag	Trop2	BEVS	Sf9	C57BL/6 mice	Cubas, et al. 2011 [45]
		SIVmac239 gag	murine mesothelin	BEVS	Sf9	C57BL/6 mice	Zhang, et al. 2013 [46]

AKR: aldoketoreductase; BEVS: baculovirus vector expression system; CAT: chloramphenicol acetyltransferase; Gag-Fcy::Fur : Gag-Cytosine Deaminase and Uracil Phosphory-bosyltransferase; HPV: human papilloma virus; M-PMV: mason-pfizer monkey virus; RSV: Rous Sarcoma Virus; SGE: stable gene expression; SIV: Simian immunodeficiency virus; SN: staphylococcal nuclease; SN\*: inactive mutant SN; TGE: transient gene expression.

The use of efficient promoters, enhancers and other regulatory elements is implemented to increase the expression of the gene of interest (GOI) in the expression cassette. On the one hand, viral or highly expressed housekeeping promoters, like CMV or the baculovirus vector expression system (BEVS), *polH* and *p10*, are widely used in mammalian and insect cells platforms, respectively [56,57]. On the other hand, the addition of A/T rich sequences or the ubiquitous chromatin region opening elements (UCOE), naturally found in chromatin, can also be included to enhance the expression of the GOI [58]. Inside this UCOE elements, the inhibition of histones deacetylases (HDAC) by interference RNA technologies has been demonstrated in CHO and HEK 293 cells for the expression of monoclonal antibodies and HIV-1 Gag VLPs, respectively [59,60]. Other regulatory elements, like episomal replication sequences in combination with engineered cells expressing the viral SV40 large T antigen or the Epstein-Bar virus Nuclear Antigen (EBNA) have been developed (i.e. CAP-T, HEK 293T or HEK 293-EBNA)[61,62]. For the stable expression of a GOI, the addition of specific-site integration sequences and the use of a selection marker is required. Cell line engineering has been also used to knock-down or insert certain genes that facilitate protein expression at several levels. Novel technologies are available to this aim like Site-specific integration sequences for RMCE (Recombinase-mediated cassette exchange) or CRISPR-Cas9 strategies [58,63].

Three main strategies could be distinguished in the obtention of viral-based products in animal cell cultures: viral infection, transient gene expression (TGE) or stable gene expression (SGE). From the three mentioned strategies, infection with alphavirus, vaccinia virus, adenoviral vectors or baculovirus has been used for the rapid production of bioproducts [64]. Among them, the BEVS is the most used system in the production of Gag VLPs (Table 2) [65]. BEVS has been widely used with the insect cell lines, Sf9 [66] and High Five [67], and the new TNMS-42 [68]. BEVS is a very productive system achieving productions of milligrams per liter [8]. However, the obtention of the recombinant viral stock is not always straight-forward and the lytic cycle caused by the infection may affect product quality. Furthermore, its main disadvantage is the baculovirus

interference in the purification process, due to their similarities with enveloped viral structures, as with Gag VLPs.

TGE on the other hand, uses non-viral vectors to introduce a DNA plasmid coding for the protein of interest. In this regard, mammalian cell lines, especially the HEK 293, is the workhorse in TGE strategies for viral-based products [65]. Still, shorter production times of 2-4 weeks are required to obtain up to grams of a protein of interest [69]. Several physical and chemical methods could be found in literature to this end, as reviewed in [70]. However, in industrial biotechnology, the use of transfection reagents such as calcium phosphate and in a more extent the cationic polymer, polyethylenimine (PEI), are almost exclusively used [69]. Alternative transfection reagents, such as cationic lipids, have been also used for DNA delivery in a highly efficient way. Nonetheless, their high cost has relegated their use to SGE strategies [50]. HEK 293 cell cultures [34,51], but also the mammalian cell lines HeLa [43], CHO [71] or CAP-T [72] have been used for the production of HIV-1 Gag VLPs by means of TGE and SGE. Alternatively, the development of SGE and TGE strategies in insect cell lines devoid of BEVS has been proven in the recent years [73–76].

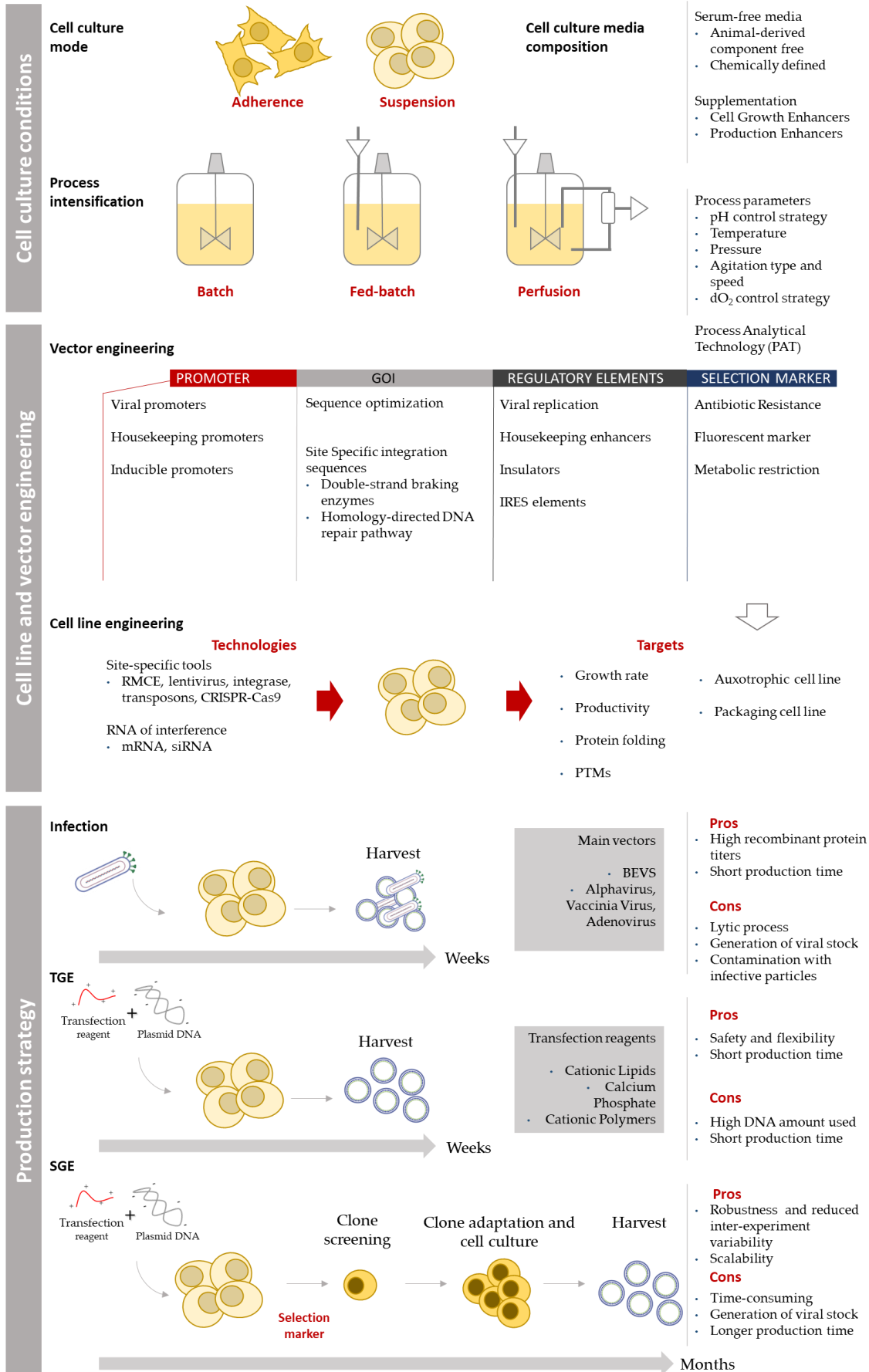


**Figure 5: Animal cell technology for protein production state-of-the-art. Cell culture conditions:** Adherence and suspension cell cultures can be used for protein production. Improvements in cell culture media include the use of serum-free, animal-derived component free and chemically defined cell culture media, as well as, supplementation strategies with boosts or chemical additives to increase production titers. Furthermore, process intensification by means of advanced production modes and the optimization of process parameters could enhance the final production. **Cell line and vector engineering:** the use of efficient promoters, enhancers and other regulatory elements is implemented to increase the expression of the gene of interest (GOI). For the stable expression of a GOI, the addition of specific-site integration sequences and the use of a selection marker is required. Cell line engineering has been also used to knock-down or insert certain genes that facilitate protein expression at several levels. Novel technologies are nowadays available for this aim. **Production strategy:** infection, TGE and SGE are the three main strategies used in recombinant protein production.

## 6. PEI-mediated production

The use of PEI for gene delivery *in vitro* and *in vivo* has been on the spotlight for more than three decades [69,77]. PEI is simple to use, efficient with suspension cells, compatible with serum free media and cost effective. Since its first use as transfection reagent described by Boussif et al. in 1995 [78], several polymer lengths and structures, namely linear and branched PEI, have been tested in DNA delivery approaches [79]. Improved PEI formulations are nowadays commercially available like JetPEI, FectoPro, PeiPro, ExGene500 or the clinical-grade PEIPro®-HQ from Polyplus transfection (Illkirch, France) [69].

PEI amine groups interact with the negatively charged phosphate groups of nucleic acids generating positively charged complexes (polyplexes). By doing so, the DNA sequences are condensed and protected from nuclease degradation (Figure 6). Once formed, polyplexes are attracted by the negatively charged cell membrane, where their cellular uptake has been reported by several endocytic and nonendocytic pathways [77]. Indeed, when one pathway is inhibited, complexes may enter by alternative means [80]. Depending on the way used, several intracellular routes have been also proposed. Besides, the endocytic way is the main uptake mechanism described, where complexes are thought to be transferred to endosomes that are lately converted to lysosomes. At that point, the so called “proton sponge effect” of PEI might cause an influx of chloride ions and increase the osmotic pressure into the lysosome, which eventually would burst and release the complexes to the cytoplasm. Despite this theory is still questioned [79].

DNA/PEI complexes must then achieve the nucleus, where the DNA is transcribed. Although this last step is not fully understood yet, and controversy on a possible passive transport during cell division [81,82], or an active transport through the nuclear pores [83,84] is still unsolved. Besides, a lack of consensus on the intracellular dynamics of the DNA delivery process is still a general concern [77,79].

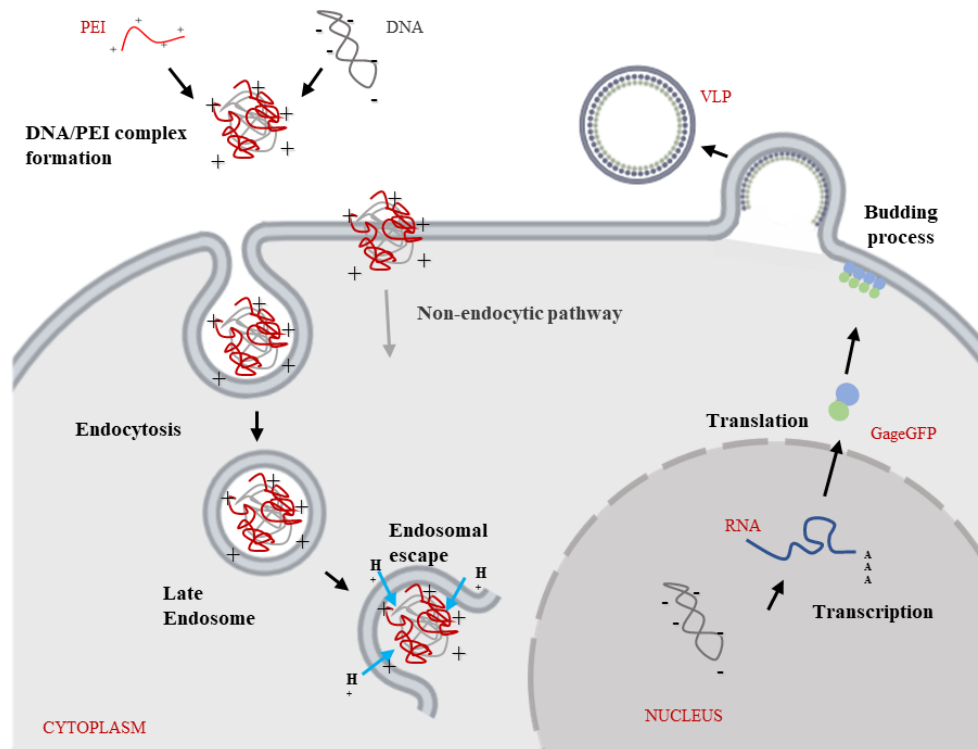


**Figure 6: PEI-mediated TGE for the production of HIV-1 Gag VLPs (figure kindly provided by Dr. Puente-Massaguer, adapted from [85]).**

One of the reasons that might contribute to this controversy is the large number of variables that affect PEI-based processes (Figure 7) [70,86]. Several chemical factors such as pH, salt concentration, temperature or incubation time have been described to highly affect the transfection efficiency [83,86–89]. DNA and PEI chain length, PEI charge density, structure and chemical modifications, the nitrogen / phosphate (N/P) ratio, the DNA and PEI concentrations or the complex preparation and addition process have also a major impact on the TGE efficiency [69,70,79,89,90]. Furthermore, the cell line, cell culture medium composition, cell concentration, time of contact of DNA/PEI complexes with cells, or the addition or replacement of medium in the transfection protocol have also a remarkable influence on the *in vitro* results [69,86,91].



Design of Experiments (DoE) have been implemented to optimize some of these multiple variables in a faster and rational way [67,72,92,93]. On top of that, the idea of DNA/PEI complexes as nanoparticles has brought new parameters, such as size, particle concentration or morphology, that might also play a role in the delivery process [94–98]. Apart from the myriad variables, a large heterogeneity in DNA/PEI polyplex population itself has been described [95].

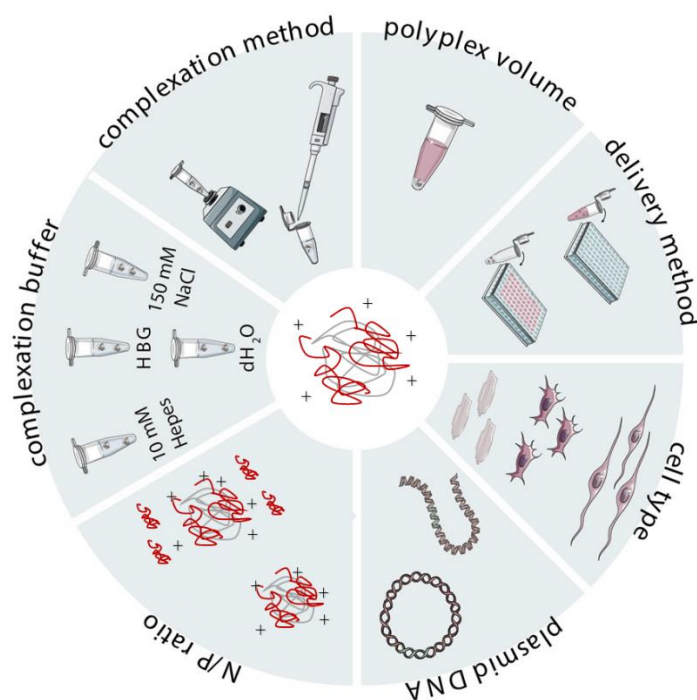


**Figure 7: Main experimental parameters influencing the *in vitro* performance of gene delivery vectors (adapted from [70] with editorial permission).**

## 7. Characterization of HIV-1 Gag VLP production process

The Quality by Design (QbD) and process analytical technologies (PAT) initiative encourage biopharmaceutical companies to design consistent processes, where the product quality is ensured beyond a unique validated condition [99]. A thorough understanding of the production process is then required in the first place.

In the case of HIV-1 Gag VLPs, the identification of the intracellular bottlenecks in their production becomes essential. The use of bulk biochemical and biological methods were primarily used to study the HIV-1 and other viruses production process, while visualization was performed by electron microscopy [100]. However, these methods do not allow the follow-up of

processes in living cells. Alternatively, the intracellular tracking of PEI-mediated DNA delivery and the HIV-1 Gag assembly have been assessed with fluorescent-based methods, such as fluorescence microscopy and flow cytometry [101,102]. Cervera et al. studied the kinetics of DNA/PEI complex entry, reporting a very rapid interaction of DNA/PEI complexes with HEK 293 cells, while its internalization was observed after one hour [85]. However, only a percentage of the cells finally triggered the production of the GOI. Thus, the intracellular fate of the internalized DNA/PEI complexes might be responsible of their transfection efficiency *in vitro*. In regards to budding, a generalized colocalization of the Gag polyprotein in the cell membrane has been described, indicating the presence of Gag taking part in this process [51,66,72]. However, no individual assembly sites could be resolved due to the size of VLPs was below the limit of detection (~200 nm) of confocal microscopy [15,77]. The use of Super-Resolution Fluorescence Microscopy (SRFM) promises to overcome these limitations (Figure 8) [102]. SRFM is defined as the resolution achieved beyond the classical Abbe diffraction limit [103]. Several studies have used SRFM to understand the mechanisms behind HIV-1 infection [102,104,105]. The application of these advanced methods in a quantitative way represents an interesting alternative to deepen into intracellular processes at nanometric scale in living cells.

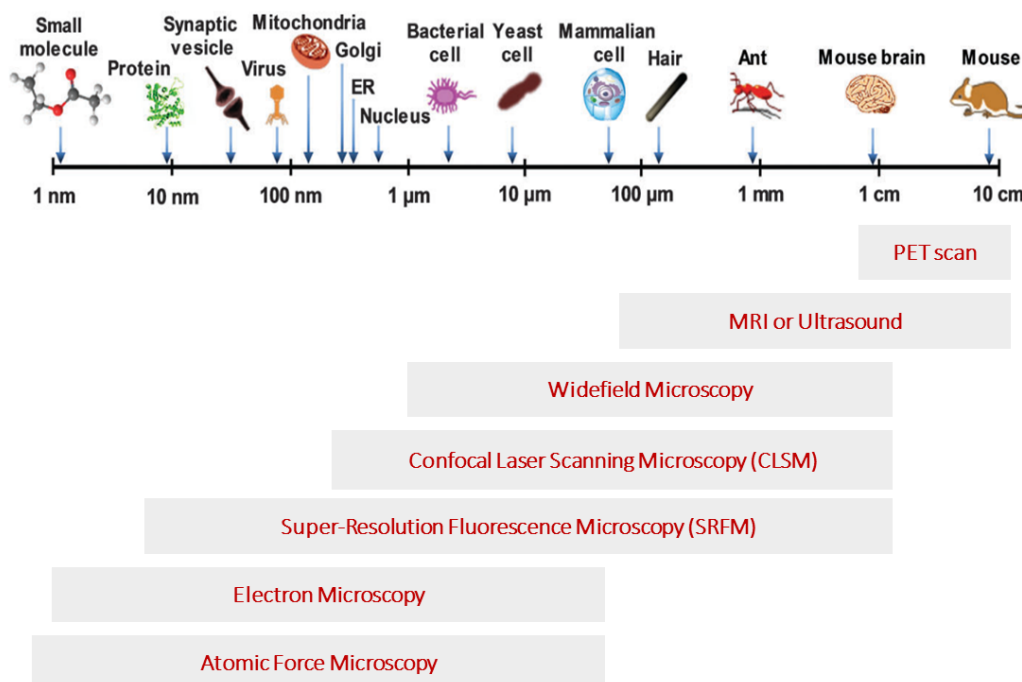


Figure 8: Spatial resolution of the different biological imaging techniques available (adapted from [106], with editorial permission)

## 8. Characterization and quantification of HIV-1 Gag VLPs

VLP quality assessment is of major importance since both, the physicochemical and biological properties, are responsible of their clinical efficacy [107]. Poorly characterized therapeutics may lead to misinterpretation of clinical effects. Moreover, wrong therapeutic titers can impact bioprocess development and can also lead to errors in administered doses. Thus, the characterization and quantification of the product is desired at every stage of the bioprocess, since the quality in the upstream will affect the downstream results [108]. In the same line, identification of the critical process parameters (CPP) that affect the critical quality attributes (CQA) is required to meet the QbD standards.

Compared to simple protein-based bioproducts, the study of CQA in the production of VLPs becomes more difficult, since not only protein composition but also their three-dimensional structure should be ensured. Biochemical, biological and biophysical methods have been used in VLP characterization (Figure 9) [15]. Biochemical protein gels and biological enzyme-linked immunosorbent assay (ELISA) or immunoblot are normally used to assess product purity and

VLP quantification, respectively [34,71,109,110]. However, these assays cannot distinguish assembled from non-assembled structures [111] and may require of biophysical methods to study the structural integrity of the obtained VLPs.

Analytical ultracentrifugation, dynamic light scattering (DLS) and transmission electron microscopy (TEM) were primarily used to assess VLP physical properties [15]. Recently, technical progress in the field of microscopy, as well as the application of nanotechnology to virology, have given rise to several single particle analytical technologies. Nanoparticle Tracking Analysis (NTA), Tunable-Resistive Pulse Sensor (TRPS), Flow Virometry, cryogenic Electron Microscopy (cryo-EM) or Atomic Force Microscopy (AFM) represent very advanced methods to evaluate VLP size, polydispersity, purity and even nanoparticle composition [111]. Of note, AFM, which is based in the detection of the interactions between a probing tip and the sample surface, could be used to study not only the shape and size but also the biochemical surface composition and nanomechanical properties of a viral shell [112].

The specific detection and quantification of VLPs entails several difficulties, especially for enveloped VLPs, which are composed of a protein capsid surrounded by the host-cell lipid membrane. These structures must be distinguished from other similar nanovesicle structures like adventitious viruses, baculoviruses, [113] and extracellular vesicles (EVs), including exosomes and microvesicles [114]. The existence of EVs was described in the 20<sup>th</sup> century, however the discovery that EVs transport several kinds of RNA and DNA, lipids and proteins brought back the attention into the vesicle field [115]. Similar to the production and purification of enveloped VLPs, EV field struggles with appropriate quantification and purification techniques to differentiate the EV subtypes [116]. Several initiatives such as the International Society for Extracellular Vesicles (ISEV) or EV-TRACK website, goal to help the field expand while keeping the highest possible level of technical accuracy and reproducibility [116].

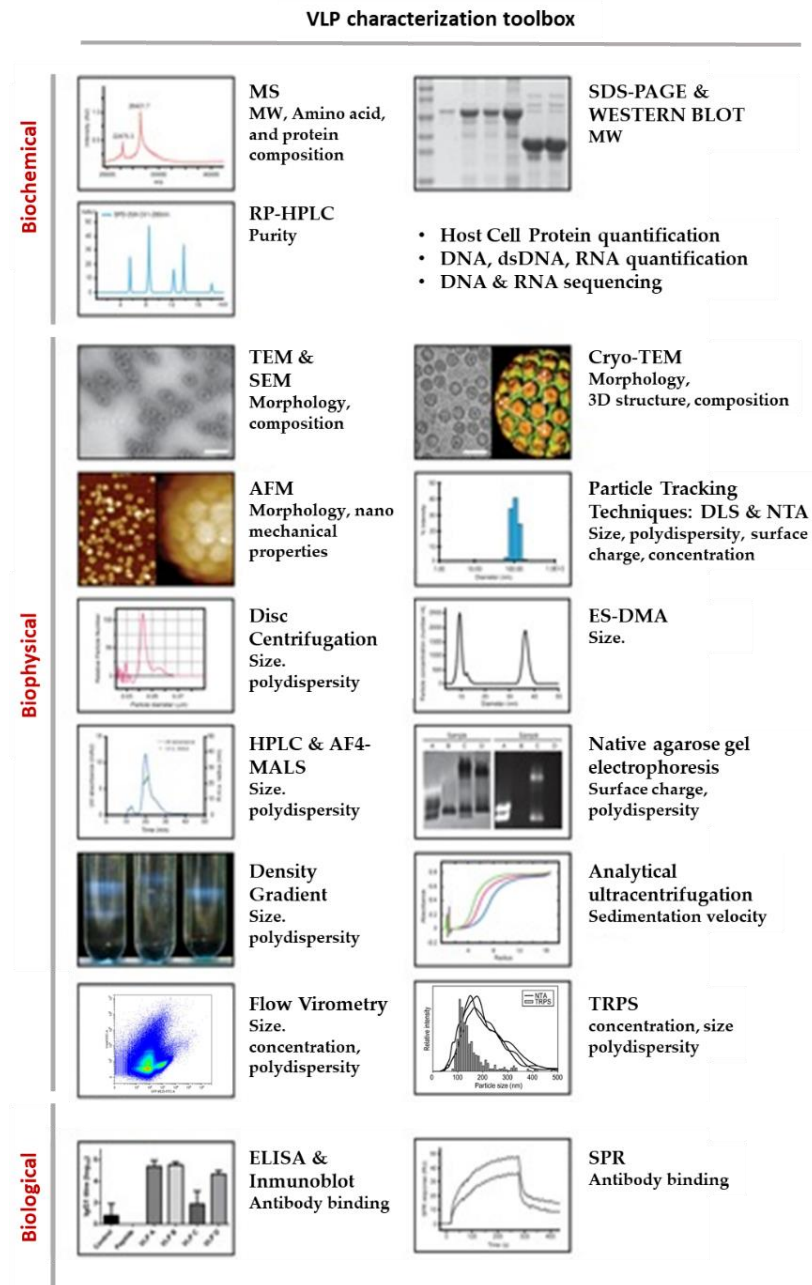


**Figure 9: Analytical tools for VLP characterization [15,72,111].** A range of analytical tools is available for VLP characterization based on their biochemical, biophysical, and biological properties. AF4-MALS: Asymmetric Flow Field-Flow Fractionation coupled with Multiple-Angle Light Scattering; AFM: Atomic Force Microscopy; BLI: Bio-layer Interferometry; Cryo-TEM: cryogenic Transmission Electron Microscopy; DLS: Dynamic Light Scattering; ELISA: Enzyme-Linked Immunosorbent Assay; ES-DMA: electrospray differential mobility analysis; HPLC: High Pressure Liquid Chromatography; MS: Mass Spectrometry; NTA: nanoparticle tracking analysis; SDS-PAGE: Sodium Dodecyl Sulphate Polyacrylamide Gel Electrophoresis; RP-HPLC; Reverse-Phase HPLC; SEM: Scanning Electron Microscopy; SPR: Surface Plasmon Resonance; TEM: Transmission Electron Microscopy; TRPS: Tunable-Resistive Pulse Sensor (Adapted from [15] with editorial permission).

In previous works, a fluorescence-based assay was developed taking advantage of the GFP tag fused to Gag polyprotein [117]. This technique has been used in this thesis to track the presence of Gag polyprotein during the production of HIV-1 Gag-eGFP VLPs, but also to selectively quantify Gag-containing particles over total nanoparticles, by means of fluorescent-based particle counting methods, like NTA or flow virometry.

### **9. Purification of HIV-1 Gag VLPs**

An optimal purification process of HIV-1 Gag VLPs should meet purity and a target concentration criterion, while ensuring a cost-effective process. Depending on the final application, these criteria might vary (veterinary, preclinical, clinical test). Regulatory agencies established a limit of 10 ng of dsDNA of less than 200 bp and 100 ppm of Host-Cell Protein (HCP) per dose in the final biological product for clinical use [118,119]. However, in the case of viruses and virus-like structures, part of these proteins could be intrinsically incorporated in the viral structure [120,121]. Thus, the limit might be product dependent. In regards to the concentration factor, 15 to 60 µg of antigen in 0.5 mL dose have been described for VLPs in clinical and approved products [19]. The route of administration, adjuvant composition and dosage number will affect the final amount of antigen required.

Centrifugation and ultracentrifugation are well-established laboratory purification methods for VLPs [122]. Nevertheless, these methods are non-scalable and labor intensive, hence inter-experimental variability is a general concern. Scalable purification technologies are then of utmost importance for operating under good manufacturing practices (GMP). Viral structures, specially enveloped ones, are more sensitive to detergents, salt concentrations, pH, and mechanical stress [123,124]. Thus, advances in viral-based applications have pushed the field toward the development of new technologies more suited for virus purification (Figure 10) [125]. Some examples of recent purification trains are depicted in Table 4. As observed, there is no general purification processes for these complex particles. Besides the different options, the simpler train the better, since an increase in the number of unit operations has a multiplicative effect in the purification yield [108].

## 10. Scalable DSP for HIV-1 Gag VLPs

The first step in VLP purification is clarification. In the case of HIV-1 Gag VLPs, they benefit from being an extracellular product, thus cell lysis step is not required [28]. More than one unit operation are sometimes used to achieve a desired clarified product. The first clarification aims to remove larger specimens, like cells, while a second one will reduce colloids and other sub-micron particles [123]. Traditional unit operations such as sedimentation or flocculation are still being used in vaccine development. These methods are simple to design and operate, but do not remove cellular debris or sub-micron particles [123,126]. Normal flow filtration (NFF, also known as dead-end filtration) or Tangential Flow Filtration (TFF) are also used in large-scale production processes. Nonetheless, process optimization and low flow rates are sometimes described due to mechanical stress or titer loss caused by virus adsorption. Depth filters, which contain filter aid, enhance retention of cell debris and contribute to improve NFF results, while the use of hollow fibers or membrane cassettes with high cutoffs, reduce the shear stress of viral particles improving TFF. In addition, membrane-based approaches might benefit from the use of inert materials such as regenerated cellulose (RC), polysulfone (PS), polyethersulfone (PES) and polyvinylidene fluoride (PVDF) [108,127].

One or more concentration steps are typically performed after clarification. Affinity, ion-exchange (IEX) or hydrophobic interaction chromatography (HIC) with different matrices, such as polymer-grafted beads, monolith, membrane adsorbers or gigapore resins have been successfully applied to VLPs and viral vectors [71,120,128–132]. Alternative methods such as two-phase extraction or flocculation have been also described [132,133]. TFF was successfully reported for influenza VLPs, where Carvalho et al. described a total recovery of 76 % in a complete membrane-based purification process [52,134]. In addition, a nuclease treatment is often added to reduce dsDNA, especially when anion IEX chromatography is applied [28].

In order to polish VLPs from process-related impurities and prepare them for formulation, diafiltration or size exclusion chromatography (SEC) are mainly used [132]. Polishing steps aim to remove dsDNA, HCP and other contaminant particles that might co-elute with VLPs, such as

EVs, adventitious viruses or BEVS. While the quantification and removal of the first two has been widely described, the separation of VLPs from other contaminant particles is highly difficult due to their similar physicochemical properties. Moleirinho et al. recently reported the development of an affinity chromatography method to separate VLPs from BV [135], whereas Reiter and co-workers achieved a reduction on BEVS content by polymer-grafted chromatography [136]. Regarding EVs, no separation method as such has been described. Limitations at analytical level for the specific quantification of VLPs and EVs present in the same sample may strongly contribute to this fact. Concretely, the available analytical tools do not allow the direct differentiation between VLPs and EVs due to their same origin, composition and physicochemical properties. On the other hand, the enrichment of HIV-1 Gag VLPs over total particles has been reported by TFF, IEX chromatography and heparin affinity chromatography [52,130,137].

Removal of adventitious agents must be demonstrated according to the regulatory authorities. Common methods to remove or inactivate viruses are UV or gamma-irradiation, sterile filtration, detergent treatments or high-temperature incubation, which may compromise the candidate integrity or biological activity. Mitigation of such risk should start at the selection of raw material level. The use of animal-component free, chemically defined cell culture media and GMP-compliant cell lines is encouraged to prevent the introduction of adventitious agents [28]. HIV-1 Gag VLPs, as well as, lentivirus and other viruses, have a mean particle diameter between 100 and 200 nm. Because of that, when sterile filtration is applied (<0.2  $\mu\text{m}$ ) a substantial titer reduction might occur [138]. Therefore, this step could be omitted when the whole process is demonstrated to be performed under aseptic conditions (FDA 1997) [28].



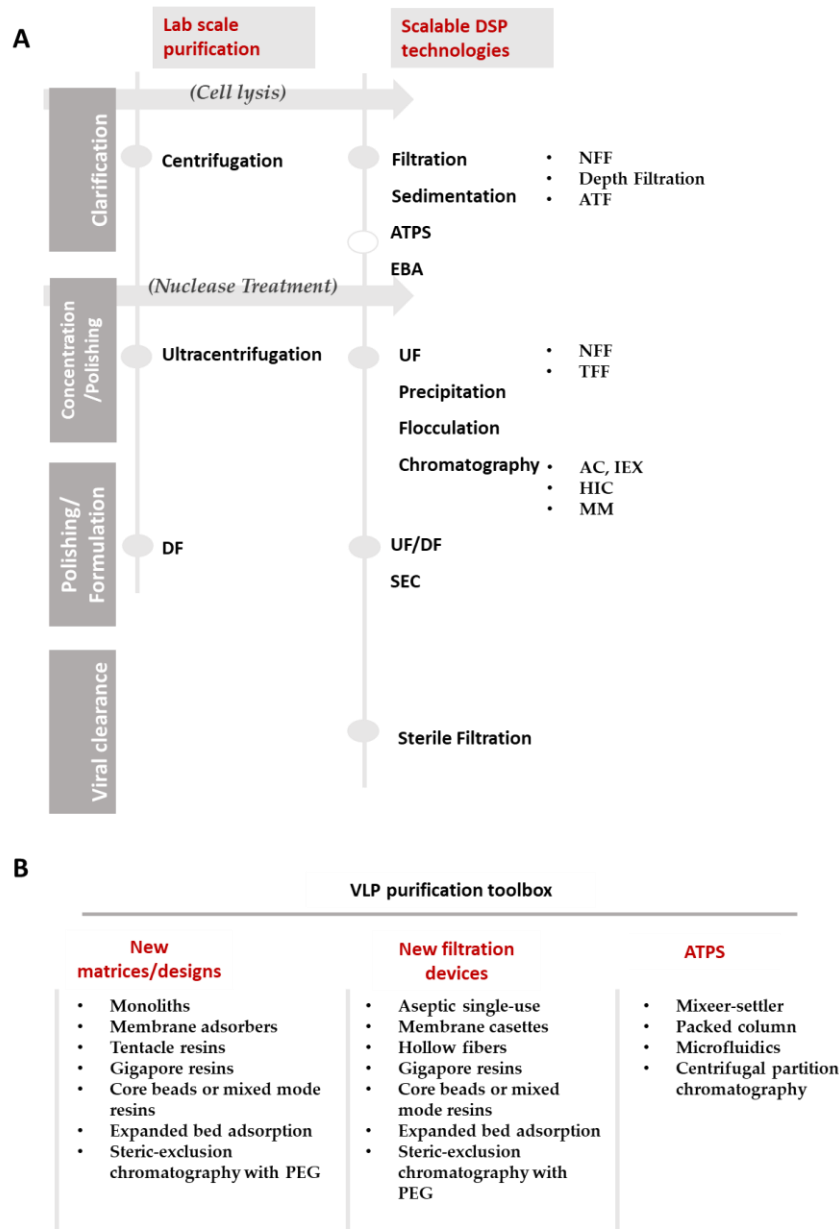


Figure 10: Purification of viral particles state-of-the-art adapted from [28,125] (A) Unit of operation in DSP processes and technologies used (B) Novel technologies for viral particles. AC: Affinity Chromatography; ATPS: Aqueous Two-Phase System; DF: Diafiltration; EBA: Expanded Bed Adsorption; HIC: Hydrophobic Interaction Chromatography; IEC: Ion Exchange Chromatography; MM: Mixed Mode Chromatography; PEG: Polyethylene Glycol; SEC: Size-Exclusion Chromatography; TFF: Tangential Flow Filtration; UF: Ultrafiltration.

Table 3: Examples of recent purification processes for different viral particles adapted from [108]

Biotherapeutic particle type	Strategy	Cell line	Purification steps	Recoveries(%)	References
<b>Virus-like particles</b>					
<b>Influenza</b>	BEVS	High Five	NFF (0.5/0.2 µm) TFF (1000 kDa) TFF (300 kDa) 0.22 µm Sterile filtration	76	Carvalho et al.[134]
	TGE+SGE	HEK293SF cells	BioSep acoustic filter NFF (78mm) NFF (0.45µm) TFF (1000 kDa)	50-71 38-44	Venereo et al. [52]
<b>Zika</b>	SGE	HEK293SF cells	NFF (0.45 µm)	84	Lima et al. [139]
			AEC (Sartobind® Q)	87	
			MMC (Capto™ Core 700)	91	
<b>Enterovirus</b>	BEVS	High Five	TFF (1000 kDa)	80	Lin et al. [140]
			HAC	100	
			TFF (300 kDa)	85	
			SEC	55	
			TFF (300 kDa)	95	
<b>Viral particles</b>					
<b>Influenza</b>	Infection	Adherent MDCK cells	AEC (Capto™ Q) MMC (Capto™ Core 700)	68-87	Tseng et al. [141]
	Infection	Adherent MDCK cells	NFF (0.45 µm) TFF (750 kDa) AEC (Capto™ Q) HIC: PPG	92	Weigel et al. [142]
<b>Adeno-associated virus</b>	TGE	Adherent HEK293 cells	TFF (750 kDa) AS precipitation IEX (Mustang SXTs) IEX (Mustang QXTs) UF (Ultracel 30 kDa) SEC	-	Tomono et al. [143]
	TGE	HEK293EB cells	TFF AS precipitation AEC (HiPrep Q) UF (Ultracel 30 kDa) SEC	20-50	Tomono et al. [144]
<b>Oncolytic Adenovirus</b>	Infection	Adherent A549 cells	NFF (0.2 µm) TFF (750 kDa) AEC (Capto™ Q impRes) TFF (300 kDa) SEC (Sephacrose 4 FF) 0.22 µm Sterile filtration	61	Moleirinho et al. [145]
<b>Extracellular Vesicles</b>	-	Adherent HEK293T cells	NFF (0.2 µm) AEC (CiMmultus™ QA)	-	Xenopoulos [146]
	-	Suspension HEK293T cells	NFF (0.2 µm) TFF (100 kDa) SEC two columns (Sephacrose 4 Fast Flow)	-	Moleirinho et al. [147]

AEC: Anion-Exchange Chromatography; AS: Ammonium Sulfate; HIC: Hydrophobic chromatography; IEX: Ion-Exchange Chromatography; MMC: Mixed Mode Chromatography; NFF: Normal Flow Filtration; PPG: Polypropylene Glycol; SEC: Size Exclusion Chromatography; TFF – Tangential Flow Filtration; UF: Ultrafiltration.

## 11. Formulation and storage of HIV-1 Gag VLPs

Formulation refers to the constituents that are present in the final administrable VLP solution, including the viral vector and excipients, and adjuvants provided that immunological responses are desired (Figure 11). This final preparation must ensure not only that potency and stability is maintained during storage, but also should be designed to be conveniently administered to patients, since concentration or volume will vary depending on the administration route [148]. Current VLP approved products are presented in Table 4. As shown, the majority of approved, as well as, under clinical evaluation candidates are liquid suspensions, ready for administration by intramuscular injection (IM) [17]. As a consequence of this, commercial Hepatitis B vaccines and HPV VLP vaccines must be stored at 2-8 °C presenting a good shelf life of 3-4 years [148]. Nonetheless, keeping these temperatures is not always feasible; the breakage of the cold-chain due to handling errors occurs frequently, even in industrialized countries [149]. This cold-chain instability could be caused by several types of water-mediated destabilization and degradation pathways. Thus, alternative frozen and powder formulations have been developed to overcome this issue and extend the lifespan of viral vectors [107].

The use of freeze-drying [149] and spray-drying [150] offer great promise in this regard. Freeze-drying allows to remove the water content by maintaining low temperatures and applying high vacuum pressures, which prevents from destabilizing temperatures. The dried product can be then easily reconstituted, without the stress of a terminal sterilization step. Live-attenuated vaccines, such as Varicella, Zoster or Rotavirus, inactivated vaccines against Rabies and Japanese Encephalitis are some examples of lyophilized viral-based products [148]. Spray-drying has also gained attention as an alternative technology, avoiding the potential mechanical damage induced by freeze-drying by instead forming a dry powder through a combination of nebulization and dehumidification. Several candidates are being tested with this method, including HPV VLPs [150,151]. The use of air or vacuum drying methods and its further dry delivery with microneedles has been also reported for influenza vaccine with comparable immune responses to intramuscular (IM) injection [17]. A novel thin-film method, able to preserve different biologicals at room

temperature, has been also recently demonstrated for the storage of adenoviruses by Bajrovic and co-authors [152].

**Table 4: Compositions of VLP-based vaccines in the market adapted from [15,148,153,154]**

Commercial Vaccine	Composition per dose				Company
	AR	Antigen	Adjuvant	Excipients	
<b>Engerix®-B hepatitis B vaccine (1 mL/dose)</b>	Liquid (IM)	HBsAg (20 µg)	Aluminum hydroxide (500 µg)	2-phenoxyethanol (5 mg)	GSK
<b>Recombivax HB® hepatitis B vaccine (1 mL/dose)</b>	Liquid (IM)	HBsAg (10 µg)	Aluminum hydroxyphosphate (500 µg)	NaCl (9 mg), Sodium borate (70 µg)	Merck
<b>Gardasil® human papillomavirus vaccine (0.5 mL/dose)</b>	Liquid (IM)	HPV 6 L1 (20 µg) HPV 11 L1 (40 µg) HPV 16 L1 (40 µg) HPV 18 L1 (20 µg)	Aluminum hydroxyphosphate sulfate (225 µg)	NaCl (9.56 mg), L-histidine (0.78 mg), Polysorbate 80 (50 µg), Sodium borate (35 µg)	Merck
<b>Cervarix® human papillomavirus vaccine (0.5 mL/dose)</b>	Liquid (IM)	HPV 16 L1 (20 µg) HPV 18 L1 (20 µg)	AS04 adjuvant system (50 µg of 3-O-desacyl-4'-monophosphoryl lipid A, 500 µg aluminum hydroxyphosphate)	NaCl (4.4 mg), NaH <sub>2</sub> PO <sub>4</sub> <sup>-</sup> (0.624 mg)	GSK
<b>Hecolin® hepatitis E vaccine (0.5 mL/dose)</b>	Liquid (IM)	HE antigen (30 µg)	Aluminum hydroxide (800 µg)	Buffered saline	Innovax
<b>Mosquirix™ malaria vaccine (0.5mL/dose)</b>	Liquid and Lyo (IM)	Portion of <i>P. falciparum</i> circumsporozoite protein fused with HBsAg (25 µg)	AS01 <sub>E</sub> (Quillaja saponaria Molina, fraction 21 (QS-21) (25 µg) and 3-O-desacyl-4'-monophosphoryl lipid A (MPL) (25 µg))	Liquid: Dioleoyl phosphatidylcholine, cholesterol, NaCl, Na <sub>2</sub> HPO <sub>4</sub> · 2H <sub>2</sub> O, KH <sub>2</sub> PO <sub>4</sub> , water for injections Lyo: Sucrose, polysorbate 80, Na <sub>2</sub> HPO <sub>4</sub> · 2H <sub>2</sub> O, NaH <sub>2</sub> PO <sub>4</sub> · 2H <sub>2</sub> O.	GSK
<b>Porcilis PCV® porcine circovirus type 2 vaccine (2mL/dose)</b>	Liquid (IM)	4.5 log <sub>2</sub> ELISA units*	DL-α-tocopheryl acetate (25 mg), Light liquid paraffin (346 mg)	Polysorbate 80, Simethicon, Water for injections	Intervet International BV

\* Antibody titre obtained according to the in vivo potency test in chickens; IM: intramuscular injection

Physicochemical factors such as temperature, pH, salt ions or exposure to light have been described to influence the stability of viral vectors [155][149]. Conformational alterations of the antigens and viral proteins, particle aggregation, and lipid damage in enveloped candidates, should also be considered, as in HIV-1 Gag VLPs. A careful selection of buffers and the addition of thermoprotectants and lyoprotectants can limit fluctuations of pH, osmolarity, oxidation, degradation or desiccation. The presence of salt ions, such as NaCl and the addition of buffers are generally present as excipients. Several classes of compounds such as disaccharides, polyols or animal-derived compounds have been used as thermoprotectants and lyoprotectants [149]. Lynch and co-workers studied the stability of HIV-1 Gag VLPs containing sorbitol, sucrose and thehalose preparations, where 15% thehalose at -70 °C was shown as the best formulation buffer over 12 months [156].

Aside from excipients, adjuvants have become a very relevant part of the formulation in vaccine approaches [157]. Aluminum sulfate salts like AS03 (GSK), AS04 (GSK), MF59 (Novartis), oil-in-water emulsions and Motanide ISA51 are some of the currently licensed adjuvants [17]. Furthermore, efforts are being undertaken to find new adjuvants that might enhance specific types of immunogenicity. New substances like imiquimod, gardiquimod or TLR7/8 have been used with VLPs against several cancers [17]. Together with the new formulations, innovative routes of administration are also being explored to activate immunogenicity at different delivery sites, like the intranasal delivery for mucosal protection against respiratory viruses [158], or the convenient oral delivery for edible vaccines [159], despite further practical and technical aspects should be improved.

Overall, viral-based product formulations have been traditionally designed through trial and error strategies, where different combinations of excipients, process conditions and particle concentrations have been tested. This process becomes very time consuming and hamper the application of many candidates. A deeper understanding of the physicochemical properties that are affected during storage would strongly benefit the development of more rational-based formulation approaches [107].

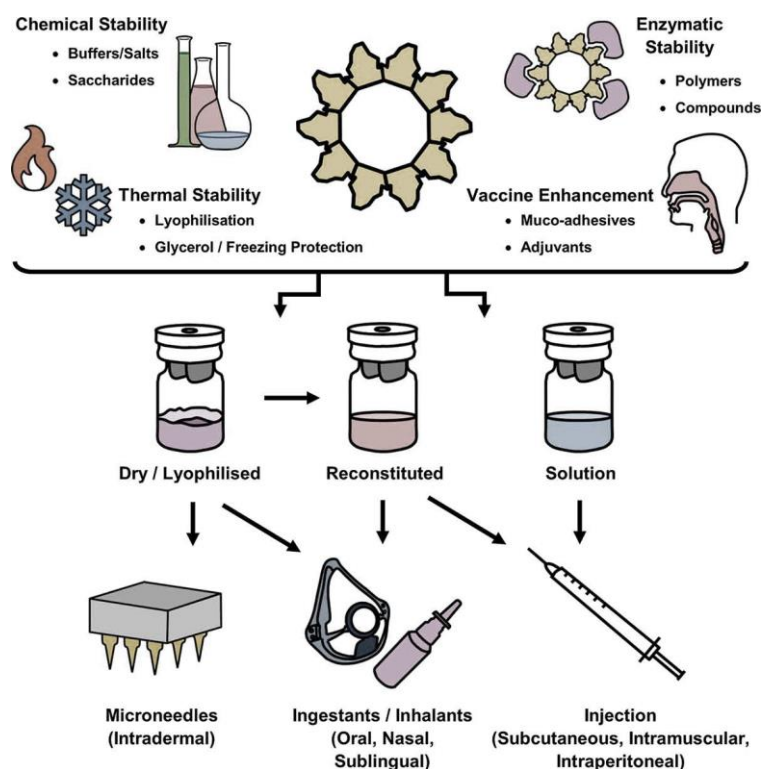


**Figure 11: The Roles of Formulation Science in VLPs, The role of formulation science in VLP vaccine manufacture includes the chemical composition of buffers, preservatives, additives and other stabilizing compounds for maintaining intact VLP. This includes protecting VLP from chemical or physical instability, and enzymatic degradation. Formulations can also include targeted delivery compounds, such as muco-adhesives, and immunogenic components such as adjuvants. Storage and distribution of VLP vaccines, and the subsequent route of administration are also important considerations in formulation science, critical in determining the efficacy and immunogenicity of a vaccine candidate (adapted from [17], with editorial permission).**

In this thesis, the characterization and purification of the production of HIV-1 Gag-eGFP VLPs has been performed. The obtention of HIV-1 Gag-eGFP VLPs by means of PEI-mediated TGE was primarily studied. The suspension adapted HEK 293 cell line cultured in chemically defined cell culture media was used to this end. Secondly, the quality of the produced HIV-1 Gag-eGFP VLPs were compared between different production strategies, like the BEVS system in insect cells at intracellular level and in the harvested productions. Thirdly, the study of several single particle analytical methods for the characterization and quantification of HIV-1 Gag-eGFP VLPs was assessed. Lastly, the development of a scalable purification train for HIV-1 Gag-eGFP VLPs was performed, where the stability of the purified product was characterized for long-term storage conditions.

## Literature

1. Plotkin, S. History of vaccination. *Proc. Natl. Acad. Sci. U. S. A.* **2014**, *111*, 12283–12287.
2. Wirth, T.; Parker, N.; Ylä-Herttuala, S. History of gene therapy. *Gene* **2013**, *525*, 162–169.
3. Ulmer, J.B.; Valley, U.; Rappuoli, R. Vaccine manufacturing: challenges and solutions. *Nat. Biotechnol.* **2006**, *24*, 1377–1383.
4. Shahryari, A.; Saghaeian Jazi, M.; Mohammadi, S.; Razavi Nikoo, H.; Nazari, Z.; Hosseini, E.S.; Burtscher, I.; Mowla, S.J.; Lickert, H. Development and Clinical Translation of Approved Gene Therapy Products for Genetic Disorders. *Front. Genet.* **2019**, *10*, 1–25.
5. Zheng, M.; Huang, J.; Tong, A.; Yang, H. Oncolytic Viruses for Cancer Therapy: Barriers and Recent Advances. *Mol. Ther. - Oncolytics* **2019**, *15*, 234–247.
6. Josefsberg, J.O.; Buckland, B. Vaccine process technology. *Biotechnol. Bioeng.* **2012**, *109*, 1443–1460.
7. Rodrigues, A.F.; Carrondo, M.J.T.; Alves, P.M.; Coroadinha, A.S. Cellular targets for improved manufacturing of virus-based biopharmaceuticals in animal cells. *Trends Biotechnol.* **2014**, *32*, 602–607.
8. Fuenmayor, J.; Gòdia, F.; Cervera, L. Production of virus-like particles for vaccines. *N. Biotechnol.* **2017**, *39*, 174–180.
9. Mäkelä, P.H. Vaccines, coming of age after 200 years. *FEMS Microbiol. Rev.* **2000**, *24*, 9–20.
10. Ghaffarifar, F. Plasmid DNA vaccines: where are we now? *Drugs of Today* **2018**, *54*, 315–333.
11. Liu, M.A. DNA vaccines: An historical perspective and view to the future. *Immunol. Rev.* **2011**, *239*, 62–84.

12. Jeong, H.; Seong, B.L. Exploiting virus-like particles as innovative vaccines against emerging viral infections. *J. Microbiol.* **2017**, *55*, 220–230.
13. Braun, M.; Jandus, C.; Maurer, P.; Hammann-Haenni, A.; Schwarz, K.; Bachmann, M.F.; Speiser, D.E.; Romero, P. Virus-like particles induce robust human T-helper cell responses. *Eur. J. Immunol.* **2012**, *42*, 330–340.
14. Zabel, F.; Mohanan, D.; Bessa, J.; Link, A.; Fettelschoss, A.; Saudan, P.; Kündig, T.M.; Bachmann, M.F. Viral Particles Drive Rapid Differentiation of Memory B Cells into Secondary Plasma Cells Producing Increased Levels of Antibodies. *J. Immunol.* **2014**, *192*, 5499–5508.
15. Lua, L.H.L.; Connors, N.K.; Sainsbury, F.; Chuan, Y.P.; Wibowo, N.; Middelberg, A.P.J. Bioengineering virus-like particles as vaccines. *Biotechnol. Bioeng.* **2014**, *111*, 425–440.
16. Charlton Hume, H.K.; Vidigal, J.; Carrondo, M.J.T.; Middelberg, A.P.J.; Roldão, A.; Lua, L.H.L. Synthetic biology for bioengineering virus-like particle vaccines. *Biotechnol. Bioeng.* **2019**, *116*, 919–935.
17. Donaldson, B.; Lateef, Z.; Walker, G.F.; Young, S.L.; Ward, V.K. Virus-like particle vaccines: immunology and formulation for clinical translation. *Expert Rev. Vaccines* **2018**, *17*, 833–849.
18. Hill, B.D.; Zak, A.; Khera, E.; Wen, F. Engineering Virus-like Particles for Antigen and Drug Delivery. *Curr. Protein Pept. Sci.* **2017**, *19*, 112–127.
19. Roldão, A.; Mellado, M.C.M.; Castilho, L.R.; Carrondo, M.J.; Alves, P.M. Virus-like particles in vaccine development. *Expert Rev. Vaccines* **2010**, *9*, 1149–1176.
20. Yan, D.; Wei, Y.-Q.; Guo, H.-C.; Sun, S.-Q. The application of virus-like particles as vaccines and biological vehicles. *Appl. Microbiol. Biotechnol.* **2015**, *99*, 10415–10432.
21. Bundy, B.C.; Franciszkowicz, M.J.; Swartz, J.R. Escherichia coli-based cell-free synthesis of virus-like particles. *Biotechnol. Bioeng.* **2008**, *100*, 28–37.



22. Kushnir, N.; Streatfield, S.J.; Yusibov, V. Virus-like particles as a highly efficient vaccine platform: Diversity of targets and production systems and advances in clinical development. *Vaccine* **2012**, *31*, 58–83.
23. Liew, M.W.O.; Rajendran, A.; Middelberg, A.P.J. Microbial production of virus-like particle vaccine protein at gram-per-litre levels. *J. Biotechnol.* **2010**, *150*, 224–231.
24. Cregg, J.M.; Tschopp, J.F.; Stillman, C.; Siegel, R.; Akong, M.; Craig, W.S.; Buckholz, R.G.; Madden, K.R.; Kellaris, P.A.; Davis, G.R.; et al. High-Level Expression and Efficient Assembly of Hepatitis B Surface Antigen in the Methylotrophic Yeast, *Pichia Pastoris*. *Nat. Biotechnol.* **1987**, *5*, 479–485.
25. Durous, L.; Rosa-Calatrava, M.; Petiot, E. Advances in influenza virus-like particles bioprocesses. *Expert Rev. Vaccines* **2019**, *18*, 1285–1300.
26. Betenbaugh, M.J.; Tomiya, N.; Narang, S.; Hsu, J.T.A.; Lee, Y.C. Biosynthesis of human-type N-glycans in heterologous systems. *Curr. Opin. Struct. Biol.* **2004**, *14*, 601–606.
27. Hye, J.L.; Yeon, K.K.; Dong, S.H.; Hyung, J.C. Expression of functional human transferrin in stably transfected *Drosophila* S2 cells. *Biotechnol. Prog.* **2004**, *20*, 1192–1197.
28. Cervera, L.; Gòdia, F.; Tarrés-Freixas, F.; Aguilar-Gurrieri, C.; Carrillo, J.; Blanco, J.; Gutiérrez-Granados, S. Production of HIV-1-based virus-like particles for vaccination: achievements and limits. *Appl. Microbiol. Biotechnol.* **2019**, *103*, 7367–7384.
29. Girard, M.P.; Koff, W.C. Human Immunodeficiency Virus Vaccines. In *Plotkin's Vaccines Seventh Edition*; Plokin, S.A., Walter A, O., Offit, P.A., Edwards, K.M., Eds.; Elsevier: Philadelphia, 2018; Vol. 29, pp. 400–429 ISBN 978-0-323-35761-6.
30. Göttlinger, H.G. *HIV-1 Gag : a Molecular Machine Driving Viral Particle Assembly and Release*; Carla KuCarla Kuiken, BrianFoley, Thomas Leitner, Cristian Apetrei, Beatrice Hahn, Ilene Mizrachi, James Mullins, Andrew Rambaut, StevenWolinsky, and B.K. editors., Ed.; Los Alamos National Laboratory, Theoretical Biology andBiophysics: Los

- Alamos, New Mexico., 2001; ISBN 0269-9370.
31. Votteler, J.; Sundquist, W.I. Virus budding and the ESCRT pathway. *Cell Host Microbe* **2013**, *14*, 232–41.
  32. Doan, L.X.; Li, M.; Chen, C.; Yao, Q. Virus-like particles as HIV-1 vaccines. *Rev. Med. Virol.* **2005**, *15*, 75–88.
  33. Zhao, C.; Ao, Z.; Yao, X. Current Advances in Virus-Like Particles as a Vaccination Approach against HIV Infection. *Vaccines* **2016**, *4*, 1–20.
  34. Venereo-Sanchez, A.; Gilbert, R.; Simoneau, M.; Caron, A.; Chahal, P.; Chen, W.; Ansorge, S.; Li, X.; Henry, O.; Kamen, A. Hemagglutinin and neuraminidase containing virus-like particles produced in HEK-293 suspension culture: An effective influenza vaccine candidate. *Vaccine* **2016**, *34*, 3371–3380.
  35. Giles, B.M.; Ross, T.M. A computationally optimized broadly reactive antigen ( COBRA ) based H5N1 VLP vaccine elicits broadly reactive antibodies in mice and ferrets. *Vaccine* **2011**, *29*, 3043–3054.
  36. Carter, D.M.; Darby, C.A.; Lefoley, B.C.; Crevar, C.J.; Alefantis, T.; Oomen, R.; Anderson, S.F.; Strugnell, T.; Cortés-garcia, G.; Vogel, T.U.; et al. Design and Characterization of a Computationally Optimized Broadly Reactive Hemagglutinin Vaccine for H1N1 Influenza Viruses. *J. Virol.* **2016**, *90*, 4720–4734.
  37. Chua, A.J.S.; Vituret, C.; Tan, M.L.C.; Gonzalez, G.; Boulanger, P.; Ng, M. A novel platform for virus-like particle-display of flaviviral envelope domain III: induction of Dengue and West Nile virus neutralizing antibodies. **2013**, 1–18.
  38. Di Bonito, P.; Grasso, F.; Mochi, S.; Petrone, L.; Fanales-belasio, E.; Mei, A.; Cesolini, A.; Laconi, G.; Conrad, H.; Bernhard, H.; et al. Anti-tumor CD8 + T cell immunity elicited by HIV-1-based virus-like particles incorporating HPV-16 E7 protein. *Virology* **2009**, *395*, 45–55.
  39. Osterrieder, N.; Wagner, R.; Brandmüller, C.; Schmidt, P.; Wolf, H.; Kaaden, O.-R.
-

- Protection against EHV-1 Challenge Infection in the Murine Model after Vaccination with Various Formulations of Recombinant Glycoprotein gp14 (gB). *Virology* **1995**, *208*, 500–510.
40. Garnier, L.; Ravallec, M.; Blanchard, P.; Chaabihi, H.; Bossy, J.; Devauchelle, G.; Jestin, A.; Cerutti, M. Incorporation of Pseudorabies Virus gD into Human Immunodeficiency Virus Type 1 Gag Particles Produced in Baculovirus-Infected Cells. **1995**, *69*, 4060–4068.
41. Voráčková, I.; Ulbrich, P.; Diehl, W.E.; Ruml, T. Engineered retroviral virus-like particles for receptor targeting. *Arch. Virol.* **2014**, *159*, 677–688.
42. Kaczmarczyk, S.J.; Sitaraman, K.; Young, H. a; Hughes, S.H.; Chatterjee, D.K. Protein delivery using engineered virus-like particles. *Proc. Natl. Acad. Sci.* **2011**, *108*, 16998–17003.
43. Wu, X.; Liu, H.; Xiao, H.; Kim, J.; Sessaiah, P.; Natsoulis, G.; Boeke, J.E.F.D.; Hahn, B.H. Targeting Foreign Proteins to Human Immunodeficiency Virus Particles via Fusion with Vpr and Vpx. **1995**, *69*, 3389–3398.
44. Deo, V.K.; Kato, T.; Park, E.Y. Chimeric Virus-Like Particles Made Using GAG and M1 Capsid Proteins Providing Dual Drug Delivery and Vaccination Platform. *Mol. Pharm.* **2015**, *12*, 839–845.
45. Cubas, R.; Zhang, S.; Li, M.; Chen, C.; Yao, Q. Chimeric Trop2 virus-like particles: A potential immunotherapeutic approach against pancreatic cancer. *J. Immunother.* **2011**, *34*, 251–263.
46. Zhang, S.; Yong, L.; Li, D.; Cubas, R.; Chen, C.; Yao, Q. Mesothelin Virus-Like Particle Immunization Controls Pancreatic Cancer Growth through CD8 + T Cell Induction and Reduction in the Frequency of CD4 + foxp3 + ICOS 2 Regulatory T Cells. **2013**, *8*.
47. Ong, H.K.; Tan, W.S.; Ho, K.L. Virus like particles as a platform for cancer vaccine development. *PeerJ* **2017**, *2017*, 1–31.
48. Li, F.; Vijayasankaran, N.; Shen, A.; Kiss, R.; Amanullah, A. Cell culture processes for
-

- monoclonal antibody production. *MAbs* **2010**, 2, 466–479.
49. Meyer, H.; Schmidhalter, D.R. *Industrial Scale Suspension Culture of Living Cells*; Meyer, H., R.Schmidhalter, D., Eds.; First Edit.; Wiley Blackwell: Weinheim, 2014; ISBN 978-3-527-68332-1.
50. Castilho, L.R.; Moraes, Â.M.; Augusto, E.F.P.; Butler, M. *Animal Cell Technology: From Biopharmaceuticals to Gene Therapy*; Castilho, L.R., Moraes, Â.M., Augusto, E.F.P., Butler, M., Eds.; Taylor & Francis: New York, 2008; ISBN 978-0-415-42304-5.
51. Cervera, L.; Gutiérrez-Granados, S.; Martínez, M.; Blanco, J.; Gòdia, F.; Segura, M.M. Generation of HIV-1 Gag VLPs by transient transfection of HEK 293 suspension cell cultures using an optimized animal-derived component free medium. *J. Biotechnol.* **2013**, 166, 152–165.
52. Venereo-Sanchez, A.; Simoneau, M.; Lanthier, S.; Chahal, P.; Bourget, L.; Ansorge, S.; Gilbert, R.; Henry, O.; Kamen, A. Process intensification for high yield production of influenza H1N1 Gag virus-like particles using an inducible HEK-293 stable cell line. *Vaccine* **2017**, 35, 4220–4228.
53. Fuenmayor, J.; Cervera, L.; Gòdia, F.; Kamen, A. Extended gene expression for Gag VLP production achieved at bioreactor scale. *J. Chem. Technol. Biotechnol.* **2019**, 94, 302–308.
54. Gutiérrez-Granados, S.; Farràs, Q.; Hein, K.; Fuenmayor, J.; Félez, P.; Segura, M.; Gòdia, F. Production of HIV virus-like particles by transient transfection of CAP-T cells at bioreactor scale avoiding medium replacement. *J. Biotechnol.* **2017**, 263, 11–20.
55. Gutiérrez-Granados, S.; Gòdia, F.; Cervera, L. Continuous manufacturing of viral particles. *Curr. Opin. Chem. Eng.* **2018**, 22, 107–114.
56. Maksimenko, O.; Gasanov, N.B.; Georgiev, P. Regulatory elements in vectors for efficient generation of cell lines producing target proteins. *Acta Naturae* **2015**, 7, 15–26.
57. Bleckmann, M.; Schürig, M.; Chen, F.-F.; Yen, Z.-Z.; Lindemann, N.; Meyer, S.; Spehr, J.; van den Heuvel, J. Identification of Essential Genetic Baculoviral Elements for
-

- Recombinant Protein Expression by Transactivation in Sf21 Insect Cells. *PLoS One* **2016**, *11*, e0149424.
58. Jazayeri, S.H.; Amiri-Yekta, A.; Bahrami, S.; Gourabi, H.; Sanati, M.H.; Khorramizadeh, M.R. Vector and Cell Line Engineering Technologies Toward Recombinant Protein Expression in Mammalian Cell Lines. *Appl. Biochem. Biotechnol.* **2018**, *185*, 986–1003.
59. Fischer, S.; Paul, A.J.; Wagner, A.; Mathias, S.; Geiss, M.; Schandock, F.; Domnowski, M.; Zimmermann, J.; Handrick, R.; Hesse, F.; et al. miR-2861 as novel HDAC5 inhibitor in CHO cells enhances productivity while maintaining product quality. *Biotechnol. Bioeng.* **2015**, *112*, 2142–2153.
60. Fuenmayor, J.; Cervera, L.; Rigau, C.; Gòdia, F. Enhancement of HIV-1 VLP production using gene inhibition strategies. *Appl. Microbiol. Biotechnol.* **2018**, *102*, 4477–4487.
61. Baldi, L.; Hacker, D.L.; Adam, M.; Wurm, F.M. Recombinant protein production by large-scale transient gene expression in mammalian cells: state of the art and future perspectives. *Biotechnol. Lett.* **2007**, *29*, 677–684.
62. Fischer, S.; Charara, N.; Gerber, A.; Wölfel, J.; Schiedner, G.; Voedisch, B.; Geisse, S. Transient recombinant protein expression in a human amniocyte cell line: The CAP-T® cell system. *Biotechnol. Bioeng.* **2012**, *109*, 2250–2261.
63. Lai, T.; Yang, Y.; Ng, S.K. Advances in mammalian cell line development technologies for recombinant protein production. *Pharmaceuticals* **2013**, *6*, 579–603.
64. Jäger, V.; Büssow, K.; Schirrmann, T. Transient Recombinant Protein Expression in Mammalian Cells. In *Animal Cell Culture*; Al-Rubeai, M., Ed.; Springer, Cham: Basel, 2015; Vol. 9, pp. 27–64 ISBN 978-3-319-10320-4.
65. Genzel, Y. Designing cell lines for viral vaccine production: Where do we stand? *Biotechnol. J.* **2015**, *10*, 728–740.
66. Puente-Massaguer, E.; Lecina, M.; Gòdia, F. Application of advanced quantification techniques in nanoparticle-based vaccine development with the Sf9 cell baculovirus
-

- expression system. *Vaccine* **2020**, *38*, 1849–1859.
67. Puente-Massaguer, E.; Lecina, M.; Gòdia, F. Integrating nanoparticle quantification and statistical design of experiments for efficient HIV-1 virus-like particle production in High Five cells. *Appl. Microbiol. Biotechnol.* **2020**, *104*, 1569–1582.
68. Strobl, F.; Ghorbanpour, S.M.; Palmberger, D.; Striedner, G. Evaluation of screening platforms for virus-like particle production with the baculovirus expression vector system in insect cells. *Sci. Rep.* **2020**, *10*, 1–9.
69. Gutiérrez-Granados, S.; Cervera, L.; Kamen, A.A.; Gòdia, F. Advancements in mammalian cell transient gene expression (TGE) technology for accelerated production of biologics. *Crit. Rev. Biotechnol.* **2018**, *38*, 1–23.
70. Bono, N.; Ponti, F.; Mantovani, D.; Candiani, G. Non-Viral in Vitro Gene Delivery: It is Now Time to Set the Bar! *Pharmaceutics* **2020**, *12*, 1–23.
71. Steppert, P.; Burgstaller, D.; Klausberger, M.; Berger, E.; Aguilar, P.P.; Schneider, T.A.; Kramberger, P.; Tover, A.; Nöbauer, K.; Razzazi-Fazeli, E.; et al. Purification of HIV-1 gag virus-like particles and separation of other extracellular particles. *J. Chromatogr. A* **2016**, *1455*, 93–101.
72. Gutiérrez-Granados, S.; Cervera, L.; Segura, M. de L.M.; Wölfel, J.; Gòdia, F. Optimized production of HIV-1 virus-like particles by transient transfection in CAP-T cells. *Appl. Microbiol. Biotechnol.* **2016**, *100*, 3935–47.
73. Shen, X.; Michel, P.O.; Xie, Q.; Hacker, D.L.; Wurm, F.M. Transient transfection of insect Sf-9 cells in TubeSpin® bioreactor 50 tubes. *BMC Proc.* **2011**, *5*, P37.
74. Vidigal, J.; Fernandes, B.; Dias, M.M.; Patrone, M.; Roldão, A.; Carrondo, M.J.T.T.; Alves, P.M.; Teixeira, A.P. RMCE-based insect cell platform to produce membrane proteins captured on HIV-1 Gag virus-like particles. *Appl. Microbiol. Biotechnol.* **2018**, *102*, 655–666.
75. Tagliamonte, M.; Visciano, M.L.; Tornesello, M.L.; De Stradis, A.; Buonaguro, F.M.;
-

- Buonaguro, L. Constitutive expression of HIV-VLPs in stably transfected insect cell line for efficient delivery system. *Vaccine* **2010**, *28*, 6417–6424.
76. Puente-Massaguer, E.; Lecina, M.; Gòdia, F. Nanoscale characterization coupled to multi-parametric optimization of Hi5 cell transient gene expression. *Appl. Microbiol. Biotechnol.* **2018**, *102*, 10495–10510.
77. Shi, B.; Zheng, M.; Tao, W.; Chung, R.; Jin, D.; Ghaffari, D.; Farokhzad, O.C. Challenges in DNA Delivery and Recent Advances in Multifunctional Polymeric DNA Delivery Systems. *Biomacromolecules* **2017**, *18*, 2231–2246.
78. Boussif, O.; Lezoualc'h, F.; Zanta, M.A.; Mergny, M.D.; Scherman, D.; Demeneix, B.; Behr, J.P. A versatile vector for gene and oligonucleotide transfer into cells in culture and in vivo: polyethylenimine. *Proc. Natl. Acad. Sci.* **1995**, *92*, 7297–7301.
79. Yue, Y.; Wu, C. Progress and perspectives in developing polymeric vectors for in vitro gene delivery. *Biomater. Sci.* **2013**, *1*, 152–170.
80. Hwang, M.E.; Keswani, R.K.; Pack, D.W. Dependence of PEI and PAMAM Gene Delivery on Clathrin- and Caveolin-Dependent Trafficking Pathways. *Pharm. Res.* **2015**, *32*, 2051–2059.
81. Tait, A.S.; Brown, C.J.; Galbraith, D.J.; Hines, M.J.; Hoare, M.; Birch, J.R.; James, D.C. Transient production of recombinant proteins by Chinese hamster ovary cells using polyethyleneimine/DNA complexes in combination with microtubule disrupting anti-mitotic agents. *Biotechnol. Bioeng.* **2004**, *88*, 707–721.
82. Grosse, S.; Thévenot, G.; Monsigny, M.; Fajac, I. Which mechanism for nuclear import of plasmid DNA complexed with polyethylenimine derivatives? *J. Gene Med.* **2006**, *8*, 845–51.
83. Han, X.Z.; Fang, Q.Y.; Yao, F.; Wang, X.N.; Wang, J.F.; Yang, S.L.; Shen, B.Q. The heterogeneous nature of polyethylenimine-DNA complex formation affects transient gene expression. *Cytotechnology* **2009**, *60*, 63–75.

84. Gillard, M.; Jia, Z.; Hou, J.J.C.; Song, M.; Gray, P.P.; Munro, T.P.; Monteiro, M.J. Intracellular trafficking pathways for nuclear delivery of plasmid DNA complexed with highly efficient endosome escape polymers. *Biomacromolecules* **2014**, *15*, 3569–3576.
85. Cervera, L.; González-Domínguez, I.; Segura, M.M.; Gòdia, F. Intracellular characterization of Gag VLP production by transient transfection of HEK 293 cells. *Biotechnol. Bioeng.* **2017**, *114*, 2507–2517.
86. van Gaal, E.V.B.; Van Eijk, R.; Oosting, R.S.; Kok, R.J.; Hennink, W.E.; Crommelin, D.J.A.; Mastrobattista, E. How to screen non-viral gene delivery systems in vitro? *J. Control. Release* **2011**, *154*, 218–232.
87. Fukumoto, Y.; Obata, Y.; Ishibashi, K.; Tamura, N.; Kikuchi, I.; Aoyama, K.; Hattori, Y.; Tsuda, K.; Nakayama, Y.; Yamaguchi, N. Cost-effective gene transfection by DNA compaction at pH 4.0 using acidified, long shelf-life polyethylenimine. *Cytotechnology* **2010**, *62*, 73–82.
88. Sang, Y.; Xie, K.; Mu, Y.; Lei, Y.; Zhang, B.; Xiong, S.; Chen, Y.; Qi, N. Salt ions and related parameters affect PEI-DNA particle size and transfection efficiency in Chinese hamster ovary cells. *Cytotechnology* **2015**, *67*, 67–74.
89. Raup, A.; Wang, H.; Synatschke, C. V.; Jérôme, V.; Agarwal, S.; Pergushov, D. V.; Müller, A.H.E.; Freitag, R. Compaction and Transmembrane Delivery of pDNA: Differences between 1-PEI and Two Types of Amphiphilic Block Copolymers. *Biomacromolecules* **2017**, *18*, 808–818.
90. Blakney, A.K.; Yilmaz, G.; McKay, P.F.; Becer, C.R.; Shattock, R.J. One Size Does Not Fit All: The Effect of Chain Length and Charge Density of Poly(ethylene imine) Based Copolymers on Delivery of pDNA, mRNA, and RepRNA Polyplexes. *Biomacromolecules* **2018**, *19*, 2870–2879.
91. Ulasov, A. V; Khramtsov, Y. V; Trusov, G.A.; Rosenkranz, A.A.; Sverdlov, E.D.; Sobolev, A.S. Properties of PEI-based polyplex nanoparticles that correlate with their



- transfection efficacy. *Mol. Ther.* **2011**, *19*, 103–12.
92. Fuenmayor, J.; Cervera, L.; Gutiérrez-Granados, S.; Gòdia, F. Transient gene expression optimization and expression vector comparison to improve HIV-1 VLP production in HEK293 cell lines. *Appl. Microbiol. Biotechnol.* **2018**, *102*, 165–174.
93. Bollin, F.; Dechavanne, V.; Chevalet, L. Design of Experiment in CHO and HEK transient transfection condition optimization. *Protein Expr. Purif.* **2011**, *78*, 61–68.
94. Visaveliya, N.R.; Köhler, J.M. Single-Step In Situ Assembling Routes for the Shape Control of Polymer Nanoparticles. *Biomacromolecules* **2018**, *19*, 1047–1064.
95. Choosakoonkriang, S.; Lobo, B.A.; Koe, G.S.; Koe, J.G.; Middaugh, C.R.R. Biophysical characterization of PEI/DNA complexes. *J. Pharm. Sci.* **2003**, *92*, 1710–22.
96. Cho, E.J.; Holback, H.; Liu, K.C.; Abouelmagd, S.A.; Park, J.; Yeo, Y. Nanoparticle Characterization: State of the Art, Challenges, and Emerging Technologies. *Mol. Pharm.* **2013**, *10*, 2093–2110.
97. Zhang, W.; Kang, X.; Yuan, B.; Wang, H.; Zhang, T.; Shi, M.; Zheng, Z.; Zhang, Y.; Peng, C.; Fan, X.; et al. Nano-structural effects on gene transfection: Large, botryoid-shaped nanoparticles enhance DNA delivery via macropinocytosis and effective dissociation. *Theranostics* **2019**, *9*, 1580–1598.
98. Pezzoli, D.; Giupponi, E.; Mantovani, D.; Candiani, G. Size matters for in vitro gene delivery: investigating the relationships among complexation protocol, transfection medium, size and sedimentation. *Sci. Rep.* **2017**, *7*, 44134.
99. Rathore, A.S.; Winkle, H. Quality by design for biopharmaceuticals. *Nat. Biotechnol.* **2009**, *27*, 26–34.
100. Chojnacki, J.; Müller, B. Investigation of HIV-1 Assembly and Release Using Modern Fluorescence Imaging Techniques. *Traffic* **2013**, *14*, 15–24.
101. Midoux, P.; Breuzard, G.; Gomez, J.P.; Pichon, C. Polymer-Based Gene Delivery: A

- Current Review on the Uptake and In- tracellular Trafficking of Polyplexes. *Curr. Gene Ther.* **2008**, *8*, 335–352.
102. Hanne, J.; Zila, V.; Heilemann, M.; Müller, B.; Kräusslich, H.-G. Super-resolved insights into human immunodeficiency virus biology. *FEBS Lett.* **2016**, *590*, 1858–1876.
103. Godin, A.G.; Lounis, B.; Cognet, L. Super-resolution Microscopy Approaches for Live Cell Imaging. *Biophysj* **2014**, *107*, 1777–1784.
104. Foster, T.L.; Pickering, S.; Neil, S.J.D. Inhibiting the Ins and Outs of HIV Replication: Cell-Intrinsic Antiretroviral Restrictions at the Plasma Membrane. *Front. Immunol.* **2018**, *8*, 1–20.
105. Chojnacki, J.; Eggeling, C. Super-resolution fluorescence microscopy studies of human immunodeficiency virus. *Retrovirology* **2018**, *15*, 1–16.
106. Yang, Z.; Sharma, A.; Qi, J.; Peng, X.; Lee, D.Y.; Hu, R.; Lin, D.; Qu, J.; Kim, J.S. Super-resolution fluorescent materials: an insight into design and bioimaging applications. *Chem. Soc. Rev.* **2016**, *45*, 4651–4667.
107. Jain, N.K.; Sahni, N.; Kumru, O.S.; Joshi, S.B.; Volkin, D.B.; Russell Middaugh, C. Formulation and stabilization of recombinant protein based virus-like particle vaccines. *Adv. Drug Deliv. Rev.* **2015**, *93*, 42–55.
108. Moleirinho, M.G.; Silva, R.J.S.; Alves, P.M.; Carrondo, M.J.T.; Peixoto, C. Current challenges in biotherapeutic particles manufacturing. *Expert Opin. Biol. Ther.* **2020**, *20*, 451–465.
109. Transfiguracion, J.; Manceur, A.P.; Petiot, E.; Thompson, C.M.; Kamen, A.A. Particle quantification of influenza viruses by high performance liquid chromatography. *Vaccine* **2015**, *33*, 78–84.
110. Fontana, D.; Kratje, R.; Etcheverrigaray, M.; Prieto, C. Immunogenic virus-like particles continuously expressed in mammalian cells as a veterinary rabies vaccine candidate. *Vaccine* **2015**, *33*, 4238–4246.
-

111. Heider, S.; Metzner, C. Quantitative real-time single particle analysis of virions. *Virology* **2014**, *462–463*, 199–206.
112. de Pablo, P.J. Atomic force microscopy of virus shells. *Semin. Cell Dev. Biol.* **2018**, *73*, 199–208.
113. Wang, Q.; Bosch, B.-J.; Vlak, J.M.; van Oers, M.M.; Rottier, P.J.; van Lent, J.W.M. Budded baculovirus particle structure revisited. *J. Invertebr. Pathol.* **2016**, *134*, 15–22.
114. Akers, J.C.; Gonda, D.; Kim, R.; Carter, B.S.; Chen, C.C. Biogenesis of extracellular vesicles (EV): exosomes, microvesicles, retrovirus-like vesicles, and apoptotic bodies. *J. Neurooncol.* **2013**, *113*, 1–11.
115. Sharma, S.; Gimzewski, J.K. Exosomes: Nanoscale Packages Contain the Health-state [Status Quo] of the Cells that Secrete them. *J. Nanomed. Nanotechnol.* **2015**, *06*, 1–3.
116. Tkach, M.; Kowal, J.; Théry, C. Why the need and how to approach the functional diversity of extracellular vesicles. *Philos. Trans. R. Soc. B Biol. Sci.* **2018**, *373*, 20160479.
117. Gutiérrez-Granados, S.; Cervera, L.; Gòdia, F.; Carrillo, J.; Segura, M.M. Development and validation of a quantitation assay for fluorescently tagged HIV-1 virus-like particles. *J. Virol. Methods* **2013**, *193*, 85–95.
118. Eaton, L.C. Host cell contaminant protein assay development for recombinant biopharmaceuticals. *J. Chromatogr. A* **1995**, *705*, 105–114.
119. Knezevic, I.; Stacey, G.; Petricciani, J. WHO Study Group on cell substrates for production of biologicals, Geneva, Switzerland, 11-12 June 2007. *Biologicals* **2008**, *36*, 203–211.
120. Pato, T.P.; Souza, M.C.O.; Silva, A.N.M.R.; Pereira, R.C.; Silva, M. V.; Caride, E.; Gaspar, L.P.; Freire, M.S.; Castilho, L.R. Development of a membrane adsorber based capture step for the purification of yellow fever virus. *Vaccine* **2014**, *32*, 2789–2793.
121. Sviben, D.; Forcic, D.; Ivancic-Jelecki, J.; Halassy, B.; Brgles, M. Recovery of infective

- virus particles in ion-exchange and hydrophobic interaction monolith chromatography is influenced by particle charge and total-to-infective particle ratio. *J. Chromatogr. B* **2017**, *1054*, 10–19.
122. Vicente, T.; Roldão, A.; Peixoto, C.; Carrondo, M.J.T.T.; Alves, P.M. Large-scale production and purification of VLP-based vaccines. *J. Invertebr. Pathol.* **2011**, *107*, S42–S48.
123. Besnard, L.; Fabre, V.; Fettig, M.; Gousseinov, E.; Kawakami, Y.; Laroudie, N.; Scanlan, C.; Pattnaik, P. Clarification of vaccines: An overview of filter based technology trends and best practices. *Biotechnol. Adv.* **2016**, *34*, 1–13.
124. Nestola, P.; Peixoto, C.; Silva, R.R.J.S.; Alves, P.M.; Mota, J.P.B.; Carrondo, M.J.T. Improved virus purification processes for vaccines and gene therapy. *Biotechnol. Bioeng.* **2015**, *112*, 843–857.
125. Effio, C.L.; Hubbuch, J. Next generation vaccines and vectors: Designing downstream processes for recombinant protein-based virus-like particles. *Biotechnol. J.* **2015**, *10*, 715–27.
126. Westoby, M.; Chrostowski, J.; Vilmorin, P. De; Smelko, J.P.; Romero, J.K.; Carolina, N. Effects of Solution Environment on Mammalian Cell Fermentation Broth Properties: Enhanced Impurity Removal and Clarification Performance. **2011**, *108*, 50–58.
127. Carvalho, S.B.; Silva, R.J.S.; Moreira, A.S.; Cunha, B.; Clemente, J.J.; Alves, P.M.; Carrondo, M.J.T.; Xenopoulos, A.; Peixoto, C. Efficient filtration strategies for the clarification of influenza virus-like particles derived from insect cells. *Sep. Purif. Technol.* **2019**, *218*, 81–88.
128. Pereira Aguilar, P.; González-Domínguez, I.; Schneider, T.A.; Gòdia, F.; Cervera, L.; Jungbauer, A. At-line multi-angle light scattering detector for faster process development in enveloped virus-like particle purification. *J. Sep. Sci.* **2019**, *42*, 2640–2648.
129. Pereira Aguilar, P.; Schneider, T.A.; Wetter, V.; Maresch, D.; Ling, W.L.; Tover, A.;
-

- Steppert, P.; Jungbauer, A. Polymer-grafted chromatography media for the purification of enveloped virus-like particles, exemplified with HIV-1 gag VLP. *Vaccine* **2019**, *37*, 7070–7080.
130. Steppert, P.; Burgstaller, D.; Klausberger, M.; Kramberger, P.; Tover, A.; Berger, E.; Nöbauer, K.; Razzazi-Fazeli, E.; Jungbauer, A. Separation of HIV-1 gag virus-like particles from vesicular particles impurities by hydroxyl-functionalized monoliths. *J. Sep. Sci.* **2017**, *40*, 979–990.
131. Fernandes, C.S.M.; Barbosa, I.; Castro, R.; Pina, A.S.; Coroadinha, A.S.; Barbas, A.; Roque, A.C.A. Retroviral particles are effectively purified on an affinity matrix containing peptides selected by phage-display. *Biotechnol. J.* **2016**, *11*, 1513–1524.
132. Ladd Effio, C.; Wenger, L.; Ötes, O.; Oelmeier, S.A.; Kneusel, R.; Hubbuch, J. Downstream processing of virus-like particles: Single-stage and multi-stage aqueous two-phase extraction. *J. Chromatogr. A* **2015**, *1383*, 35–46.
133. Gencoglu, M.F.; Heldt, C.L. Enveloped virus flocculation and removal in osmolyte solutions. *J. Biotechnol.* **2015**, *206*, 8–11.
134. Carvalho, S.B.; Silva, R.J.S.; Moleirinho, M.G.; Cunha, B.; Moreira, A.S.; Xenopoulos, A.; Alves, P.M.; Carrondo, M.J.T.; Peixoto, C. Membrane-Based Approach for the Downstream Processing of Influenza Virus-Like Particles. *Biotechnol. J.* **2019**, *14*, 1–12.
135. Moleirinho, M.G.; Fernandes, R.P.; Carvalho, S.B.; Bezemer, S.; Detmers, F.; Hermans, P.; Silva, R.J.S.; Alves, P.M.; Carrondo, M.J.T.; Peixoto, C. Baculovirus affinity removal in viral-based bioprocesses. *Sep. Purif. Technol.* **2020**, *241*, 1–9.
136. Reiter, K.; Aguilar, P.P.; Grammelhofer, D.; Joseph, J.; Steppert, P.; Jungbauer, A. Separation of influenza virus-like particles from baculovirus by polymer grafted anion-exchanger. *J. Sep. Sci.* **2020**, 1–21.
137. Reiter, K.; Aguilar, P.P.; Wetter, V.; Steppert, P.; Tover, A.; Jungbauer, A. Separation of virus-like particles and extracellular vesicles by flow-through and heparin affinity
-

- chromatography. *J. Chromatogr. A* **2019**, *1588*, 77–84.
138. Merten, O.-W.; Hebben, M.; Bovolenta, C. Production of lentiviral vectors. *Mol. Ther. - Methods Clin. Dev.* **2016**, *3*, 1–14.
139. Lima, T.M.; Souza, M.O.; Castilho, L.R. Purification of flavivirus VLPs by a two-step chromatographic process. *Vaccine* **2019**, *37*, 7061–7069.
140. Lin, S.-Y.Y.; Chiu, H.-Y.Y.; Chiang, B.-L.L.; Hu, Y.-C.C. Development of EV71 virus-like particle purification processes. *Vaccine* **2015**, *33*, 5966–5973.
141. Tseng, Y.-F.F.; Weng, T.-C.C.; Lai, C.-C.C.; Chen, P.-L.L.; Lee, M.-S.S.; Hu, A.Y.-C.C. A fast and efficient purification platform for cell-based influenza viruses by flow-through chromatography. *Vaccine* **2018**, *36*, 3146–3152.
142. Weigel, T.; Soliman, R.; Wolff, M.W.; Reichl, U. Hydrophobic-interaction chromatography for purification of influenza A and B virus. *J. Chromatogr. B Anal. Technol. Biomed. Life Sci.* **2019**, *1117*, 103–117.
143. Tomono, T.; Hirai, Y.; Okada, H.; Adachi, K.; Ishii, A.; Shimada, T.; Onodera, M.; Tamaoka, A.; Okada, T. Ultracentrifugation-free chromatography-mediated large-scale purification of recombinant adeno-associated virus serotype 1 (rAAV1). *Mol. Ther. - Methods Clin. Dev.* **2016**, *3*, 1–8.
144. Tomono, T.; Hirai, Y.; Okada, H.; Miyagawa, Y.; Adachi, K.; Sakamoto, S.; Kawano, Y.; Chono, H.; Mineno, J.; Ishii, A.; et al. Highly efficient ultracentrifugation-free chromatographic purification of recombinant AAV serotype 9 (rAAV9). *Mol. Ther. - Methods Clin. Dev.* **2018**, *11*, 180–190.
145. Moleirinho, M.G.; Rosa, S.; Carrondo, M.J.T.; Silva, R.J.S.; Hagner-McWhirter, Å.; Ahlén, G.; Lundgren, M.; Alves, P.M.; Peixoto, C. Clinical-Grade Oncolytic Adenovirus Purification Using Polysorbate 20 as an Alternative for Cell Lysis. *Curr. Gene Ther.* **2018**, *18*, 366–374.
146. Xenopoulos, A. [Recorded Webinar] Production and Purification of Virus-like Particles.
-

147. Moleirinho, M.G.; Silva, R.J.S.; Carrondo, M.J.T.; Alves, P.M.; Peixoto, C. Exosome-based therapeutics: Purification using semi-continuous multi-column chromatography. *Sep. Purif. Technol.* **2019**, *224*, 515–523.
148. Kumru, O.S.; Joshi, S.B.; Smith, D.E.; Middaugh, C.R.; Prusik, T.; Volkin, D.B. Vaccine instability in the cold chain: Mechanisms, analysis and formulation strategies. *Biologicals* **2014**, *42*, 237–259.
149. Hansen, L.J.J.; Daoussi, R.; Vervaeet, C.; Remon, J.P.; De Beer, T.R.M. Freeze-drying of live virus vaccines: A review. *Vaccine* **2015**, *33*, 5507–5519.
150. Kanojia, G.; Soema, P.C.; Frijlink, H.; Amorij, J.; Kersten, G. Developments in the formulation and delivery of spray dried vaccines. **2017**, *13*, 2364–2378.
151. Peabody, J.; Muttillb, P.; Chackeriana, B.; Tumbanc, E. Characterization of a spray-dried candidate HPV L2-VLP vaccine stored for multiple years at room temperature. *Papillomavirus Res.* **2017**, *3*, 116–120.
152. Bajrovic, I.; Schafer, S.C.; Romanovicz, D.K.; Croyle, M.A. Novel technology for storage and distribution of live vaccines and other biological medicines at ambient temperature. **2020**, 1–14.
153. EMEA EMA/CHMP/439337/2015, *Mosquirix<sup>TM</sup>*, Annex I; London, 2015;
154. EMEA EMA/V/C/000135 *Porcilis PCV Annex i*; London, 2009;
155. Croyle, M.; Cheng, X.; Wilson, J. Development of formulations that enhance physical stability of viral vectors for gene therapy. *Gene Ther.* **2001**, *8*, 1281–1290.
156. Lynch, A.; Meyers, A.E.; Williamson, A.-L.; Rybicki, E.P. Stability studies of HIV-1 Pr55gag virus-like particles made in insect cells after storage in various formulation media. *Viol. J.* **2012**, *9*, 210.
157. Mckee, A.S.; Marrack, P. Old and new adjuvants. *Curr. Opin. Immunol.* **2017**, *47*, 44–51.
158. Jiao, Y.-Y.; Fu, Y.-H.; Yan, Y.-F.; Hua, Y.; Ma, Y.; Zhang, X.-J.; Song, J.-D.; Peng, X.-

- L.; Huang, J.; Hong, T.; et al. A single intranasal administration of virus-like particle vaccine induces an efficient protection for mice against human respiratory syncytial virus. *Antiviral Res.* **2017**, *144*, 57–69.
159. Scotti, N.; Rybicki, E.P. Virus-like particles produced in plants as potential vaccines. *Expert Rev. Vaccines* **2013**, *12*, 211–224.





## Objectives

---



The main objective of this work is to increase the current knowledge on the production of HIV-1 Gag-eGFP VLPs by PEI-mediated transient gene expression (TGE), studying the characteristics of the produced HIV-1 Gag-eGFP VLPs which enable the development of an efficient and scalable purification process. In more detail, the following specific objectives are defined:

1. Characterize the PEI-mediated DNA delivery in the production of HIV-1 Gag-eGFP VLPs
  - a. Characterize the PEI-mediated TGE strategy in a physicochemical manner.
  - b. Study the physicochemical factors that affect PEI-mediated TGE strategies by means of Design of Experiments (DoE)
  - c. Study the delivery of DNA at intracellular level
2. Characterize the HIV-1 Gag-eGFP VLP budding process at intracellular level
3. Assess the quality attributes of HIV-1 Gag-eGFP VLPs by advanced nanoparticle analytical methods.
  - a. Study of the nanomechanical properties of an individual HIV-1 Gag-eGFP VLP
  - b. Compare different biophysical methods at single particle level for the characterization and quantification of HIV-1 Gag-eGFP VLPs
4. Develop a scalable purification process for HIV-1 Gag-eGFP VLPs



## Results

---



## **Chapter 1**

# **Impact of physicochemical properties of DNA/PEI complexes on transient transfection of mammalian cells**

---

Published in *New Biotechnology*, 2019 (49) 88-97



## **Abstract**

Polyethylenimine (PEI) has been used extensively for transient gene expression (TGE) in mammalian cell cultures. However, the relationship between DNA/PEI complex preparation and their biological activity has not been fully established. Here, a systematic study of DNA/PEI complexes, their physicochemical properties during formation and their transfection efficiency was performed on a virus-like particle (VLP) production platform. The same chemically defined cell culture medium for DNA/PEI complex formation was used as an alternative to simple ionic solutions to minimize changes in complex properties during transfection. Upon formation, an initial concentration of  $1E+10$  DNA/PEI complexes/mL underwent partial aggregation with an average size of 300 nm. The participation of NaCl ions in the evolution of complexes was analyzed by X-ray spectroscopy, stressing the relevance of complexing media composition in TGE strategies. After 15 minutes incubation, 250 complexes plus aggregates per cell were estimated at the time of transfection. Such heterogeneous preparations cannot be easily characterized; subsequently, nanoparticle tracking analysis (NTA) and cryo-electron microscopy were combined to achieve a complete picture of the preparation. Finally, the contribution of each DNA/PEI complex subpopulation was tested by drug inhibition endocytosis. Interestingly, all complexes delivered DNA efficiently and high size aggregates, which enter through macropinocytosis, when inhibited presented a major contribution. There is a need to understand the physicochemical factors that participate in DNA delivery protocols. Hence, this study provides new insights into the characterization of DNA/PEI complexes that will assist in more productive and reproducible TGE strategies.

**Keywords:** Transient Transfection, DNA/PEI complexes, Mammalian cells, Particle tracking analysis, Electron Microscopy

## 1. Introduction

Cationic polymers represent a very widely used means for the delivery into cells of large DNA plasmids and small oligonucleotides [1,2]. Polyethyleneimine (PEI) has become a major reagent in this field [1,3]. PEI is simple to use, efficient with suspension cells, compatible with serum free media and cost effective [4]. This bulk chemical comprises amino groups with high cationic charge density capable of being protonated, that were discovered to efficiently introduce DNA into cells [5]. Over the last three decades, it has been used in large-scale production of recombinant proteins by transient gene expression (TGE) [4]. TGE enables the rapid screening of potential therapeutic candidates, and the generation of sufficient quantities of biomaterial for preclinical and early clinical studies [4]. Its use in vaccine production platforms to mitigate emerging epidemics is of particular relevance, and huge efforts are being undertaken in this direction [6–8]. In previous studies, intracellular tracking of a PEI-mediated TGE for the production of HIV-1 based virus-like particles (VLP) as vaccine candidates was conducted [9,10]. It was found that DNA/PEI complex enter every cell, whereas only a percentage produced VLPs. Hence, the assessment of the intracellular fate of those complexes might explain to what extent protein production is achieved.

From a molecular point of view, cationic amines reduce the negative charges of DNA and thereby protect DNA from nuclease degradation. The resulting positively charged complexes interact with the negatively charged cell membranes [1]. Subsequently, their cellular uptake by several endocytic pathways has been widely described [1,11]. While clathrin and caveolae-mediated endocytosis have been the most studied routes, there are other mechanisms, such as macropinocytosis or non-endocytic pathways, that have also been reported [1,11,12]. Indeed, when one pathway is inhibited, complexes may enter by alternative means [13]. Thereafter, PEI molecules are thought to escape from endosomes through the known “proton sponge” effect and liberate the complexes into the cytoplasm, from where they enter the nucleus and liberate the plasmid DNA [5]. However, this theory has not yet been confirmed [1]. For instance, the role of

free polycations has also been reported to participate actively in intracellular trafficking of the complexes [1].

Overall, there is a high level of heterogeneity reported in PEI-mediated processes, which is likely caused by the variety of transfection protocols developed over the years [4,11,14]. Firstly, several physicochemical factors critically affect the DNA/PEI complexation process, such as incubation time, temperature, medium viscosity, salt ion concentration or pH [4,14–18]. Secondly, DNA concentrations and DNA/PEI ratios also determine the stability and charge density of the complexes formed, as well as PEI composition [3,19,20]. Moreover, cell culture conditions (i.e. medium, cell concentration at time of transfection), cell type and the product of interest also have a relevant impact on TGE yields [4,14]. In addition, essential parameters of nanocarriers have recently been described in the nanomedicine field, including particle concentration and shape, which must also be considered in PEI-mediated processes [19,21,22].

Here, a comprehensive study of how preparation time affects physicochemical properties of DNA/PEI complexes and their correlation with transfection performance has been conducted. The work was performed using a previously characterized VLP production method with suspension-adapted HEK 293 cells cultured in a chemically defined culture medium, which was also used for the incubation of complexes before transfection [9,10]. The use of the same cell culture medium to prepare complexes reduced the alterations of DNA/PEI complex properties between their formation and their addition to the cells. In addition, its use is beneficial for the cultured cells, being a more nutritional solution compared with standard saline preparations used in TGE strategies, hence not diluting the medium during transfection.

## **2. Materials and methods**

### **2.1. HIV-1 Gag-GFP VLP expression plasmid**

Complexes were formed by using a pGag-eGFP plasmid, encoding a Rev independent HIV-1 Gag protein fused in frame to the enhanced GFP (eGFP) [23]. The plasmid from the NIH AIDS Reagent Program (Cat 11468) was constructed by cloning the Gag sequence from pCMV55M1-

10 [24] into the pEGFP-N1 plasmid (Clontech, Palo Alto, CA, USA). It was prepared and purified as previously described [25].

## **2.2. Cell line, culture conditions and transient transfection**

The cell line used was a serum-free suspension-adapted HEK 293 cell line (HEK293SF-3F6) kindly provided by Dr. Amine Kamen from McGill University (Montreal, Canada). Cells were cultured in FreeStyle™ 293 medium (FreeStyle) (Invitrogen, Carlsbad, CA, USA) supplemented with 0.1% Pluronic® (Invitrogen, Paisley, UK). Medium for cell growth was also supplemented with 1.6 mg/L of r-transferrin (Merck Millipore, Kankakee, IL, USA), 19.8 mg/L of r-insulin (Novo Nordisk Pharmatech, Køge, Denmark) and 0.9X of an in-house developed lipid mixture to maximize cell growth, as previously described [9]. Cells were maintained routinely at 20 mL final volume in exponential growth phase in 125 mL disposable polycarbonate erlenmeyer flasks (Corning, New York, NY, USA), shaken at 120 rpm in a humidified incubator at 37°C and 5% CO<sub>2</sub> in air.

HEK 293 cells were transiently transfected using 25-kDa linear polyethylenimine (PEI) (PolySciences, Warrington, PA, USA) at 2E+6 cells/mL after a medium exchange with fresh FreeStyle medium. Transfections were performed using a final DNA concentration of 1 µg/mL. DNA/PEI complexes were formed by adding PEI to plasmid DNA diluted in fresh culture medium (10% of the total culture volume to be transfected). Briefly, pGag-eGFP plasmid was diluted with FreeStyle medium (Invitrogen, Carlsbad, CA, USA) and vortexed for 10 sec (10µg/mL). PEI was then added at a 1:2 (w/w) DNA:PEI ratio and vortexed 3 times for one sec. The mixture was incubated for 15 minutes (min) at room temperature (RT) and added to the cell culture [9]. Sampling was conducted every 24 hours post transfection (hpt). Cell growth and viability were assessed with the NucleoCounter® NC-3000 automatic cell counter (Chemometec, Allerød, Denmark).

## **2.3. Dynamic Light Scattering (DLS)**

DNA/PEI complexes were immediately added to the cell cuvette for analysis. Dynamic light scattering (DLS) experiments were performed using a Zetasizer Nano ZS instrument (Malvern instruments, Malvern, UK) with a He/Ne 633 nm laser at 173°. The hydrodynamic diameter and polydispersity index (PDI) were calculated with cumulative fit correlation at 25°C and 0.8872 cP. Briefly, DNA/PEI complexes were prepared in 1 mL final volume, and placed in disposable plastic macro cuvettes (Scharlab S.L., Barcelona, Spain) followed by automated experimental data collection. Complex formation was observed for 30 min; 11 scans were performed in each independent measurement.

#### **2.4. Nanoparticle Tracking Analysis (NTA)**

DNA/PEI complexes were immediately injected for sample analysis. Nanoparticle tracking analysis (NTA) was performed with a NanoSight® LM20 device (NanoSight Ltd., Malvern Panalytical Ltd, Malvern, UK). The data were analyzed with NanoSight® NTA 3.2 software. Samples were diluted in sterile PBS (HyClone, Little Chalfont, GE Healthcare, UK) prior to injection into the device chamber to obtain a concentration of approximately 1E+08 particles/mL. Samples were injected, and independent analyses were carried out. Video recordings of 60sec length were made. Subsequently, particles were identified and tracked by their Brownian motion at RT. Capture settings were recorded with an sCMOS camera (camera level of 5 for complexes, and 11 for controls, viscosity: 0.9 cP) and analyzed with a detection threshold of 5.

#### **2.5. Cryo-Transmission Electron Microscopy (Cryo-TEM)**

DNA/PEI complexes incubated for the desired time, were immediately plunged into liquid ethane. Their morphology was studied by Cryo-TEM. A 2-3 µL amount of sample was blotted onto holey carbon grids (Quantifoil Micro Tools, Großlobenichau, Germany and Micro to Nano, Haarlem, Netherlands) previously glow discharged in a PELCO easiGlow glow discharger unit. The samples were subsequently plunged into liquid ethane at -180°C using a Leica EM GP cryo workstation and observed in a JEM-2011 electron microscope (JEOL Ltd., Tokyo, Japan) operating at 200 kV. During imaging, samples were maintained at -173°C, and pictures were taken using a CCD-multiscan camera (Gatan Inc., Pleasanton, CA, USA).

## **2.6. Electron Microscopy and X-ray spectroscopy**

DNA/PEI complexes incubated for the desired time were immediately deposited onto the grid for preparation by air-dried negative staining. Briefly, 8  $\mu\text{L}$  of the mixture was placed onto grids and incubated at RT for 1 min. Excess sample was carefully drained off the grid with the aid of Whatman filter paper. Sample was negatively stained with 8  $\mu\text{L}$  uranyl acetate (2%) by incubation for 1 min at RT. Excess stain was drained off, and the grids were dried. Transmission electron microscopy (TEM) examination was performed with a JEM-1400 (JEOL USA Inc., Pleasanton, CA, USA) transmission electron microscope equipped with an ES1000W Erlangshen charge-coupled device camera (Model No. 785; Gatan, Pleasanton, CA, USA). Scanning electron microscopy (SEM) images were assessed with a FE-SEM Merlin (Zeiss, Jena, Germany) scanning electron microscope. Images were taken with in-lens mode with an EHT of 2-5 eV at 3 or 5.5 mm working distance and 100  $\mu\text{m}$  spot size. Samples prepared for SEM analysis were further characterized by X-ray spectroscopy. Samples coated with uranyl acetate were scanned and analyzed with a coupled energy dispersive X-ray spectroscopy (EDS) unit at a resolution of 138 eV. Samples were scanned in X-ray mode with an EHT of 5 eV, a 5.5 mm working distance and a size spot of 500  $\mu\text{m}$  in 20,000-30,000X. Phosphorous, chloride, sodium and uranyl elements were tracked and quantified with Inca software (Oxford Instruments, Abingdon, UK).

## **2.7. Covalent labeling of PEI**

Linear 25 kDa PEI (25 kDa, Polysciences, Warrington, PA, USA) was covalently labeled with Cy5 monoreactive dye (Amersham, GE Healthcare, Little Chalfont, UK) by suspending one vial with 2 mg of PEI dissolved in 1 mL PBS at pH 8.0, adapted from [16]. Reaction was performed for 4 h at RT under continuous mixing. To eliminate Cy5 excess, the resultant Cy5-labeled PEI solution was dialyzed through a 5 kDa-cutoff cellulose membrane (Sigma Aldrich, San Luis, MO, USA) in a 2 L PBS solution and pH 7.4 at RT for 7 days. Dialysis solutions were changed every 24 hours. PEI labeling was confirmed by absorbance measurement with Nanodrop 1000 (Thermo Fisher Scientific, Waltham, MA, USA). Maintenance of PEI activity was confirmed by its

consistency with the standard transient transfection protocol. Cy5-labeled PEI was stored at -20 °C protected from light.

### **2.8. Flow cytometry**

The percentage of GFP-positive cells and of cells interacting with DNA/PEI complexes was assessed using a BD FACS Canto flow cytometer (BD Biosciences, San Jose, CA, USA) with a two-laser configuration (488 nm and 635 nm). Laser 488 was used for GFP measurement and detected with GFP FITC-A detector, and laser 635 and detector APC-A were used for Cy5 measurement. A total of 20,000 events were analyzed in every sample. First, SSC-H vs FSC-A and FSC-A vs. FSC-H density plots were used to gate individual HEK 293 cell populations. Secondly, positive Cy5 and GFP populations were assessed with GFP FITC-A vs. APC-A density plot and the individual histogram for each fluorochrome. Gating was adjusted manually for each channel with an intensity between 5E+2 and 1E+3 multiple fluorescence units. The results were analyzed with FACS DIVA software (BD Biosciences, San Jose, CA, USA).

### **2.9. HIV-1 Gag VLP quantitation**

The concentrations of HIV-1 Gag-eGFP VLPs were assessed by fluorimetry using an in-house developed and validated quantification assay [26]. VLP containing supernatants were recovered by cell culture centrifugation at 1000×g for 5 min. Relative fluorescence unit (RFU) values were calculated by subtraction of fluorescence unit (FU) values of non-transfected negative control samples.

### **2.10. Inhibition of cell DNA/PEI complex uptake**

To selectively inhibit endocytosis pathways, the following compounds were used: 10-30 μM chlorpromazine, 20-60 μM nystatin, and 10-50 μM 5(N-ethyl-N-isopropyl) amiloride (EIPA) (Sigma Aldrich, San Luis, MO, USA). Passive transport was evaluated by maintaining the cells at 4 °C for 4 hours after transfection. Specific inhibitors were incubated for 1 h at 37 °C at 120 rpm after a medium exchange process. Transient transfections were then performed with Cy5-

labeled PEI, and at 4 hpt, a second medium exchange was performed. Sampling was conducted every 24 hpt until 96 hpt.

Prior to the definitive experiment, different concentrations of each inhibitor were tested to select the one showing transfection effects with minimal side effects on cell viability. To explore these conditions, preliminary experiments were conducted in 6-well culture plates (Thermo Fisher Scientific, Waltham, MA, USA), whereas the validation experiment was performed using standard cell culture conditions, as described previously.

### **3. Results**

#### **3.1. Size determination of DNA/PEI complexes**

DNA/PEI complexes used in a standard transient transfection protocol of HEK 293 cells were examined with particle tracking techniques. The evaluation of DNA/PEI complexes over time was followed by DLS and NTA. In Figure 1A, the mean hydrodynamic diameter and the relative kilo counts per second (kcps) determined by DLS are depicted, while in Figure 1B, the mean hydrodynamic diameter and the concentration of particles analyzed by NTA are shown.

DLS revealed a rapid increase in size of DNA/PEI complexes. A mean hydrodynamic diameter of approximately 344 nm was recorded as the initial point, which increased up to 690 nm at 30 min of incubation. Interestingly, the kcps decreased during this period. The kcps value is proportional to the total light scattered intensity, which in turn, is proportional to the concentration of particles and size. The decreased kcps was likely to be due to aggregation or precipitation phenomena. Because no precipitation was observed, and the hydrodynamic diameter increased with time, an aggregation process was the probable cause of this observation.

NTA measurements presented a slight growth in DNA/PEI complex size starting from 220 nm and reaching a plateau at 30 min (300 nm). Interestingly, while the mean hydrodynamic diameter was nearly constant during the entire process, the concentration of particles quickly decreased by an order of magnitude within the first 5 min. In the entire process analyzed, DNA/PEI complexes began at a concentration of  $1.08\text{E}+10$  particles/mL, which was reduced to  $1.80\text{E}+9$  particles/mL



by 30 min of incubation. Three kinetic rates could be identified within this period: a rapid fall in the first 5 min, a second trend until the 15 min and a third period with a slow rate from that time on. The background levels detected in the controls (FreeStyle medium, free DNA and free PEI) are included in Supplementary materials S1 (Supplementary Materials S1). Furthermore, the presence of particles in the controls was only detected using high laser intensities (Camera level 11), whereas in DNA/PEI complexes the laser intensity was much lower (Camera level 5).

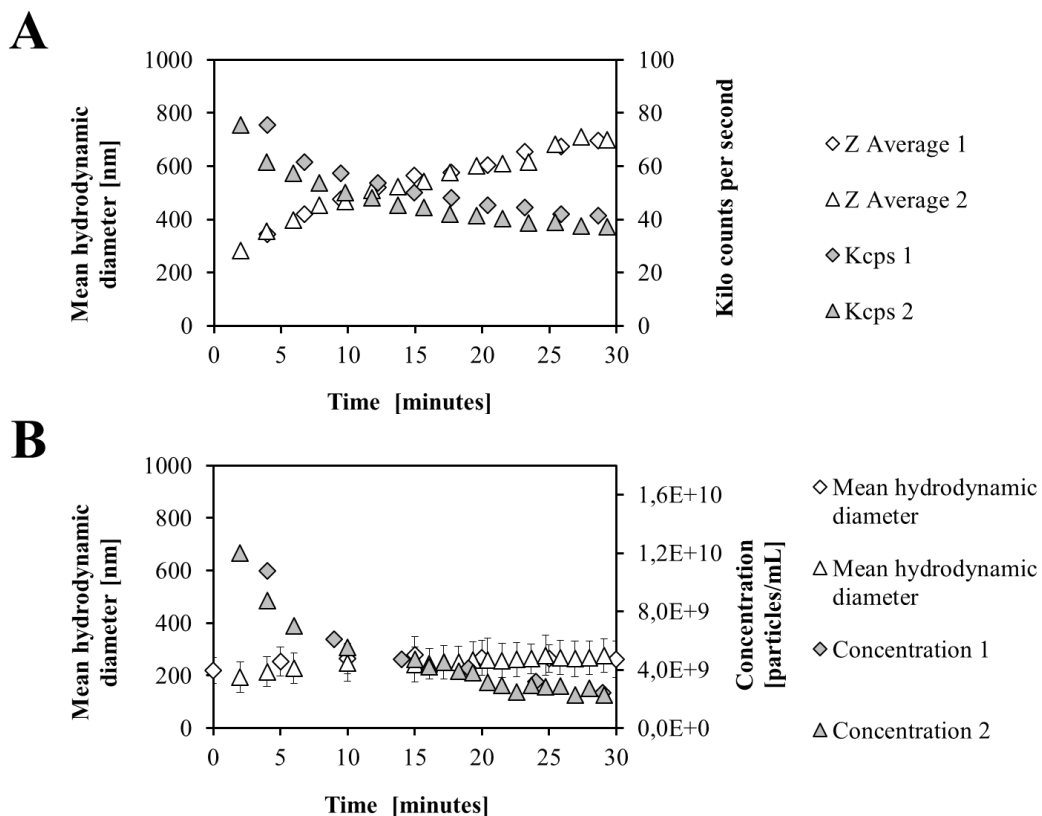


**Figure 1: Particle tracking analysis of DNA/PEI complex kinetics in FreeStyle medium.** DNA/PEI complexes were formed instantaneously after the mixing of DNA and PEI; a partial aggregation of the population was observed by (A) DLS measurement of mean size and kilo count per second (kcps), respectively, and (B) NTA analysis with Nanosight® of mean size and particle concentration, respectively, in the range from 0 to 1000 nm; standard deviation (SD) in every mean size measurement is also shown. Samples were diluted 1:10 with PBS to achieve a concentration between  $10^8$ - $10^9$  particles/mL.

Overall, a DNA/PEI complex aggregation process is proposed. DLS is highly affected by large aggregates because the scattered light is proportional to the hydrodynamic diameter, which occludes or prevents the detection of small particles. NTA is unable to analyze large aggregates; consequently, only smaller particles are observed. When both analytical methods are combined,

insights into DNA/PEI complexes can be obtained. First, DNA/PEI complexes are formed immediately. They then evolve during incubation in cell culture medium and some small complexes aggregate with time. After 30 min, the samples contain small complexes with sizes of approximately 300 nm (detected by NTA) and large aggregates of micron-size (detected by DLS).

Due to the intrinsic limitation of each methodology, such heterogeneous systems cannot be characterized by one technique alone, to avoid misleading results. A similar approach has been taken by van Gaal et al. [27], where flow cytometry was assessed to analyze DNA/PEI complex populations. The heterogeneous results found in TGE protocols could be better explained by these combined characterizations [21].

### **3.2. Morphological study of DNA/PEI complexes**

Cryo-TEM, TEM and SEM have been used to evaluate DNA/PEI complex morphology. This feature has been recently described as highly relevant in DNA and drug delivery strategies [28,29]. Cryo-TEM enables the study of nanoscopic molecular assemblies in their aqueous form; Cryo-TEM analysis of DNA/PEI complexes after 1 min incubation (Figure 2A, 2D), 15 min (Figure 2B, 2E) and 30 min (Figure 2C,2F) are shown in Figure 2. DNA/PEI complexes showed electrodense structures with ellipsoid-like shapes (Figure 2, white arrows) with sizes of approximately 150-200 nm (Figure 2A). The observed density was elevated, in agreement with the previous NTA measurements (Figure 1B). After 15 min incubation, the heterogeneity of DNA/PEI complex population and the aggregation process was evident: micrometric aggregates with irregular shapes (Figure 2, black arrows) were present and the apparent concentration of particles was reduced. At 30 min, aggregates with diameters greater than 3  $\mu\text{m}$  could be observed. However, this technique cannot identify objects with thicknesses larger than 1  $\mu\text{m}$  [30], suggesting that the positively charged complexes may deform in the grid since it is negatively charged after glow discharge.

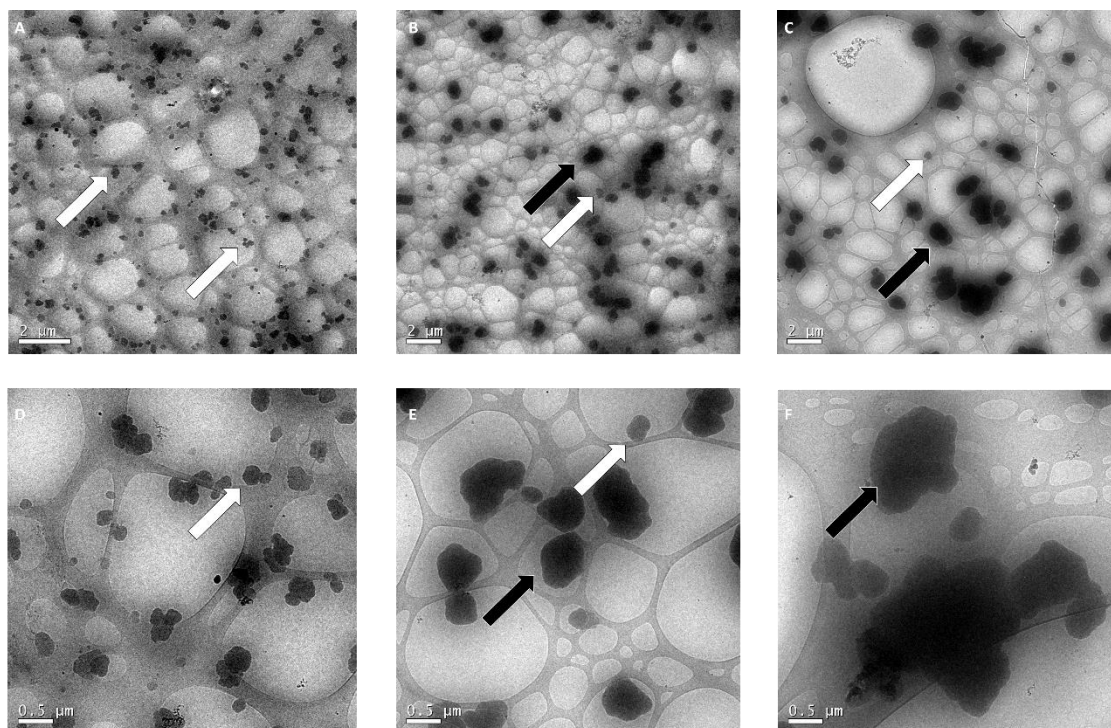


**Figure 2: Cryo-electron microscopy analysis of DNA/PEI complexes in FreeStyle medium.** DNA/PEI complexes were observed as electrodense sphere-like structures just after mixing DNA and PEI. A heterogenous population in size was observed after incubation: large DNA/PEI aggregates appeared at 15 min incubation and increased in size at 30 min with diameters up to 3  $\mu\text{m}$ . (A, D) Cryo-TEM images at 0 min incubation; (B,E) 15 min incubation; (C,F) 30 min incubation. White arrows indicate  $\sim 300\text{nm}$ -size DNA/PEI complexes, and black arrows indicate  $\geq 1\ \mu\text{m}$ -size DNA/PEI complex aggregates.

SEM and TEM are simpler characterization techniques; nonetheless, these measurements are carried out on negatively stained and dried samples which may result in artifacts. To improve image resolution and reduce background, samples were deposited on holey nickel carbon grids (Copper-carbon grid preparations of DNA/PEI complexes are presented in Supplementary Materials S2, for comparison). Changing the nature of the support improved the resolution: DNA/PEI complexes of  $\sim 300\ \text{nm}$  (Figure 3, white arrows) and micron-sized aggregates were clearly distinguishable (Figure 3, black arrows) in both TEM (Figure 3A and C) and SEM (Figure 3B and D). Background noise caused by the precipitation of the salts present in the FreeStyle medium was also reduced (higher levels are detected in the control and in the copper-carbon grid, Supplementary Materials S1 and S2, respectively). Of note, DNA/PEI complexes maintained their three-dimensional structure under SEM analysis. In addition, the heterogeneity of the complex population was evidenced by all the analyses. The presence of a DNA/PEI complex subpopulation

was suggested by Choosakoonkriang et al. more than 10 years ago [21]. In this work, the novel application of NTA and Cryo-TEM have confirmed this hypothesis in the system tested (Figures 1 and 2).

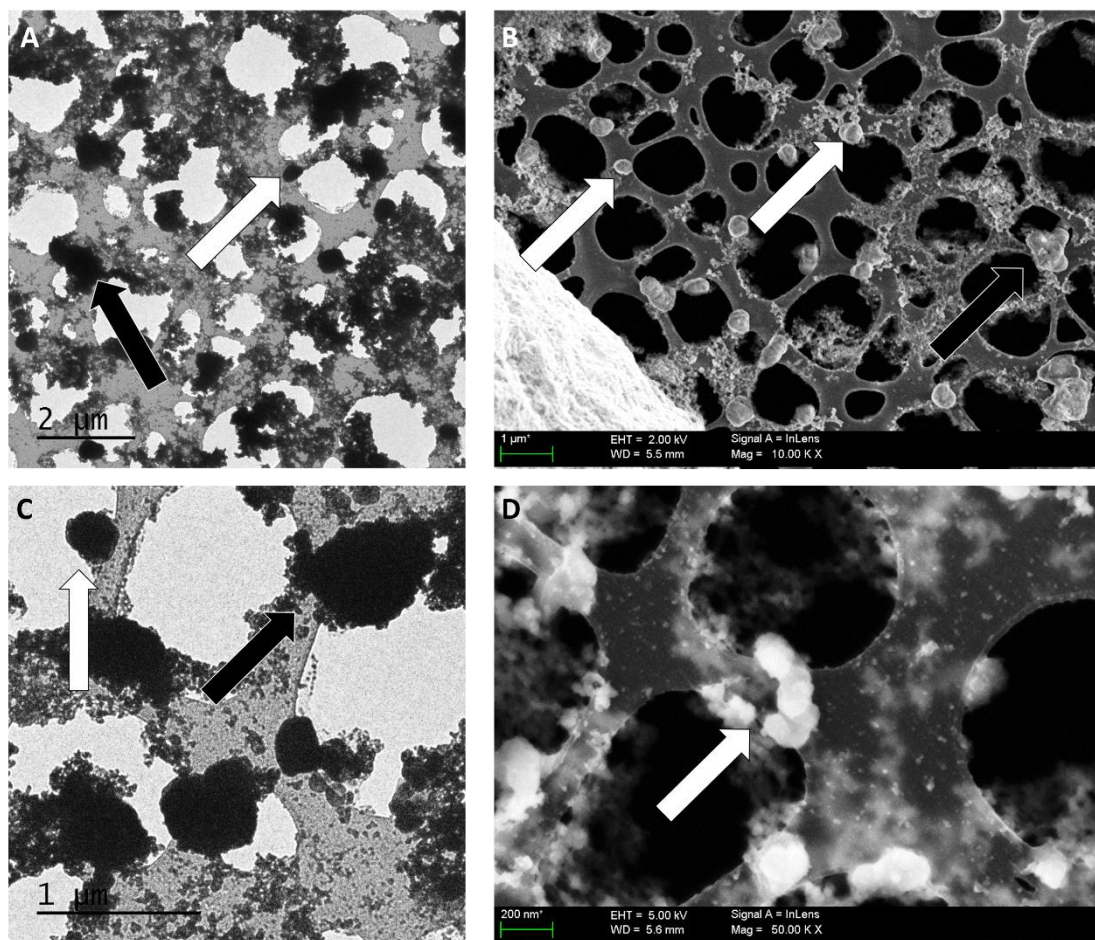


**Figure 1:** Electron microscopy analysis of DNA/PEI complexes at 15 min incubation in holey-nickel grids in FreeStyle medium. Identification of DNA/PEI complexes with negative staining was achieved using holey grids. (A, C) TEM analysis and (B, D) SEM analysis. White arrows indicate ~300nm-size DNA/PEI complexes, and black arrows indicate  $\geq 1 \mu\text{m}$ -size DNA/PEI complex aggregates.

### 3.3. Elemental analysis of DNA/PEI complexes

Aggregation of DNA/PEI complexes has been evidenced by particle tracking analyses (Figure 1) and EM (Figures 2 and 3). This process has been widely reported in simpler hypertonic solutions [13,15,18]. In this work, the use of cell culture medium to form DNA/PEI complexes was used: FreeStyle medium is protein-free and chemically defined but its composition is proprietary. In this regard, cell culture media have been reported to change the properties of the formed

complexes after its addition [15,18]. Moreover, since some cell culture media contain proteins, such as albumin, they would interact with the complexes, complicating the interpretation of physicochemical properties in TGE processes [27,31]. Since FreeStyle has no protein, the problems presented in the literature should not affect the present approach, although unknown compounds could be participating in the complexation process.

To go further into DNA/PEI complex formation in the present methodology, SEM was coupled with X-ray spectroscopy to determine the distribution of molecules within complexes. Figure 4 presents an example of an elemental analysis obtained. Figure 4A presents the SEM image coupled to the profile line analyzed in a 200 nm size DNA/PEI complex. Four other elements were detected, other than carbon and oxygen from the grid (Figure 4B and 4C): phosphorus (P), chloride (Cl), sodium (Na) and uranium (U). All 4 pooled within the DNA/PEI complex structure. For additional information, Supplementary Materials S3 shows an X-ray spectroscopic elemental analyses of a series of DNA/PEI particles observed by SEM.

Remarkable levels of Na and Cl were detected in the particle, which may come from the FreeStyle medium. Consequently, NaCl salt is indicated as the driving force for DNA/PEI complex evolution in the cell culture medium. It is possible to infer that the presence of counter ions in the DNA/PEI complex accounted for salt precipitates in the SEM and TEM images in all DNA/PEI particles observed (Figure 3). This was more evident on the carbon-coated grids where all salt precipitates were retained on the grid due to the lack of holes (Supplementary Materials S2).

To confirm this hypothesis, transfections were performed in simpler PBS buffer and Milli Q water following the same DNA/PEI complex preparation. In those cases, complexes prepared in salt buffer produced almost the same protein yield upon transfection (96hpt); otherwise, complexes prepared in water showed inefficient TGE yields in terms of protein production, despite having a similar percentage of producing cells (Supplementary Materials S4). In addition, DNA/PEI complex formation was analyzed in both media, and aggregation was found only in the salt buffer (PBS) (data not shown), thus corroborating the hypothesis of direct salt intervention in PEI-mediated TGE processes (as also reported in the literature)[15,18].

Apart from salt ions, the presence of phosphorous (P) might derive from the phosphate group of the DNA, whereas the presence of uranium was due to the negative staining pretreatment required for the vacuum conditions. Although phosphorous was clearly identified, it did not appear in the whole spectrum due to its low concentration compared with the other elements (Figure 4B). The surrounding counter ions might hinder the detection of DNA/PEI atomic composition. To assess that possibility, an extra wash step with MiliQ water was performed before negative staining addition. After sample drying, MiliQ water was added to the grid and dried with filter paper to decrease salt concentration (Supplementary Materials S3). At this point, a nitrogen peak, characteristic of DNA and PEI molecules, was clearly detected.

In short, NaCl was indicated as being the main cause of the DNA/PEI complex aggregation shown. Raup et al [18] recently analyzed the behavior of DNA/PEI complexes in different concentrations of NaCl and observed aggregation in all, despite showing different aggregation rates.

#### **3.4. Average of DNA/PEI load in cell culture**

Prior to any biological assay, the number of complexes in the cell culture was determined to calculate transfection efficiency. DNA complexation by PEI was confirmed by gel retardation assay (data not shown). Preliminary theoretical calculations of the number of pGag-eGFP plasmid copies per complex based on the data obtained were then performed (Table I). Based on the NTA results (number of DNA/PEI complexes of 220-nm size recorded at the beginning of the incubation) and the concentration of pGag-eGFP plasmids, 144 plasmid copies per DNA/PEI complex was obtained. Moreover, at the time of transfection (after 15 min incubation;  $4.90\text{E}+9$  particles/mL from NTA data), approximately 250 complexes of 279-nm average size per cell plus aggregates were expected after incubation. The number of complexes per cell should be sufficient to guarantee efficient transfection. In previous confocal microscopy studies, similar estimations were performed by considering only large DNA/PEI aggregates visualized in mammalian cells, leading to results of fewer than 10 aggregates per cell [10,32]. The presence of small complexes of  $\sim 300$ -nm sizes could not be visualized due to optical limitations

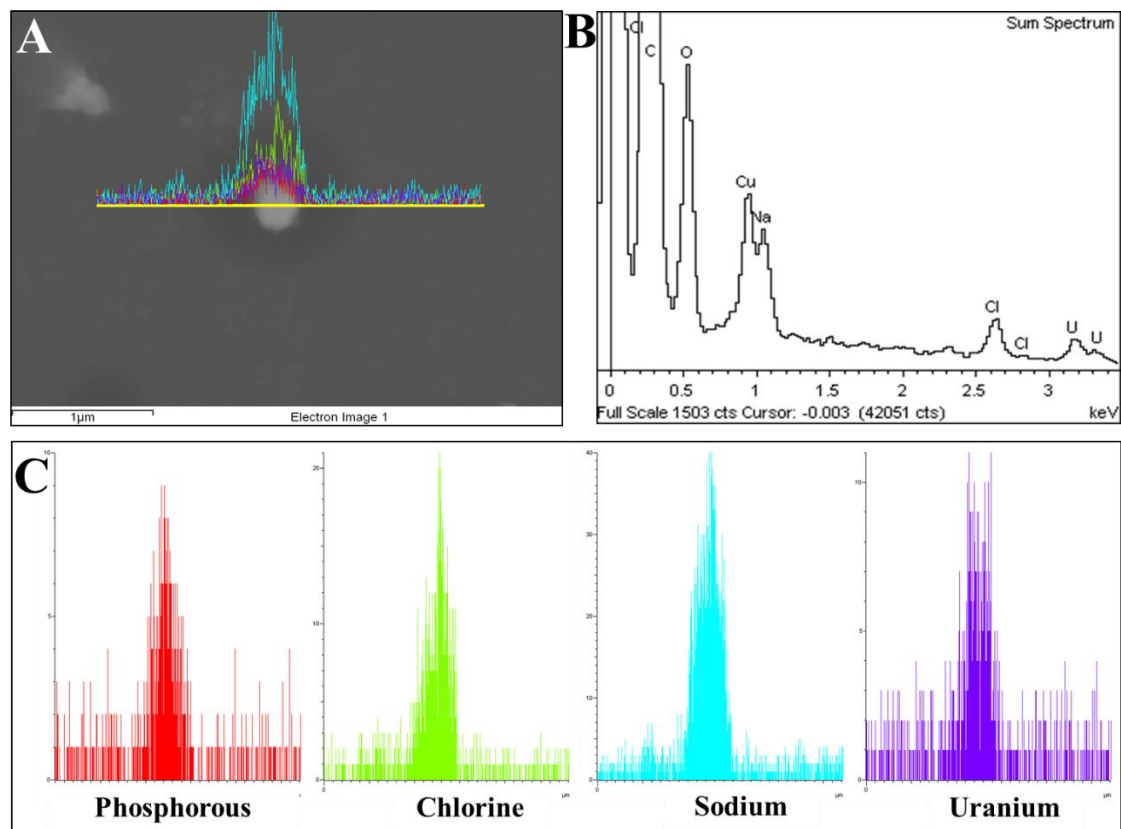


Figure 4: X-ray spectroscopy mapping elemental analysis of a DNA/PEI complex. Presence of Na and Cl ions surrounding DNA/PEI complexes were identified as the driving force in complex formation and aggregation. (A) SEM image of the particle analyzed; histogram analyzed is presented as a yellow line. (B) Sum spectrum of X-ray analysis. (C) Specific X-ray spectra composition for the elements found in more abundance: phosphorous (P) represented (red), chlorine (Cl) (green), sodium (Na) (blue) and uranium (U) (purple).

Table I. Theoretical calculation of pGag-eGFP plasmid copies in DNA/PEI complexes with a hydrodynamic diameter of 220 nm. \* DNA/PEI complexes concentration has been adjusted to the final transfected cell culture volume.

pGag-eGFP concentration	1 (μg/mL) / 6.022+14(kDa/mL)
pGag-eGFP	6274 (bp) / 3880 (kDa)*
Cell Concentration at transfection time	2.00E+6 (cells /mL)
pGag-eGFP copies	1.55E+11 (copies/mL)
pGag-eGFP copies/cell	7.75E+4 (copies/cell)
DNA/PEI complex concentration at t= 0 of incubation. with a mean hydrodynamic diameter of 220 nm at the transfected cell culture	1.08E+9 (complex /mL)**
pGag-eGFP copies/ DNA/PEI complex of 200nm at t:0 of incubation	1.44E+2 (copies/complex)
DNA/PEI complexes/cell	5.40E+2 (complex/cell)

\*Molecular Weight calculated with Snap Gene Viewer® (GSL Biotech LLC);\*\* DNA/PEI complexes concentration has been adjusted to the final transfected cell culture volume.

### **3.5. Effect of DNA/PEI physicochemical heterogeneity in transient transfection**

The influence of the physicochemical properties of DNA/PEI complexes aggregation in transient transfection was investigated. A previously optimized TGE protocol for the production of HIV-1 based VLPs was used [9]. These VLP vaccine candidates are based on the self-assembly capacity of the Gag-polyprotein of the HIV-1. Upon expression, Gag is able to accumulate underneath the plasma membrane and, through a budding process, VLPs are released to the cell culture medium. Gag polyprotein was labeled with eGFP; thus, its production could be monitored by fluorescence-based techniques.

DNA/PEI complexes formed under the same DNA:PEI (w:w) ratio, but with different incubation times prior to transfection, were prepared (Preparations 1-2-3 with 0-15-30 min of incubation, respectively; Figure 5A). Figure 5B shows that HEK 293 cell growth and viability were not affected by the presence of small complexes, aggregates or mixtures of the two. Hence, size and particle concentration did not show cytotoxic effects. However, complexation time affected the production of HIV-1 Gag-eGFP VLPs, determined in terms of GFP-positive cells (Figure 5C) and relative fluorescence units (RFU) in the supernatant corresponding to the final HIV-1 Gag-eGFP VLP production (based on an in-house developed quantification assay) (Figure 5D) [26]. Preparation 1 with non-incubated complexes had no aggregates and showed the lowest production. No significant differences were observed between preparations 2 and 3 (incubation times of 15 and 30 min, respectively). Thus, even though complexation kinetics are rapid, a minimum complexation time is necessary to allow for aggregation before cell transfection. These data suggested that aggregation critically contributed to the transient transfection process and 15 min was enough to produce the highest yield.

### **3.6. Effect of endocytosis inhibition in transient transfection**

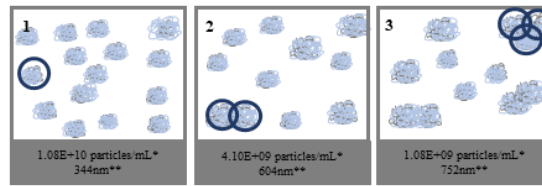
To determine which type of complex had a higher impact on transient transfection, specific inhibitors of endocytosis were used to block entry of the different DNA/PEI complexes subpopulations (complexes were formed with DNA:PEI ratio 1:2 w:w and 15 min incubation, corresponding to Preparation 2 in Figure 5). A scheme of the experimental approach is shown in



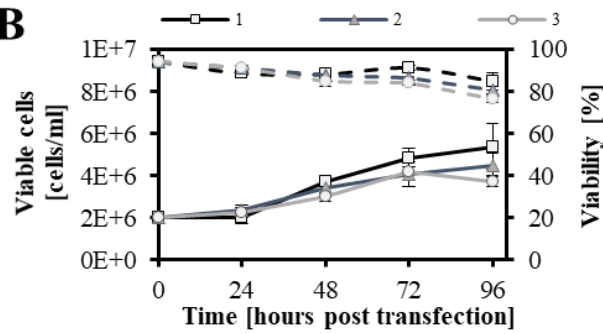
Figure 6A. Four main pathways in DNA/PEI complex entry into HEK 293 cells have been reported: clathrin-mediated endocytosis (typically identified by entry of particles with sizes between 100-150 nm), caveolae-mediated endocytosis (characterized by entry of particles of 50-100 nm), macropinocytosis (typically identified for particles between 1-5  $\mu$ m) and passive transport. Phagocytosis was not considered in this work because it is a special endocytosis pathway specific in phagocyte cells (the HEK 293 cells used in this work are derived from human kidney cells, lacking this ability).

The results of endocytosis inhibition are found in Figure 6. First, as shown in Figure 6B, cell growth and viability were only slightly affected by the addition of inhibitors. Secondly, when the transfection efficiency was evaluated in terms of GFP-positive cells (Figure 6C), at 24 hpt, different effects on transfection were observed. These effects were attenuated during the production phase (48-96 hpt). The same results were observed when the final HIV-1 Gag-eGFP VLP production was quantified in the supernatant. For all conditions, cells were successfully transfected and HIV-1 Gag-eGFP VLPs were produced, suggesting that DNA/PEI complex transfection occurred through all tested pathways. However, when cell-DNA/PEI complex interactions in the presence of inhibitors were evaluated using Cy5-labeled PEI, no significant changes in the percentage of cells interacting with a complex were observed (Supplementary Materials S5). This indicated that DNA/PEI complex trafficking to the cell membrane was not affected by endocytosis inhibition and suggests that the recovery of GFP-positive cells at 48 hpt in nearly all endocytosis inhibition tests could have been due to the decreased effectiveness of inhibitors, i.e., complexes entered through their natural pathways. This may also account for the levels of transfection achieved by passive transport, where a fast recovery in the percentage of GFP-positive cells was observed between 24 and 48 hpt despite decreased overall production.

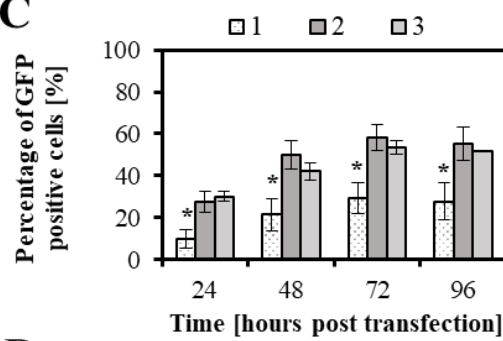
A



B



C



D

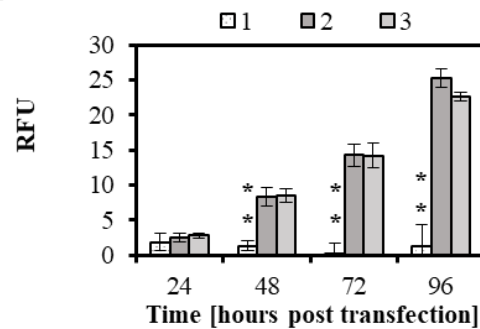


**Figure 2: DNA/PEI complex formation effect on the production of HIV-1 Gag-eGFP VLPs by transient transfection of HEK 293 cells. Aggregation of DNA/PEI complexes before transfection was required to obtain higher yields. (A) Scheme of the different DNA/PEI complexes aggregation levels 1, 2 and 3 prepared by non-incubation, 15 and 30-min incubation in FreeStyle medium, respectively. \*NTA data \*\*DLS data. (B) Viable cell concentration and cell viability. (C) Percentage of GFP-positive cells. (D) Relative fluorescence units (RFUs) in the supernatant. Experiments were performed in triplicate. Mean values  $\pm$  SD are presented. Student t-test analysis for every condition with the control of each time is also included: \*  $P < 0.05$ , \*\*  $P < 0.01$ , \*\*\*  $P < 0.001$ .**

Different concentrations of product were obtained depending on the pathway inhibited. In the inhibition of clathrin-mediated endocytosis (CPZ), a slightly negative effect was observed in terms of GFP-positive cells and RFU, indicating that a percentage of DNA/PEI complexes may enter via the clathrin pathway. Caveolae-mediated inhibition (Nys) showed a slight but not significantly positive effect in transfection, suggesting that DNA/PEI complexes might not use this pathway, which agrees with previous DNA/PEI complex characterizations, where small populations had hydrodynamic mean diameters of approximately 300 nm. Finally, when the macropinocytosis pathway was inhibited, a significant reduction in HIV-1 Gag VLP production was observed, achieving levels like those observed with passive transport. These results suggested that, from the two previously characterized populations (Complexes 2 in Figure 5), the large aggregates contributed to a greater extent to the final transfection efficiency. This was probably because large aggregates carried more DNA and likely acted as reservoirs. Cervera et al. [10] showed the presence and efficient endocytosis of DNA/PEI complex aggregates in all transfected cells after 1 hour of incubation, despite only partial production of HIV-1 Gag-eGFP VLPs by the cells. Note that the drug inhibitor endocytosis approach is an indirect method since the drugs used could have other effects in the cell metabolism hindering the experimental objective [11,33]. In this sense, the characterization of complexes and the previous confocal microscopy analyses contribute to the hypothesis; nevertheless, the effectiveness of ~300-nm complexes have also been largely reported in other systems, as well as the present work [1,11,13].

On the whole, PEI-mediated TGE will still be a reference methodology in industrial biotechnology. There is a high heterogeneity in PEI-mediated processes for both intracellular fate and TGE yields. Other from the cell line, this could be caused by (1) the large number of variables which change the physicochemical properties of DNA/PEI complexes and/or (2) the polydispersity of the DNA/PEI complexes formed [1,14,21,27]. Here, the use of a chemically defined and protein-free cell culture media for all complex formation and cell culture has enabled the comprehensive correlation between its formation and its efficiency, since no chemical alteration is made when complexes are added to the cell culture aside for dilution. Furthermore,

the improvements in the nanotechnology field have enabled a better description of the present HIV-1 Gag-eGFP VLP production platform. The aggregation of DNA/PEI complexes has been directly visualized by Cryo-TEM and quantified by NTA. The present study will allow one to decipher the key aspects of PEI-mediated process and enhance TGE yields.

#### **4. Conclusion**

A strong relationship between DNA/PEI complex aggregation level and transient transfection efficiency was observed. Aggregation did not affect the entire population evenly, resulting in heterogeneous complexes. The combination of particle tracking and electron microscopy techniques enabled the comprehensive characterization of DNA/PEI complexes.

The extent of aggregation was correlated with incubation time, which is a relevant parameter to be considered at the moment of complex preparation. Moreover, the concentrations of Na and Cl ions in culture media played important roles in DNA/PEI complex formation. Interestingly, DNA/PEI complex aggregates seemed to significantly contribute to transient transfection. This was likely to be because these aggregates carried more DNA and acted as reservoirs.

This work provides highlights for a better understanding of DNA/PEI complexes to improve TGE processes, reducing transfection variability and increasing production yields by adjusting simple parameters, such as incubation time. This approach can aid characterization of similar nanocarriers used in biomedicine for non-viral DNA delivery strategies.

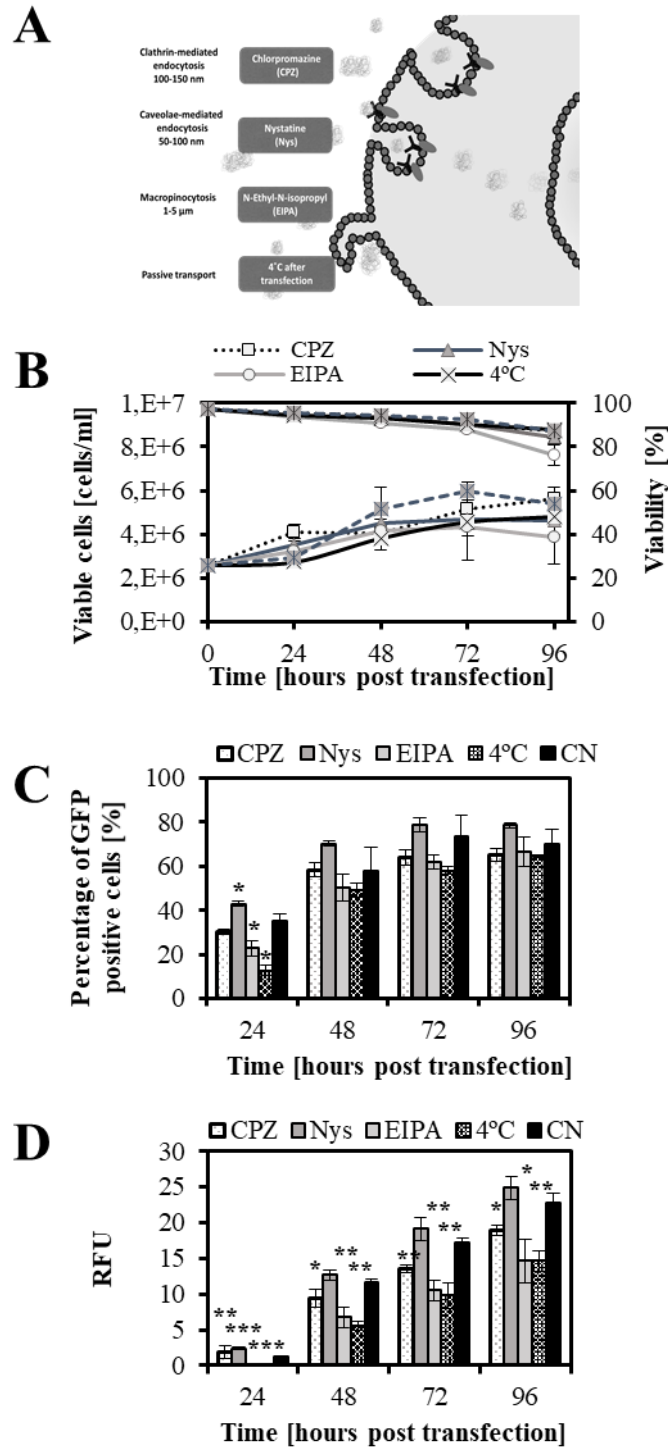


**Figure 6: Effect of endocytosis inhibition on transient transfection efficiency in the production of HIV-1 Gag-eGFP VLPs in HEK 293 cells.** DNA/PEI complexes may enter through several endocytic pathways and DNA/PEI aggregates are required to obtain the highest TGE yields. (A) Endocytosis inhibition experimental design. Four pathways were analyzed through drug inhibition endocytosis. Each pathway was specifically inhibited with a drug inhibitor or with a temperature treatment: chlorpromazine 25  $\mu\text{M}$  (CPZ), nystatin 30  $\mu\text{M}$  (Nys), N-ethyl-N-isopropyl 30  $\mu\text{M}$  (EIPA) for evaluation of clathrin-mediated endocytosis, caveolae-mediated endocytosis and macropinocytosis, respectively. Passive transport was evaluated by maintaining the cells at 4  $^{\circ}\text{C}$  after transfection until 4 hpt and transfection with no treatment

was performed for comparison (CN) (B) Cell growth and viability of HEK 293 cells. (C) Percentage of GFP-positive cells. (D) Relative fluorescence units (RFUs) in the supernatant. After medium replacement, HEK 293 cells were pretreated with inhibitors 1 hpt; a second medium replacement was performed at 4hpt. Experiments were performed in triplicate. Mean values  $\pm$  SD are shown. Student t-test analysis for every condition with the control of each time is also included: \* P<0.05, \*\* P<0.01, \*\*\* P<0.001.

## 5. Acknowledgements

The authors thank Dr. Amine Kamen (McGill University, Montreal, Canada) for providing the HEK 293 SF-3SF6. The following reagent was obtained through the National Institutes of Health AIDS Reagent Program, Division AIDS, National Institute of Allergy and Infectious Diseases, National Institutes of Health: pGag-eGFP (Cat# 11468) from Dr. Marilyn Resh. We thank Dr Jose Amable Bernabé from the Institute of Material Science of Barcelona (ICMAB-CSIC, Barcelona, Spain) for his support with particle tracking techniques. The help of Dr. Emma Rossinyol and Martí de Cabo from the Microscopy Service from the Autonomous University of Barcelona (Barcelona, Spain) in the performance of electron microscopy analysis is greatly appreciated. Cy5 monoreactive fluorochrome was kindly provided by the Sequencing Service from Biotechnology and Biomedicine Institute (IBB, UAB, Barcelona, Spain).

## 6. Literature

1. Yue, Y.; Wu, C. Progress and perspectives in developing polymeric vectors for in vitro gene delivery. *Biomater. Sci.* **2013**, *1*, 152–170.
2. Ramamoorth, M.; Narvekar, A. Non viral vectors in gene therapy- an overview. *J. Clin. Diagn. Res.* **2015**, *9*, GE01-6.
3. Lai, W.-F. In vivo nucleic acid delivery with PEI and its derivatives: current status and perspectives. *Expert Rev. Med. Devices* **2011**, *8*, 173–85.
4. Gutiérrez-Granados, S.; Cervera, L.; Kamen, A.A.; Gòdia, F. Advancements in mammalian cell transient gene expression (TGE) technology for accelerated production of biologics. *Crit. Rev. Biotechnol.* **2018**, *38*, 1–23.
5. Boussif, O.; Lezoualc'h, F.; Zanta, M.A.; Mergny, M.D.; Scherman, D.; Demeneix, B.; Behr, J.P. A versatile vector for gene and oligonucleotide transfer into cells in culture and

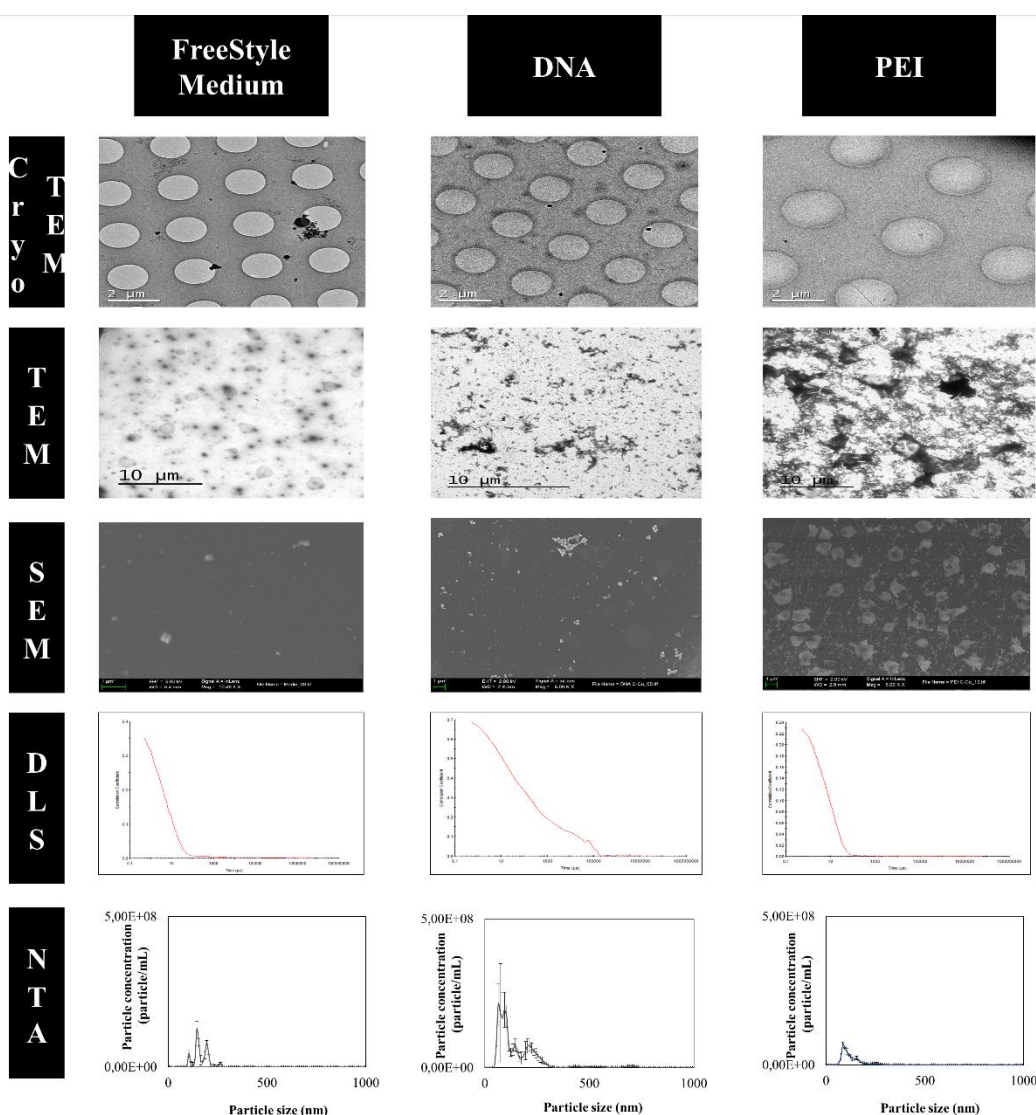
- in vivo: polyethylenimine. *Proc. Natl. Acad. Sci.* **1995**, *92*, 7297–7301.
6. Milián, E.; Julien, T.; Biaggio, R.; Venereo-Sanchez, A.; Montes, J.; Manceur, A.P.; Ansoerge, S.; Petiot, E.; Rosa-Calatrava, M.; Kamen, A. Accelerated mass production of influenza virus seed stocks in HEK-293 suspension cell cultures by reverse genetics. *Vaccine* **2017**, *35*, 3423–3430.
  7. Cervera, L.; Gutiérrez-Granados, S.; Berrow, N.S.; Segura, M.M.; Gòdia, F. Extended gene expression by medium exchange and repeated transient transfection for recombinant protein production enhancement. *Biotechnol. Bioeng.* **2015**, *112*, 934–946.
  8. Venereo-Sanchez, A.; Simoneau, M.; Lanthier, S.; Chahal, P.; Bourget, L.; Ansoerge, S.; Gilbert, R.; Henry, O.; Kamen, A. Process intensification for high yield production of influenza H1N1 Gag virus-like particles using an inducible HEK-293 stable cell line. *Vaccine* **2017**, *35*, 4220–4228.
  9. Cervera, L.; Gutiérrez-Granados, S.; Martínez, M.; Blanco, J.; Gòdia, F.; Segura, M.M. Generation of HIV-1 Gag VLPs by transient transfection of HEK 293 suspension cell cultures using an optimized animal-derived component free medium. *J. Biotechnol.* **2013**, *166*, 152–165.
  10. Cervera, L.; González-Domínguez, I.; Segura, M.M.; Gòdia, F. Intracellular characterization of Gag VLP production by transient transfection of HEK 293 cells. *Biotechnol. Bioeng.* **2017**, *114*, 2507–2517.
  11. Xiang, S.; Tong, H.; Shi, Q.; Fernandes, J.C.; Jin, T.; Dai, K.; Zhang, X. Uptake mechanisms of non-viral gene delivery. *J. Control. Release* **2012**, *158*, 371–8.
  12. Lazebnik, M.; Keswani, R.K.; Pack, D.W. Endocytic Transport of Polyplex and Lipoplex siRNA Vectors in HeLa Cells. *Pharm. Res.* **2016**, *33*, 2999–3011.
  13. Hwang, M.E.; Keswani, R.K.; Pack, D.W. Dependence of PEI and PAMAM Gene Delivery on Clathrin- and Caveolin-Dependent Trafficking Pathways. *Pharm. Res.* **2015**, *32*, 2051–2059.
  14. van Gaal, E.V.B.; Van Eijk, R.; Oosting, R.S.; Kok, R.J.; Hennink, W.E.; Crommelin, D.J.A.; Mastrobattista, E. How to screen non-viral gene delivery systems in vitro? *J.*

- Control. Release* **2011**, *154*, 218–232.
15. Sang, Y.; Xie, K.; Mu, Y.; Lei, Y.; Zhang, B.; Xiong, S.; Chen, Y.; Qi, N. Salt ions and related parameters affect PEI-DNA particle size and transfection efficiency in Chinese hamster ovary cells. *Cytotechnology* **2015**, *67*, 67–74.
  16. Han, X.Z.; Fang, Q.Y.; Yao, F.; Wang, X.N.; Wang, J.F.; Yang, S.L.; Shen, B.Q. The heterogeneous nature of polyethylenimine-DNA complex formation affects transient gene expression. *Cytotechnology* **2009**, *60*, 63–75.
  17. Fukumoto, Y.; Obata, Y.; Ishibashi, K.; Tamura, N.; Kikuchi, I.; Aoyama, K.; Hattori, Y.; Tsuda, K.; Nakayama, Y.; Yamaguchi, N. Cost-effective gene transfection by DNA compaction at pH 4.0 using acidified, long shelf-life polyethylenimine. *Cytotechnology* **2010**, *62*, 73–82.
  18. Raup, A.; Wang, H.; Synatschke, C. V.; Jérôme, V.; Agarwal, S.; Pergushov, D. V.; Müller, A.H.E.; Freitag, R. Compaction and Transmembrane Delivery of pDNA: Differences between 1-PEI and Two Types of Amphiphilic Block Copolymers. *Biomacromolecules* **2017**, *18*, 808–818.
  19. Ulasov, A. V; Khramtsov, Y. V; Trusov, G.A.; Rosenkranz, A.A.; Sverdlov, E.D.; Sobolev, A.S. Properties of PEI-based polyplex nanoparticles that correlate with their transfection efficacy. *Mol. Ther.* **2011**, *19*, 103–12.
  20. Fuenmayor, J.; Cervera, L.; Gutiérrez-Granados, S.; Gòdia, F. Transient gene expression optimization and expression vector comparison to improve HIV-1 VLP production in HEK293 cell lines. *Appl. Microbiol. Biotechnol.* **2018**, *102*, 165–174.
  21. Choosakoonkriang, S.; Lobo, B.A.; Koe, G.S.; Koe, J.G.; Middaugh, C.R.R. Biophysical characterization of PEI/DNA complexes. *J. Pharm. Sci.* **2003**, *92*, 1710–22.
  22. Cho, E.J.; Holback, H.; Liu, K.C.; Abouelmagd, S.A.; Park, J.; Yeo, Y. Nanoparticle Characterization: State of the Art, Challenges, and Emerging Technologies. *Mol. Pharm.* **2013**, *10*, 2093–2110.
  23. Hermida-Matsumoto, L.; Resh, M.D. Localization of human immunodeficiency virus type 1 Gag and Env at the plasma membrane by confocal imaging. *J. Virol.* **2000**, *74*, 8670–9.

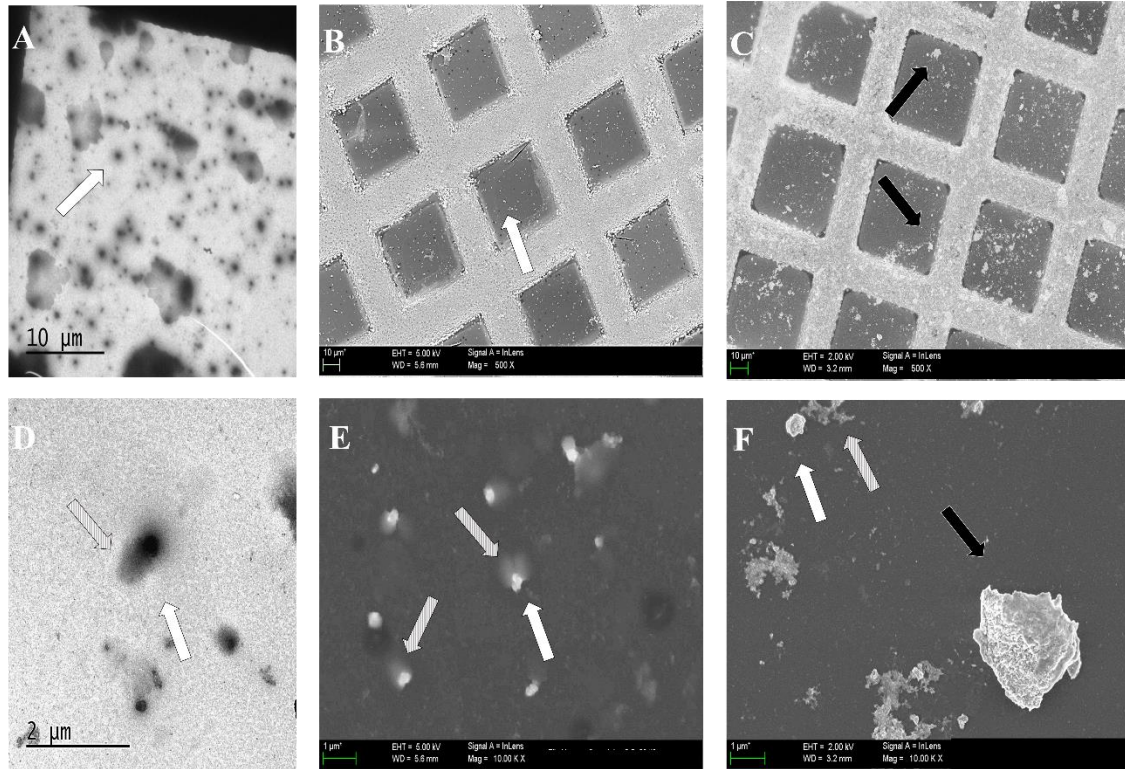


24. Schwartz, S.; Campbell, M.; Nasioulas, G.; Harrison, J.; Felber, B.K.; Pavlakis, G.N. Mutational inactivation of an inhibitory sequence in human immunodeficiency virus type 1 results in Rev-independent gag expression. *J. Virol.* **1992**, *66*, 7176–82.
25. Segura, M.M.; Garnier, A.; Durocher, Y.; Coelho, H.; Kamen, A. Production of lentiviral vectors by large-scale transient transfection of suspension cultures and affinity chromatography purification. *Biotechnol. Bioeng.* **2007**, *98*, 789–799.
26. Gutiérrez-Granados, S.; Cervera, L.; Gòdia, F.; Carrillo, J.; Segura, M.M.; Gutierrez-Granados, S.; Cervera, L.; Godia, F.; Carrillo, J.; Segura, M.M.; et al. Development and validation of a quantitation assay for fluorescently tagged HIV-1 virus-like particles. *J. Virol. Methods* **2013**, *193*, 85–95.
27. van Gaal, E.V.B.; Spierenburg, G.; Hennink, W.E.; Crommelin, D.J.A.; Mastrobattista, E. Flow cytometry for rapid size determination and sorting of nucleic acid containing nanoparticles in biological fluids. *J. Control. Release* **2010**, *141*, 328–338.
28. Chu, Z.; Zhang, S.; Zhang, B.; Zhang, C.; Fang, C.-Y.; Rehor, I.; Cigler, P.; Chang, H.-C.; Lin, G.; Liu, R.; et al. Unambiguous observation of shape effects on cellular fate of nanoparticles. *Sci. Rep.* **2014**, *4*, 4495.
29. Chen, L.; Xiao, S.; Zhu, H.; Wang, L.; Liang, H. Shape-dependent internalization kinetics of nanoparticles by membranes. *Soft Matter* **2016**, *12*, 2632–2641.
30. Glaeser, R.M. How good can cryo-EM become? *Nat Methods* **2016**, *13*, 28–32.
31. Kim, S.H.; Jeong, J.H.; Lee, S.H.; Kim, S.W.; Park, T.G. Local and systemic delivery of VEGF siRNA using polyelectrolyte complex micelles for effective treatment of cancer. *J. Control. Release* **2008**, *129*, 107–116.
32. Godbey, W.T.; Barry, M. a.; Saggau, P.; Wu, K.K.; Mikos, A.G. Poly(ethylenimine)-mediated transfection: a new paradigm for gene delivery. *J. Biomed. Mater. Res.* **2000**, *51*, 321–8.
33. Vercauteren, D.; Vandenbroucke, R.E.; Jones, A.T.; Rejman, J.; Demeester, J.; De Smedt, S.C.; Sanders, N.N.; Braeckmans, K. The Use of Inhibitors to Study Endocytic Pathways of Gene Carriers: Optimization and Pitfalls. *Mol. Ther.* **2010**, *18*, 561–569.

## 7. Supplementary Materials



Supplementary Materials S1. FreeStyle medium, free DNA and free PEI controls for electron microscopy analysis and particle tracking analysis. Cryo-TEM, TEM and SEM images samples were prepared immediately after DNA and PEI addition. DLS and NTA analyses were performed in three independent measurements. DLS analyses of FreeStyle medium had a mean hydrodynamic diameter of  $6 \text{ nm} \pm 3 \text{ nm}$  with stable and monodisperse population (Atn:11; kcps:60); free DNA had a mean hydrodynamic diameter of  $485 \text{ nm} \pm 1 \text{ nm}$  with unstable and polydisperse population (Atn:11; kcps:90); and free PEI had a mean hydrodynamic diameter of  $8 \text{ nm} \pm 0$  stable and polydisperse population (Atn:11; kcps:90). NTA analyses of FreeStyle medium had a mean hydrodynamic diameter of  $174 \text{ nm} \pm 4 \text{ nm}$  with a concentration of  $6.35 \pm 0.55 \text{ E}+8$  particles/ml; free DNA had a mean hydrodynamic diameter of  $150 \pm 12 \text{ nm}$  with a concentration of  $1.87 \pm 0.20 \text{ E}+9$  particles/ml; and free PEI had a mean hydrodynamic diameter of  $130 \pm 2 \text{ nm}$  with a concentration of  $4.25 \pm 0.29 \text{ E}+8$  particles/ml. All NTA measurements for the control samples were performed with a Camera Level of 11 and detection threshold of 5 for medium and PEI and 3 for DNA.



**Supplementary Materials S2. DNA/PEI complex analysis by TEM and SEM at 0 and 15 min incubation in FreeStyle medium in carbon-coated grids. White arrows indicate ~300nm-size DNA/PEI complexes, black arrows indicate  $\geq 1 \mu\text{m}$ -size DNA/PEI complex aggregates, and grey arrows indicate NaCl precipitates surrounding DNA/PEI complexes.**

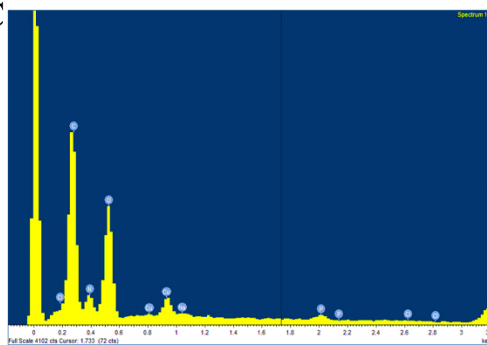
**A**

C	Na	P	Cl	O	Total
25.87	0.97	1.09	1.4	70.67	100
26.39	0.73	0.5	1.15	71.22	100
25.26	1.44	1.26	2.62	69.43	100

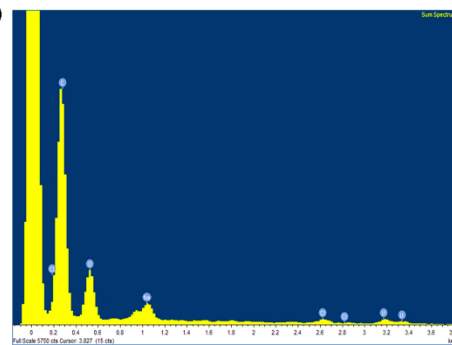
**B**

C	N	Na	P	Cl	Cu	O	Total
19.76	4.21	0.47	1.88	-0.03	5.14	68.56	100

**C**

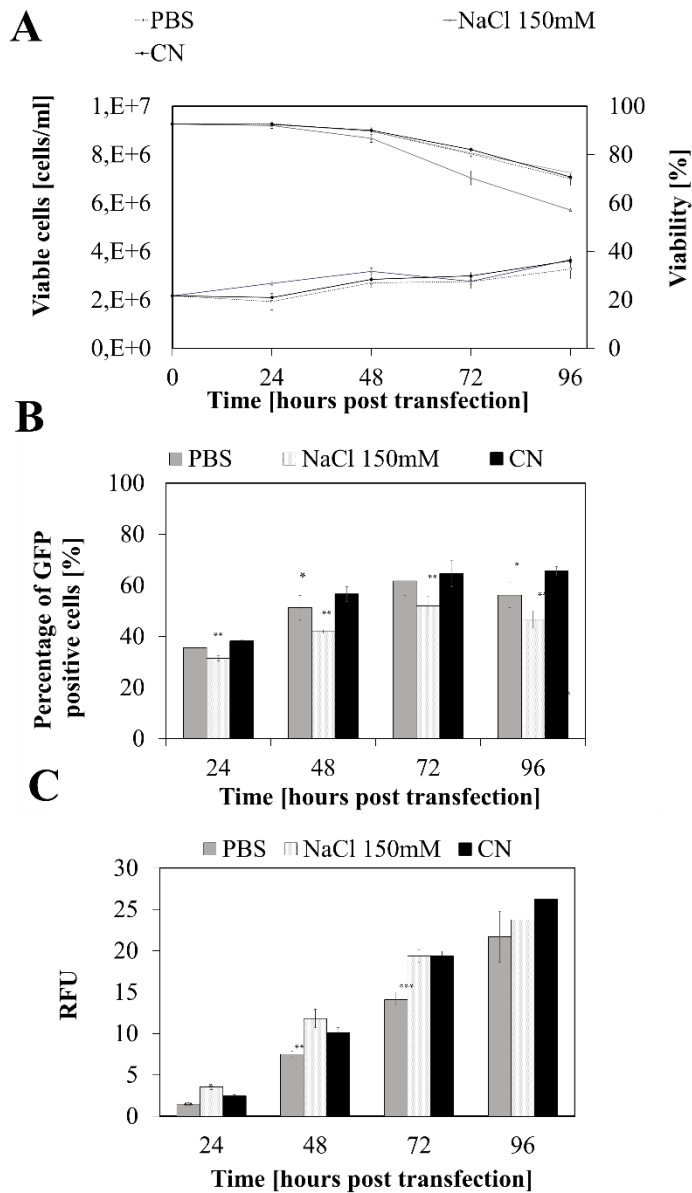


**D**

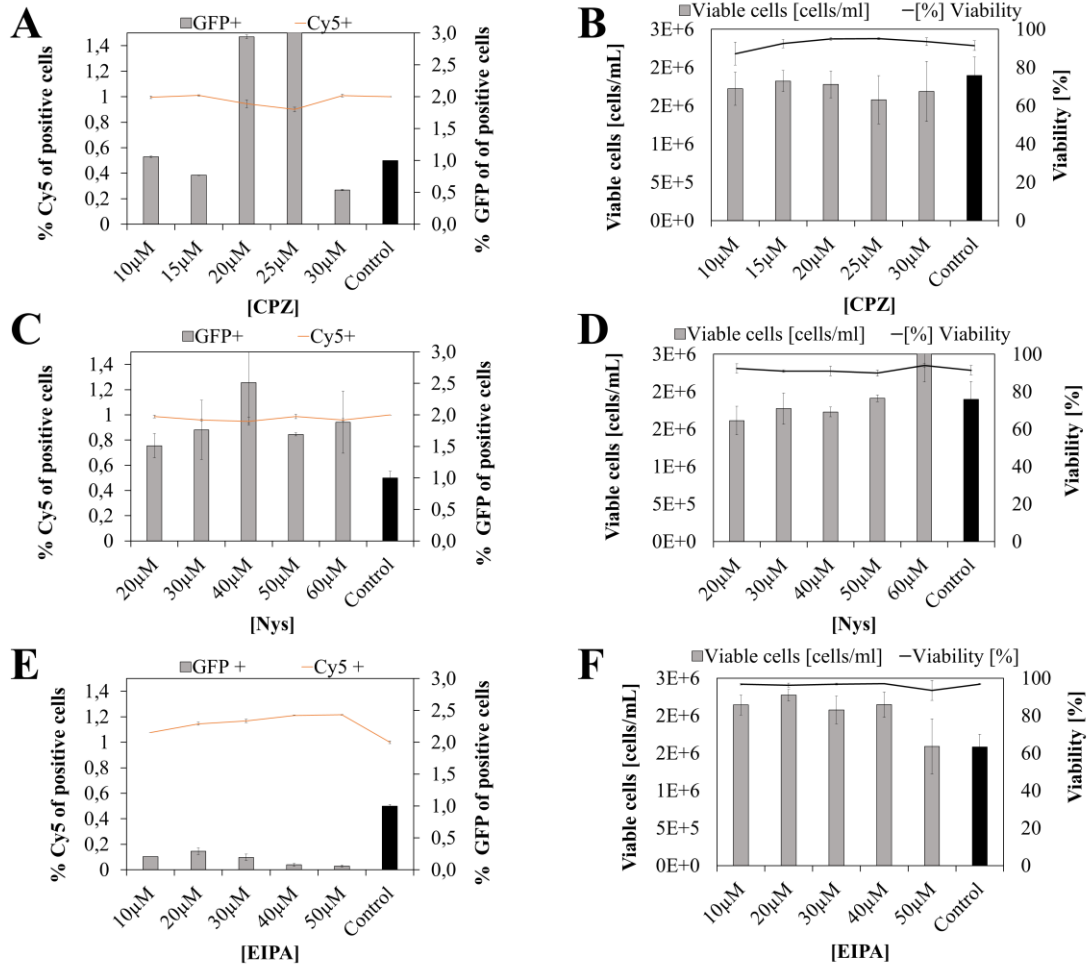


**Supplementary Materials S4. X-ray spectroscopy results of different DNA/PEI complexes from SEM analysis. (A) Table of DNA/PEI histogram final composition and its (C) Summarized**

spectrum from an example histogram (B) DNA/PEI complex analysis by X-ray spectroscopy after its wash with MiliQ water and its (D) Summarized spectrum from an example histogram.



Supplementary Materials S4. Evaluation of other complex incubation media in transient transfection of HEK 293 cells. HEK 293 cells were incubated with the standard transfection process of 15 min of incubation prior to transfection previously described but changing the media complexation: Standard incubation in FreeStyle (CN), incubation PBS (PBS), MilliQ filtered water (MilliQ) and direct addition of DNA and PEI to the cell culture (DIRECT) were tested. (A) Viable cell concentration and cell viability. (B) Percentage of GFP-positive cells. (C) Relative fluorescence units (RFUs) in the supernatant. Experiments were performed in triplicate. Mean values  $\pm$  SD are presented. Student t-test analysis for every condition with the control of each time is also included: \*  $P < 0.05$ , \*\*  $P < 0.01$ , \*\*\*  $P < 0.001$



**Supplementary Materials S5. Endocytosis inhibition preliminary studies in 6-well plates of HEK 293 cells transfection efficiency.** DNA/PEI complexes were formed with Cy5-labeled PEI and the transfection was performed according to the standard methodology. Transfection efficiency was analyzed in terms of GFP (grey bars) and Cy5 (orange line) positive cells and cell concentration and viability associated at 10 hpt are also present, respectively: Chlorpromazine (CPZ) (A,B), nystatin (Nys) (C,D) and N-ethyl-N-isopropyl (EIPA) (E,F). Experiments were performed in triplicate. Mean values  $\pm$  SD are presented.

## **Chapter 2**

# **Rational design of the DNA/PEI complex physicochemical properties for DNA delivery in mammalian cells**

---

**Abstract**

DNA delivery with polyethylenimine (PEI) has been widely used in the last three decades for the transfection of mammalian cells. Advancements in novel characterization techniques at the nanometric scale offer new opportunities to study the physicochemical properties of DNA/PEI polyplexes that lead to an efficient transfection. In this work, these properties are tuned by optimizing simple parameters such as NaCl concentration, pH and incubation time in the preparation of DNA/PEI polyplexes. A Design of Experiments (DoE) approach is used to this end, enabling to identify that the presence of branched-like DNA/PEI aggregates bigger than 1 $\mu$ m in the pre-complexation solution, is essential for an efficient transient transfection. The findings presented in this study will aid to better understand the role of micrometric DNA/PEI aggregates in other transient gene expression strategies since similar complexation protocols and saline solutions are typically used.

**Keywords:** Polyplexes, DNA delivery, Design of Experiments (DoE), Polyethylenimine (PEI), Transient transfection, Particle size

## 1. Introduction

The use of polyethylenimine (PEI) for gene delivery *in vitro* and *in vivo* has been on the spotlight for more than three decades [1,2]. PEI contains an amine group every three atoms, providing a high positive charge density at physiological conditions [3]. These amine groups interact with the negatively charged phosphate groups of nucleic acids generating positively charged complexes (polyplexes). By doing so, the DNA sequences are condensed and protected from nuclease degradation. Once formed, polyplexes interact with the negatively charged cell membrane, where their cellular uptake has been reported to occur by several endocytic and nonendocytic pathways [2]. Among the different routes proposed, the endocytic path is the main uptake mechanism described, where complexes are thought to be trapped into endosomes that later fuse to lysosomes. At this point, the so called “proton sponge effect” of PEI might cause an influx of chloride ions with the consequent increase of osmotic pressure in the lysosomes, which eventually would burst and release the complexes to the cytoplasm. Other theories have also been proposed to explain this phenomenon, including pore formation in the endosomal membrane, or photochemical disruption. Finally, DNA/PEI complexes must reach the nucleus through a process that remains unknown, where DNA is transcribed and maintained as an episome. Despite the use of PEI in DNA delivery has been successfully demonstrated in a myriad of studies, a lack of consensus on the intracellular process dynamics still exists [2,3].

Numerous factors are thought to influence the DNA/PEI complexation processes in transient gene expression (TGE) strategies [4,5]. Physicochemical and biochemical properties of DNA/PEI complexes, and the biological and bioprocess-related aspects of transfection are known to impact the DNA delivery. On the one hand, the DNA/PEI formation is affected by several chemical factors such as pH, salt concentration, temperature or incubation [4,6–9]. Secondly, DNA and PEI chain length, PEI charge density, structure and chemical modifications, the nitrogen/phosphate (N/P) ratio and concentrations, or the complex preparation protocol may alter the physicochemical properties of the formed complexes [1,3,5,9,10]. Furthermore, the development of novel analytical technologies to assess DNA/PEI complexes as nanoparticles has contributed to enlarge



this list, highlighting that particle concentration or morphology might also play a role in the delivery process, as also described for other nanoparticles [11–15]. On the other hand, the cellular uptake, DNA release at intracellular level, or the cytotoxic effect of PEI upon transfection also play a significant role. Biological and bioprocess-related factors like the cell type, cell culture medium composition, cell concentration, time of contact between DNA/PEI complexes and cells, or the addition or replacement of medium in the transfection protocol have also a remarkable influence on transfection efficiency [1,4,16]. Besides the numerous amount of variables, the DNA/PEI complexing process has shown to be highly heterogenous, as polyplex populations with different sizes can be encountered, and thus several biological processes might be taking place within the same transfection, simultaneously [12].

Among the different applications of PEI as complexing agent for DNA, its usage to speed up the screening of novel bioproducts is of great relevance in the initial stages of biopharmaceutical development. Furthermore, PEI-mediated TGE strategies have been optimized and scaled-up for the obtention of sufficient amounts of recombinant product for pre-clinical and early-clinical studies [1], especially in viral vector and vaccine manufacturing [17]. In this work, a rational design approach is proposed as a strategy to optimize the production of virus-like particle (VLPs) as vaccine candidates. To this purpose, a Design of Experiments (DoE) methodology is implemented in order to detect synergies between factors in a reduced amount of runs [18]. DoE has been already applied to TGE optimization where the DNA, PEI and cell concentration at the time of transfection have been studied [19–21]. In addition, a large part of the literature is dedicated to generate modified PEI structures to improve its delivery yields [2,3]. However, the combined effect of simple chemical factors that are known to affect DNA/PEI complex formation individually has not been characterized yet. A three-factor variable encompassing pH, salt concentration and incubation time was studied here. While pH is known to affect the protonation state of PEI [3,22], the complex incubation in saline solutions has been described to increase the polyplex size over time [9,15,23]. The application of DoE with simple chemical reagents is desired to increase the reproducibility of the optimum achieved and allow to translate the present

results to other delivery strategies. These thorough characterizations have been developed with a previously optimized VLP production method in suspension-adapted HEK 293 cells, where the formation process of DNA/PEI complexes in the same cell culture medium has been characterized in a physicochemical manner [23] and at intracellular level [24]. In particular, it has been demonstrated the presence of two polyplex population in size (300 nm and  $>1\mu\text{m}$ ) [23].

The use novel methodologies, such as cryogenic electron microscopy (cryo-EM) or flow virometry, have also been applied here to study the polyplex population at single particle level. While cryo-TEM allow the study of DNA/PEI complex morphology and ultrastructure in its native conditions, flow virometry allow to quantify DNA/PEI complex concentration [25], which joined to Dynamic Light Scattering (DLS) analyses provides a complete physicochemical characterization of the formed complexes. The present results will bring light into the DNA/PEI polyplex formation and its effect on PEI-mediated gene delivery strategies.

## **2. Materials and Methods**

### **2.1. Plasmid DNA**

The plasmid DNA used in this work was pGag-eGFP, which encodes for a Rev independent HIV-1 Gag protein fused in frame to the enhanced green fluorescent protein (eGFP).[26] The plasmid from the NIH AIDS Reagent Program (Cat# 11468) was constructed by cloning the Gag sequence from pCMV55M1-10 [27] into the pEGFP-N1 plasmid (Clontech, Palo Alto, CA, USA). It was prepared and purified as previously described [28].

### **2.2. Cell line, culture conditions and standard transient transfection**

The cell line used was a serum-free suspension-adapted HEK 293 cell line (HEK293SF-3F6, NRC, Canada) kindly provided by Dr. Amine Kamen from McGill University (Montreal, Canada). Cells were cultured in FreeStyle™ 293 medium (FreeStyle, Invitrogen, Carlsbad, CA, USA) supplemented with 0.1% Pluronic® (Invitrogen, Paisley, UK). Medium for cell growth was also supplemented with 1.6 mg/L of r-transferrin (Merck Millipore, Kankakee, IL, USA), 19.8 mg/L of r-insulin (Novo Nordisk Pharmatech, Køge, Denmark) and 0.9 X of an in-house

developed lipid mixture, as previously described [29]. Cells were routinely maintained at exponential growth phase in 125 mL disposable polycarbonate Erlenmeyer flasks with 20 mL volume (Corning, New York, NY, USA), shaken at 130 rpm in a humidified incubator at 37°C and 5% CO<sub>2</sub> enriched air.

HEK 293 cells were transiently transfected using 25 kDa linear polyethylenimine (PEI) (PolySciences, Warrington, PA, USA) at  $2 \cdot 10^6$  cells/mL after medium replacement with fresh FreeStyle 293 medium. Transfections were performed using a final DNA concentration of 1 µg/mL. DNA/PEI complexes were formed by adding PEI to plasmid DNA diluted in the different complexing solutions (10% of the total culture volume to be transfected). Briefly, the pGag-eGFP plasmid was diluted and vortexed for 10 seconds (sec). PEI was then added at a 1:2 DNA/PEI (w:w) ratio and vortexed 3 times for 1 sec. The mixture was incubated for 15 minutes (min) at room temperature (RT) and added to the cell culture.[29] Sampling was performed every 24 hours post transfection (hpt). Cell growth and viability were assessed with the NucleoCounter® NC-3000 automatic cell counter (Chemometec, Allerød, Denmark).

### **2.3. Dynamic Light Scattering (DLS)**

DLS measurements were performed using a Zetasizer Nano ZS instrument (Malvern Panalytical, Malvern, UK) equipped with a He/Ne 633 nm laser at 173° as previously described [23]. The hydrodynamic diameter was calculated by cumulative fit correlation at 25°C and 0.8872 cP. The derived count rate (dCR), defined as the measured count rate divided by the attenuation factor, was also monitored and compared between samples according to the standardized values given by the Zetasizer Nano software 7.12 (Malvern Panalytical). DNA/PEI complexes were prepared in 1 mL final volume and placed in disposable plastic macro cuvettes immediately after its preparation (Scharlab S.L., Barcelona, Spain).

### **2.4. Cryogenic-Transmission Electron Microscopy (Cryo-TEM)**

Cryo-TEM experiments were performed as previously described [23]. Briefly, 2-3 µL of DNA/PEI complexes were incubated for the desired time and were subsequently plunged into

liquid ethane at  $-180^{\circ}\text{C}$  using a Leica EM GP cryo workstation and observed in a JEM-2011 electron microscope (JEOL Ltd., Tokyo, Japan) operating at 200 kV. During imaging, samples were maintained at  $-173^{\circ}\text{C}$ , and pictures were taken using a CCD-multiscan camera (Model# 895, Gatan Inc., Pleasanton, CA, USA).

### **2.5. Flow cytometry**

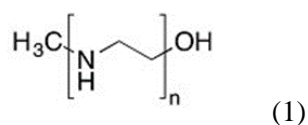
The percentage of eGFP-positive cells was assessed using a BD FACS Canto II flow cytometer (BD Biosciences, San Jose, CA, USA) equipped with a 488 nm laser and GFP FITC-A detector. A total of 20,000 events were analyzed in each sample. First, SSC-H vs. FSC-A and FSC-A vs. FSC-H density plots were used to gate the individual HEK 293 cell population. Afterwards, the percentage of eGFP positive cells was assessed in a GFP FITC-A vs. APC-A density plot. Gating was manually adjusted between  $5 \cdot 10^2$  and  $1 \cdot 10^3$  multiple fluorescence units. Results were analyzed with the FACS DIVA software (BD Biosciences).

### **2.6. Spectrofluorometry analysis**

Quantification of HIV-1 Gag-eGFP VLPs in sample supernatants was assessed using an *in-house* developed and validated spectrofluorometry assay.[30] Green fluorescence was measured at RT using a Cary Eclipse fluorescence spectrophotometer (Agilent Technologies, Santa Clara, CA, USA) with the following settings:  $\lambda_{\text{ex}} = 488 \text{ nm}$  (slit 5 nm),  $\lambda_{\text{em}} = 510 \text{ nm}$  (slit 10 nm). Relative fluorescence units (RFU) were calculated by subtracting fluorescence units (FU) values from non-transfected samples. RFU values were normalized with a 0.1 mg/mL quinine sulphate solution as internal control.

### **2.7. N/P Ratio theoretical approximation**

The nitrogen/phosphate (N/P) ratio was calculated as the theoretical amount of PEI amine groups that are mixed with the phosphate groups of plasmid DNA in a 1:2 (w:w) ratio [5]. Theoretical amine groups in 25 kDa linear PEI (PolySciences, Warrington, PA, USA) were calculated according to its chemical structure and assuming an  $n$  average number of monomers in the polymer chain, where each monomer contains an amino group:



where the monomer molecular weight (MW) is 43 g/mol and  $n$  is 581. Thus, a concentration of 20  $\mu\text{g}/\text{mL}$  corresponds to a concentration of  $4.8 \cdot 10^{14}$  PEI polymers/mL and 465 nitrogen (N) nmol/mL. On the other hand, the number of phosphate groups in a double stranded plasmid DNA sequence was calculated as 2-times the number of base pairs (bp). The MW (3880 kDa) and the number of base pairs (6274 bp) from the pGag-eGFP plasmid used in this work were obtained from Snap Gene Viewer® (GSL Biotech LLC), as previously described.[23] A concentration of 10  $\mu\text{g}/\text{mL}$  corresponds to a concentration of  $1.6 \cdot 10^{12}$  plasmid DNA/mL and 32 phosphate (P) nmol/mL. The N/P ratio is then calculated with equation (2):

$$N/P = \frac{465 \text{ N nmol}}{32 \text{ P nmol}} = 14 \quad (2)$$

### 2.8. Optimization of DNA:PEI complexation process using DoE

Transient transfection was optimized to maximize cell growth at 72 hpt, percentage of eGFP positive cells at 48 hpt and HIV-1 Gag-eGFP VLP production at 72 hpt using a methodology based on Design of Experiments (DoE). NaCl (mM), pH and incubation time (min) in complex formation were the independent variables selected for optimization.

### 2.9. Preparation of complexing media

The different solutions were prepared immediately before transfection. First, NaCl solutions were made from a concentrated solution (Thermo Fisher Scientific, Waltham, MA, USA) with ultrapure water, and pH was subsequently adjusted. Thereafter, solutions were 0.22  $\mu\text{m}$  filtered in sterile conditions and DNA and PEI reagents were added and incubated before its addition to the cell culture.

### 2.10. Toxicity Assays

Definition of the of NaCl concentration and pH ranges in the DNA/PEI complexing solution was conducted by the Cell Titer 96 AQueous One Solution Cell Proliferation Assay (Promega, Madison,

WI, USA) as previously described [31]. Briefly, 100  $\mu\text{L}$  of HEK 293 cells at 0.5 million cells/mL were added per well in 96-well plates (Nalgene Nunc International, Rochester, NY, USA) together with 10  $\mu\text{L}$  of different concentrations of NaCl and pH with and without the addition of DNA/PEI complexes. After 48 hours, 20  $\mu\text{L}$  of Cell Titer 96 reagent were added per well and plates were maintained at 37 °C for 1 hour. The absorbance in each well was measured in a Victor<sup>3</sup> spectrophotometer (PerkinElmer, Waltham, MA, USA) at a wavelength of 490 nm and converted to cell/mL based on a calibration curve of known cell concentration. Statistical analyses were performed by One-way ANOVA and Holm-Sidak tests in SigmaPlot v.12.0 (Systat Software Inc., Chicago, IL, USA).

### 2.11. Full factorial designs

Three sequential  $2^3$  full factorial designs were used to initially study the design space and delimit the ranges of NaCl concentration, pH and incubation time of DNA/PEI complexes in which responses achieved the highest values. Each full factorial design consisted of two coded levels for each independent variable (-1, 1), which were combined in 8 experiments as indicated in Table 1. Three different responses were considered: cell growth (72 hpt), transfection efficiency (48 hpt) and VLP production (72 hpt). A central point was included in the first two factorial designs ( $n = 4$ ) and in the third one ( $n = 2$ ) to detect curvature in the workspace selected for the independent variables and for measurement of the error of the technique (pure error). The curvature, which accounts for regions of the design space with higher levels of the responses, was evaluated by comparing the linear model with and without considering a pseudo-quadratic term and using the *p-value* of the model and  $R^2$  coefficients as statistics. Data were analyzed with R software (R Development Core Team, Vienna, Austria).

**Table 1. Experimental matrix of the  $2^3$  full factorial design. A quadruplicated or duplicated central point (0,0,0) was included to measure the system curvature and pure error**

Experimental run	NaCl (mM)	pH	Incubation time (min)
1	-1	-1	-1
2	+1	-1	-1
3	-1	+1	-1
4	+1	+1	-1
5	-1	-1	+1
6	+1	-1	+1

7	-1	+1	+1
8	+1	+1	+1
9	0	0	0
10	0	0	0
11	0	0	0
12	0	0	0

### 2.12. Central Composite Design (CCD) and multiple response optimization

The third  $2^3$  full factorial design with two central points (Table 3) was amplified with a group of 8 additional experiments (Table 2) to generate a five-level three-factor CCD, including 6-star points ( $\alpha = \pm \sqrt{2}$ ), and two additional central points. This statistical design was used to optimize the levels of NaCl, pH and incubation time of DNA/PEI complexes mediating the best conditions for three responses: transient transfection, VLP production and cell growth. Data obtained for each response were fitted to a second-order polynomial equation (Equation 3) by linear regression analysis with R software (R Development Core Team, Vienna, Austria), as previously described [20].

$$Y = \beta_0 + \sum_{i=1}^k \beta_i \cdot X_i + \sum_{i=1}^k \beta_{ii} \cdot X_i^2 + \sum_{i=1}^k \sum_{j>1}^k \beta_{ij} \cdot X_i \cdot X_j + \varepsilon \quad (3)$$

where  $Y$  corresponds to each response analyzed,  $\beta_0$  is the model intercept term,  $\beta_i$  the linear coefficient,  $\beta_{ii}$  is the quadratic coefficient,  $\beta_{ij}$  the interaction coefficient,  $X_i$  and  $X_j$  are the studied variables and  $\varepsilon$  is the experimental error. The quality of model regression equations was evaluated by the  $R^2$  coefficients. The overall significance of the model was determined by ANOVA F test and the significance of each coefficient was determined with the corresponding t test. The lack of fit test was used to evaluate differences between experimental and pure error of the models. An overall optimum from the three responses considered was obtained by the combination of the individual optima using desirability functions [32]. Briefly, relevance values (s-value) of 0.5, 2 and 2 were given to cell growth, transient transfection and VLP production models, respectively, and an iteration process was conducted to determine the best conditions integrating the different responses of the study.

**Table 2. Star and central points added to the  $2^3$  full factorial design**

Experimental run	NaCl (mM)	pH	Incubation time (min)
------------------	-----------	----	-----------------------

1	$-\alpha$	0	0
2	$\alpha$	0	0
3	0	$-\alpha$	0
4	0	$\alpha$	0
5	0	0	$-\alpha$
6	0	0	$\alpha$
7	0	0	0
8	0	0	0

### 2.13. Flow Virometry

DNA/PEI complexes analysis was performed in a CytoFLEX LX (Beckman Coulter Inc., Brea, CA, USA) equipped with a violet side scatter (V-SSC) 405 nm filter configuration. The threshold of height trigger signal was manually adjusted to 1200 in the V-SSC and laser gains were set as 72, 9 and 106 for FSC, V-SSC and B525-FITC, respectively. 500.000 events were analyzed per sample at a flow rate of 10  $\mu\text{L}/\text{min}$ . V-SSC vs B525-FITC density plots were used to gate the DNA/PEI complexes. Results were analyzed with the CytExpert v.2.3 software (Beckman Coulter) and DNA/PEI complex concentrations were calculated with equation (4):

$$\text{DNA /PEI complex} \left( \frac{\text{events}}{\text{mL}} \right) = \frac{\text{events}}{\mu\text{L}} \cdot \frac{\mu\text{L}}{\text{mL}} \cdot \text{Dilution} \quad (4)$$

## 3. Results and Discussion

### 3.1. Effect of complexing media in DNA/PEI polyplex formation

Exploratory experiments were firstly performed to study whether a change in the DNA/PEI complexation medium had an impact on DNA/PEI complex formation and on its efficiency *in vitro*. Analysis of DNA/PEI polyplex formation was evaluated in different complexing media, including ultrapure water ( $\text{H}_2\text{O}$ ), 3 and 150 mM NaCl solutions and PBS. DNA/PEI complexes were added in a 1:2 (w:w) ratio, corresponding to a N/P ratio of 14 and incubated for 15 min at RT. DLS and cryo-TEM were used to study the mean hydrodynamic diameter and morphology of DNA/PEI complexes (Figure 1). DNA and PEI were separately analyzed in each of these solutions as negative controls (Figure S1). A constant mean hydrodynamic diameter of  $94 \pm 4$  nm and  $70 \pm 1$  nm was obtained in ultrapure  $\text{H}_2\text{O}$  and 3 mM NaCl solution, respectively. Low derived count rate (dCR) values of  $1001 \pm 19$  arbitrary units (a.u.) and  $181.6 \pm 4.9$  a.u., which represent the amount of scattered light, and the presence of  $\sim 80$  nm electrodense structures in cryo-TEM

---



micrographs indicated the formation of small and stable DNA/PEI complexes in these media with time [20]. In the case of 150 mM NaCl and PBS solutions, an aggregation process of DNA/PEI complexes was observed as a result of the simultaneous increase of the mean hydrodynamic diameter and the decrease of the dCR in the two cases [8,23]. A DNA/PEI polyplex mean hydrodynamic diameter of 369 nm and 353 nm were initially recorded, increasing until 732 nm and 649 nm after 15 min incubation in 150 mM NaCl and PBS, respectively. Cryo-TEM micrographs in these conditions revealed the existence of branched-like structures with heterogenous sizes in the micrometric scale for both solutions. Larger structures were likely formed by the initial interaction of DNA/PEI complexes of around 300 nm of diameter that aggregated with time, as illustrated when analyzing DNA/PEI aggregates at higher magnifications (i.e. 10000x, Figure 1B and 1D).

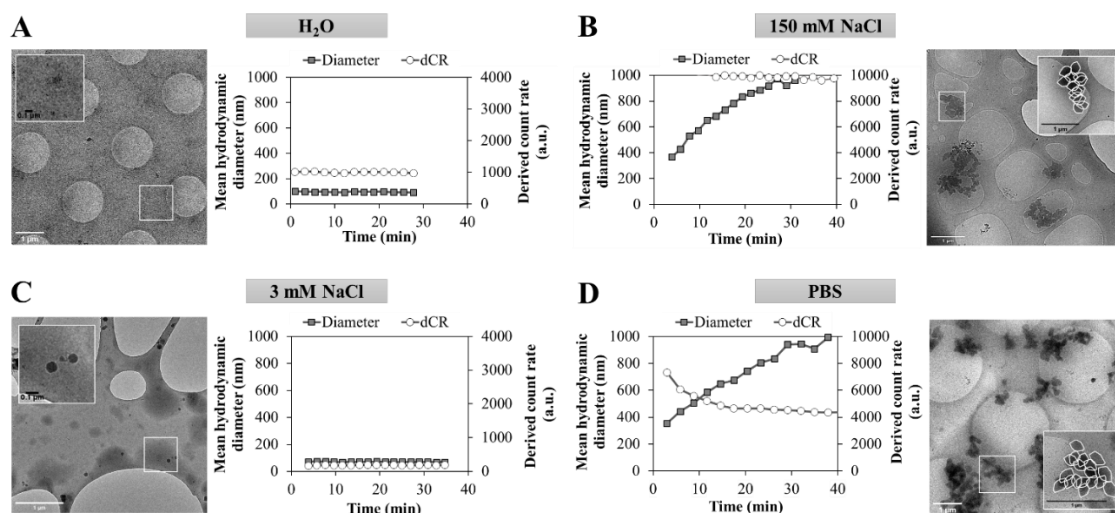


**Figure 1.** DNA/PEI complex formation in different solutions: Ultrapure H<sub>2</sub>O (A), 150 mM NaCl (B), 3 mM NaCl (C) and PBS (D). DLS measurement of the mean hydrodynamic diameter (nm) and the corresponding scattered light by means of derived count rate (dCR) units. Cryo-TEM micrographs of DNA/PEI polyplexes were taken after 15 min of incubation in each solution. DNA/PEI complexes were prepared in a 1:2 (w:w) ratio corresponding to N/P of 14 with DNA at a concentration of 10 µg/mL.

The impact of DNA/PEI polyplexes pre-formed on each medium was tested *in vitro* (Figure 2).

A previously defined transient gene expression (TGE) methodology for the generation of HIV-1 Gag-eGFP VLPs in HEK 293 cells was used.[23,29] Briefly, upon recombinant Gag-eGFP expression, Gag accumulates underneath the plasma membrane and VLPs are released to the extracellular space through a budding process [33]. The fusion of eGFP to the Gag polyprotein

enabled the monitoring of Gag-eGFP expression in HEK 293 cells by flow cytometry, as well as VLP quantification by spectrofluorometry (relative fluorescence units, RFU) in cell supernatants [30]. A non-transfected condition was included as a negative control (NC), whereas DNA/PEI complex formation in FreeStyle 293 cell culture media was considered as the positive control, in agreement with previous works [29,34,35]. No differences were observed in terms of cell growth and viability regarding the DNA/PEI complexing media used, in comparison to the positive control. Hence, the different DNA/PEI complex sizes obtained in the different solutions did not present cytotoxic effect on cultured cells.

DNA/PEI polyplex formation in the different media succeed in delivering plasmid DNA, as shown by the presence of GFP positive cells in all cases (Figure 2B). Nevertheless, lower transfection efficiencies were observed when complexes were formed in H<sub>2</sub>O and 3 mM NaCl. The same was observed for the mean fluorescence intensity (MFI) of transfected cells (Figure 2C), and also with respect to VLP production (Figure 2D). DNA/PEI complexes formed in hypotonic solutions had half the MFI and 4-fold less VLP production, compared to the positive control at the time of harvest (72 hpt, *p-value* < 0.05). As for hypertonic solutions (150 mM NaCl and PBS), similar levels of MFI and VLP production were achieved with 150 mM NaCl, whereas a 30% lower VLP production was reported with PBS (*p-value* >0.001) compared to the positive control at 72 hpt. Different assumptions can be made when considering these data in combination with the physicochemical characterization of the DNA/PEI complexes (Figure 1): (1) DNA delivery to HEK 293 cells is achieved independently of the complexing solution used if DNA and PEI are mixed; (2) large DNA/PEI complexes, as those obtained in 150 mM NaCl and PBS, achieve higher transfection and production yields in this cell line; (3) salt ions actively participate in the aggregation process of DNA/PEI complexes; (4) there is a critical concentration of salt that allows the highest TGE levels, as observed when comparing 3 and 150 mM NaCl solutions; (5) the presence of buffer molecules or other ions present in PBS, does not have a positive effect on TGE. Based on these results, NaCl solutions could serve as a simple reference media to

understand the DNA/PEI formation in the absence of other salt ions, buffer molecules or additives as those present in other complexing solutions (i.e. cell culture medium).

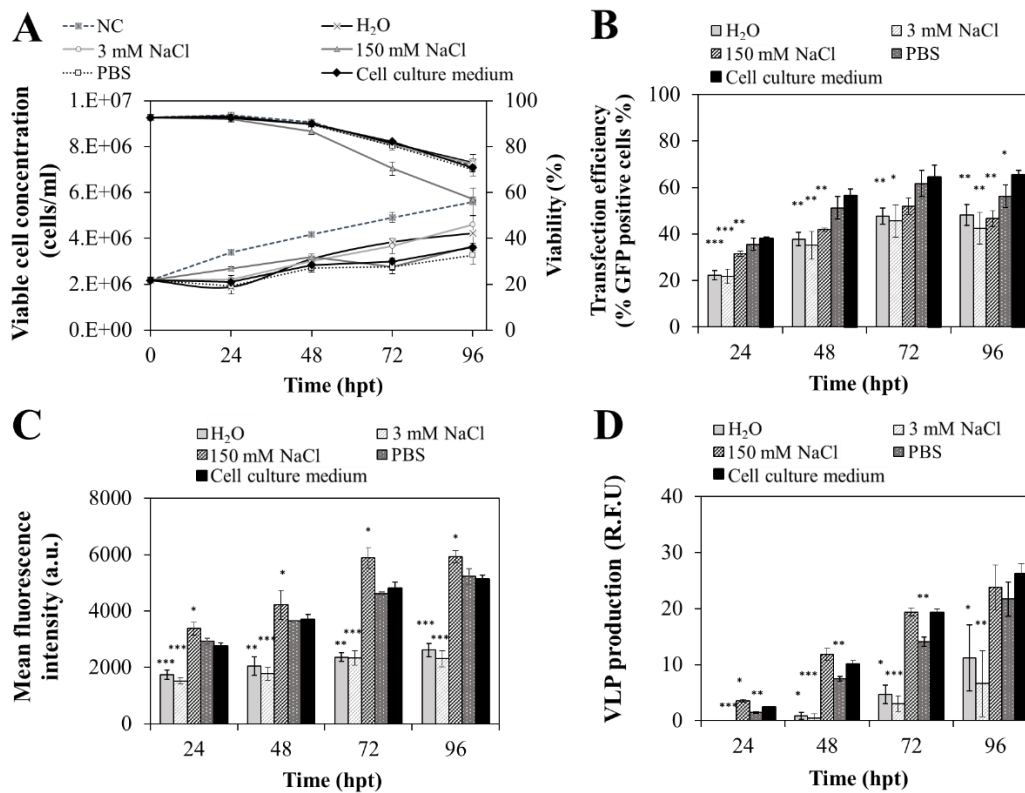


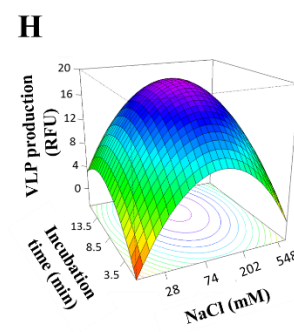
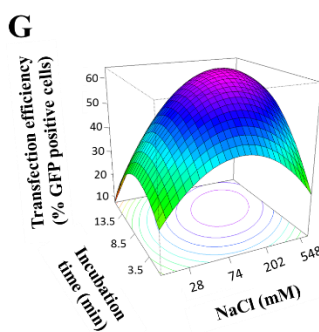
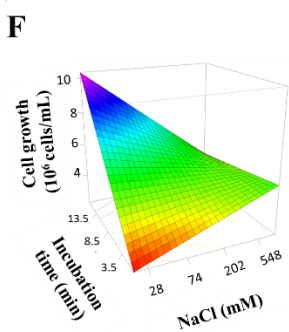
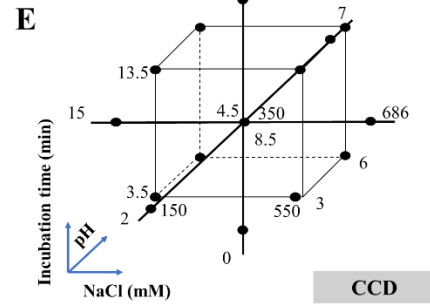
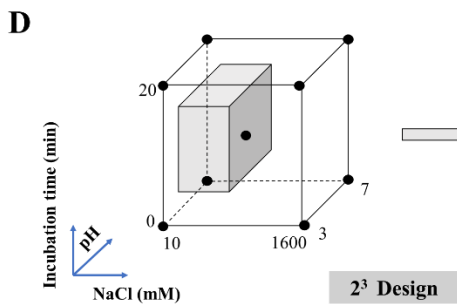
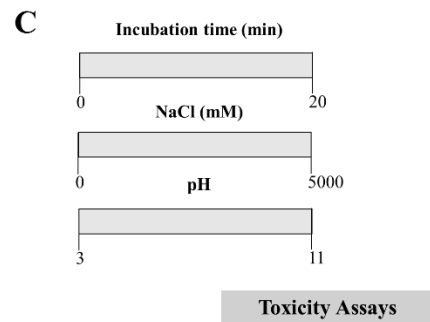
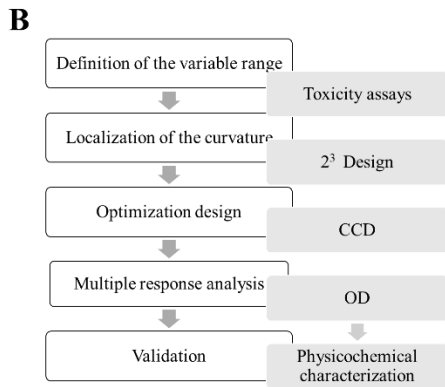
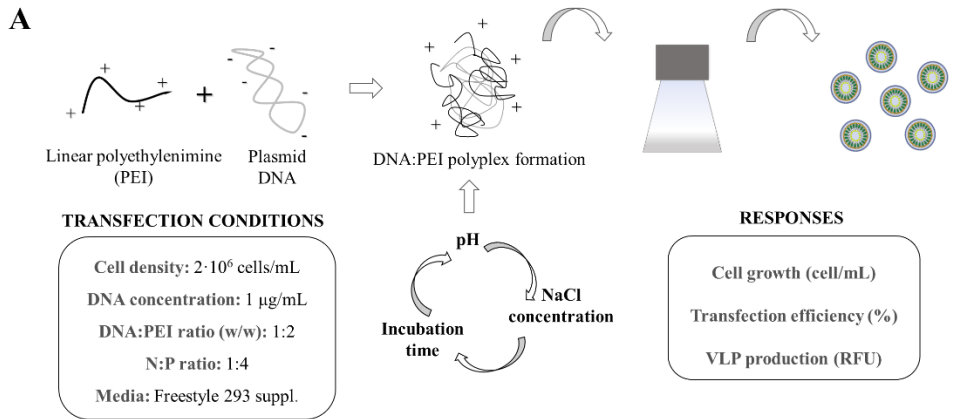
**Figure 2.** Effect of DNA/PEI complex formation in different solutions on the production of HIV-1 Gag-eGFP VLPs by TGE of HEK 293 cells. (A) Viable cell concentration and cell viability. (B) Percentage of GFP-positive cells. (C) Mean fluorescence intensity (MFI) of transfected cells. (D) Quantification of VLP production as relative fluorescence units (RFUs) in the supernatant. DNA/PEI complexes at 1:2 (w:w) ratio with DNA at a concentration of 10  $\mu\text{g}/\text{mL}$  of were prepared and incubated for 15 min. Experiments were performed in triplicate and mean values  $\pm$  SD are presented. Student t-test analysis of every condition against the positive control (FreeStyle 293 cell culture medium) is also included, for comparison. \* p-value < 0.05, \*\* p-value < 0.01, \*\*\* p-value < 0.001. NC: negative control; H<sub>2</sub>O: ultrapure water.

### 3.2. Study of the DNA/PEI complexing conditions using DoE

The efficiency of PEI-mediated TGE in HEK 293 cells has been shown to be highly dependent on the DNA/PEI complexation process. Three independent variables, including NaCl concentration, pH and incubation time, were selected to study the optimization of DNA/PEI complex formation for the generation of HIV-1 Gag-eGFP VLPs. PEI is known to be protonated at physiological conditions (pH  $\sim$ 7.4) and its protonation state decreases with lower pH values [36]. The effect of NaCl concentration on DNA/PEI formation has been observed here, and described previously [9,37]; whereas the impact of complex incubation time, resulting in an

aggregation process, has also been reported in other studies [8,9,23]. However, the synergies between these variables have not yet been investigated. To obtain a holistic view of the process, three different responses were assessed and optimized, simultaneously. Concretely, the cell growth at harvest time (72hpt), transfection efficiency as the percentage of producing cells at mid-production phase (48hpt) and VLP volumetric production in RFU at 72hpt were selected.

To this purpose, a Design of Experiments (DoE) and desirability functions approach was implemented (Figure 3). A schematic representation of the experimental procedure is presented in Figure 3A and the five-step workflow followed is shown in Figure 3B. Initially, the ranges of the different variables considered were delimited to avoid cytotoxic conditions for HEK 293 cells. Afterwards, a series of  $2^3$  full factorial designs were used to reduce the design space by following the path of steepest ascent to experimental regions where responses achieved higher values [38]. At this point, a Central Composite Design (CCD) was performed to define the optimal combination of NaCl concentration, pH and DNA/PEI polyplex incubation time mediating the maximization of each response. Once the three responses were optimized, they were combined into a global TGE optimum by means of desirability functions, as reported by Derringer and co-authors [39]. A final validation experiment was conducted to corroborate the optimal condition and compared to the physicochemical properties of the DNA/PEI complexes obtained in these conditions.



Cell growth (10<sup>6</sup> cells/mL) =  $7.39 - 0.41 \cdot \ln(\text{NaCl}) + 4.26 \cdot \text{Time} - 0.69 \cdot \ln(\text{NaCl}) \cdot \text{Time}$

Transfection efficiency (%) =  $-73.0 + 53.0 \cdot \ln(\text{NaCl}) - 13.8 \cdot \text{Time} + 3.4 \cdot \ln(\text{NaCl}) \cdot \text{Time} - 5.1 \cdot \ln(\text{NaCl})^2 - 5.6 \cdot \text{Time}^2$

VLP Production (RFU) =  $-67.2 + 36.2 \cdot \ln(\text{NaCl}) + 2.3 \cdot \text{Time} - 3.8 \cdot \ln(\text{NaCl})^2 - 2.4 \cdot \text{Time}^2$

**I**

NaCl (mM)	Incubation time (min)	pH	OD
125	11	N.S.	

**Figure 2. DNA/PEI complexing medium optimization by DoE.** (A) Scheme of PEI-mediated TGE protocol for HIV-1 Gag-eGFP VLP production in suspension-adapted HEK 293 cells. DNA/PEI complexes were formed by mixing plasmid DNA (10µg/mL) with PEI in a 1:2 (w:w) ratio, corresponding to a N/P of 14 in 10% of the total volume to be transfected. The effect of NaCl concentration, pH and incubation time (independent variables) was studied on cell growth, transfection efficiency and VLP production (responses). (B) DoE experimental workflow. (C) Variable ranges assessed in the cytotoxicity assays. (D) Study of the design workspace and localization of curvature with  $2^3$  full factorial designs. (E) Optimization of the different responses using a central composite design (CCD). (F – H) Three dimensional plots for cell growth (F), transfection efficiency (G) and VLP production (H) in the CCD. These plots show the synergies between NaCl concentration and DNA/PEI polyplex incubation time on each response. pH was found as not significant. (I) Global optimum condition obtained after maximizing the overall desirability function (OD). N.S.: non-significant, ln: logarithm.

### 3.3. Definition of the design space

Several preliminary studies were conducted in order to define a suitable workspace for each independent variable and avoid cell cytotoxicity (Figure 3C). Initial ranges were selected based on the solubility of NaCl in ultrapure water (0 – 5 M), PEI stability on different pH (3 – 11) and reported studies, as for DNA/PEI complexing time (0 – 20 min).[8,23] The addition of NaCl solutions and different pH with and without DNA/PEI polyplexes was performed to evaluate their effect on HEK 293 cells, respectively. The level of cell cytotoxicity was evaluated at 48 h after supplementation with the different solutions (Figure S2). NaCl concentrations higher than 1.6 M reduced cell growth by  $55 \pm 2$  % (Figure S2A), while no cell cytotoxicity was observed with varying pH conditions (Figure S2B).

### 3.4. Following the path of steepest ascent

A series of two  $2^3$  full factorial designs with central points were conducted to find regions of design space with higher response outputs (Figure 3D). Central points (0,0,0) were included in order to account for internal regions of the workspace that could have superior levels than the design space limit values (-1,-1,-1) and (1,1,1), known as curvature. Ranges for the initial screening design were selected according to cytotoxicity experiments and consisted of 10 – 1600 mM for NaCl concentration, 3 – 11 for pH and 0 – 20 min for DNA/PEI polyplex incubation time (Figure S3). A non-linear additive effect of NaCl on the different responses with increasing salt concentrations was detected. Therefore, this variable was transformed with the logarithmic function to accurately detect its effect on the different responses. A strong cytostatic effect was

observed at increasing NaCl concentrations (Figure S3). In these conditions, cell growth was arrested after transfection ( $\sim 2 \cdot 10^6$  cells/mL) and barely no VLP production could be detected ( $\sim 1$  RFU). Consequently, NaCl concentration was the most significant variable on the three responses in the workspace selected (Figure S3). Interestingly, the inclusion of central points enabled the detection of positive curvature for transient transfection (Figure S4A) and VLP production (Figure S4B) at mid-NaCl, indicating region of the workspace with higher response outputs. To evaluate this, a second  $2^3$  full factorial with a reduced range for NaCl concentration (5 – 800 mM) but maintaining pH and incubation time limit values was performed (Figure S5).

In the second full factorial design, NaCl concentration was maintained as the main variable affecting all three responses ( $p$ -value < 0.001). Nevertheless, pH and the incubation time also showed a significant effect that varied depending on the response under consideration (Figure S5). The cytostatic effect of high NaCl concentrations (800 mM) on cell growth was still remarkable, albeit at a lower degree, compared to that observed in the first full factorial, arresting cell growth at  $\sim 3 \cdot 10^6$  cells/mL ( $p$ -value < 0.001). As for transfection efficiency and VLP production, increasing pH and the interaction between incubation time and pH exhibited a negative effect on both responses ( $p$ -value < 0.05) besides NaCl concentration effect. The latter indicates that DNA/PEI polyplexes incubated in basic pH conditions for longer times (10 – 20 min) impact on the TGE process, possibly related to a higher level of protonation of these complexes in this context.[22] The highest transfection ( $49 \pm 3$  %) and VLP production values ( $8.6 \pm 0.9$  RFU) were achieved at the central experimental point (Figure S5 and S6). Consequently, the design space could be narrowed down to lower NaCl concentrations, acidic to neutral pH and intermediate DNA/PEI polyplex incubation times, as shown in contour plots built for each response (Figure S6).

### **3.5. Central composite design**

The second  $2^3$  full factorial design allowed to encounter a reduced workspace with higher response values. A CCD, consisting of a  $2^3$  full factorial design augmented with 6-star points, was used to explore and optimize the combination of NaCl concentration, pH and DNA/PEI polyplex

---

incubation time maximizing each response (Table 3). Five levels, coded as  $-\alpha$ ,  $-1$ ,  $0$ ,  $1$  and  $\alpha$ , were studied for each independent variable and resulted in a total of 18 experiments in which the central point was quadruplicated to account for the experimental error (Figure 3E). Interestingly, an average concentration of  $5.1 \pm 0.7 \cdot 10^6$  cells/mL and a cell viability of  $92 \pm 1$  % was calculated for the 18 experiments conducted, proving that the variables ranges selected were adequate for cell culture. Experimental results for each response were fitted to a second-order polynomial equation by the method of least squares method (Table 3). The statistical significance of each model was confirmed by ANOVA analysis ( $p$ -value  $< 0.01$ ). The three response equations were subjected to a refinement process to eliminate non-statistically significant terms according to the hierarchy principle[40]. Three-dimensional plots were generated using these equations to facilitate the interpretation of the effects of independent variables on each response (Figure 3F – H). In all cases, pH was not found significant for any of the responses evaluated in the 2 – 7 pH range. Regarding cell growth, minimum NaCl concentrations and large DNA/PEI polyplex incubation times resulted in the highest viable cell concentration (Figure 3F). As for transfection efficiency and VLP production, a NaCl concentration in the range of 100 – 200 mM and an incubation time of 8 – 14 min enabled to obtain the best response levels.

From these responses, it is here highlighted that a certain concentration of NaCl and incubation time for DNA/PEI complexes to form is required to mediate an efficient transfection. Although the combination of both variables has not been described in other works, Bono *et al.* reported 150 mM NaCl, together with 10mM HEPES and 5% (w/v) glucose, as the most common ionic solution used [5], whereas an incubation time of 10 to 20 minutes has been typically encountered in TGE processes [1]. In addition, linear experiments of DNA/PEI complexes incubation time and salt concentrations in CHO cells [8,41] or HEK 293 [9,23] have shown similar 10 minutes incubation as the best condition while non-significant or even detrimental effect was presented for longer incubation times and NaCl concentrations, early suggesting the presence of a combined optimum.

### **3.6. Multiple response optimization by desirability functions**



The equations obtained with the CCD for each one of the responses yielded different optima (Figure 3F – H). Therefore, a single DNA/PEI complexation condition encompassing cell growth, transfection efficiency and VLP production would be desirable. To this purpose, a modelling approach based on response weighting by means of desirability functions was implemented, with successful results reported in different strategies of process optimization [42–44]. Weight assignment to each response (*s*-value) was performed according to their relative contribution to the process, with a higher relevance given to transfection efficiency and VLP production (*s*-value = 2) and a lower restriction for cell growth (*s*-value = 0.5). Then, responses were transformed to the same scale and combined to maximize the overall desirability (OD) function via an iteration process. After this process, a global DNA/PEI complexation optimal consisting of 125 mM of NaCl and an incubation time of 11 min was obtained (Figure 3I).

### **3.7. Validation and physicochemical characterization of DNA/PEI complexes**

A validation experiment was carried out to corroborate the global optimal condition predicted by the combination of the CCD and multiple response optimization (Table 4). The global optimal condition was compared to the predicted response: a transfection efficiency of  $69.3 \pm 4.0$  % at 48 hpt and a VLP production of  $18.6 \pm 0.8$  RFU at 72 hpt was obtained for the global optimum condition, in agreement with model prediction of  $63.1 \pm 7.7$  % and a VLP titer of  $18.6 \pm 3.2$  RFU, respectively. Thus, the three CCD responses and the overall desirability were perfectly validated.

**Table 3. Ranges for NaCl concentration, pH and incubation time, experimental matrix, results and ANOVA analysis of the equations obtained in the CCD.**

Central Composite Design						
Variables	Coding levels					
	$-\alpha$	-1	0	1	$\alpha$	
NaCl (mM)	15	150	350	550	686	
pH	2	3	4.5	6	7	
Incubation time (min)	0	3.5	8.5	13.5	17	

Experimental run	Independent variables			Responses		
	NaCl (mM)	pH	Incubation time (min)	Cell growth (cells·10 <sup>6</sup> /mL)	Transfection efficiency (%)	VLP production (RFU)
1	-1	-1	-1	4.61	52.7	12.8
2	1	-1	-1	4.24	46.9	5.9
3	-1	+1	-1	4.94	57.3	14.8
4	+1	+1	-1	4.87	42.7	4.3
5	-1	-1	+1	5.7	59.2	16.6
6	+1	-1	+1	4.41	52.7	6.6
7	-1	+1	+1	7.15	60.3	18.3
8	+1	+1	+1	4.56	61.2	9.1
9	0	0	0	4.44	59.8	12.3
10	0	0	0	5.24	61.7	13.4
11	$-\alpha$	0	0	5.92	31.2	1.5
12	$\alpha$	0	0	5.05	52.6	4.7
13	0	$-\alpha$	0	5.28	56.8	12.2
14	0	$\alpha$	0	4.89	63.1	12.6
15	0	0	$-\alpha$	4.61	32.5	0
16	0	0	$\alpha$	4.93	58.2	11.2
17	0	0	0	4.8	62.1	12.5
18	0	0	0	5.31	63.3	13.2

Analysis				
Model	F test, <i>p</i> -value <sup>a</sup>	Lack of fit test, <i>p</i> -value	R <sup>2</sup>	Adjusted R <sup>2</sup>
(A) Cell growth	**	> 0.05	0.63	0.55
(B) Transfection efficiency	****	> 0.05	0.93	0.90
(C) VLP production	****	> 0.05	0.95	0.93

Parameters Model			
(A)	Coefficient	<i>t</i> -value	<i>p</i> -value
Constant	7.39	10,39	****
Ln[NaCl]	-0.41	-3.32	***
[Inc.Time]	4.26	3.01	**

Parameters Model (B)	Coefficient	<i>t-value</i>	<i>p-value</i>
Ln[NaCl] x [Inc.Time]	-0.69	-2.83	*
Constant	-73.0	-5.19	****
Ln[NaCl]	53.0	8.57	****
[Inc.Time]	-13.8	-1.45	> 0.05
Ln[NaCl] <sup>2</sup>	-5.1	-7.89	****
[Inc.Time] <sup>2</sup>	-5.6	-6.47	****
Ln[NaCl] x [Inc.Time]	3.4	2.05	*

Parameters Model (C)	Coefficient	<i>t-value</i>	<i>p-value</i>
Constant	-67.2	-11.2	****
Ln[NaCl]	36.2	13.7	****
[Inc.Time]	2.3	6.5	****
[NaCl] <sup>2</sup>	-3.8	-13.8	****
[Inc.Time] <sup>2</sup>	-2.4	-6.5	****

<sup>a</sup>*p-value* codification: \*: 0.05, \*\*: 0.01, \*\*\*: 0.001\*\*\*\*: 0.0001, Inc.Time: incubation time, Ln: logarithm

**Table 4. Experimental validation of the global optimal conditions and comparison to model predictions. Prediction interval represent the lower and upper limits according to the logistic response.**

Response	Cell Growth (10 <sup>6</sup> viable cells/mL)	Transfection Efficiency (%)	VLP Production (RFU)
Model Prediction	[4.74 - 6.88]	[55.3 - 70.7]	[15.3 - 21.8]
Experimental	4.87 ± 0.54	68.9 ± 4.6	18.6 ± 0.8

Different cutting-edge methodologies were applied to gain insight into the DNA/PEI complexing process in the optimum condition (Figure 4). The DNA/PEI complex formation process was analyzed by DLS, Flow Virometry and NTA. The mean hydrodynamic diameter and derived count rate (dCR) were monitored using DLS, whereas polyplex concentration was quantified by flow virometry and *in vivo* analysis of the DNA/PEI behavior was observed by NTA. In all three cases, an aggregation tendency was observed with time. An initial mean hydrodynamic diameter of 320 nm was tracked increasing until 810 nm, while the dCR values decreased from 11565 a.u. to 9563 a.u. by DLS after 20 minutes of incubation in 125 mM NaCl. When the particle size distribution (PSD) in volume was analyzed with time, the presence of micrometric aggregates

was detected at high incubation times (Figure 4B). Furthermore a 5-fold decrease in DNA/PEI complex concentration was obtained in flow virometry analyses after the 20 minutes of incubation. From the highest DNA/PEI complex concentration of  $2.3 \cdot 10^8$  complexes/mL, a reduction in particle number until  $0.5 \cdot 10^8$  complexes/mL was obtained after the incubation. However, due to the limit of detection in flow virometry for analyzing nanometric particles, and the high electronic abort rate recorded at that time (17.8%), it is probable that the concentration of DNA/PEI complexes is being underestimated. The same conclusion could be taken from the NTA analyses (Figure S7), since a concentration of nanoparticles above the allowed 60 particles per frame is present at shorter times [45]. Of note, in previous NTA analyses of DNA/PEI complex formation, where complexes were diluted before the measurement, an initial DNA/PEI complex concentration of  $1 \cdot 10^{10}$  complexes per mL have been reported [23]. Similar concentration issues have been reported by Van der Pol and co-workers, where a 15 to 300-fold difference concentration was obtained in flow cytometry results compared to NTA in the study of extracellular vesicles [46]. Furthermore, changes in size of the DNA/PEI complexes over time could be inferred from the amount of scattered light of the individual DNA/PEI complexes analyzed in flow virometry by Violet-SSC area signal (V-SSC-A) (Figure 4D). Of note, Mie correlations between these values and nanoparticle size are nowadays being used in the study of the size nanoparticles [47]. An increase from  $3.4 \cdot 10^3$  to  $6.2 \cdot 10^4$  mean V-SSC-A values was recorded after incubation.

From the different levels of aggregation observed, the optimal condition obtained in the DoE was further characterized by Cryo-TEM (11 minutes of incubation, black arrow, Figure 4A and 4C and Figure 4E). The morphology and ultrastructure of DNA/PEI polyplexes presented branched-like DNA/PEI complexes with micrometric sizes. These branched structures were previously depicted in the preliminary analyses, where similar salt concentrations were used, (Figure 1). This aggregation phenomenon at high N/P in the presence of salt has been recently modeled at molecular level (N/P 10 in 150 mM KCl).[48] In previous works, DNA/PEI complexes formed in FreeStyle 293 cell culture media after 15 min of incubation showed a different round and

compact-like complexes of 300 nm mixed with large aggregates of the same shape of more than one micron [23]. These different morphologies despite the similar aggregation point ions and media components as the driving force leading three-dimensional conformation of DNA/PEI complexes, as for the Na and Cl ions in the optimum presented here. A deep look into the PSD of these complexes reveal a mean hydrodynamic diameter of 650 nm with a polydispersity index (PDI) of 0.25, where a second population of 5.4  $\mu\text{m}$  was also detected (Figure 4G). In the same line, in the V-SSC-A density plot, a main population with a broad V-SSC-A scattered light distribution, together with a second population presenting V-SSC-A and FSC-A values higher than the sixth decade and fourth decade, respectively, could be distinguished. Thus, suggesting also the presence of micrometric DNA/PEI branched structures.

Overall, a certain degree of aggregation of DNA/PEI complexes prior to their addition to the cell culture seems to be the key physicochemical parameter, to ensure an efficient production by means of PEI-mediated TGE. To assess this hypothesis, several combinations of NaCl concentrations and incubation times with the same DNA/PEI complexes concentration and N/P ratio were analyzed in the DLS and flow virometry and correlated with the three predicted model responses (Figure 5). Different trends are found according to the predicted model responses shown in Figure 3F-H, respectively. In the case of cell growth response, a linear correlation between size and expected cell growth was obtained, whereas an opposite tendency is found for complex concentration. Thus, it is pointed that a decrease in the number of complexes with larger sizes might reduce the cytotoxicity on the cell culture. However, further studies might be performed in this regard since a low  $R^2$  coefficient of 0.65 was reported for this model (Table 3). For transfection efficiency and VLP production, optimal mean hydrodynamic diameter and concentration are predicted. In these analyses, the impact of the DNA/PEI physicochemical properties on TGE results is clearly evidenced. Interestingly, two trends were found depending on the salt concentration used. With 125 and 150 mM NaCl solutions, a maximum response was found with mean hydrodynamic diameter of around 450 nm for both responses. On the other hand, a mean hydrodynamic diameter of around 630 nm gave the best results, when higher NaCl

concentrations of 350 mM and 550 mM were used. Contrarily, a unique trend was observed in particle concentration, obtaining its maximum when  $0.8 \cdot 10^8$  complexes/mL were used like in the optimum found (Figure 4F). Moreover, these simulations predict a 30% loss in VLP production if the mean hydrodynamic size or particle concentration is too small ( $\sim 320$  nm and  $\sim 0.4 \cdot 10^8$  complexes/mL) or too high ( $\sim 820$  nm,  $\sim 1.5 \cdot 10^8$  complexes/mL). For these two models, high  $R^2$  coefficients of 0.93 and 0.95 were obtained, highlighting the significance of these predicted responses, and the need for a controlled DNA/PEI complex formation to ensure the highest production titers.

Although the recommended DNA/PEI complex size has been typically considered to be in the  $\sim 50$ - $200$  nm range [2], recent physicochemical characterizations on DNA/PEI complexes have observed the positive impact of micrometric DNA/PEI aggregates in the transfection of CHO-S[8], HEK 293 cells [23], HeLa cells [14,15], primary Human Umbilical Artery Smooth Muscle Cells (HUASMCs) [15] and HeLa cervical tumor xenograft mouse model and peritoneal HeLa tumor model [14]. The present findings would also have implications at large-scale TGE processes. In a recent review on PEI-mediated TGE at bioreactor scale, 19 out of 23 of the reviewed cases performed pre-complexation of DNA/PEI complexes in ionic solutions, including 150 mM NaCl, PBS and fresh culture medium, for 10 to 15 min [1]. Cell culture media contains inorganic salts, typically NaCl ( $\sim 100$  mM), KCl (5 mM) and  $\text{CaCl}_2$ , among others [49]. Thus, the presence of large DNA/PEI aggregates might also have been obtained in those transfection protocols, according to the present model. The process of PEI-mediated TGE has been also studied in insect cell cultures, where shorter incubation times in 150 mM NaCl or no-complexation have been reported [20,50,51]. An optimal mean hydrodynamic diameter of 300-400 nm has been reported for the transfection of High Five cells [20]. Hence, different pathways might be participating in other non-mammalian cell lines.

Despite the physicochemical properties of DNA/PEI complexes in the complexing solution have been correlated with their transfection efficiency, the actual properties that may take place are those present upon its addition to the cell culture. The behavior of DNA/PEI complexes in the cell

culture media has been studied in several works [9,15,23]. Raup *et al.* described the dilution 1:10 (v:v) of DNA/PEI complexes previously pre-complexed in different NaCl concentrations, from 150 to 900 mM, where a disaggregation tendency was observed after its addition to Opti-MEM cell culture medium. Despite the dilution effect, adsorption of DNA/PEI complexes to the cell membrane has been described as a very rapid process [24]. Moreover, the endocytosis of the DNA/PEI complex aggregates preparations was studied in HEK 293 and HeLa models by drug inhibition endocytosis, where macropinocytosis was highlighted as the most important pathway [14,23]. Macropinocytosis typically interact with particles between 1-5  $\mu\text{m}$  that are lately transferred to endosomes, hence supporting the uptake of large aggregates by the cells[52]. Furthermore, the presence of large DNA/PEI complexes has also been visualized in the surrounding of the cell nucleus at 24 hpt [24,53]. The maintenance of large DNA/PEI complexes in the nuclear envelope could work as a DNA reservoir, where the plasmid DNA is progressively liberated to the cell nucleus [53]. Moreover, Zhang *et al.* showed a higher DNA release in the cell nucleus of HeLa cells of DNA/PEI large aggregates compared to small DNA/PEI complexes [14].

#### **4. Conclusions**

In summary, this work bring light into the critical parameters affecting PEI-mediated TGE process from a physicochemical point of view. The tailoring of simple variables like NaCl salt ion concentration and incubation time have enabled the controlled production of optimal DNA/PEI complexes for TGE in HEK 293 cells. The optimization of these parameters has been rationally designed by means of a DoE approach. By doing so, the multiple effects in a transfection process, as cell growth, percentage of producing cells and production yields, have been studied to find the optimum condition. DNA/PEI polyplexes prepared in 125 mM NaCl and 11 min of incubation was shown to be the best condition. The characterization of this optimum presented DNA/PEI complexes with branched-like structures with large particle size distribution, where the presence of micrometric DNA/PEI aggregates could be identified by several means. Furthermore, the correlation of DNA/PEI complex physicochemical properties with the predicted model responses highlighted the need for controlled DNA/PEI complex formation to obtain adequate degree of

aggregation to ensure the highest transfection yields. The present models will also aid to better understand PEI-mediated TGE approaches at large scale in mammalian cells, where similar complexation procedures are normally used.

### **5. Acknowledgments**

The support from Manuela Costa (Servei de Cultius Cel·lulars, Producció d'Anticossos i Citometria, UAB), Ángel Calvache and Jorge Fomaro (Beckman Coulter) for facilitating access to the Cytoflex LX equipment is very appreciated. The authors would like to acknowledge Llorenç Badiella (Servei d'Estadística Aplicada, UAB), Martí de Cabo (Servei de Microscòpia, UAB) and Jose Amable Bernabé (Service of Preparation and Characterization of Soft Materials, Institut de Ciència de Materials de Barcelona, ICMAB, CSIC) for the assistance with DoE, cryo-TEM and DLS, respectively.



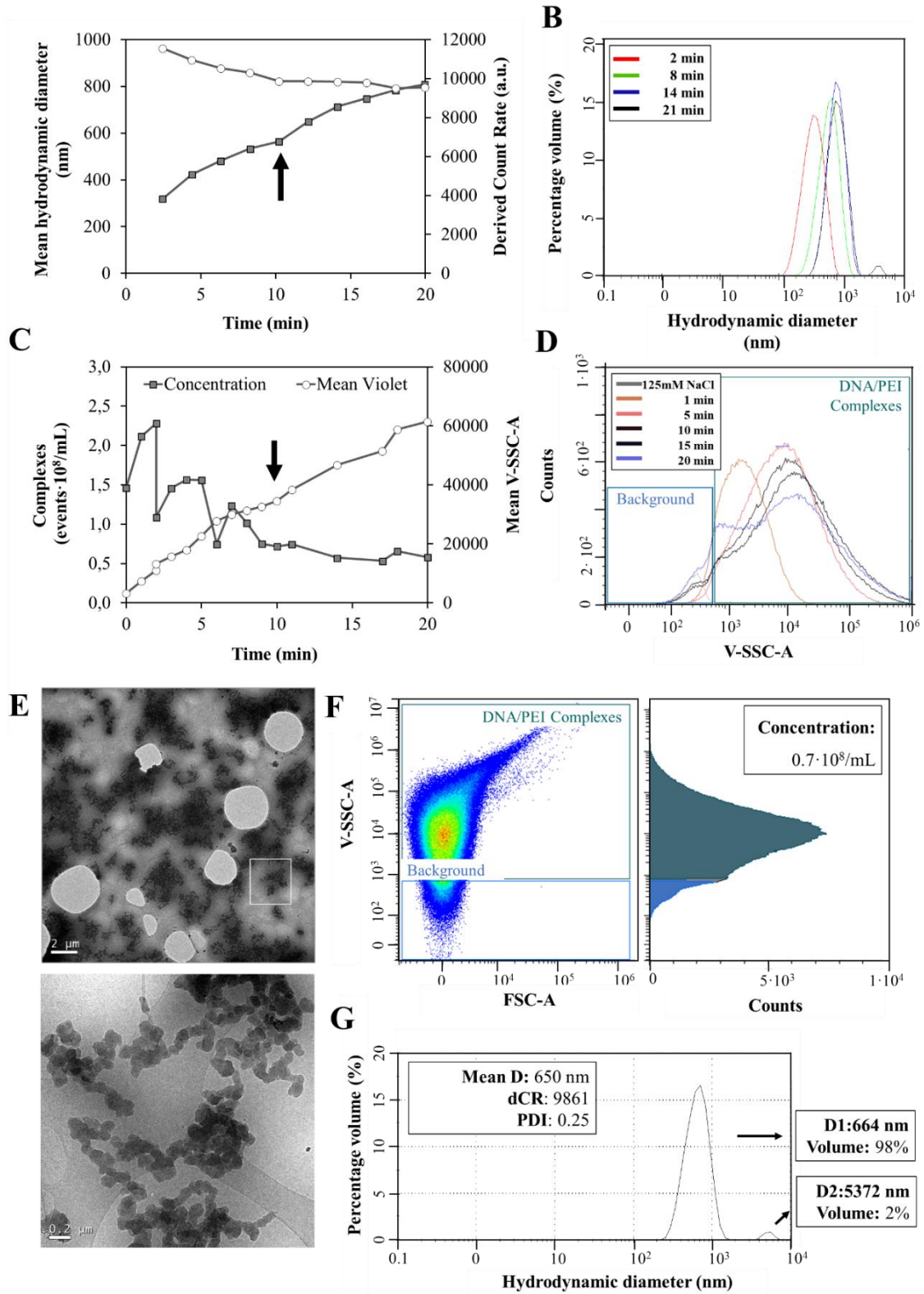


Figure 4. Physicochemical characterization of the DNA/PEI complexation process in the optimum condition (125 mM NaCl, 11 min of incubation). DNA/PEI complexes were prepared in a 1:2 (w:w) ratio corresponding to N/P of 14 with DNA at a concentration of 10  $\mu\text{g}/\text{mL}$ . (A - D) DNA/PEI complex kinetics analyzed by DLS (A & B) and Flow Virometry (C & D). DLS measurements of the mean hydrodynamic diameter (nm) and the corresponding scattered light by means of derived count rate (dCR) units (A) and the particle size distribution in percentage volume (B) have been analyzed. Flow Virometry measurements of DNA/PEI complexes concentration (events/mL) and mean violet (V) SSC-A values (C) and histogram distribution (D) are presented. Analysis of 125 mM NaCl salt as negative control is also depicted. Cryo-TEM micrographs of the optimum DNA/PEI polyplexes taken after 11 min of incubation (E) and its corresponding flow virometry density plot and histogram (F) and particle size distribution in percentage volume by DLS (G) are depicted.

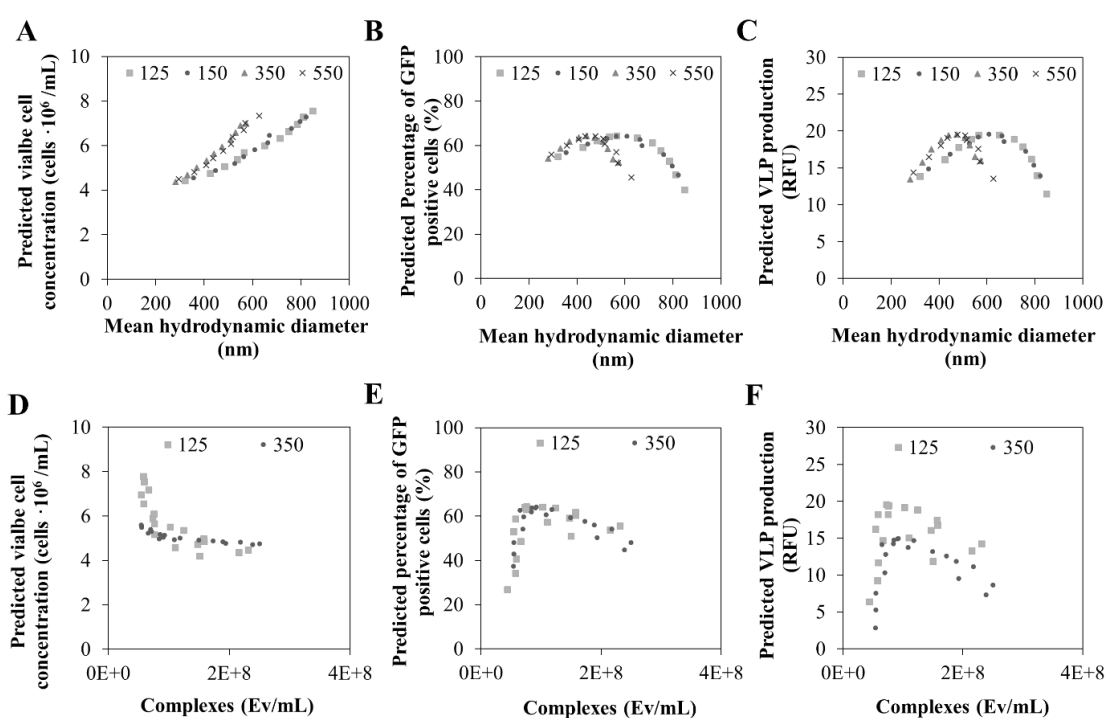


Figure 5. Comparison of DNA/PEI complexes physicochemical properties obtained in different NaCl solution and incubation times with the predicted responses from CCD design. Mean hydrodynamic diameter was assessed with DLS, whereas DNA/PEI complex concentration was quantified by flow virometry.

## 6. Literature

1. Gutiérrez-Granados, S.; Cervera, L.; Kamen, A.A.; Gòdia, F. Advancements in mammalian cell transient gene expression (TGE) technology for accelerated production of biologics. *Crit. Rev. Biotechnol.* **2018**, *38*, 1–23.
2. Shi, B.; Zheng, M.; Tao, W.; Chung, R.; Jin, D.; Ghaffari, D.; Farokhzad, O.C. Challenges in DNA Delivery and Recent Advances in Multifunctional Polymeric DNA Delivery Systems. *Biomacromolecules* **2017**, *18*, 2231–2246.
3. Yue, Y.; Wu, C. Progress and perspectives in developing polymeric vectors for in vitro gene delivery. *Biomater. Sci.* **2013**, *1*, 152–170.
4. van Gaal, E.V.B.; Van Eijk, R.; Oosting, R.S.; Kok, R.J.; Hennink, W.E.; Crommelin, D.J.A.; Mastrobattista, E. How to screen non-viral gene delivery systems in vitro? *J. Control. Release* **2011**, *154*, 218–232.
5. Bono, N.; Ponti, F.; Mantovani, D.; Candiani, G. Non-Viral in Vitro Gene Delivery: It is Now Time to Set the Bar! *Pharmaceutics* **2020**, *12*, 1–23.
6. Fukumoto, Y.; Obata, Y.; Ishibashi, K.; Tamura, N.; Kikuchi, I.; Aoyama, K.; Hattori, Y.; Tsuda, K.; Nakayama, Y.; Yamaguchi, N. Cost-effective gene transfection by DNA compaction at pH 4.0 using acidified, long shelf-life polyethylenimine. *Cytotechnology* **2010**, *62*, 73–82.
7. Han, X.Z.; Fang, Q.Y.; Yao, F.; Wang, X.N.; Wang, J.F.; Yang, S.L.; Shen, B.Q. The heterogeneous nature of polyethylenimine-DNA complex formation affects transient gene expression. *Cytotechnology* **2009**, *60*, 63–75.
8. Sang, Y.; Xie, K.; Mu, Y.; Lei, Y.; Zhang, B.; Xiong, S.; Chen, Y.; Qi, N. Salt ions and related parameters affect PEI-DNA particle size and transfection efficiency in Chinese hamster ovary cells. *Cytotechnology* **2015**, *67*, 67–74.
9. Raup, A.; Wang, H.; Synatschke, C. V.; Jérôme, V.; Agarwal, S.; Pergushov, D. V.; Müller, A.H.E.; Freitag, R. Compaction and Transmembrane Delivery of pDNA:

- Differences between 1-PEI and Two Types of Amphiphilic Block Copolymers. *Biomacromolecules* **2017**, *18*, 808–818.
10. Blakney, A.K.; Yilmaz, G.; McKay, P.F.; Becer, C.R.; Shattock, R.J. One Size Does Not Fit All: The Effect of Chain Length and Charge Density of Poly(ethylene imine) Based Copolymers on Delivery of pDNA, mRNA, and RepRNA Polyplexes. *Biomacromolecules* **2018**, *19*, 2870–2879.
  11. Visaveliya, N.R.; Köhler, J.M. Single-Step In Situ Assembling Routes for the Shape Control of Polymer Nanoparticles. *Biomacromolecules* **2018**, *19*, 1047–1064.
  12. Choosakoonkriang, S.; Lobo, B.A.; Koe, G.S.; Koe, J.G.; Middaugh, C.R.R. Biophysical characterization of PEI/DNA complexes. *J. Pharm. Sci.* **2003**, *92*, 1710–22.
  13. Cho, E.J.; Holback, H.; Liu, K.C.; Abouelmagd, S.A.; Park, J.; Yeo, Y. Nanoparticle Characterization: State of the Art, Challenges, and Emerging Technologies. *Mol. Pharm.* **2013**, *10*, 2093–2110.
  14. Zhang, W.; Kang, X.; Yuan, B.; Wang, H.; Zhang, T.; Shi, M.; Zheng, Z.; Zhang, Y.; Peng, C.; Fan, X.; et al. Nano-structural effects on gene transfection: Large, botryoid-shaped nanoparticles enhance DNA delivery via macropinocytosis and effective dissociation. *Theranostics* **2019**, *9*, 1580–1598.
  15. Pezzoli, D.; Giupponi, E.; Mantovani, D.; Candiani, G. Size matters for in vitro gene delivery: investigating the relationships among complexation protocol, transfection medium, size and sedimentation. *Sci. Rep.* **2017**, *7*, 44134.
  16. Ulasov, A. V; Khramtsov, Y. V; Trusov, G.A.; Rosenkranz, A.A.; Sverdlov, E.D.; Sobolev, A.S. Properties of PEI-based polyplex nanoparticles that correlate with their transfection efficacy. *Mol. Ther.* **2011**, *19*, 103–12.
  17. Gutiérrez-Granados, S.; Gòdia, F.; Cervera, L. Continuous manufacturing of viral particles. *Curr. Opin. Chem. Eng.* **2018**, *22*, 107–114.
  18. Box, G.E.P.; Wilson, K.B. On the Experimental Attainment of Optimum Conditions. *J. R.*

- Stat. Soc. Ser. B* 1951, *13*, 1–45.
19. Fuenmayor, J.; Cervera, L.; Gutiérrez-Granados, S.; Gòdia, F. Transient gene expression optimization and expression vector comparison to improve HIV-1 VLP production in HEK293 cell lines. *Appl. Microbiol. Biotechnol.* **2018**, *102*, 165–174.
  20. Puente-Massaguer, E.; Lecina, M.; Gòdia, F. Nanoscale characterization coupled to multi-parametric optimization of Hi5 cell transient gene expression. *Appl. Microbiol. Biotechnol.* **2018**, *102*, 10495–10510.
  21. Gutiérrez-Granados, S.; Cervera, L.; Segura, M. de L.M.; Wölfel, J.; Gòdia, F. Optimized production of HIV-1 virus-like particles by transient transfection in CAP-T cells. *Appl. Microbiol. Biotechnol.* **2016**, *100*, 3935–47.
  22. Rezvani Amin, Z.; Rahimizadeh, M.; Eshghi, H.; Dehshahri, A.; Ramezani, M. The effect of cationic charge density change on transfection efficiency of polyethylenimine. *Iran. J. Basic Med. Sci.* **2013**, *16*, 150–6.
  23. González-Domínguez, I.; Grimaldi, N.; Cervera, L.; Ventosa, N.; Gòdia, F. Impact of physicochemical properties of DNA/PEI complexes on transient transfection of mammalian cells. *N. Biotechnol.* **2019**, *49*, 88–97.
  24. Cervera, L.; González-Domínguez, I.; Segura, M.M.; Gòdia, F. Intracellular characterization of Gag VLP production by transient transfection of HEK 293 cells. *Biotechnol. Bioeng.* **2017**, *114*, 2507–2517.
  25. Zamora, J.L.R.; Aguilar, H.C. Flow virometry as a tool to study viruses. *Methods* **2017**, *134–135*, 87–97.
  26. Hermida-Matsumoto, L.; Resh, M.D. Localization of human immunodeficiency virus type 1 Gag and Env at the plasma membrane by confocal imaging. *J. Virol.* **2000**, *74*, 8670–9.
  27. Schwartz, S.; Campbell, M.; Nasioulas, G.; Harrison, J.; Felber, B.K.; Pavlakis, G.N. Mutational inactivation of an inhibitory sequence in human immunodeficiency virus type 1 results in Rev-independent gag expression. *J. Virol.* **1992**, *66*, 7176–82.

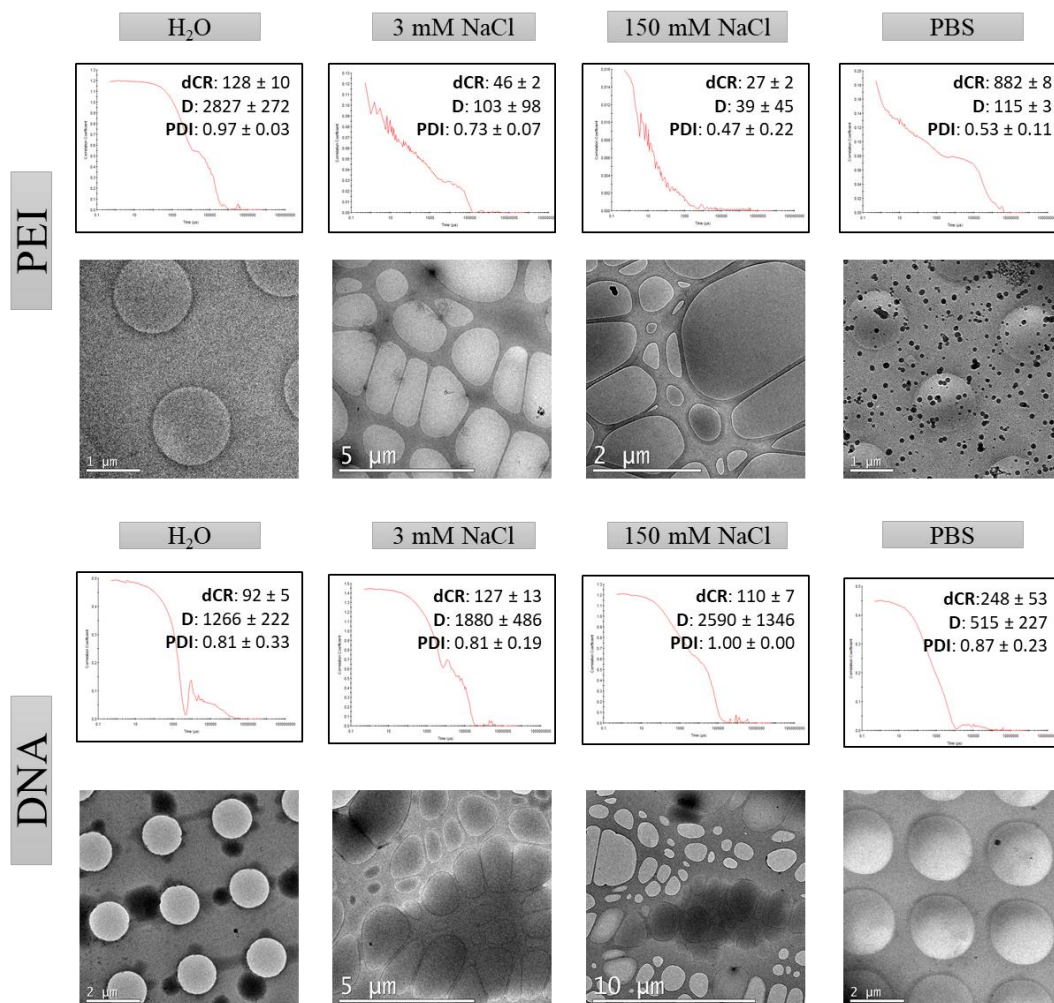
28. Segura, M.M.; Garnier, A.; Durocher, Y.; Coelho, H.; Kamen, A. Production of lentiviral vectors by large-scale transient transfection of suspension cultures and affinity chromatography purification. *Biotechnol. Bioeng.* **2007**, *98*, 789–799.
29. Cervera, L.; Gutiérrez-Granados, S.; Martínez, M.; Blanco, J.; Gòdia, F.; Segura, M.M. Generation of HIV-1 Gag VLPs by transient transfection of HEK 293 suspension cell cultures using an optimized animal-derived component free medium. *J. Biotechnol.* **2013**, *166*, 152–165.
30. Gutiérrez-Granados, S.; Cervera, L.; Gòdia, F.; Carrillo, J.; Segura, M.M. Development and validation of a quantitation assay for fluorescently tagged HIV-1 virus-like particles. *J. Virol. Methods* **2013**, *193*, 85–95.
31. Puente-Massaguer, E.; Badiella, L.; Gutiérrez-Granados, S.; Cervera, L.; Gòdia, F. A statistical approach to improve compound screening in cell culture media. *Eng. Life Sci.* **2019**, *19*, 315–327.
32. Puente-Massaguer, E.; Lecina, M.; Gòdia, F. Integrating nanoparticle quantification and statistical design of experiments for efficient HIV-1 virus-like particle production in High Five cells. *Appl. Microbiol. Biotechnol.* **2020**, *104*, 1569–1582.
33. Göttlinger, H.G. *HIV-1 Gag: a Molecular Machine Driving Viral Particle Assembly and Release*; Carla KuCarla Kuiken, BrianFoley, Thomas Leitner, Cristian Apetrei, Beatrice Hahn, Ilene Mizrachi, James Mullins, Andrew Rambaut, StevenWolinsky, and B.K. editors., Ed.; Los Alamos National Laboratory, Theoretical Biology andBiophysics: Los Alamos, New Mexico., 2001; ISBN 0269-9370.
34. Durocher, Y.; Perret, S.; Kamen, A. High-level and high-throughput recombinant protein production by transient transfection of suspension-growing human 293-EBNA1 cells. *Nucleic Acids Res.* **2002**, *30*, 9e – 9.
35. Carpentier, E.; Paris, S.; Kamen, A. a.; Durocher, Y. Limiting factors governing protein expression following polyethylenimine-mediated gene transfer in HEK293-EBNA1 cells.

- J. Biotechnol.* **2007**, *128*, 268–280.
36. Suh, J.; Paik, H.J.; Hwang, B.K. Ionization of Poly(ethylenimine) and Poly(allylamine) at Various pH's. *Bioorg. Chem.* **1994**, *22*, 318–327.
37. van Gaal, E.V.B.; Spierenburg, G.; Hennink, W.E.; Crommelin, D.J.A.; Mastrobattista, E. Flow cytometry for rapid size determination and sorting of nucleic acid containing nanoparticles in biological fluids. *J. Control. Release* **2010**, *141*, 328–338.
38. Montgomery, D.C. *Design and Analysis of Experiments*; 5th ed.; John Wiley & Sons Inc.: Arizona, 2012; Vol. 2; ISBN 1118146921.
39. Derringer, G.; Suich, R. Simultaneous optimization of several response variables. *J. Qual. Technol.* **1980**, *12*, 214–219.
40. Peixoto, J.L. Hierarchical Variable Selection in Polynomial Regression Models. *Am. Stat.* **1987**, *41*, 311.
41. Derouazi, M.; Girard, P.; Van Tilborgh, F.; Iglesias, K.; Muller, N.; Bertschinger, M.; Wurm, F.M. Serum-free large-scale transient transfection of CHO cells. *Biotechnol. Bioeng.* **2004**, *87*, 537–45.
42. Pinzi, S.; Leiva, D.; Arzamendi, G.; Gandia, L.M.; Dorado, M.P. Multiple response optimization of vegetable oils fatty acid composition to improve biodiesel physical properties. *Bioresour. Technol.* **2011**, *102*, 7280–7288.
43. Honary, S.; Ebrahimi, P.; Hadianamrei, R. Optimization of particle size and encapsulation efficiency of vancomycin nanoparticles by response surface methodology. *Pharm. Dev. Technol.* **2014**, *19*, 987–998.
44. Puente-Massaguer, E.; Lecina, M.; Gòdia, F. Application of advanced quantification techniques in nanoparticle-based vaccine development with the Sf9 cell baculovirus expression system. *Vaccine* **2020**, *38*, 1849–1859.
45. Kramberger, P.; Ciringer, M.; Štrancar, A.; Peterka, M. Evaluation of nanoparticle

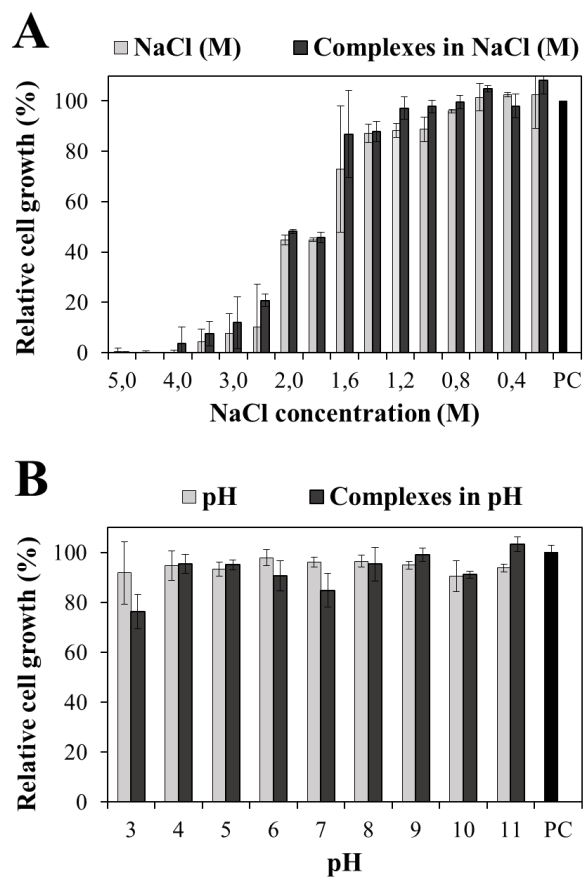
- tracking analysis for total virus particle determination. *Viol. J.* **2012**, *9*, 265.
46. van der Pol, E.; Coumans, F. a W.; Grootemaat, A.E.; Gardiner, C.; Sargent, I.L.; Harrison, P.; Sturk, A.; van Leeuwen, T.G.; Nieuwland, R. Particle size distribution of exosomes and microvesicles determined by transmission electron microscopy, flow cytometry, nanoparticle tracking analysis, and resistive pulse sensing. *J. Thromb. Haemost.* **2014**, *12*, 1182–1192.
47. Welsh, J.A.; Horak, P.; Wilkinson, J.S.; Ford, V.J.; Jones, J.C.; Smith, D.; Holloway, J.A.; Englyst, N.A. FCM<sub>PASS</sub> Software Aids Extracellular Vesicle Light Scatter Standardization. *Cytom. Part A* **2019**.
48. Mahajan, S.; Tang, T. Polyethylenimine-DNA Ratio Strongly Affects Their Nanoparticle Formation: A Large-Scale Coarse-Grained Molecular Dynamics Study. *J. Phys. Chem. B* **2019**, *123*, 9629–9640.
49. Arora, M. Cell Culture Media: A Review. *Mater. Methods* **2013**, *3*.
50. Bleckmann, M.; Schürig, M.; Endres, M.; Samuels, A.; Gebauer, D.; Konisch, N.; van den Heuvel, J. Identifying parameters to improve the reproducibility of transient gene expression in High Five cells. *PLoS One* **2019**, *14*, 1–18.
51. Mori, K.; Hamada, H.; Ogawa, T.; Ohmuro-Matsuyama, Y.; Katsuda, T.; Yamaji, H. Efficient production of antibody Fab fragment by transient gene expression in insect cells. *J. Biosci. Bioeng.* **2017**, *124*, 221–226.
52. Rewatkar, P. V.; Parton, R.G.; Parekh, H.S.; Parat, M.-O. Are caveolae a cellular entry route for non-viral therapeutic delivery systems? *Adv. Drug Deliv. Rev.* **2015**, *91*, 92–108.
53. González-Domínguez, I.; Cervera, L.; Gòdia, F.; Roldán, M. Quantitative colocalization analysis of DNA delivery by PEI-mediated cationic polymers in mammalian cells. *J. Microsc.* **2019**, *273*, 53–64.



## 7. Supplementary Materials



Supplementary Materials S1. DLS and cryo-TEM analysis of single DNA and PEI addition (negative controls) in the different complexing solutions: ultrapure H<sub>2</sub>O, 3 and 150 mM NaCl and PBS, respectively. DLS analyses showed unstable and polydisperse raw correlograms in all four conditions with low derived count rates (dCR), high polydispersity index (PDI) and non-significant mean hydrodynamic diameter results. (D) Sample visualization by cryo-TEM was performed after DNA or PEI addition in each solution. No structures were observed in PEI controls except for the PBS condition where small PEI aggregates were detected. DNA-containing micrographs showed the presence of large aggregates in ultrapure H<sub>2</sub>O and 3 and 150 mM NaCl conditions.



Supplementary Materials S2. Cytotoxicity assays of the complexing medium on HEK 293 cells containing different concentrations of NaCl, pH and with or without the addition of DNA/PEI complexes. (A) Effect of NaCl concentration and (B) pH in the complexing medium on cell growth. Briefly, 100  $\mu\text{L}$  of HEK 293 cells at  $0.5 \cdot 10^6$  cell/mL were seeded in each well of a 96-well plate, and 10  $\mu\text{L}$  of the complexing solution without (light grey) or with DNA/PEI complexes (dark grey) at different NaCl concentrations or pH was added into each of the wells. After 48h, a Cell Titer 96® AQueous One Solution Cell Proliferation Assay was used according to manufacturer's instructions to determine the effect of the different conditions on cell growth. Relative values  $\pm$  standard deviation of triplicate experiments are represented and compared to a positive control (PC, black bar).

**Supplementary Materials S3. Matrix design, response and ANOVA analysis for the first 2<sup>3</sup> full factorial design.**

First 2 <sup>3</sup> Full factorial design						
Variables	Coding levels					
	-1	0	1			
NaCl (mM)	10	800	1600			
pH	3	7	11			
Incubation time (min)	0	10	20			

Experimental run	Independent variables			Responses		
	NaCl (mM)	pH	Incubation time (min)	Cell growth (cells·10 <sup>6</sup> /mL)	Transfection efficiency (%)	VLP production (RFU)
1	-1	-1	-1	5.55	48.2	12.0
2	+1	-1	-1	2.45	12.6	1.1
3	-1	+1	-1	5.29	47.7	14.4
4	+1	+1	-1	2.52	12.1	1.6
5	-1	-1	+1	5.41	56.6	13.6
6	+1	-1	+1	2.08	23.8	3.3
7	-1	+1	+1	5.85	48.0	18.4
8	+1	+1	+1	2.47	6.9	1.4
9	0	0	0	3.80	66.6	9.8
10	0	0	0	3.07	70.0	10.7
11	0	0	0	3.89	67.3	10.0
12	0	0	0	4.46	53.1	6.7

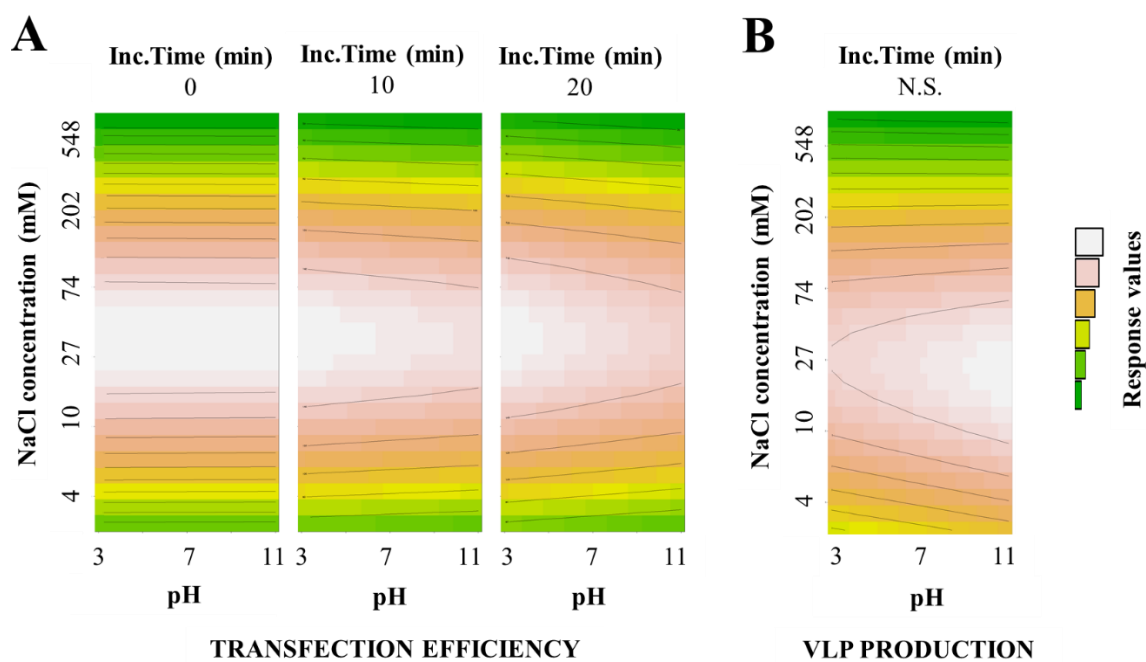
  

Analysis						
Significant parameters	Cell growth		Transfection efficiency		VLP production	
	Coefficient	<i>p-value</i> <sup>a</sup>	Coefficient	<i>p-value</i>	Coefficient	<i>p-value</i>
Constant	6.41	****	60.3	****	8.3	****
Ln[NaCl]	-0.55	****	-6.3	****	-1.0	****

Model	No quadratic terms			With quadratic terms		
	R <sup>2</sup>	Adjusted R <sup>2</sup>	Model <i>p-value</i>	R <sup>2</sup>	Adjusted R <sup>2</sup>	Model <i>p-value</i>
(A) Cell Growth	0.92	0.79	*	0.98	0.93	*
(B) Transfection efficiency (%)	0.17	-1.07	>0.05	1	0.99	****
(C) VLP production (RFU)	0.75	0.34	>0.05	0.99	0.97	**

<sup>a</sup>*p-value* codification: \*: 0.05, \*\*: 0.01, \*\*\*: 0.001, \*\*\*\*: 0.0001, Inc.Time: incubation time, Ln: logarithm



Supplementary Materials S4. Graphical representation of results from the first  $2^3$  full-factorial using contour plots. (A – B) Effect of NaCl concentration, pH and DNA/PEI polyplex incubation time on transfection efficiency (A) and VLP production (B). Contour plots were obtained by considering a pseudo-quadratic term in the model. N.S.: non-significant

**Supplementary Materials S5. Independent variable ranges, matrix design, response and ANOVA analysis for the second 2<sup>3</sup> full factorial design.**

Second 2 <sup>3</sup> Full factorial design						
Variables	Coding levels					
	-1	0	1			
NaCl (mM)	5	400	800			
pH	3	7	11			
Incubation time (min)	0	10	20			

Experimental run	Independent variables			Responses		
	NaCl (mM)	pH	Incubation time (min)	Cell growth (cells·10 <sup>6</sup> /mL)	Transfection efficiency (%)	VLP production (RFU)
1	-1	-1	-1	5.62	33.9	6.6
2	+1	-1	-1	3.1	15.3	0.2
3	-1	+1	-1	5.78	37.4	6.3
4	+1	+1	-1	3.53	8.5	0.0
5	-1	-1	+1	6.62	49.5	9.3
6	+1	-1	+1	4.66	43.2	4.4
7	-1	+1	+1	6.6	30.1	2.5
8	+1	+1	+1	4.07	4.0	0.0
9	0	0	0	4.66	48.1	7.4
10	0	0	0	4.73	53.5	8.7
11	0	0	0	4.97	46.8	9.7
12	0	0	0	5.03	48.3	8.9

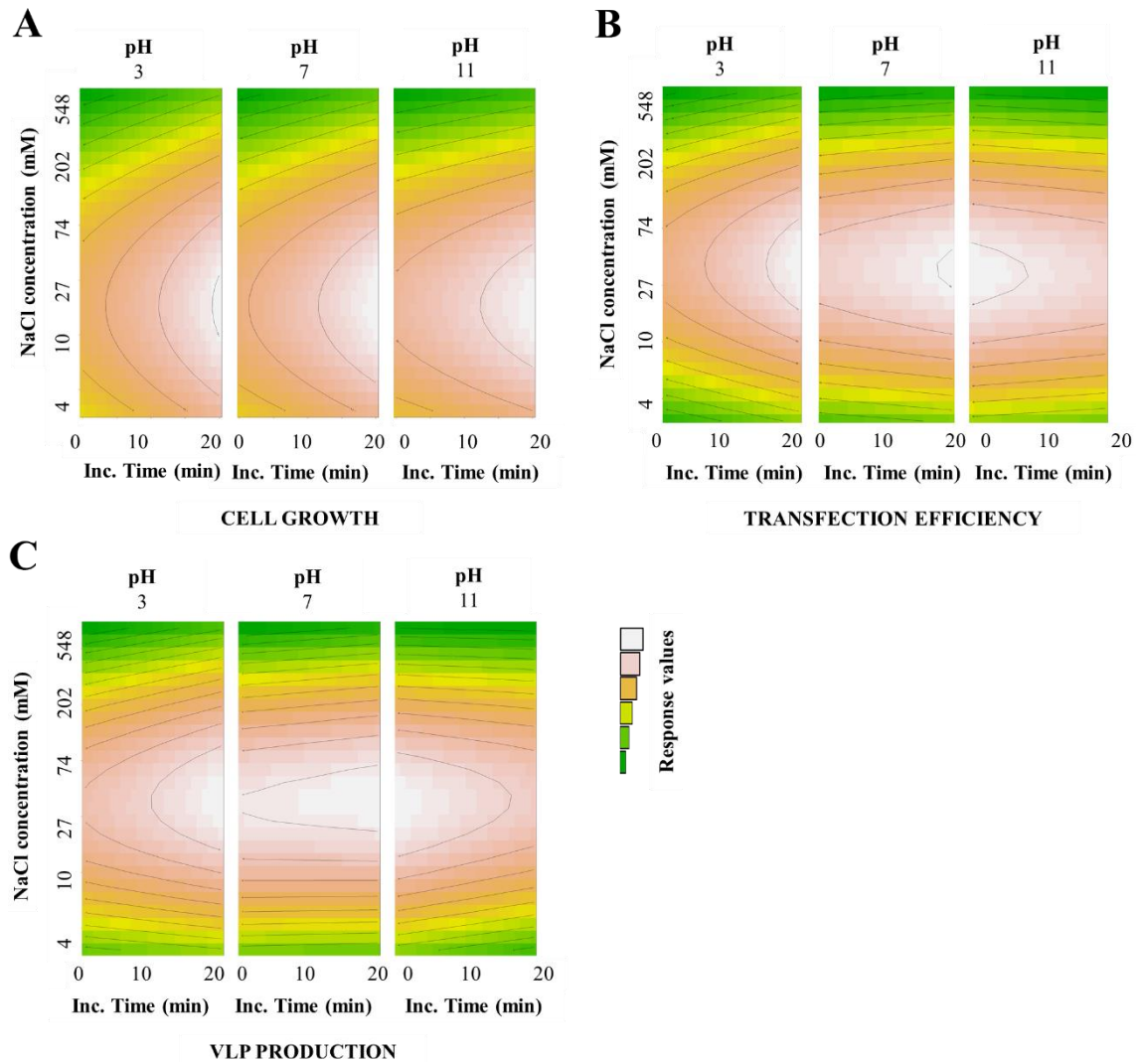
  

Analysis						
Significant parameters	Cell growth		Transfection efficiency		VLP production	
	Coefficient	<i>p</i> -value <sup>a</sup>	Coefficient	<i>p</i> -value	Coefficient	<i>p</i> -value
Constant	6.80	****	43.3	***	4.2	***
Ln[NaCl]	-0.40	***	-3.5	**	-0.5	**
[pH]	-	> 0.05	-7.7	*	-0.8	**
[Inc. Time]	-	> 0.05	4.0	> 0.05	0.2	> 0.05
[pH] x [Inc. Time]	-	> 0.05	-6.9	*	-0.7	*

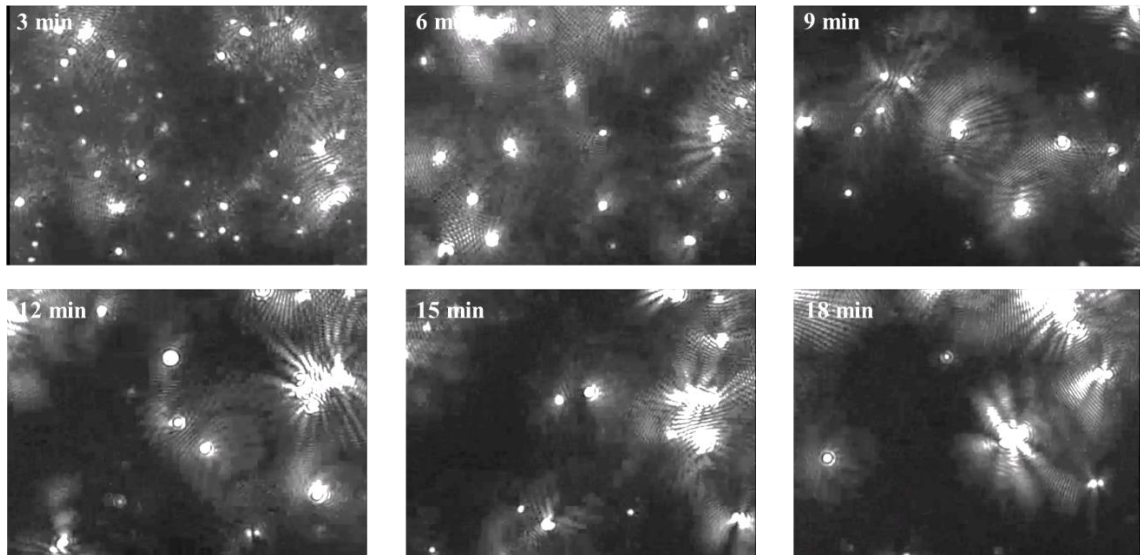
  

Model	No quadratic terms			With quadratic terms		
	R <sup>2</sup>	Adjusted R <sup>2</sup>	Model <i>p</i> -value	R <sup>2</sup>	Adjusted R <sup>2</sup>	Model <i>p</i> -value
(A) Cell growth	0.89	0.77	*	0.99	0.96	**
(B) Transfection efficiency (%)	0.40	-0.33	> 0.05	0.99	0.97	**
(C) VLP production (RFU)	0.31	-0.53	> 0.05	0.98	0.94	**

<sup>a</sup>*p*-value codification: \*: 0.05, \*\*: 0.01, \*\*\*: 0.001, \*\*\*\*: 0.0001, Inc.Time: incubation time, Ln: logarithm



Supplementary Materials S6. Contour plots from the second  $2^3$  full-factorial. (A – B) Effect of NaCl concentration, pH and DNA/PEI polyplex incubation time on cell growth (A) transfection efficiency (B) and VLP production (C). Contour plots were generated by including a pseudo-quadratic term in the model.



**Supplementary Materials S7. NTA video of DNA/PEI polyplex formation in the optimum condition**

## **Chapter 3**

# **Quantitative colocalization analysis of DNA delivery by PEI-mediated cationic polymers in mammalian cells**

---

Published in Journal of Microscopy, 2019 (273) 53-64



## **Abstract**

Although cationic polymers are widely used for DNA delivery, the relationship between the properties of the formed-complexes and their biological activity is not fully understood. Here, we propose a novel procedure consisting in super-resolved images coupled with quantitative colocalization to analyze DNA release in living cells. This work compares the different workflows available in a quantitative colocalization study of DNA delivery using polyethylenimine (PEI) as transfection reagent.

A nimble workflow with deconvolution in 3D-images was developed. Among the different colocalization coefficients, Manders' colocalization coefficient was the best to track the complexes. Results showed that DNA/PEI complexes were tightly interacting at the time of transfection and their disassembly was observed between 2 and 10 hours after their up-take. Heterogenicity was found in the intracellular fate of each complex. At 24 hours some complexes were still present underneath the nuclear envelope. Overall, this study opens the door for particle tracking assessment with 3D imaging at intracellular level.

**Keywords:** DNA/PEI complexes, transient transfection, characterization, confocal microscopy, deconvolution, 3D imaging.

## 1. Introduction

Transient gene expression is a widely used strategy in the early development stages of bioprocess development. Typically, a DNA-coding plasmid is added to cells and the product is recovered between 1 and 15 days post transfection from the cell culture [1]. One of the most used DNA complexing reagents is polyethylenimine (PEI). PEI is simple to use, compatible with suspension cells and serum-free media [1]. PEI molecules have demonstrated their ability to efficiently introduce DNA into cells [2]. The cationic amines from PEI neutralize the negative charges of DNA upon complexation, protecting it from nuclease degradation. The resulting positively charged complexes interact with the cell membrane and are up-taken by the cells via endocytosis [3–5]. By means of the known “proton sponge” effect, complexes are thought to escape from the endosomal/lysosomal pathway to the cytoplasm, releasing the DNA plasmid into the nucleus [2,5]. Although other mechanisms have also been claimed to be involved in this process [5,6].

DNA/PEI complex formation has been characterized *in vitro* by several techniques including gel retardation assay, dynamic light scattering (DLS) or fourier-transform infrared spectroscopy (FTIR), among others [7,8]. Godbey et al. [9] were the first to observe the process in living cells, and further studies of DNA/PEI complexes trafficking have been performed [7,10,11]. Despite the aforementioned works, the relationship between the DNA/PEI complex properties and its biological activity has not been completely established yet [8]. For this reason, more efforts must be undertaken to better understand DNA release from DNA/PEI complexes [5]. Here, we propose a novel application consisting in confocal laser scanning microscopy (CSLM) coupled with quantitative colocalization to study this process. A standard PEI-mediated transfection protocol in HEK 293 cells was used as a study case [12]. In previous studies, Cervera *et al.* [13] showed the presence of DNA/PEI complexes in all transfected cells, while just a percentage of them finally presented protein production. Thus, it can be considered that the different behavior of complexes, in terms of DNA release, promote a favorable or unfavorable expression of the gene of interest.

CSLM has been used for the characterization of intracellular processes. Colocalization is commonly carried out in biological sciences to investigate localization of proteins, organelles, ions and cells [14–16]. This technique is based on a pixel-wise correlation between signals of two or more color channels. However, its quantitative application is highly sensitive to artifacts and outcomes can be influenced by a variety of parameters, such as sample preparation and image pre-processing and post-processing [16,17]. In the last decade, quantitative colocalization approaches have increased due to the development of new technologies in the CSLM field. One of these advances is the use of 3D imaging software, involving a set of digital tools for image treatment with many quantitative colocalization coefficients [16]. Due to the novelty of the technique and the need for unbiased and reproducible analysis protocols, there are several workflows for the quantification of colocalization that should be optimized for each specific sample.

The application of quantitative colocalization for tracking DNA/PEI disassembly requires a deep analysis of the different alternatives available [18]. In Figure 1, a scheme of the steps performed in this study is depicted. On the one hand, labeling and detection of such particles requires a low intrusive strategy to reduce side effects on DNA/PEI complexes biological activity. It has been reported that the alteration of complex size or charge density can affect particle efficiencies [19,20]. In this work, the covalent labeling of DNA and PEI with Cy3 and Cy5 fluorochromes, respectively, was performed to monitor the process. On the other hand, acquisition conditions and pre-processing parameters are also relevant aspects that should be improved [18,21].

In addition, super-resolution by deconvolution could be also included [22]. This means aim to remove corruption and out-of-focus contribution within image data. However, a wrongly executed method can severally bias the results. Overall, there are several software available to this end [14]. Here, two programs have been chosen: (1) JACoP (Just Another Co-localization Plug-in) [23] a free software, which is continuously updated by users with new generation advances; and (2) Imaris software (Bitplane), which allows the analysis of 3D-volume image

quantitative colocalization [24]. Moreover, in Figure 1 a summary of the different colocalization coefficients analyzed in this study is presented.

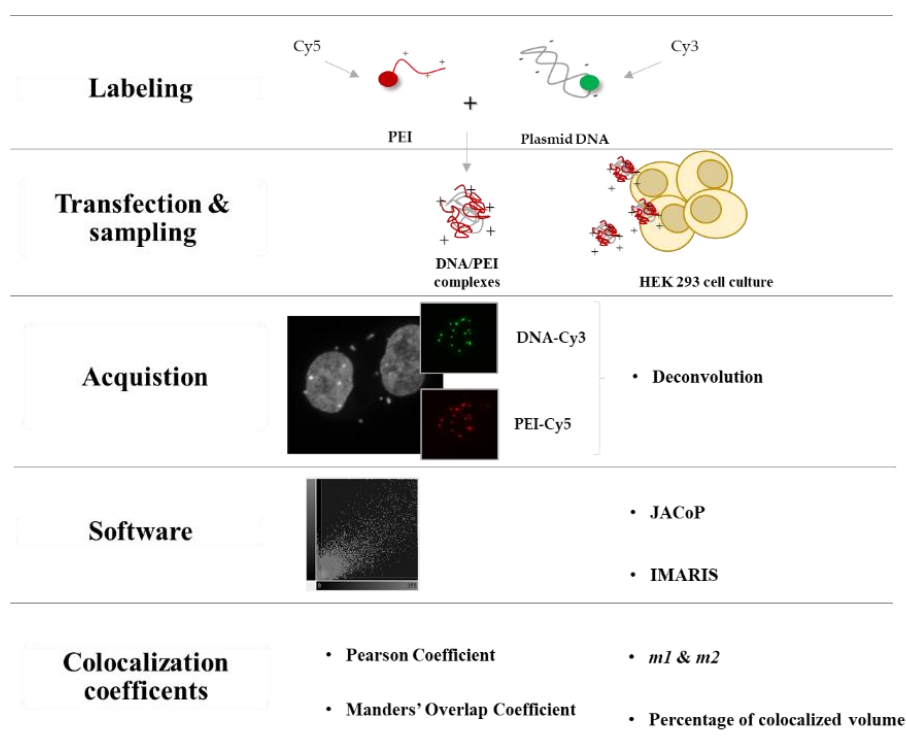


**Figure 1.** Workflow of DNA/PEI disassembly kinetics study by quantitative colocalization. **Labeling:** DNA-Cy3 and PEI-Cy5 were covalently labeled and its biological activity was validated before the experiment. Prior to transfection, HEK 293 cell nucleus were stained with Hoechst and resuspended in Freestyle culture media. **Transfection & sampling:** A mixture of 50% DNA-Cy3 and 50% unlabeled DNA was complexed with PEI-Cy5. After an incubation of 15 minutes, DNA/PEI complexes were added to the cell culture. Samples were collected every two hours and fixed with formaldehyde 2%. **Acquisition:** Five or six field images were taken from each sample containing around 5 cells per field. Acquisition parameters and pre-processing data were optimized prior to the sample recording. Deconvolution treatment in 3D quantitative colocalization was analyzed. **Software:** Two available software were evaluated in terms of colocalization coefficient availability and digital imaging analysis possibilities. **Colocalization coefficients:** The kinetics of DNA/PEI complex disassembly was quantified by several colocalization coefficients. The effect of deconvolution on those mathematical formulas was studied as well as its usefulness to quantitatively describe DNA delivery process.

The aim of this work is to evaluate the applicability of quantitative colocalization to track DNA/PEI disassembly process in a previously developed platform for the generation of HIV-1 based Virus-like particles (VLPs). To achieve this end, several points were studied: (1) the optimization of acquisition parameters, (2) the improvement of sample quality by deconvolution,

(3) a comparison of two different software available and (4) the study of the different colocalization coefficients. All data obtained from these analyses enabled the selection of the best workflow to study the DNA/PEI complexes at intracellular level and thus, could be used in other studies of tracking particles in live cells.

## **2. Materials and Methods**

### **2.1. Cell line, media and culture conditions**

A serum-free suspension-adapted HEK 293 cell line (HEK293SF-3F6) was kindly provided by Dr. Amine Kamen (McGill University, Montreal, Canada). Cells were cultured in supplemented Freestyle 293 medium (Invitrogen, Carlsbad, USA) as previously described [12]. Cell count and viability were determined using Nucleocounter NC-3000 (Chemometec, Allerod, Denmark).

### **2.2. Covalent labeling of PEI**

Linear 25-kDa PEI (Polysciences, Warrington, PA, USA) was covalently labeled with Cy5 monoreactive dye (Amersham, GE Healthcare, Little Chalfont, UK) by suspending one vial with 2 mg of PEI dissolved in 1 mL of PBS at pH 8.0. Protocol was adapted from Han et al.[7]. The reaction was performed for 4 hours at room temperature (RT) with continuous mixing. The excess of Cy5 was removed by dialysis with a 5-kDa cutoff tubing cellulose membrane (Sigma Aldrich, San Luis, MO, USA) in a 2 L solution with PBS pH 7.4 at RT for 7 days. PBS replacement was performed every 24 hours. PEI labeling was confirmed by absorbance measurements with Nanodrop 1000 (Thermo Scientific, Waltham, MA, USA). PEI-Cy5 was stored at -20 °C protected from light.

### **2.3. Covalent labeling of DNA**

pGag-eGFP plasmid, used in this work for the production of HIV-1 Gag-GFP virus-like particles, was obtained and prepared as previously described [25]. The DNA-plasmid was labeled with Cy3 fluorochrome using the Label IT® Tracker™ Kit (Mirus Bio Technology, Madison, WI, USA) following manufacturer's instructions. Briefly, labeling reaction was incubated for 1 hour at 37 °C with 0.25:1 (v:w) ratio of Label IT® Tracker Reagent to DNA. Unreacted Label IT®

Tracker™ Reagent was removed by ethanol precipitation. 0.1 volume of 5M NaCl and 2 volumes of ice cold 100 % ethanol were added to the reaction and placed in a –20 °C freezer for 30 minutes. Then, the supernatant was discarded by centrifugation at 17.000xg for 10 minutes (min). Finally, the pellet was washed with 70 % ethanol and centrifuged during 10 minutes at 17.000xg. Supernatant was discarded from this centrifugation. The plasmid was quantified after staining using NanoDrop 1000 (Thermo Scientific, Waltham, MA, USA) and diluted to a concentration of 100 µg/mL in ultrapure water.

#### **2.4. Sample preparation and transient transfection of HEK 293 cells**

Prior to transfection, HEK 293 cells were dyed with Hoechst 33342, Trihydrochloride, Trihydrate 10 µg/mL (Life Technologies, Carlsbad, CA, USA), which stains the nuclear DNA in blue color at a final concentration of 1 µL/mL. After 10 minutes of incubation protected from light at room temperature, the mixture was centrifuged at 300 xg for 5 min and cell pellet was resuspended with non-supplemented FreeStyle fresh cell culture media (Invitrogen, Carlsbad, CA, USA). Then, transient transfection was performed by the addition of DNA/PEI complexes to the cell culture. HEK 293 cells were cultured in 6-well plates and samples were collected every 2 hours after transfection and fixed with formaldehyde 2%.

DNA/PEI complexes were formed as previously described [12] . Briefly, Cy3 labeled pGag-eGFP plasmid and pGag-eGFP in 1:1(w:w) ratio were diluted in FreeStyle 293 medium (Invitrogen, Carlsbad, USA), and vortexed for 10 sec. Complexes were formed with the addition of PEI-Cy5 (PolySciences, Warrington, PA, USA) in 1:2 (w:w) DNA:PEI ratio and vortexed three times. The mixture was incubated for 15 min at RT and added to the cell culture.

#### **2.5. Confocal laser scanning microscopy**

Confocal microscopy analysis was performed by TCS SP5 Leica Spectral confocal microscope (Leica Microsystems, Wetzlar, Germany). The confocal images were acquired using a HC x PL APO Lambda blue 63X/1,4 oil immersion objective at Servei de Microscòpia (Universitat Autònoma de Barcelona, Barcelona Spain).

Hoechst 33342 was excited with a blue diode laser (405 nm) and detected in the 425–490 nm. DNA-Cy3 was excited with an orange diode laser (561 nm) and detected in the 575–630 nm. PEI-Cy5 was excited with a HeNe laser (633 nm) and detected in the 650–795 nm range. Bright field was visualized using the last laser. The detector gain and offset values were adjusted to use the entire dynamic range of the detector and to avoid oversaturated voxels. Sequential acquisition settings were used to avoid inter-channel cross-talk. The confocal pinhole was set to 1 Airy unit. To study the colocalization in three dimensions, Z stacks of 15 sections were acquired every 1  $\mu\text{m}$  along the cell thickness. Appropriate negative controls were used to adjust confocal settings to avoid non-specific fluorescence artefacts. To compare the confocal data, identical confocal settings were used for image acquisition of different experiments. Final images were examined with LAS AF<sup>TM</sup> software (Leica Microsystems).

## **2.6. Quantitative colocalization analysis**

Image deconvolution was performed with Huygens Essential software v 4.4 Op6 (SVI, Leiden, The Netherlands). The point-spread function was calculated theoretically based on the imaging parameters. Signal-to-noise ratio was set to 30-40 (SNR). Deconvolution was performed by means of maximum likelihood estimation algorithm. Quantitative colocalization analysis was performed using raw and deconvolved images with Imaris x64 v7.2.1 software (Bitplane, Oxford Instruments, Zurich Switzerland) and ImageJ Fiji (Image J, Public Domain) with JACoP (Just Another Co-localization Plug-in) [23]. The specific threshold conditions for each channel were 14 a.u. (arbitrary units) for the DNA channel and 7 a.u. for the PEI channel. 3D-imaging reconstructions were performed with Imaris x64 v7.2.1 software (Bitplane, Oxford Instruments, Zurich Switzerland).

## **3. Results**

### **3.1. Experimental design and qualitative results**

DNA delivery and release at intracellular level in a PEI-mediated transient transfection process was successfully tracked by CSLM (Figure 2). The use of covalently labeled DNA and PEI enabled the reproduction of the standard HIV-1 Gag-eGFP VLP production process. Flow

cytometry and fluorometry analysis results (data not shown) were similar to those present in previous works [12,13]. Furthermore, the staining of cell nucleus with Hoechst was stable throughout 24 hours post transfection (hpt).

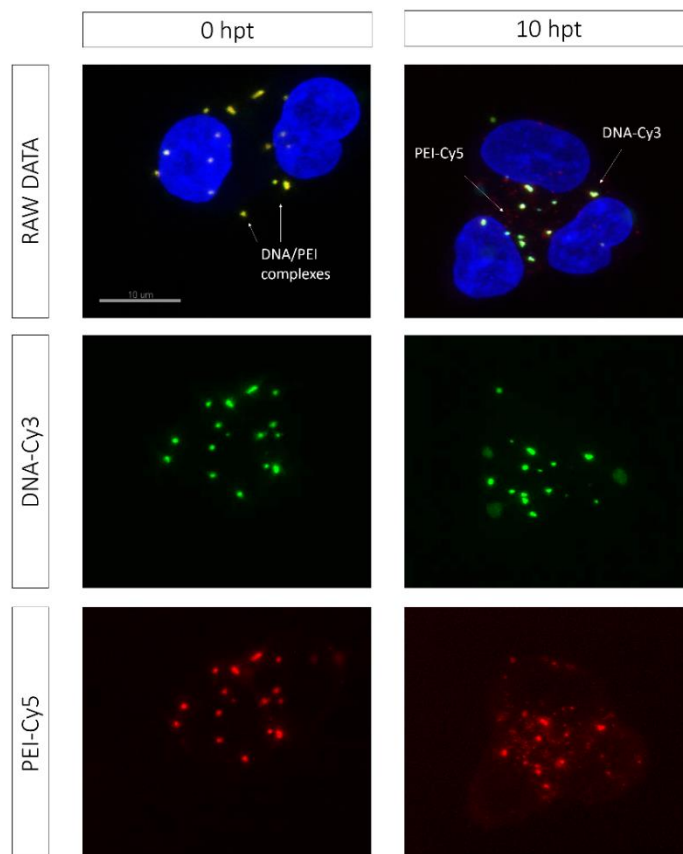


**Figure 2.** CLSM images of DNA/PEI disassembly kinetics. DNA/PEI complexes observed as yellow dots, DNA-Cy3 signal (Green), PEI-Cy5 (Red), cell nucleus stained with Hoechst (Blue) and the overlap of all three channels is presented, respectively. Representative images of 0 and 10 hours post transfection (hpt) are depicted. White arrows indicate the presence of DNA/PEI complexes at 0 hpt and DNA-Cy3 and PEI-Cy5 individual signal at 10 hpt.

Disassembly of DNA/PEI complexes was clearly evidenced in Figure 2. DNA/PEI complexes were observed as small aggregates with a micrometric size, depicted as yellow dots, just after their delivery to the cells (Figure 2, white arrows at 0 hpt). Complexes were spread throughout the cell volume. Different behaviors were pointed when the DNA (green) and PEI (red) were traced during complex internalization (Figure 2) and separated signals are observed at 10 hpt (Figure 2, white arrows at 10 hpt).

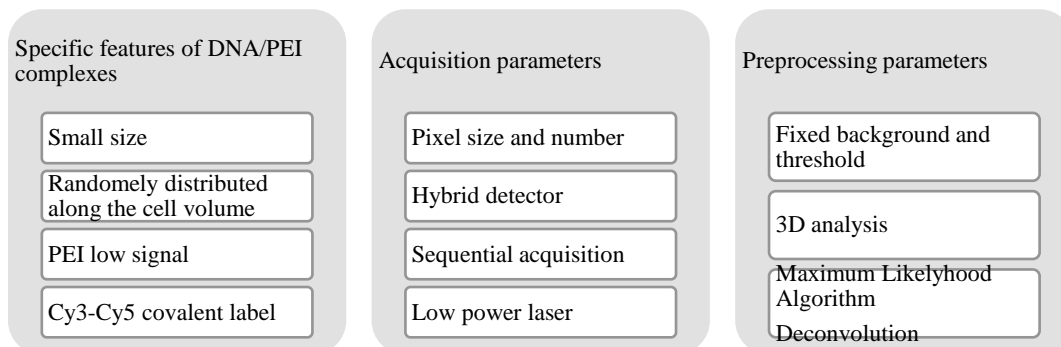


### 3.2. Optimization of data acquisition and pre-processing image treatment

The features present in DNA/PEI complexes required the optimization of the acquisition settings in quantitative colocalization. In Table 1 the optimized conditions are shown. The use of non-digital zoom, and the application of low laser intensities with hybrid detector intended to reduce potential photobleaching due to the small size of complexes. Overall, images were taken sequentially, avoiding cross-talk fluorescence emission and keeping the same acquisition parameters between samples.

Once the images were recorded, a correct assessment of colocalization required the set of several conditions. Background correction and threshold set up are the most important factors that could affect quantitative results. It is important to note that in confocal images, 30 % of all signal recorded from one channel could be background noise values since is the accepted percentage of noise level [26]. The extent of background depends on several factors, like the fluorescence of dyes and the acquisition parameters and settings. Background can be also suppressed using filters and deconvolution. Filtering recovers a pixel value from surrounding areas and compute a weighted average. It could result in loss of resolution as well as introduction of artifacts. With the aim to avoid these side effects, background and threshold were fixed at low values in all the colocalization analyses based on negative controls.

**Table 1. Acquisition and pre-processing parameters optimization for the detection of DNA/PEI disassembly kinetics by CSLM. Detection was adapted to DNA/PEI complexes characteristics by optimizing acquisition parameters. Furthermore, with views to perform quantitative colocalization studies, images were processed as 3D-image volumes by fixing background and threshold values (as described in Section 2.6 of Materials and Methods). Finally, the application of deconvolution was assessed.**



\*Parameters have been maintained during all the experiment

Furthermore, data can be processed in several ways. Numerous studies of colocalization have been done in 2D and 3D-images. For the detection of DNA/PEI complexes, the use of 3D-approach was selected since they were distributed throughout the volume of the cell and a different mode of analysis could underestimate the colocalization results. Moreover, images can be analyzed as a whole or divided in regions of interest (ROI), which could be delimited automatically or manually. Manual selection, which is the option sometimes selected, may imply the introduction of bias and error and is both time consuming and complicated for 3D-images [18]. Preliminary studies were performed by processing the images with ROI (Supplementary Materials S1), achieving similar results to those obtained by using whole images. Therefore, the analysis of whole 3D-images was chosen for further analysis.

### **3.3. Effect of deconvolution on image quality**

Deconvolution uses the image properties of the optical system in the form of point spread function (PSF) for returning the light to where it was originated. This mathematical method improves noise levels and produces more contrasted images [27]. Despite being an attractive proposal, the use of deconvolution remains widely unknown in this area of research. One of the possible reasons that contribute to this fact is the absence of a generalized workflow for imaging denoising processes [21]. Upon the available deconvolution methods, the use of maximum likelihood algorithm was selected (Table 1). This iterative algorithm is highly recommended in the presence of high noise levels. Furthermore, allows its usage without any previous optimization which would be really difficult to perform on DNA/PEI complexes due to their small size [27]. In Figure 3, the scatter plots of DNA/PEI channels before and after deconvolution treatment are depicted. In a scatter plot, the intensity of every pixel for each intensity channel analyzed is plotted one against another. Scatter plot of every volume sample at each time was analyzed (data not shown).

The kinetics of DNA/PEI disassembly was observed in these graphs. At 0 hpt, all pixels were concentrated in the diagonal of the scatter plot with same intensity for both channels in colocalized pixels. Colocalization decreased at 4 hpt and 10 hpt since fewer pixels were in the diagonal. Of

note, pixels under PEI threshold increased, suggesting PEI-Cy5 dissociation along the DNA release.

Image quality improved with deconvolution when compared with raw data. Colocalized pixels were better detected since the ones in the diagonal of the scatter plot presented higher intensities. Furthermore, the mathematical treatment enabled the removal of practically all noise level below the threshold values being more efficient with structured images, as in DNA channel (X-axis, green). Overall, deconvolution improved raw individual pixel colocalization detection, notwithstanding the general trend was clearly traced for both raw and deconvolved data.

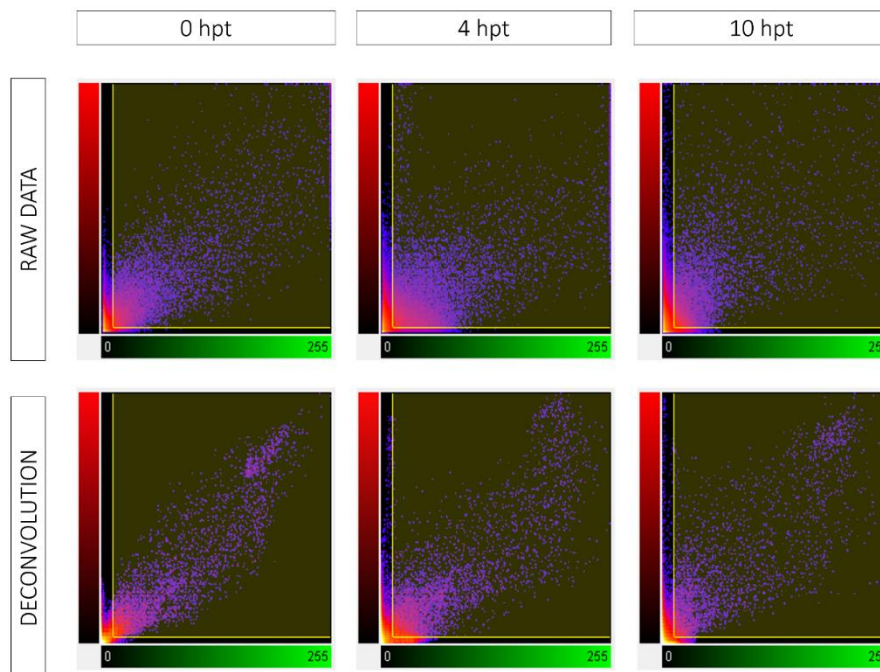


**Figure 3.** Comparison of quantitative colocalization of DNA/PEI disassembly scatter plots with and without deconvolution. Evolution with time of DNA-Cy3 signal (Green X-axis), PEI-Cy5 (Red Y-axis) specimens regarding its raw pixel-by-pixel signal is presented. Yellow contour box presents the values from each channel above the threshold fixed for all the studies. Representative images of each time point are depicted at 0 hpt, 4 hpt and 10 hpt. Scatter plots were given by Imaris software as raw image data for every volume analyzed a total of 255 greyscales were given per each channel.

### 3.4. Evaluation of deconvolution treatment in colocalization coefficients

Despite it was clearly evidenced in the scatter plots the improvements obtained through deconvolution, less is known about its effect on colocalization coefficients. The aim of this section

was (1) to evaluate this impact on the study of DNA delivery processes and (2) to select the best one for its further use in similar studies.

Several algorithms have been developed for the calculation of colocalization. As it was observed in Figure 2, DNA/PEI complexes were visualized as micrometric structures. Consequently, the colocalization analysis of these complexes presents intrinsic problems, since these currently established formulas are normally used for the study of subcellular location, which normally presents higher areas. The quantification of colocalization between two fluorescence channels can be broadly divided into two categories: (1) methods that consider only the presence of both fluorophores in individual pixels and (2) those that examine the relationship between intensities [28]. It has been previously reported that Type II are highly recommended in receptor trafficking studies [21]. In this work, Type II coefficients have been evaluated. Nonetheless, the percentage of colocalized volume (Type I) was also studied for comparison (Supplementary Materials, S2).

In Table 2 the coefficients studied are summarized. JACoP and Imaris software were compared here. Within Type II correlation coefficients, Pearson's coefficient and Manders' Overlap Coefficient are the most extended algorithms in quantitative colocalization [28]. Each piece of software offers different colocalization parameters and it is not always easy to make a decision beforehand. In addition, the same mathematical algorithm was presented with a different nomenclature depending on the program. Of note, Imaris software presents three Pearson coefficients; data set in volume, ROI volume and colocalized volume (data not shown), where only the data set volume responds to the original Pearson definition (Table 2) [24].

### **Pearson's Coefficient**

Pearson's coefficient was firstly applied to confocal microscopy in the 90's by Manders [29]. In Figure 4 (A-B) the results of Pearson's coefficient before and after the deconvolution are depicted. DNA/PEI complexes were completely assembled at the time of transfection ( $0.60 \pm 0.11$  in raw data;  $0.90 \pm 0.03$  deconvolved data) and their interaction decreased in time but never achieved negative values ( $0.16 \pm 0.07$  at 24 hpt in raw data as minimum value). Of note,

all values proportionally increased with deconvolution, since noise was reduced, which highly influences Pearson's coefficient [28].

### **Manders' Overlap Coefficient**

Its closely related alternative, Manders' Overlap Coefficient, is analyzed in Figure 4 (C-D):  $0.90 \pm 0.03$  ( $0.86 \pm 0.05$  in raw data) values were obtained at 0 hpt and decrease until  $0.57 \pm 0.19$  values at 24 hpt ( $0.55 \pm 0.16$  in raw data). Manders' values were stable after the deconvolution treatment, highlighting its robustness in facing the presence of noise in particle analysis [30]. Moreover, the lack of background in raw data has also contributed to this stability. Manders' is independent of different intensities between the evaluated channels, which is of benefit in the DNA/PEI analysis since the PEI signal obtained is lower than the DNA one, probably due to its more diffuse labeling. Furthermore, by eliminating the mean signal, Manders' prevents negative values which may difficult data interpretation [14].

### **$m_1$ and $m_2$ coefficients**

Manders' coefficient could be split into  $m_1$  (DNA) and  $m_2$  (PEI) values to study the interaction of each channel separately (Table 2). These coefficients allowed the colocalization quantification independently from signal proportion. DNA  $m_{1\text{JACO}P}$  trend was like Manders' ( $0.94 \pm 0.03$  and  $0.98 \pm 0.02$  in deconvolved and raw data, respectively); whereas PEI  $m_{2\text{JACO}P}$  value was restored after deconvolution, because of noise removal (which coupled with its low signal highly affect these coefficients). Thus, PEI-Cy5 suffered a fast drop within the first 2 hpt and, afterwards, it progressively disassembled in a minor extent. This fact was also pointed in the scatter plot analysis (Figure 3).

Interestingly, the calculation of  $m_{1\text{IMARIS}}$  and  $m_{2\text{IMARIS}}$  through Imaris software gave a different trend from that obtained with JACO-P. No relevant differences were found for the other coefficients analyzed with both software. Finally, when these results were compared with the co-occurrence of DNA and PEI signal analyzed with the percentage of colocalized volume

(Supplementary Materials, S2), same behavior that JACoP  $m1_{JACoP}$  and  $m2_{JACoP}$  was observed. Thus, DNA/PEI disassembly was also corresponded in number of pixels.

From the different results, the usefulness of deconvolution treatment to improve colocalization results is evidenced. This comparison has emphasized that (1) every software only permits the use of certain coefficients, (2) different algorithms present the same trend but with different values, (3) the most robust coefficient to evaluate DNA/PEI disassembly is the Manders' Overlap coefficient with raw data and (4) coefficient trends are normalized after deconvolution.

**Table 2. Summary of quantitative colocalization coefficients available in the different software. A comparison of the different formulas and nomenclature present in JACoP and Imaris software is presented. The definition and the possible range values of every colocalization coefficient are also depicted.  $Ch_i$ : individual pixel intensity of a specific channel;  $Ch_{i,av}$ : mean average intensity of a channel;  $(Ch_i)_{coloc}$ : every intensity pixel that colocalizes from a channel;  $(Ch_i)_{total}$ : every pixel intensity from a channel.**

Formula	JACoP nomenclature	IMARIS nomenclature	Definition	Range
$r = \frac{\sum(Ch1_i - Ch1_{av})(Ch2_i - Ch2_{av})}{\sqrt{\sum(Ch1_i - Ch1_{av})^2 \sum(Ch2_i - Ch2_{av})^2}}$	Pearson's coefficient	Pearson's coefficient on the dataset	Describes the correlation of the intensity distribution between channels[14]	Ranges from -1 to 1
$r = \frac{\sum(Ch1_i)(Ch2_i)}{\sqrt{\sum(Ch1_i)^2 \sum(Ch2_i)^2}}$	Manders' Overlap Coefficient	None	Indicates an actual overlap of the signals, represents the true degree of colocalization	Ranges from 0 to 1
$m1 = \frac{\sum(Ch1_i)_{coloc}}{\sum(Ch1_i)_{total}}$	Manders' Coefficient $m1$ and $m2$ and Thresholded:	Original Manders' coefficient A and B.* Thresholded Original Manders' coefficient A and B.*	Describe the contribution of each channel from two selected ones to the pixels of interest.	Ranges from 0 to 1
$m2 = \frac{\sum(Ch2_i)_{coloc}}{\sum(Ch2_i)_{total}}$	Manders' Coefficient $m1$ and $m2$	Where A refers to Ch1 and B refers to Ch2		

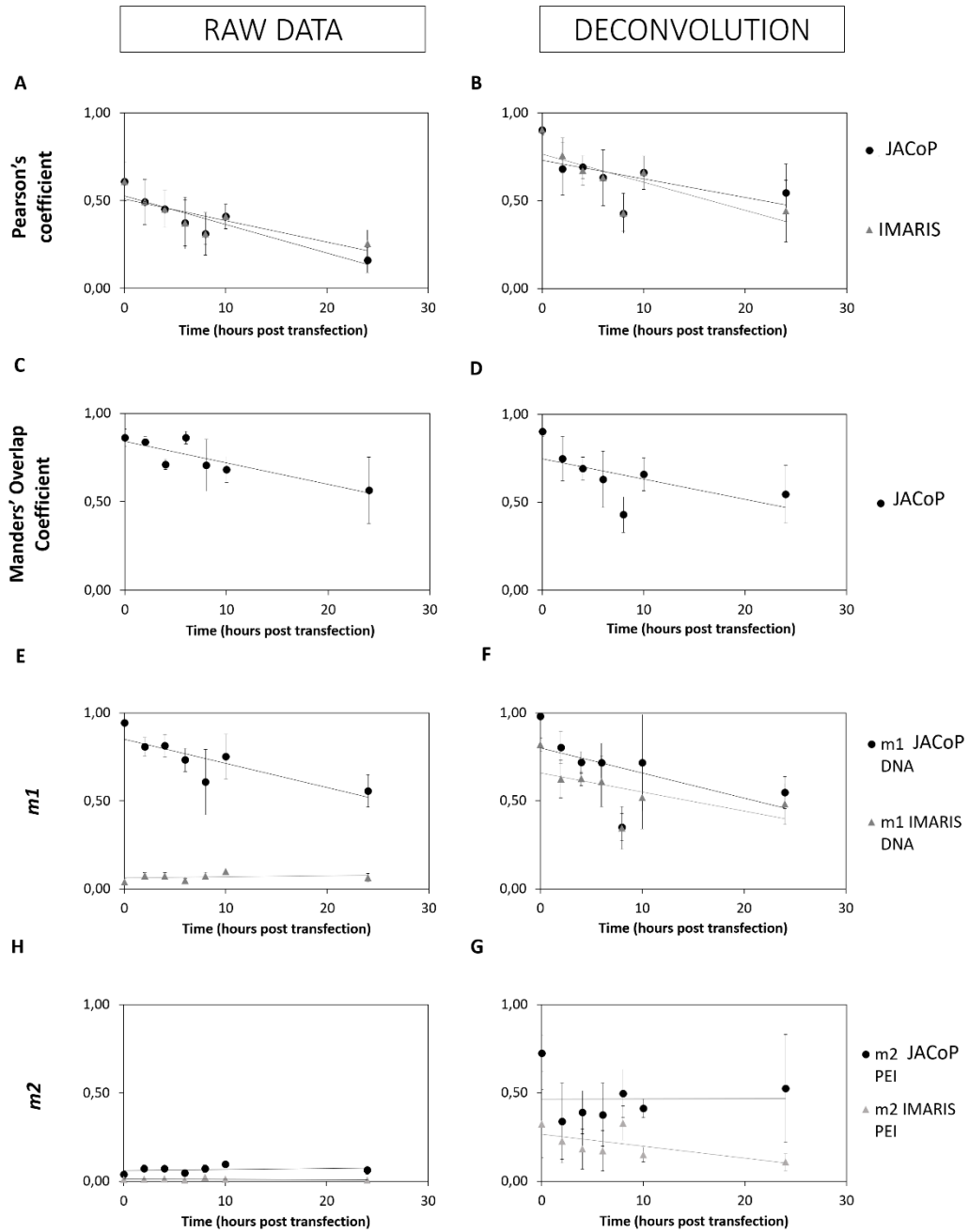


**Figure 4.** Comparison of quantitative colocalization analysis of DNA/PEI disassembly kinetics by JACoP and IMARIS software. The quantitative separation of DNA-Cy3 and PEI-Cy5 signal with time after their uptake by the cells is depicted. The study of the Pearson Coefficient without and with deconvolution, respectively (A,B), Manders' Overlap Coefficient without and with deconvolution, respectively (C, D),  $m_1$  (DNA) &  $m_2$  (PEI) without and with deconvolution, respectively (E,F and H,G) were studied. Colocalization was determined in 5 3D-fields with 3-5 cells per field at each time point. Mean values  $\pm$  standard deviations are presented in every chart.

### 3.5. 3D qualitative analysis

In Figure 5, a 3D-representation of DNA/PEI disassembly process is observed. Qualitative observation together with the quantitative information, gave a global description of what is occurring intracellularly. First, all complexes were strongly formed when added to the cell culture, which is supported by the high colocalization coefficients at 0 hpt. Then, DNA/PEI disassembly appeared as an heterogenous process: some complexes remained interacting, whereas others started to disassemble. DNA (green) was further observed as microparticles partially complexed by PEI, while PEI (red) was dissociated at longer times. Consequently, Manders' Overlap Coefficient is observed to decrease with time while the standard deviation increased (Figure 4).

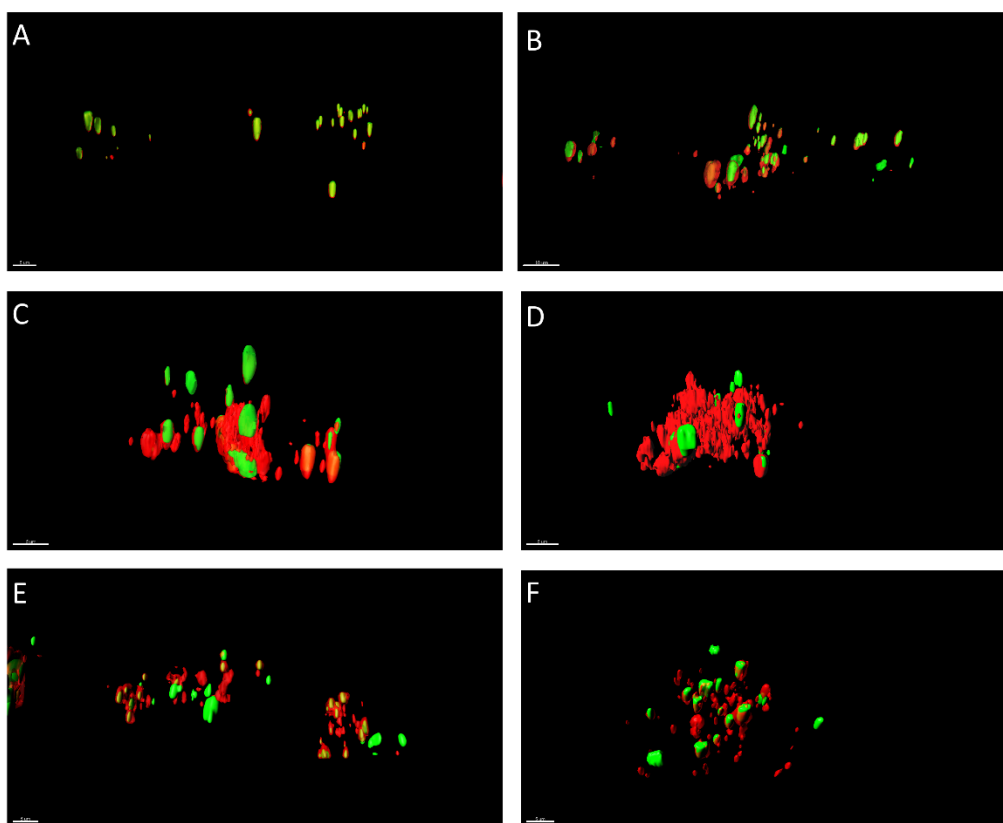


**Figure 5.** 3D-reconstruction of super-resolved images by deconvolution of DNA/PEI disassembly process. In depth characterization of DNA/PEI complex evolution with time is presented. DNA-Cy3 signal (Green), PEI-Cy5 (Red). Representative images of each time point are depicted at 0 hpt (A), 2 hpt (B), 4 hpt(C), 6 hpt (D), 8 hpt (E) and 10 hpt (F). 3D-images performed with IMARIS® software.



In addition, a relevant question in the DNA delivery field is how complexes arrive into the cell nucleus. In Figure 6, a 3D-reconstruction of the three channels analyzed in this work (DNA, PEI and cell nuclei) is depicted. Of note, Imaris software offers the mask reconstruction channel of the colocalized pixels (represented with a grey mask, Figure 6). DNA/PEI microparticles of bigger size were in the surroundings of cell nuclei and smaller DNA particles and PEI were visualized spread out the nuclei. These results show the potential of 3D imaging plus super-resolution by deconvolution as a useful approach to study DNA release and particle tracking in live cells.

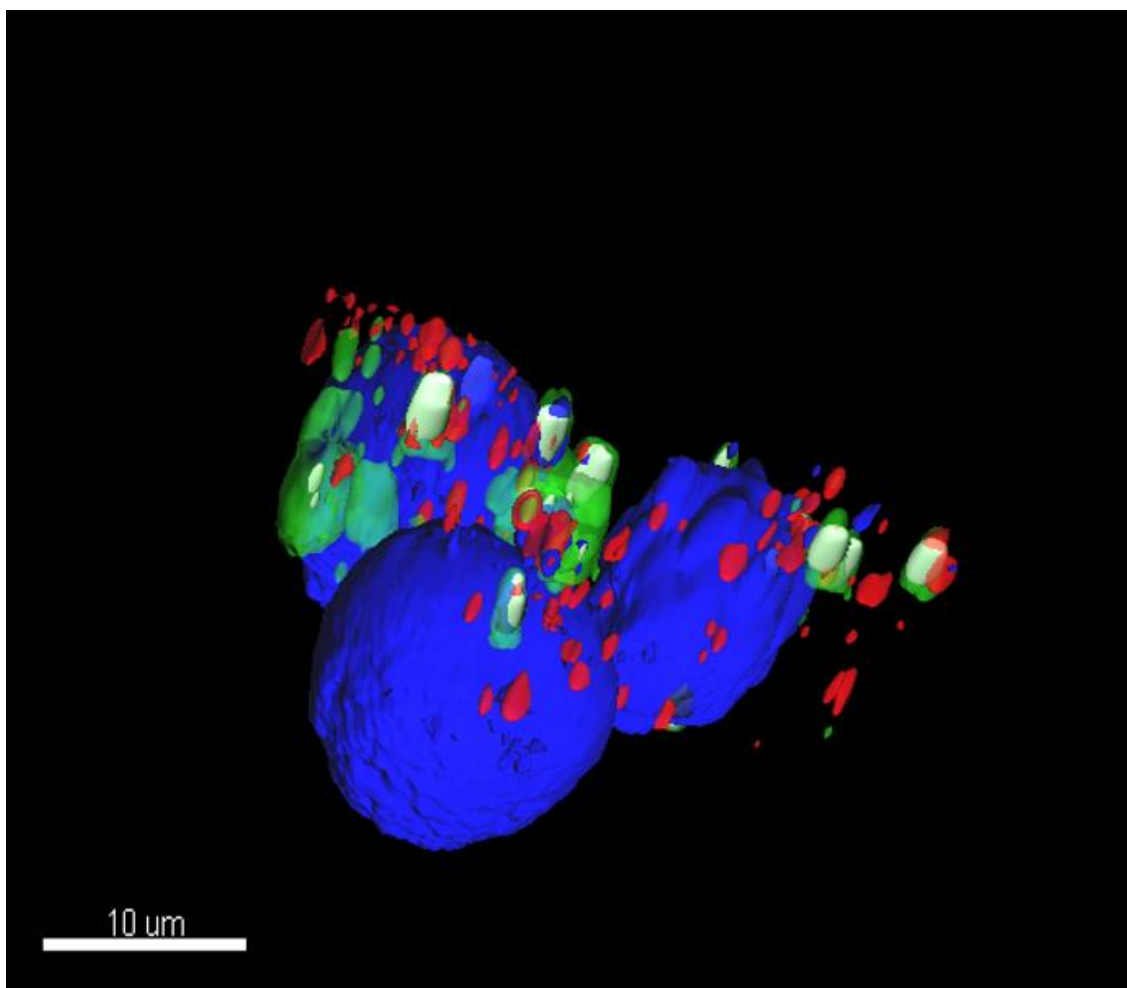


**Figure 6.** 3D-reconstruction super-resolved images by deconvolution of DNA/PEI disassembly process at 24 hpt. Presence of DNA/PEI complexes (Grey) underneath the nuclear envelope (nucleus stained with Hoechst detected in blue) are observed, whereas free DNA-Cy3 signal (light-Green) and PEI-Cy5 (light-Red) and cell nucleus (Blue) are also visualized pointing the heterogeneity of DNA/PEI complexes within cells. 3D-images performed with IMARIS® software.

#### 4. Discussion

DNA/PEI disassembly process has been successfully tracked by CSLM colocalization. Within the different acquisition parameters and computational image tools, several conditions have been adapted to the special features of DNA/PEI complexes, including magnification or laser power. In addition, the application of deconvolution has been tested in different colocalization coefficients using two different programs, for comparison.

The use of quantitative colocalization for the study of the DNA release from DNA/PEI complexes has been investigated here. After deconvolution, both Pearson's Coefficient and Manders' Overlap Coefficient (Figure 4) have values around  $0.90 \pm 0.03$  (0 hpt) and decreased until  $0.66 \pm 0.09$  (10 hpt), being Manders' the most robust against high noise presence and less sensitive to different channel intensities (Figure 4). Moreover, due to the low volumes occupied by DNA/PEI complexes, just a small percentage of analyzed pixels were positive for at least one channel. Thus, these results support the use of these technologies as a complementary tool for bioprocess characterization and diagnosis at nanometric range [18,21,31]. For instance, Manders' has been recently used to track the presence of siRNA/PEI complexes in endocytic vesicles [32]. Compared to other quantitative techniques, quantitative colocalization is time-consuming and require technical expertise. However, it enables the study of dynamic processes at intracellular level. Moreover, the specific detection of the desired molecules has been tracked by fluorescence. Therefore, despite colocalization results should be taken as a relative quantification, the significant differences along DNA/PEI disassembly kinetics are significative to characterize DNA release. Finally, the possibility to take 3D images with specialized software and colocalization masks enabled the better understanding of the process.

In this work, DNA/PEI complexes were observed in the nuclear envelope at 24 hpt. The presence of micrometric complexes near the nucleus (Figure 2, Figure 6) could work as a DNA reservoir. Meanwhile the disassembly starts at 2 hpt, some DNA/PEI complexes are maintained at 24 hpt and production yields still increase until longer production times. This fact has been also observed in other transient transfection processes [5,7,33]. There are several hypothesis in the literature

since the trafficking of DNA to the cell nucleus has not been fully characterized [5]. Some authors propose DNA/PEI complexes enter into the nucleus during cell division [34,35], while others reported a DNA active transport through the nuclear pores [7,36]. The data presented here support the hypothesis of nuclear entry since no big DNA/PEI complexes were observed inside them. Cervera et al. [13] showed the presence of DNA/PEI complexes in the perinuclear region. Furthermore, Han et al. [7] reported that DNA/PEI disassembly of DNA/PEI complexes to allow for protein production. Nonetheless, due to the improvements obtained in image acquisition and post processing optimization, the number of complexes per cell shown in the study is higher (7 complexes/nuclei at 0 hpt, Figure 1) and the signal of DNA and PEI alone is clearly evidenced (Figure 3).

Along with the aforementioned improvements in CSLM, new technologies such as white laser and hybrid detectors for optimizing stimulation and emission of selected fluorochromes, as well as the latest generation of super-resolution techniques, such as HyVolution and Stimulated emission depletion 3D (Leica Microsystems) or Airyscan systems (Zeiss), will become fundamental technologies in further colocalization studies, thereby allowing the performance of more rigorous analyses. These systems allow optimal observation of capture within a set parameter, together with deconvolution and improved optical resolution. This fact is especially relevant in the nanotechnology field, for instance, nm-size DNA/PEI complexes subpopulations have been described in literature, but have not been visualized by CLSM yet [5,8,37]. The improvements obtained in this work coupled with these new technologies will enable the systematic study of DNA delivery in living cells by CSLM since is still the reference methodology in the field.

## **5. Acknowledgments**

The authors wish to thank Dr. Amine Kamen (McGill University, Montreal, Canada) for providing the HEK 293 SF-3SF6. The following reagent was obtained through the National Institutes of Health AIDS reagent Program, Division AIDS, National Institute of Allergy and Infectious Diseases, National Institutes of Health: pGag-eGFP (Cat# 11468) from Dr. Marilyn

Resh. Cy5 monoreactive fluorochrome was nicely provided by the Servei of Sequenciació from Institut de Biotecnologia i Biomedicina (IBB, UAB, Bellaterra, Spain). The discussions with Dr. Delissa Garcia (Bitplane AG) was greatly appreciated.

## 6. Literature

1. Gutiérrez-Granados, S.; Cervera, L.; Kamen, A.A.; Gòdia, F. Advancements in mammalian cell transient gene expression (TGE) technology for accelerated production of biologics. *Crit. Rev. Biotechnol.* **2018**, *38*, 1–23.
2. Boussif, O.; Lezoualc'h, F.; Zanta, M.A.; Mergny, M.D.; Scherman, D.; Demeneix, B.; Behr, J.P. A versatile vector for gene and oligonucleotide transfer into cells in culture and in vivo: polyethylenimine. *Proc. Natl. Acad. Sci.* **1995**, *92*, 7297–7301.
3. Xiang, S.; Tong, H.; Shi, Q.; Fernandes, J.C.; Jin, T.; Dai, K.; Zhang, X. Uptake mechanisms of non-viral gene delivery. *J. Control. Release* **2012**, *158*, 371–8.
4. Hwang, M.E.; Keswani, R.K.; Pack, D.W. Dependence of PEI and PAMAM Gene Delivery on Clathrin- and Caveolin-Dependent Trafficking Pathways. *Pharm. Res.* **2015**, *32*, 2051–2059.
5. Yue, Y.; Wu, C. Progress and perspectives in developing polymeric vectors for in vitro gene delivery. *Biomater. Sci.* **2013**, *1*, 152–170.
6. Benjaminsen, R. V; Matthebjerg, M.A.; Henriksen, J.R.; Moghimi, S.M.; Andresen, T.L. The Possible “Proton Sponge ” Effect of Polyethylenimine (PEI) Does Not Include Change in Lysosomal pH. *Mol. Ther.* **2012**, *21*, 149–157.
7. Han, X.Z.; Fang, Q.Y.; Yao, F.; Wang, X.N.; Wang, J.F.; Yang, S.L.; Shen, B.Q. The heterogeneous nature of polyethylenimine-DNA complex formation affects transient gene expression. *Cytotechnology* **2009**, *60*, 63–75.
8. Choosakoonkriang, S.; Lobo, B.A.; Koe, G.S.; Koe, J.G.; Middaugh, C.R.R. Biophysical characterization of PEI/DNA complexes. *J. Pharm. Sci.* **2003**, *92*, 1710–22.
9. Godbey, W.T.; Wu, K.K.; Mikos, G. Tracking the intracellular path of poly(ethylenimine)/DNA complexes for gene delivery. *Proc. Natl. Acad. Sci. U. S. A.* **1999**, *96*, 5177–5181.

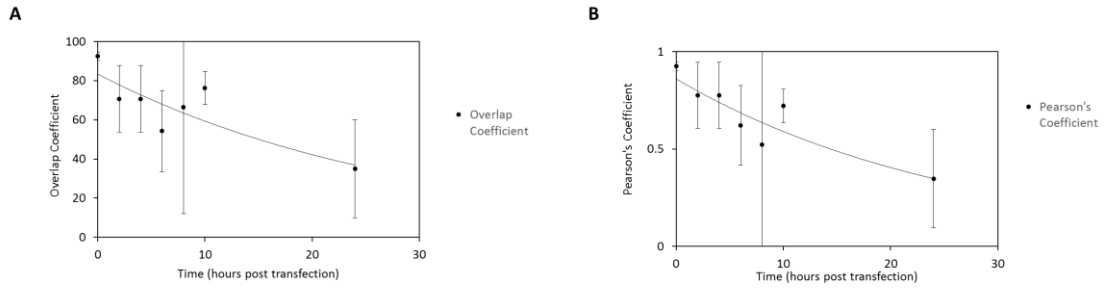
10. Suh, J.; Dawson, M.; Hanes, J. Real-time multiple-particle tracking: applications to drug and gene delivery. *Adv. Drug Deliv. Rev.* **2005**, *57*, 63–78.
11. Shi, J.; Chou, B.; Choi, J.L.; Ta, A.L.; Pun, S.H. Investigation of Polyethylenimine/DNA Polyplex Transfection to Cultured Cells Using Radiolabeling and Subcellular Fractionation Methods. *Mol. Pharm.* **2013**, *10*, 2145–2156.
12. Cervera, L.; Gutiérrez-Granados, S.; Martínez, M.; Blanco, J.; Gòdia, F.; Segura, M.M. Generation of HIV-1 Gag VLPs by transient transfection of HEK 293 suspension cell cultures using an optimized animal-derived component free medium. *J. Biotechnol.* **2013**, *166*, 152–165.
13. Cervera, L.; González-Domínguez, I.; Segura, M.M.; Gòdia, F. Intracellular characterization of Gag VLP production by transient transfection of HEK 293 cells. *Biotechnol. Bioeng.* **2017**, *114*, 2507–2517.
14. Dunn, K.W.; Kamocka, M.M.; McDonald, J.H. A practical guide to evaluating colocalization in biological microscopy. *AJP Cell Physiol.* **2011**, *300*, C723–C742.
15. Sheng, H.; Stauffer, W.; Lim, H.N. Systematic and general method for quantifying localization in microscopy images. *Biol. Open* **2016**, *5*, 1882–1893.
16. Bolte, S.; Cordelières, F.P. A guided tour into subcellular colocalization analysis in light microscopy. *J. Microsc.* **2006**, *224*, 213–232.
17. Zinchuk, V.; Grossenbacher-Zinchuk, O. Quantitative Colocalization Analysis of Fluorescence Microscopy Images. In *Current Protocols in Cell Biology*; John Wiley & Sons, Inc.: Hoboken, NJ, USA, 2014; Vol. 62, pp. 4.19.1-4.19.14 ISBN 0471143030.
18. Pike, J.A.; Styles, I.B.; Rappoport, J.Z.; Heath, J.K. Quantifying receptor trafficking and colocalization with confocal microscopy. *Methods* **2017**, *115*, 42–54.
19. Chu, Z.; Zhang, S.; Zhang, B.; Zhang, C.; Fang, C.-Y.; Rehor, I.; Cigler, P.; Chang, H.-C.; Lin, G.; Liu, R.; et al. Unambiguous observation of shape effects on cellular fate of nanoparticles. *Sci. Rep.* **2014**, *4*, 4495.

20. Chen, L.; Xiao, S.; Zhu, H.; Wang, L.; Liang, H. Shape-dependent internalization kinetics of nanoparticles by membranes. *Soft Matter* **2016**, *12*, 2632–2641.
21. Reitan, N.K.; Sporsheim, B.; Bjorkoy, A.; Strand, S.; Davies, C. de L. Quantitative 3-D colocalization analysis as a tool to study the intracellular trafficking and dissociation of pDNA-chitosan polyplexes. *J. Biomed. Opt.* **2012**, *17*, 026015.
22. Zeng, Z.; Xie, H.; Chen, L.; Zhanghao, K.; Zhao, K.; Yang, X.; Xi, P. Computational methods in super-resolution microscopy. *Front. Inf. Technol. Electron. Eng.* **2017**, *18*, 1222–1235.
23. Image J. Image processing and Analysis in Java.
24. BITPLANE, O.I. Colocalization Tools Colocalization as a tool for multichannel analysis •. *Appl. note*, 2016.
25. Gutiérrez-Granados, S.; Cervera, L.; Godia, F.; Carrillo, J.; Segura, M.M.; Gutierrez-Granados, S.; Cervera, L.; Godia, F.; Carrillo, J.; Segura, M.M.; et al. Development and validation of a quantitation assay for fluorescently tagged HIV-1 virus-like particles. *J. Virol. Methods* **2013**, *193*, 85–95.
26. Landmann, L.; Marbet, P. Colocalization analysis yields superior results after image restoration. *Microsc. Res. Tech.* **2004**, *64*, 103–112.
27. Sarder, P.; Nehorai, A. Deconvolution methods for 3-D fluorescence microscopy images. *IEEE Signal Process. Mag.* **2006**, *23*, 32–45.
28. Adler, J.; Parmryd, I. Quantifying colocalization by correlation: The pearson correlation coefficient is superior to the Mander's overlap coefficient. *Cytom. Part A* **2010**, *77*, 733–742.
29. Manders, E.M.; Stap, J.; Brakenhoff, G.J.; van Driel, R.; Aten, J.A. Dynamics of three-dimensional replication patterns during the S-phase, analysed by double labelling of DNA and confocal microscopy. *J. Cell Sci.* **1992**, 857–62.

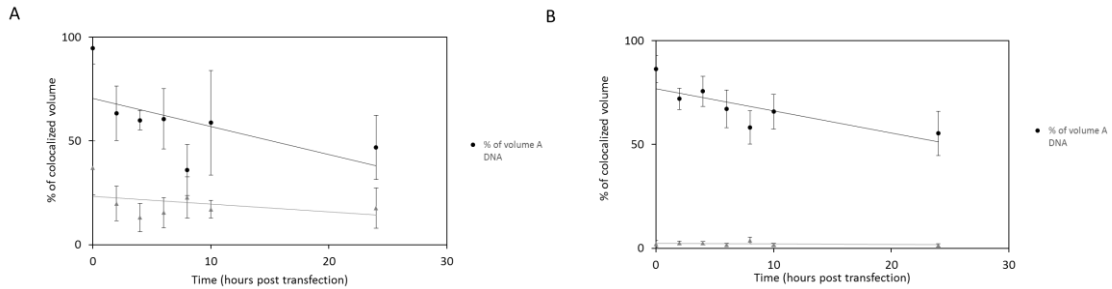
30. Manders, E.M.M.; Verbeek F J; Aten J A Measurement of co-localization of objects in dual-colour confocal images. *J. Microsc.* **1993**, *169*, 375–382.
31. Ping-Jie Xiao, Chengwen Li, A.N. and R.J.S.; Xiao, P.J.; Li, C.; Neumann, A.; Samulski, R.J. Quantitative 3D tracing of gene-delivery viral vectors in human cells and animal tissues. *Mol. Ther.* **2012**, *20*, 317–328.
32. Lazebnik, M.; Pack, D.W. Rapid and facile quantitation of polyplex endocytic trafficking. *J. Control. Release* **2017**, *247*, 19–27.
33. Baldi, L.; Hacker, D.L.; Adam, M.; Wurm, F.M. Recombinant protein production by large-scale transient gene expression in mammalian cells: state of the art and future perspectives. *Biotechnol. Lett.* **2007**, *29*, 677–684.
34. Tait, A.S.; Brown, C.J.; Galbraith, D.J.; Hines, M.J.; Hoare, M.; Birch, J.R.; James, D.C. Transient production of recombinant proteins by Chinese hamster ovary cells using polyethyleneimine/DNA complexes in combination with microtubule disrupting anti-mitotic agents. *Biotechnol. Bioeng.* **2004**, *88*, 707–721.
35. Grosse, S.; Thévenot, G.; Monsigny, M.; Fajac, I. Which mechanism for nuclear import of plasmid DNA complexed with polyethylenimine derivatives? *J. Gene Med.* **2006**, *8*, 845–51.
36. Gillard, M.; Jia, Z.; Hou, J.J.C.; Song, M.; Gray, P.P.; Munro, T.P.; Monteiro, M.J. Intracellular trafficking pathways for nuclear delivery of plasmid DNA complexed with highly efficient endosome escape polymers. *Biomacromolecules* **2014**, *15*, 3569–3576.
37. González-Domínguez, I.; Grimaldi, N.; Cervera, L.; Ventosa, N.; Gòdia, F. Impact of physicochemical properties of DNA/PEI complexes on transient transfection of mammalian cells. *N. Biotechnol.* **2019**, *49*, 88–97.



## 7. Supplementary materials



**Supplementary Materials S1: Comparison of quantitative colocalization analysis of DNA/PEI disassembly kinetics by ROI in JACoP software. The study of Manders' Overlap Coefficient (A) and Pearson's Coefficient (B) has been studied respectively.**



**Supplementary Materials S2: Comparison of quantitative colocalization analysis of DNA/PEI disassembly kinetics by the percentage of colocalized volume of DNA-Cy3 (black dots) and PEI-Cy5 (grey dots) disassembly kinetics by IMARIS software. (A) Raw data and (B) deconvolved data.**

## **Chapter 4**

# **Quantification of the HIV-1 virus-like particle production process by super-resolution imaging: from VLP budding to nanoparticle analysis**

---

Published in Biotechnology and Bioengineering, 2020

## **Abstract**

Virus-like particles (VLPs) offer great promise in the field of nanomedicine. Enveloped VLPs are a class of these nanoparticles and their production process occurs by a budding process, which is known to be the most critical step at intracellular level. In this work, we developed a novel imaging method based on super-resolution fluorescence microscopy (SRFM) to assess the generation of VLPs in living cells.

This methodology was applied to study the production of Gag VLPs in three animal cell platforms of reference: HEK 293-transient gene expression (TGE), High Five-baculovirus expression vector system (BEVS) and Sf9-BEVS. Quantification of the number of VLP assembly sites per cell ranged from 500 to 3000 in the different systems evaluated. While the BEVS was superior in terms of Gag polyprotein expression, the HEK 293-TGE platform was more efficient regarding the assembly of Gag as VLPs. This was translated into higher levels of non-assembled Gag monomer in BEVS harvested supernatants. Furthermore, the presence of contaminating nanoparticles was evidenced in all three systems, specifically in High Five cells. The SRFM-based method here developed was also successfully applied to measure the concentration of VLPs in crude supernatants. The lipid membrane of VLPs and the presence of nucleic acids alongside these nanoparticles could also be detected using common staining procedures.

Overall, a complete picture of the VLP production process was achieved in these three production platforms. The robustness and sensitivity of this new approach broaden the applicability of SRFM toward the development of new detection, diagnosis and quantification methods based on confocal microscopy in living systems.

**Keywords:** Super-resolution fluorescence microscopy, HIV-1, Budding, Virus-like particle, Nanoparticle quantification.

## 1. Introduction

Virus-like particles (VLPs) represent a new biological tool to develop novel functionalized materials. VLPs are multiprotein nanoparticles that structurally mimic the native virus but are devoid of viral genome. Their success as immunogens and nanocarriers has been demonstrated in numerous preclinical and clinical trials over the last years [1]. Among the different VLP candidates, enveloped HIV-1 Gag VLPs are on the spotlight as a scaffold for antigen presentation against different diseases [1,2] and as reference material for the production of extracellular vesicles (EVs) [3]. The HIV-1 structural polyprotein (Gag) has the capacity to form non-infective viral particles on their own [4]. Upon expression, the Gag polyprotein accumulates underneath the plasma membrane of the cell host, where oligomerization occurs. During this process, the ESCRT (Endosomal Sorting Complexes Required for Transport) machinery is recruited into the assembly site, enabling the viral particle to bud [5]. This step, which takes part of the lipid membrane of the producer cell to form the enveloped nanoparticle, has been pointed as the major bottleneck in the production of Gag VLPs (Figure 1) [6]. Thus, the characterization of individual VLP assembly sites at cell membrane level is essential to better understand the VLP production process.

The preferred strategies to produce enveloped VLPs are transient gene expression (TGE) in mammalian cell lines and the baculovirus expression vector system (BEVS) in insect cells (Table 1) [7]. These production platforms are widely used in industry, and have been brought to production scale, achieving competitive production yields for preclinical studies [8–10]. Whilst transiently produced VLPs in mammalian cells show lower productivities, the BEVS present a major bottleneck in product purity [2]. In fact, co-purification between Gag VLPs and baculoviruses is of general concern, owing to their similar physicochemical and biochemical properties [11]. Moreover, the concomitant production of EVs in both, mammalian and insect cells, including exosomes, microvesicles and apoptotic vesicles has to be carefully considered [12,13]. In Table 1, potential contaminants previously reported for each system are listed [13–

15]. Altogether, the characterization of this mixture of contaminating particles is essential in early stages of process development toward selecting the most adequate production strategy.

**Table 1. Comparison of the different animal cell lines used in this work for the production of VLPs.**

	<b>HEK 293</b>	<b>High Five</b>	<b>Sf9</b>
<b>Cell-line description</b>	Suspension-adapted to chemically defined culture media [16]	Suspension-adapted to protein-hydrolysate containing culture media [17]	Suspension-adapted to protein-hydrolysate containing culture media [18]
<b>Production system</b>	Non-viral [19]	Viral [20]	Viral [20]
<b>Scale</b>	Bioreactor [9]	Flask [20]	Bioreactor [10]
<b>Clinical status</b>	Preclinical	Preclinical	Preclinical
<b>Described contaminants</b>	EVs, HCD and HCP [9,12]	Baculoviridae (infection), Nodaviridae, EVs, HCD and HCP [21] [22]	Baculoviridae (infection), Rhabdoviridae, EVs, HCD and HCP [23] [24]

The quantification of VLPs is also a challenge as it cannot rely on conventional methods for virus quantification, such as infectivity assays, due to the absence of viral genome. Biochemical, biological and biophysical methods are used for VLP analysis [25]. While the first two can distinguish the presence and activity of a specific protein, they fail in evaluating the conformational integrity of assembled VLPs. Therefore, biophysical methods are needed to ensure the structural integrity of these nanoparticles. Analytical ultracentrifugation and dynamic light scattering (DLS) were primarily used to this end, whereas electron microscopy (EM) has been the preferred methodology for VLP visualization, since nanometric or even atomic resolution can be achieved [26]. Alternatively, atomic force microscopy (AFM) has emerged as a powerful tool to study viruses [27]. However, the requirement of sample pre-treatment and the complexity of EM and AFM techniques pose an obstacle when the goal is to investigate a dynamic process in living cells. In this regard, the use of Super-Resolution Fluorescence Microscopy (SRFM) promises to overcome these limitations [28]. SRFM, also termed nanoscopy, has been defined as the resolution achieved beyond the classical Abbe diffraction limit [29]. Several studies

have used SRFM to understand the mechanisms behind HIV-1 infection [28,30–32]. Of note, a 2-fold increase in resolution could be achieved by improving optical acquisition, as for Structured Illumination (SIM) and Airyscan [32], or by computational restoration of the point spread function using deconvolution [29,33]. On the other hand, resolutions below 20 nm have been achieved with Stimulated Emission Depletion (STED) or Stochastic Optical Reconstruction Microscopy (STORM) technologies [28,34]. These approaches are based on the capacity to transit from activated to inactivated states of certain fluorophores but are not easily implemented, since they require specific sample labelling, equipment infrastructure and a high expertise. In addition, the characterization of a process in living cells, such as VLP budding, has to deal with live cell compatibility, acquisition speed, multicolor imaging and resolution as the most relevant parameters [35], thus limiting the application of STED and STORM. The appearance of HyVolution2, now updated to Lightning (Leica Microsystems), which combines optical super-resolution principles at sub-Airy pinhole sizes and subsequent computational deconvolution, has allowed to resolve below the 140 nm [36]. Moreover, HyVolution2 is compatible with conventional fluorophores and prevents from photodamage caused by using a high energetic laser source [28,32]. Hence, HyVolution2 represents a user-friendly SRFM alternative that can simultaneously achieve super-resolution and high-speed acquisition for multiple fluorochromes. Advancements in imaging software are also of mention since they have allowed the study and quantification of three-dimensional (3D) biological samples in an automatic and holistic way.

In this work, a novel methodology has been developed to analyze the complete process of HIV-1 Gag VLP production in living cells, from VLP formation in membrane VLP assembly sites to direct VLP characterization and quantification in the supernatant. This methodology was applied to study and compare the VLP production process in three animal cell platforms and validated by means of reference orthogonal techniques. The enhanced green fluorescent protein (eGFP) was fused in frame to the Gag polyprotein to facilitate process characterization and VLP quantification (Figure 1A). To our knowledge, this is the first time that HyVolution2 SRFM and 3D imaging have been implemented in living cells. These data provide new insights of VLP production in

animal cell lines and highlights the use of this methodology in process development with applicability to other complex nanoparticles.

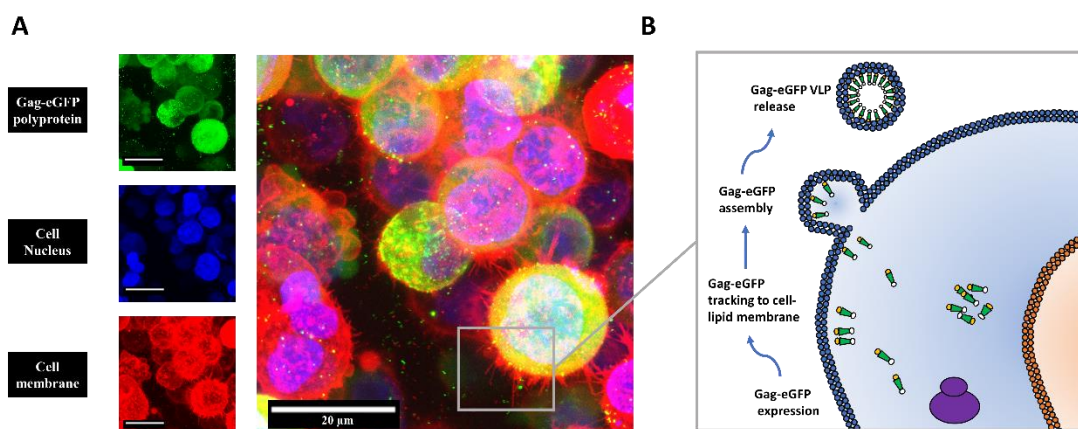


**Figure 1.** HIV-1 Gag-eGFP VLP production. (A) Confocal microscopy image of HEK 293 cells producing VLPs. Cell nucleus was stained with Hoechst (blue), lipid membrane was stained with CellMask™ (red) and the green signal corresponds to Gag-eGFP. (B) Scheme of HIV-1 Gag VLP production at intracellular level adapted from Cervera and co-authors [6]. The Gag-eGFP polyprotein is produced in the cytoplasm and travels to the cell membrane. Their oligomerization occurs in VLP assembly sites and the resulting VLPs bud to the extracellular space taking part of the host-cell lipid membrane.

## 2. Materials and Methods

### 2.1. Mammalian cell line, culture conditions and transient gene expression

The mammalian cell line used in this work is a serum-free suspension-adapted HEK 293 cell line (HEK 293SF-3F6, NRC, Montreal, Canada) kindly provided by Dr Amine Kamen from McGill University (Montreal, Canada). Cells were cultured as previously described [19]. HIV-1 Gag-eGFP VLPs were obtained by transient gene expression with the pGag-eGFP plasmid, which codes for a Rev independent HIV-1 Gag polyprotein fused in frame to the enhanced GFP [37]. The plasmid was obtained from the NIH AIDS Reagent Program (cat. Num. 11468) and constructed by cloning the Gag sequence from pCMV55M1-10 [38] into the pEGFP-N1 plasmid (Clontech, Palo Alto, CA, USA). The plasmid was prepared and purified as previously described [39]. HEK 293 cells were transfected using 25-kDa linear polyethylenimine (PEI) (PolySciences, Warrington, PA, USA) at  $2 \cdot 10^6$  cells/mL and a final DNA concentration of 1  $\mu$ g/mL with a DNA

to PEI mass ratio of 1:2. DNA/PEI complexes were formed by adding PEI to plasmid DNA diluted in fresh FreeStyle 293 culture medium, representing the 10 % of the total cell culture volume to be transfected. The mixture was incubated at room temperature for 15 min to allow DNA/PEI complex formation, and a medium exchange to fresh FreeStyle 293 medium was performed prior to DNA/PEI complex addition [19]. Transfected cultures were sampled every 24 hours post transfection (hpt) by centrifugation at 1000 xg during 15 min. Harvested supernatants were stored at 4 °C and cell pellets at -20 °C until analysis. Non-transfected negative controls reproducing cell growth conditions were also analyzed, for comparison.

## **2.2. Insect cell lines, culture conditions and baculovirus infection protocol**

The suspension-adapted lepidopteran insect cell lines used in this work are *Spodoptera frugiperda* (Sf9, cat. num. 71104, Merck) and *Trichoplusia ni* BTI-TN-5B1-4 cells (High Five, cat. num. B85502, Thermo Fisher Scientific) gently provided by Dr Nick Berrow (Institute for Research in Biomedicine, Barcelona, Spain) and Dr Paula Alves (Instituto de Biologia Experimental e Tecnológica, Oeiras, Portugal), respectively. Both insect cell lines were cultured in Sf900III medium (Thermo Fisher Scientific, Grand Island, NY, USA) in 125-mL disposable polycarbonate Erlenmeyer flasks. All cultures were shaken at 130 rpm using an orbital shaker (Stuart, Stone, UK) and maintained at 27 °C.

HIV-1 Gag-eGFP VLP production was achieved through infection with the baculovirus *Autographa californica* multiple nucleopolyhedrovirus (AcMNPV) coding for the recombinant Gag-eGFP polyprotein (BD Biosciences, San José, CA, USA). Shortly, High Five and Sf9 cells were grown to  $3 \cdot 10^6$  cells/mL and infected at a multiplicity of infection (MOI) of 1. Infected cell cultures were sampled every 24 hours post infection (hpi) and VLP containing supernatants were harvested by centrifugation at 1000 xg during 15 min. Supernatants were maintained at 4 °C and cell pellets were stored at -20 °C until analysis. Non-infected insect cell cultures were also analyzed for comparison to baculovirus infected cell conditions.



### **2.3. Sample preparation for confocal microscopy analysis**

Transfected HEK 293 and infected insect cells were analyzed at 48 hpt or 40 hpi, respectively. Prior to the analysis, cells were stained with CellMask™ and Hoechst 33342, trihydrochloride, trihydrate (Thermo Fisher Scientific), which stained plasma membrane in a deep red color and nucleic acid in a blue cyan color, respectively. Briefly, a concentration of 0.1 % v/v of each dye was added to the different animal cell lines, respectively. After 10 min of incubation at room temperature and protected from light, the mixture was centrifuged at 300 xg for 5 min, and the cell pellet was resuspended in fresh FreeStyle 293 cell culture media. Samples were placed on glass bottom dishes (MatTek, Ashland, MA, USA) for visualization under the confocal microscope [6].

HIV-1 Gag-eGFP VLP samples were stained with 0.1 % v/v of CellMask™ and 0.1% v/v of Hoechst 33342, or 0.05 % v/v in the case of Sf9 harvested supernatants. Preliminary experiments were performed to test several incubation time and dye concentrations ranges. 50 µL of sample were placed on 76 x 26 mm microscope slides (Linea LAB, Barcelona, Spain) with 24 x 60 mm premier cover glass (Leica Microsystems, Wetzlar, Germany). Prior to analysis, an incubation of 30 min at room temperature protected from light was performed to allow VLP deposition and reduce particle movement in suspension. Images were taken from the cover glass, where deposited VLPs could be observed.

### **2.4. Confocal microscopy settings**

SRFM analysis was performed using TCS SP8 confocal microscope equipped with Huygens deconvolution suite and GPU arrays (Leica Microsystems) at Servei d'Anatomia Patològica from Hospital Sant Joan de Déu (Esplugues de Llobregat, Barcelona, Spain). 3 - 4 cells with 30 x 30 x 4 µm physical length in *xyz* average per sample were imaged with 63 X magnification (zoom 8 – 10 X) with HC PL APO CS2 63x/1.40 OIL objective with HyVolution2 (Lightning) mode (Leica Microsystems), 8,000 Hz speed and 5-line average. 405 nm (Hoechst), 488 nm (Gag-eGFP VLPs) and 633 nm (CellMask™) laser lines and HyD detectors with BrightR mode (425 - 480 nm, 500 – 570 nm and 656 - 794 nm, respectively) were used. Image acquisition was optimized

according to cell diameter and Gag-eGFP intensity was adjusted below saturation, which was more intense in the case of baculovirus infected insect cells. High-speed 3D time-lapses were recorded by the high-speed acquisition mode (resonant) with images taken every 9 - 13 s per *xyz*. Two time-lapses per cell system of  $5 \pm 2$  min average were conducted. HyVolution2 deconvolution was performed with SVI Huygens Professional software using the high-speed imaging strategy (Scientific Volume Imaging, Hilversum, The Netherlands), which increased the greyscale from 8 to 16-bit and improved the resolution by 2-fold with  $40 \pm 5$  nm in *xy* pixel size after deconvolution. Cell volumes of 20 - 30 *z* sections per image with one producing cell per field were analyzed.

HIV-1 Gag-eGFP VLP preparations were analyzed in the same conditions with 100 X magnification (zoom 5), 496 x 496 – 633 Hz and a line average of 3. To this purpose, the intensities of 405 and 633 nm lasers and HyD detector gains were increased. 5-field sections of 13 *z* in harvested HIV-1 Gag-eGFP VLP supernatants and 3-field for the corresponding non-transfected/infected conditions were studied in triplicate conditions. HyVolution2 deconvolution was performed with SVI Huygens Professional program using the best resolution strategy (Scientific Volume Imaging).

### **2.5. Quantitative imaging analyses**

FWHM (Full Width at Half Maximum) measurements and histograms in 2D-images were performed with LAS X 3.1.5.16308 (Leica Microsystems). Regions of Interest (ROI) were used to analyze VLP assembly sites (threshold 50, width 3). Oversaturated and out-of-focus planes were removed from deconvolved raw data images. 3D imaging reconstructions of Gag-eGFP producing cells and Gag-eGFP VLPs were performed with the 3D module package in Imaris 8.2.1 (Bitplane, Oxford Instruments, Zurich, Switzerland) at Servei de Microscòpia from Institut de Neurociències (Universitat Autònoma de Barcelona, Barcelona, Spain).

#### **2.5.1. Cell membrane surface area**

Cell membrane surface was defined as the outer contour of the cell membrane in deconvolved images corrected by a membrane thickness factor. Cell surface area analysis is presented in Supplementary Materials S1 and was calculated according to Equation 1:

$$\begin{aligned} & \textit{Cell surface area} (\mu\text{m}^2) \\ &= (\textit{Outer surface area} (\mu\text{m}^2)) \cdot (1 - \textit{Membrane thickness factor}) \quad (1) \end{aligned}$$

The outer surface area was obtained as the difference between the total surface area and the inner surface area (Supplementary Materials S1). Total surface area was calculated by cell membrane 3D reconstruction with the Surface module package of the Imaris software. The mask threshold was manually adjusted in the range of 3.000 to 9.000 arbitrary units (a.u.) for each cell line and extracellular membrane fragments were also removed for further surface analysis. The inner surface area was calculated from the spherical segment equation given by:

$$\textit{Inner surface area} (\mu\text{m}^2) = 2 \cdot \pi \cdot R \cdot (\mu\text{m}) \cdot h \quad (2)$$

where  $R$  is the inner radius of the cell and  $h$  is the height of the segment. Cell diameter and segment height were measured with the LAS X software (Leica Microsystems) and the data is presented in Supplementary Materials S1. A minimum outer cell membrane surface area of  $1000 \mu\text{m}^2$  was analyzed in each cell system. Surface area was corrected by the membrane thickness factor according to Equation 3:

$$\begin{aligned} & \textit{Membrane thickness factor} (\%) \\ &= \frac{(4 \cdot \pi \cdot R^2) - (4 \cdot \pi \cdot (R - (\textit{membrane thickness}))^2)}{(4 \cdot \pi \cdot R^2)} \cdot 100 \quad (3) \end{aligned}$$

where  $R$  is the radius of the cell, and the cell membrane thickness was defined as  $0.5 \mu\text{m}$  according to previous image analyses.

### 2.5.2. Gag-eGFP membrane colocalization studies

The 3D mask function of the Imaris software was applied to assess the percentage of cell membrane volume that colocalized with Gag-eGFP polyprotein (%). This value was calculated as follows:

*Percentage of colocalized membrane (%)*

$$= \frac{\text{Gag - eGFP positive membrane volume } (\mu\text{m}^3)}{\text{total membrane volume } (\mu\text{m}^3)} \cdot 100 (\%) \quad (4)$$

Briefly, unprocessed Gag-eGFP colocalized membrane signal was obtained based on the colocalization of cleaned cell membrane signal and Gag-eGFP raw signal with the colocalization module of Imaris (Supplementary Materials S2). The colocalization threshold was set at 3000 a.u. in both channels. Cleaned cell membrane signal was obtained by cell membrane 3D reconstruction, as previously described. Gag-eGFP volume was calculated by 3D reconstruction conducted with the Surface module of Imaris.

### **2.5.3. VLP assembly sites analysis**

HIV-1 Gag-eGFP VLP assembly sites per membrane area were obtained using the spot function of Imaris. Positive spots with a diameter of 0.5  $\mu\text{m}$  were identified ( $z$  diameter of 1  $\mu\text{m}$ ; spot region type by local contrast; region growing diameter from the border). Specific quality and threshold were adjusted manually for each channel and sample and false positive spots were manually removed prior to quantification. Concentration of VLP assembly sites per membrane area, *i.e.* the percentage of membrane volume that is occupied by VLP assembly sites (Equation 5), and the ratio between VLP assembly site volume and the colocalized membrane from Equation 4 were calculated.

$$\begin{aligned} & \textit{Percentage of assembly sites colocalized membrane} (\%) \\ & = \frac{\textit{Assembly sites volume } (\mu\text{m}^3)}{\textit{total membrane volume } (\mu\text{m}^3)} \cdot 100 (\%) \quad (5) \end{aligned}$$

### **2.5.4. Calculation of VLP assembly sites per cell**

Theoretical calculations of HIV-1 Gag-eGFP VLP assembly sites per cell were made under the assumption of cells as spherical bodies. Average VLP assembly sites per inner surface area were used. Average cell diameters were obtained using the NucleoCounter®NC-3000 automated cell counter (Chemometec, Allerod, Denmark) at 24 hpt or hpi for negative controls, and at 48 hpt or 40 hpi for HIV-1 Gag VLP productions. Alternatively, average cell diameters were measured

---

from HyVolution2 SRFM images when values were out of range in the NucleoCounter®NC-3000 (>20µm).

## **2.6. Analysis and quantification of nanoparticles**

Nanoparticles were measured in harvested supernatants using the spot function (Supplementary Materials S4.A). Direct SRFM Gag-eGFP VLP concentration, named as SRFM-upper limit, was calculated based on the division of the green particle number by 3D image volume. Briefly, SRFM-upper limit quantification was performed on deposited HIV-1 Gag-eGFP VLP samples with 23 x 23 x 3 µm in *xyz* 3D image from a total loaded volume of 50 µL distributed in 24 x 60 mm under the cover glass with a total height of 34 µm. Assuming complete sample deposition, minimum concentration of Gag-eGFP VLPs was also calculated and defined as the SRFM-low limit (Supplementary Materials S4.B). 2 by 2 spot colocalization between these channels was also studied with the 2 by 2 colocalization spot algorithm of Imaris.

## **2.7. Flow Cytometry**

The percentage of Gag-eGFP producing cells (GFP-positive cells) was assessed using a BD FACS Canto II flow cytometer (BD Biosciences) with a two-laser configuration (488 and 635 nm). The 488 nm laser was used for GFP-measurement in the FITC-A detector. A total of 20000 events were analyzed in every sample. First, SSC-H vs FSC-A and FSC-A vs FSC-H density plots were used to gate the individual cell population. Then, the GFP-positive population was assessed in a GFP FITC-A vs APC-A density plot and in a GFP FITC-A histogram. Gating was manually adjusted for each channel with multiple fluorescence intensity values comprised between 0.5 and  $1 \cdot 10^3$  a.u. Data were analyzed with the FACS DIVA software (BD Biosciences).

## **2.8. Nanoparticle Tracking Analysis (NTA)**

NTA was used as the reference technique to quantify the concentration of nanoparticles. A NanoSight® NS300 device (Malvern Panalytical, Malvern, United Kingdom) equipped with a blue laser module (488 nm) for Gag-eGFP VLP quantification, and a neutral density filter for total nanoparticle measurement using light diffraction. Non-fluorescent particles were calculated by subtracting GFP-fluorescent particles to total particles in each sample. The measurements were

performed at Service of Preparation and Characterization of Soft Materials (Institut de Ciència de Materials de Barcelona, ICMAB, Cerdanyola del Vallès, Spain). Data were analyzed with the NanoSight® NTA 3.2 software (Malvern Panalytical) and the camera level and detection threshold were manually adjusted for each sample. Prior to injection in the device chamber, samples were diluted to a final volume of 1 mL with a nanoparticle concentration around  $10^8$  particles/mL. All measurements were performed in triplicate and normalized by an internal control consisting of HIV-1 Gag-eGFP VLPs.

### 2.9. Gag-eGFP quantification

Quantification of Gag-eGFP concentration in sample supernatants and pelleted cells was assessed using an *in-house* spectrofluorometric assay [40]. Pelleted cells were prepared as previously described [41]. Briefly, they were subjected to three freeze-thaw cycles (2.5 h frozen at  $-20$  °C and thawed at  $37$  °C for 0.5 h). Samples were vortexed for 5 s between cycles. Lysed pellets were resuspended in 0.5 mL of TMS buffer (50 mM Tris-HCl, 150 mM NaCl, 2 mM MgCl<sub>2</sub>, pH 8.0) and centrifuged at  $13700 \times g$  during 20 min. Green fluorescence was measured at room temperature using a Cary Eclipse Fluorescence Spectrophotometer (Agilent Technologies, Santa Clara, CA, USA) set as follows:  $\lambda_{ex}$  = 488 nm (slit 5 nm),  $\lambda_{em}$  = 510 nm (slit 10 nm). Relative fluorescence units (RFU) were calculated by subtracting fluorescence units (FU) values from non-transfected/infected samples. There is a linear correlation between fluorescence intensity and p24 values determined by HIV INNOTEST ELISA (Innogenetics NV, Gent, Belgium). Therefore, RFU values can be converted to Gag-eGFP concentration values with the following equation:

$$Gag - eGFP \left( \frac{ng}{mL} \right) = 3,245 \cdot RFU - 1,6833 \cdot 36 \quad (6)$$

where Gag-eGFP is the estimated concentration of polyprotein and RFU is the measured GFP fluorescence intensity in the samples. RFU values were normalized with a 0.1 mg/mL quinine sulphate solution as internal control.

### 2.10. Transmission Electron Microscopy

Gag-eGFP VLP samples were prepared using the air-dried negative staining method. Briefly, 8  $\mu$ L of sample were placed on carbon-coated copper or holly carbon 200 mesh grids and incubated

---

at room temperature for 1 min. Excess sample was carefully drained off the grid with the aid of filter paper. Samples were negatively stained with 8  $\mu\text{L}$  of 2 % uranyl acetate for 1 min at room temperature. Excess stain was drained off as mentioned, and grids were maintained in dry conditions until analysis. Grids were previously glow discharged in a PELCO easiGlow™ glow discharger unit (PELCO, Fresno, CA, USA). Sample visualization was performed in a JEM-1400 transmission electron microscope (JEOL, Pleasanton, CA, USA) equipped with an ES1000W Erlangshen charge-coupled device camera (Gatan, Pleasanton, CA, USA).

### 3. Results and discussion

#### 3.1. Study of VLP budding using HyVolution2 SRFM

The application of HyVolution2 to assess the VLP budding process *in vivo* resulted in a significant improvement compared to standard confocal laser scanning microscopy (CLSM), as demonstrated in Figure 2. Three biological platforms, including HEK 293-transient gene expression (TGE) (Figure 2A), High Five-baculovirus expression vector system (BEVS) (Figure 2B) and Sf9-BEVS (Figure 2C) were evaluated with this technique. Upon expression, the Gag-eGFP polyprotein was distributed throughout the cytoplasm in these platforms with higher Gag-eGFP intensities found for the insect cell/BEVS. Image treatment by deconvolution successfully removed the signal from non-assembled Gag-eGFP monomers, thus enhancing the visualization of nanometric clusters embedded in the lipid membrane (Figure 2A-C). These data differ from the generalized membrane colocalization concept previously reported by standard CLSM analyses [40,42,43], in agreement with current knowledge about the Gag VLP formation and release process, as described in Figure 1 [28].

Insights into cellular architecture of suspension-adapted cells, including the organization of genomic DNA, were clearly visualized. A singular nucleus morphology was observed in insect cells in the form of grained-like structures (Figure 2B-C), likely due to nuclear envelope fragmentation during baculovirus infection, as reported elsewhere [44]. Interestingly, VLPs were

detected in filopodia from the outer part of the cell membrane in the three systems (white arrow, Figure 2A-C). These filopodia were observed throughout the cell membrane with an approximate thickness of 0.3  $\mu\text{m}$  and finger-like structures, as described by Mattila and co-workers [45].

A decrease in VLP assembly site diameter was also observed after deconvolution by means of FWHM (Full Width at Half Maximum) measurements (Figure 2D.2). 64 VLP assembly sites were analyzed in HEK 293 cells (Figure 2D.1), resulting in more than 60 % of them with a FWHM value comprised between 220 and 330 nm (Figure 2D.3). Similar ranges were found in baculovirus infected insect cells (data not shown). Typically, the diameter of Gag assembly clusters is in the range of 100 - 200 nm [28]. These larger clusters have also been described as late VLP assembly sites where the budding of multiple VLPs can occur [28,46]. In this respect, it should be considered that the fluorescence volume does not necessarily correlate with the real particle size since it can be overestimated due to the high Gag-eGFP intensity [47]. Individual VLP assembly sites were successfully distinguished using HyVolution2 in the three transfected/infected cell lines. VLP tracking from cell membrane to the extracellular space was also examined using HyVolution2 coupled to the high-speed acquisition mode (Figure 2E.1-1-3A). Surprisingly, the majority of VLPs analyzed remained in the VLP assembly sites during the 3D time-lapses recorded for  $5 \pm 2$  min in average (data not shown). Altogether, these data evidence that particle assembly in the form of VLPs is a slow intracellular step during budding as previously described by Manley and co-authors [46].

Overall, the combination of HyVolution2 and SRFM improved sample resolution by 2-fold in living cells compared to standard CLSM. Deconvolution was simultaneously applied to the three channels considered, Gag-eGFP (green), cell membrane (red) and cell nucleus (blue), in large 3D images with  $30 \mu\text{m} \times 30 \mu\text{m} \times 4 \mu\text{m}$  physical length in average. Using the high-speed capture mode, image acquisition speed could be reduced to less than one second per frame considering the three channels simultaneously. This configuration was applied to each cell line by simply tailoring the acquisition parameters. Despite better acquisition speeds and higher resolutions have been separately reported for SRFM [28], no efficient balance between them has been achieved in



2D and 3D multiple color imaging studies *in vivo*. The approach here presented offers a good compromise between acquisition speed and resolution to study nanoparticle membrane phenomena in living cells.

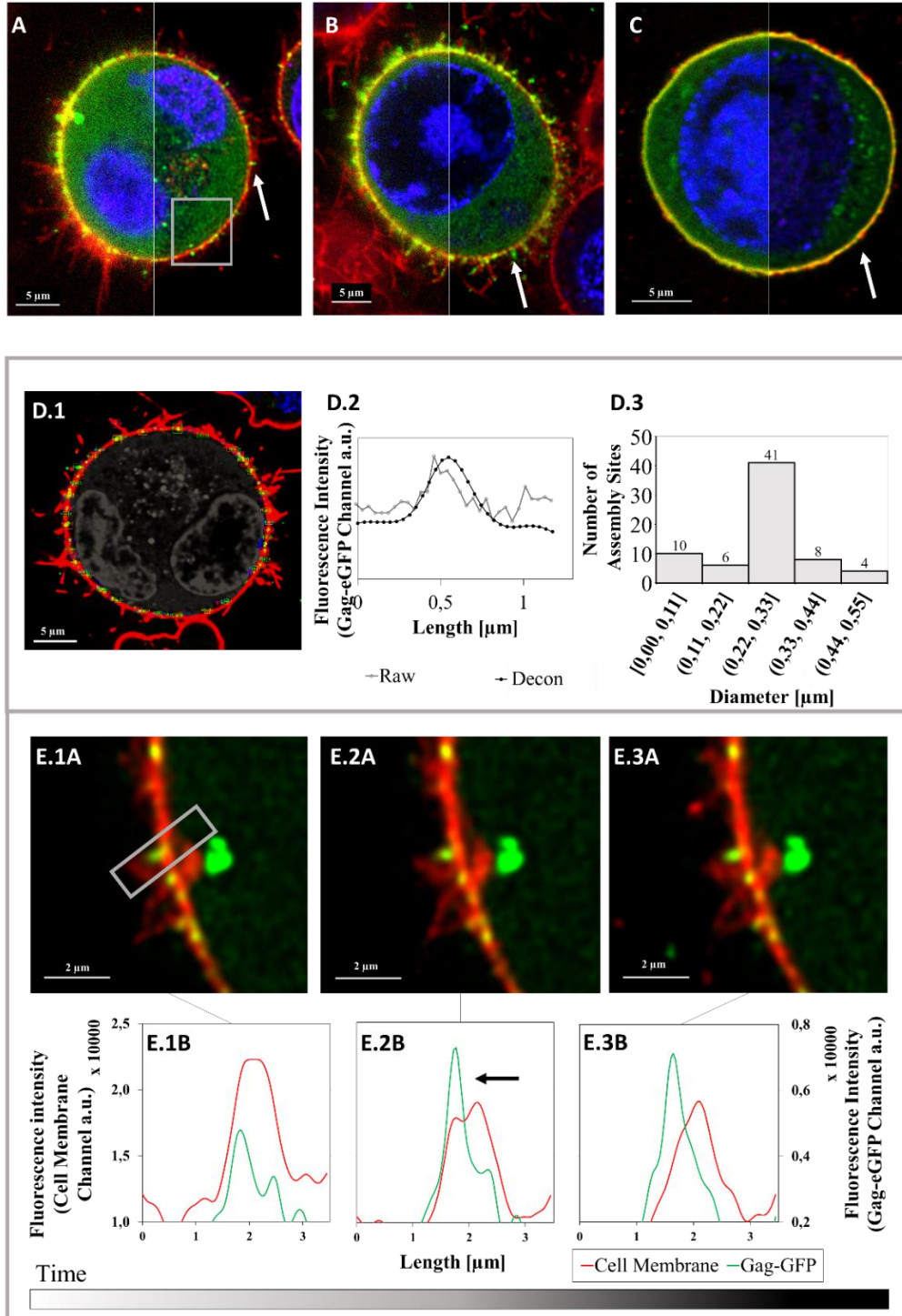


Figure 2. Analysis of live VLP budding process by HyVolution2 SRFM. (A) Transfected HEK 293 cells at 48 hpt, (B) baculovirus infected High Five (Hi5) and (C) Sf9 cells at 40 hpi; (A-C, half-left) unprocessed images and (A-C, half-right) deconvolved images. (D) Representative FWHM analysis of VLP assembly sites in a producing cell; (D.1) Cell membrane analyzed with the different ROIs; (D.2) histogram comparison of an unprocessed VLP assembly site (Raw)

and deconvolved (Decon); (D.3) histogram of the different VLP assembly sites analyzed in each ROI from D.1. (E1A-3A) VLP budding time-lapse using the high-speed capture mode and HyVolution2. (E1B-3B) Cell membrane histogram during the VLP budding process. White arrows indicate individual VLPs.

### 3.2. Quantification of VLP budding in living cells

Considering the advantages offered by HyVolution2, a novel method to measure the concentration and distribution of VLP assembly sites was developed (Supplementary Materials S1 & 2). To this purpose, 3D images of individual transfected/infected living cells acquired by HyVolution2 SRFM were used (Figure 3A). Two different contours were initially described in the cell surface: the outer one, comprising the cell filopodia and the cell lipid bilayer, and the inner membrane, representing the sphere-like lipid bilayer. Although the lipid bilayer has a reported thickness of approximately 30 Å [48], cell membrane averaged 0.5 µm after CellMask™ staining, as shown in other studies conducted with CLSM [6]. Here, cell surface calculation was based on the outer surface area and corrected with a membrane thickness factor to ensure a more realistic representation of VLP formation (see Materials and Methods and Supplementary Materials S1). From these 3D reconstructions, the percentage of VLP assembly sites per colocalized membrane and their concentration per cell surface area were calculated (Figure 3C). The image treatment analysis workflow is presented in Supplementary Materials S2.

The percentage of colocalized membrane was significantly different in each system (Figure 3B). In the case of HEK 293 cells,  $13 \pm 7$  % of the cell membrane was associated with Gag-eGFP at 48 hpt, suggesting that only a small percentage of the cell membrane is participating in the budding process. These results open a window of opportunity to increase VLP production by means of TGE in HEK 293 cells. In contrast, a significantly higher colocalization was observed in baculovirus infected cells, with  $66 \pm 17$  and 100 % of the cell membrane colocalizing in High Five and Sf9 cells at 40 hpi, respectively. The differences in terms of production between TGE in HEK 293 cells and the BEVS could be very much appreciated here. Indeed, the membrane of baculovirus infected cells was oversaturated with Gag-eGFP even with a reduction of the laser gain compared to transfected HEK 293 cells (Figure 3B). The quantification of VLP assembly

---

sites revealed that Sf9 and High Five cells were the most productive platforms (Figure 3C). Transfected HEK 293 cells displayed  $0.2 \pm 0.0$  VLP assembly sites/ $\mu\text{m}^2$  of cell membrane, whereas infected Sf9 and High Five cells presented  $0.6 \pm 0.1$  and  $0.6 \pm 0.2$  VLP assembly sites/ $\mu\text{m}^2$ , respectively. However, the number of VLP assembly sites could be underestimated in insect cells due to cell membrane Gag-eGFP oversaturation, as revealed when comparing the ratio between the percentage of VLP assembly sites and the percentage of colocalizing membrane volumes of the three systems (Figure 3B). The size of VLP assembly sites was also analyzed (Figure 3D), with sizes ranging from 0.01 to  $0.08 \mu\text{m}^3$  in the three platforms.

According to these results,  $518 \pm 164$ ,  $3045 \pm 1733$  and  $1682 \pm 716$  VLP assembly sites per cell were calculated for transfected HEK 293 cells and baculovirus infected High Five cells and Sf9, respectively (Supplementary Materials S3). Compared to non-transfected/infected conditions, a remarkable increase of  $61 \pm 35$  % in cell size was observed in High Five cells upon infection. The increase was less pronounced in infected Sf9 cells ( $45 \pm 19$  %) and neglectable in transfected HEK 293 cells (Supplementary Materials S3). Of note, a higher surface area represents an advantage for VLP formation since there is an increase in the availability of cell membrane to generate VLP assembly sites, as shown for High Five cells.

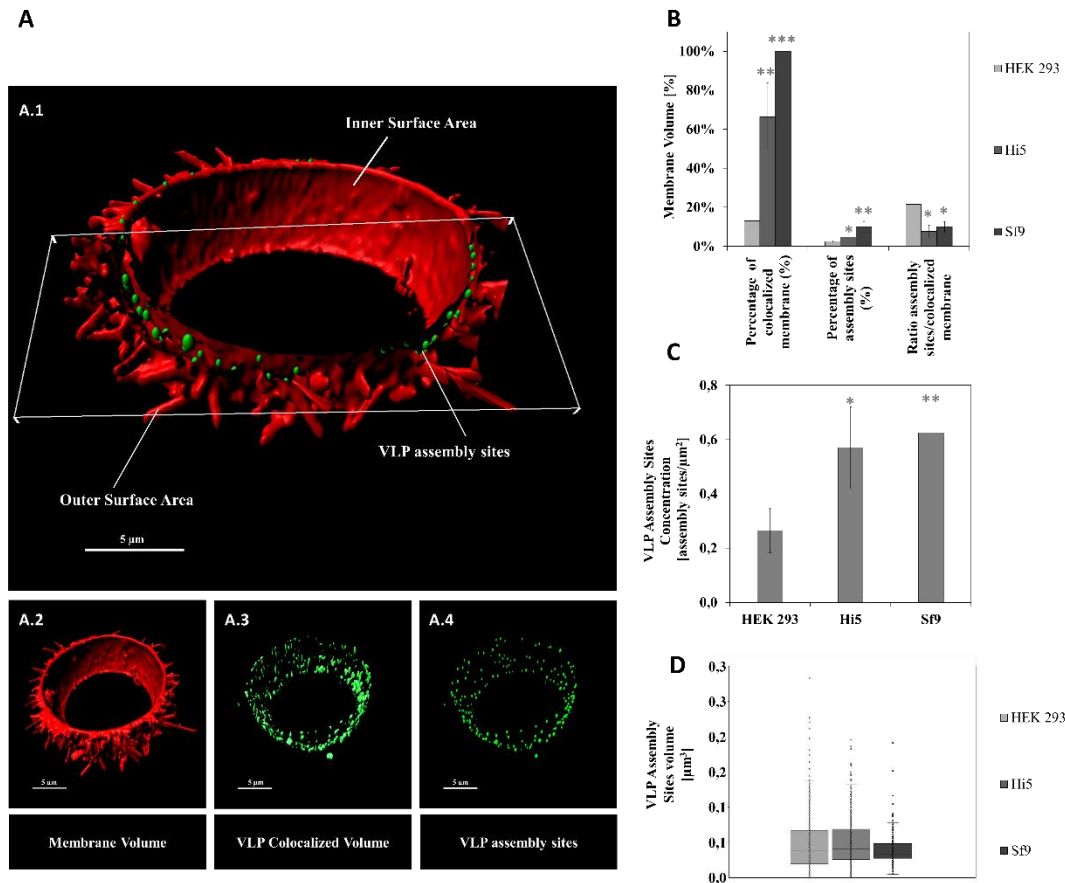


**Figure 3. Quantitative comparison of the VLP budding process in transfected HEK 293 and baculovirus infected High Five (Hi5) and Sf9 cells by 3D imaging. (A) 3D reconstruction of a VLP producing cell. (A.1) Detection of VLP assembly sites in the cell membrane, (A.2) 3D reconstruction of the cell membrane, (A.3) VLP/cell membrane colocalization (A.4) and individual VLP assembly sites. (B) Analysis of cell membrane colocalization. (C) Concentration of VLP assembly sites per membrane surface area. (D) Box and Whiskers plot of the VLP assembly sites diameter distribution. Statistical analyses were performed using the student's t-test using transfected HEK 293 cells as the reference condition: \*p-value <0.05, \*\* p-value<0.01, \*\*\*p-value <0.001. Mean values  $\pm$  standard deviation of triplicate experiments are represented.**

### 3.3. Comparison of VLP production in animal cell lines

Several orthogonal techniques were used in combination to HyVolution2 SRFM to gain additional information in the characterization of these production systems (Figure 4). Cell culture integrity was preserved with viabilities above the 70 % at harvest time (72 hpt and 40 hpi for mammalian and insect cells, respectively). Cell growth in non-transfected/infected cultures were also included

for comparison (grey line, Figure 4A). Flow cytometry analysis of the percentage of producing cells revealed that  $74 \pm 1$  % of HEK 293 cells was transfected at 72 hpt, whereas almost all insect cells were infected at 40 hpi (Figure 4A-C).

Nanoparticle volumetric production and specific cell productivity were calculated for each animal cell line using nanoparticle tracking analysis (NTA). The whole nanoparticle content in the harvested supernatants was quantified using the NTA diffraction filter and compared to the number of fluorescent nanoparticles (HIV-1 Gag-eGFP VLPs) measured with the NTA fluorescence channel. The insect cell/BEVS presented more than 2-fold VLP specific productivity than the mammalian cell/TGE system, specifically  $23 \pm 3$ ,  $67 \pm 17$  and  $77 \pm 17$  HIV-1 Gag-eGFP VLP/producing cell·h in HEK 293, High Five and Sf9 cells, respectively. Significant amounts of contaminant nanoparticles were calculated in all platforms, estimated as the difference between scattered light (total nanoparticles) and fluorescent emitting particles (HIV-1 Gag-eGFP VLPs) (Figure 4D-E). Infected High Five cells exhibited the highest overall nanoparticle production, more than 2-fold compared to infected Sf9 and transfected HEK 293 cells. Hence, it should be noted that the different animal cell lines have a basal EV production, which may hinder VLP purity, especially for High Five cells (Figure 4D). Also, particle-like contaminants are more critical when the target product is a viral vector or a nanoparticle. This is even worse when EVs and the nanoparticle of interest share similar properties, encompassing surface charge, size, origin or biochemical composition [15,49]. Thus, these critical quality attributes (CQA) have to be carefully considered in the production of nanoparticle-based biologicals in animal cells, such as the VLPs addressed in this work.

Gag-eGFP polyprotein production in the supernatant and intracellularly (cell pellet) at harvest time was measured by means of fluorimetry (Figure 4F). Infected Sf9 and High Five cells were 41 and 100-fold more productive than transfected HEK 293 cells in terms of Gag-eGFP polyprotein at intracellular level. These results are in agreement with SRFM analyses of infected insect cell lines, where cell membranes were oversaturated with Gag-eGFP. While an adequate correlation of fluorescence in the supernatant with VLP concentrations measured by NTA was

obtained in transfected HEK 293 and baculovirus infected Sf9 cells, there was no efficient correlation in High Five cell supernatants. Assuming that a VLP contains 2000 – 2500 Gag monomers in average [50], the results here presented suggest that only  $2 \pm 0.4$  % of the Gag produced is assembled in the form of VLPs in High Five cells, revealing the existence of important amounts of non-assembled Gag particles in this system compared to HEK 293 ( $72 \pm 9$  %) and Sf9 ( $55 \pm 7$  %) cells, as recently reported in a previous work [51].

The combination of the results shown in previous sections enabled to define a complete picture of each production platform under study. VLP assembly sites in baculovirus infected insect cells and in transfected HEK 293 cells presented an average of 1.6 to  $14.8 \cdot 10^9$  VLP assembly sites/mL at harvest time (Supplementary Materials S3). In this context, the ratio between budded VLPs and assembly sites was  $4 \pm 2$ ,  $2 \pm 1$  and  $2 \pm 1$  VLP/assembly site in HEK 293, Hi5 and Sf9, respectively. These data arise two different hypotheses: either more than one VLP can bud from each assembly site, or that VLP assembly sites are regenerated, thus supporting the presence of late VLP assembly sites as previously suggested (Figure 2). Additional SRFM studies of individual cells at different times post infection/transfection could shed more light on this matter. In parallel, baculovirus infected insect cell lines showed the highest VLP productivity. Among them, Sf9 cells demonstrated a better compromise between total VLP production and contaminant nanoparticles [52]. High Five cells attained similar VLP levels as those produced by Sf9 cells but non-assembled Gag-eGFP monomers and contaminant particles reached their maximum in the former. Transiently transfected HEK 293 cells showed the lowest VLP productivity but this system offered the best balance between VLPs, contaminant particles and non-assembled Gag-eGFP monomer, which is of special relevance in terms of product quality (Figure 4).

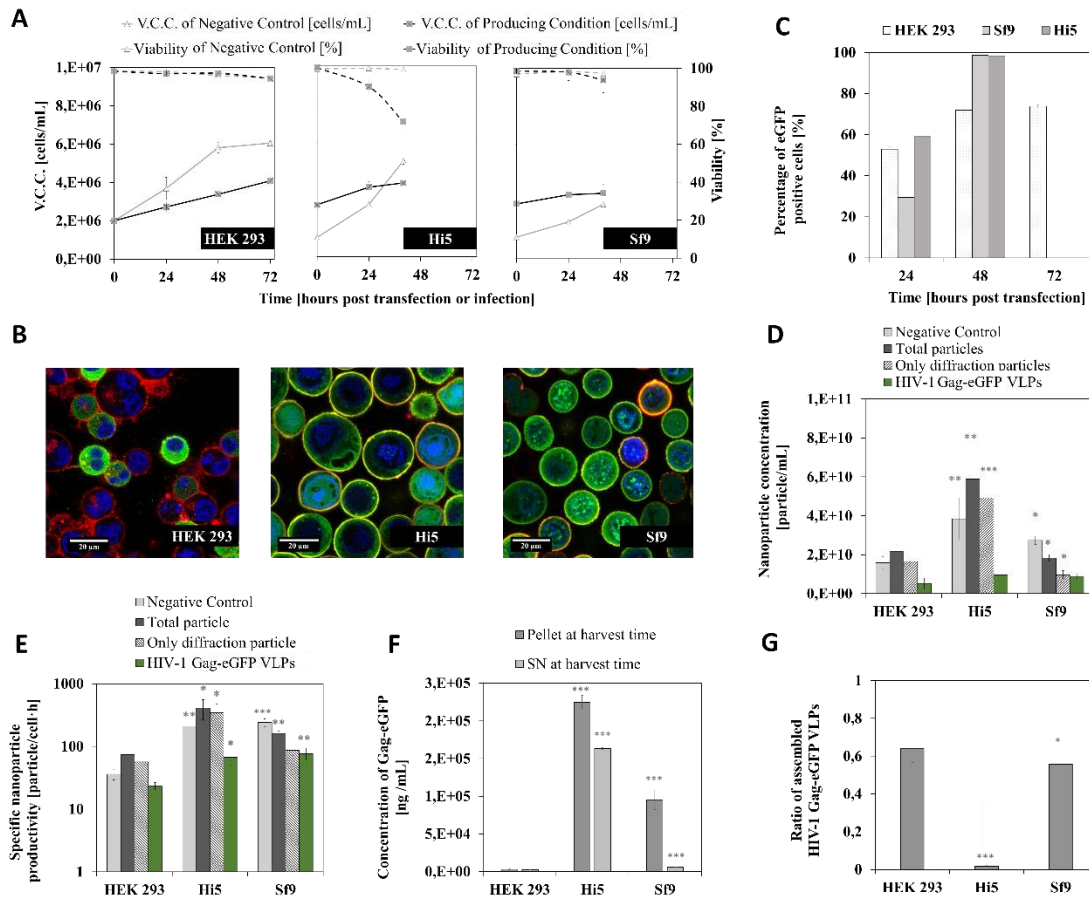


**Figure 4. Quantification and comparison of VLP production in the different systems: transfected HEK 293 and baculovirus infected High Five (Hi5) and Sf9 cells. (A) Viable cell concentration (V.C.C.) and viability of transfected/infected cells (producing condition) and non-transfected/infected conditions (negative controls). (B) CLSM of transfected and infected cells at 48 hpt or 40 hpi, respectively. (C) Percentage of producing cells analyzed using flow cytometry. (D) Quantification of total nanoparticle and HIV-1 Gag-eGFP VLPs by NTA in the 0 – 1000 nm range. (E) Quantification of specific nanoparticle productivity by NTA. (F) Quantification of the Gag-eGFP concentration in SN and pellet. (G) Ratio of assembled HIV-1 Gag VLPs in the different platforms. Statistical analyses were performed using student's t-test compared to the HEK 293 cells condition: \*p-value <0.05, \*\* p-value<0.01, \*\*\*p-value <0.001. Mean values  $\pm$  standard deviation of triplicate experiments are represented.**

### 3.4. Quality assessment of VLP production

The combination of HyVolution2 SRFM and 3D imaging was successfully applied to directly characterize and quantify VLPs and co-produced nanoparticles in harvested supernatants (Figure 5). Common staining procedures used for CLSM at micrometric scale were successfully translated to the nanoscale, notably simplifying sample preparation for visualization [6]. The aim to stain nanoparticles in harvested supernatants centered toward studying the presence of nucleic acids within VLPs/EVs (blue, Hoechst), as well as identifying their lipid membrane (red, CellMask™). After staining, preparations were incubated for 30 min at room temperature and directly visualized under the confocal microscope. The green fluorescence signal corresponding to Gag-eGFP VLPs was clearly observed without deconvolution, but a better resolution was achieved after this treatment (Figure 5A). The background levels detected in the red and blue channels were remarkable since washing steps were avoided to simplify sample preparation. Thus, the detection of the lipid membrane and nucleic acid in nanoparticles was clearly improved upon deconvolution, mainly due to background signal removal. Similar features were observed for both dyes in non-transfected/infected conditions.

Relative quantifications of the nanoparticles in SRFM images are presented in Figure 5B. The amount of VLPs, CellMask™ positive particles and Hoechst positive particles are depicted in the bar chart, while the colocalization ratio of VLPs with each dye is observed in the line chart for the three systems. Of note, VLPs were better resolved than CellMask™ and Hoechst positive nanoparticles probably due to a loss of sensitivity caused by the high background signal. A significant percentage of nanoparticles and VLPs contained nucleic acids in transfected HEK 293 cell productions, probably due to plasmid DNA addition required for TGE [53,54]. Consequently, double positive colocalization of Gag-eGFP with CellMask™ and Hoechst was more frequently detected in the HEK 293/TGE system (Figure 5B). On the other hand, nanoparticles produced in both infected insect cell lines showed larger CellMask™ positive particles, which could be caused by the presence of baculoviruses and the aggregation of lipophilic structures (Figure 5A). Regulatory agencies established a limit of 10 ng of dsDNA and 100 ppm of HCP per dose in the

---



final biological product [55,56]. However, in the case of viruses and virus-like structures, part of these contaminants could be incorporated into the viral structure [57,58]. The presence of host-cell nucleic acids such as RNA or DNA is of general concern in the VLP field. The existence of RNA in retrovirus-like particles was described by Shiba and co-workers in the 80's in naturally produced VLPs from *Drosophila Melanogaster* [59]. In addition, recent proteomic analyses of HIV-1 Gag VLPs have identified histones associated with DNA co-purifying with VLPs [14,60]. Thereby, the quantification of those biomolecules in biological products is critical to delimit the safety levels of those impurities. This new and straightforward methodology could be of special interest in anticipating CQA determination, since the possibility to specifically stain nanoparticles has been demonstrated here. Of note, additional refinement of the staining method is still required to improve the sensitivity of the technique since lower nanoparticle concentrations were obtained in SRFM images compared to NTA results (Figure 4D and 5B).

A 3D surface reconstruction of VLPs was conducted using HyVolution2 SRFM and 3D imaging to determine the VLP size and morphology (Figure 6A). VLPs showed elongated structures due to the point spread function convolution effect in the  $z$  plane [33]. This phenomenon was substantially corrected by means of deconvolution, and a VLP diameter of around 250 nm was measured in the  $xy$  plane [28,61]. As for Transmission Electron Microscopy (TEM), VLPs were observed as electron-dense sphere-like structures surrounded by a bright corona (Figure 6B). In this case, VLP size was comprised in the 100 - 200 nm range, as described in a previous work [12]. However, TEM requires the use of contrast staining, which considerably alters the natural nanoparticle conformation. The SRFM approach represents a step forward since nanoparticles can be directly characterized in native conditions in an automatic, high-throughput and simple manner.

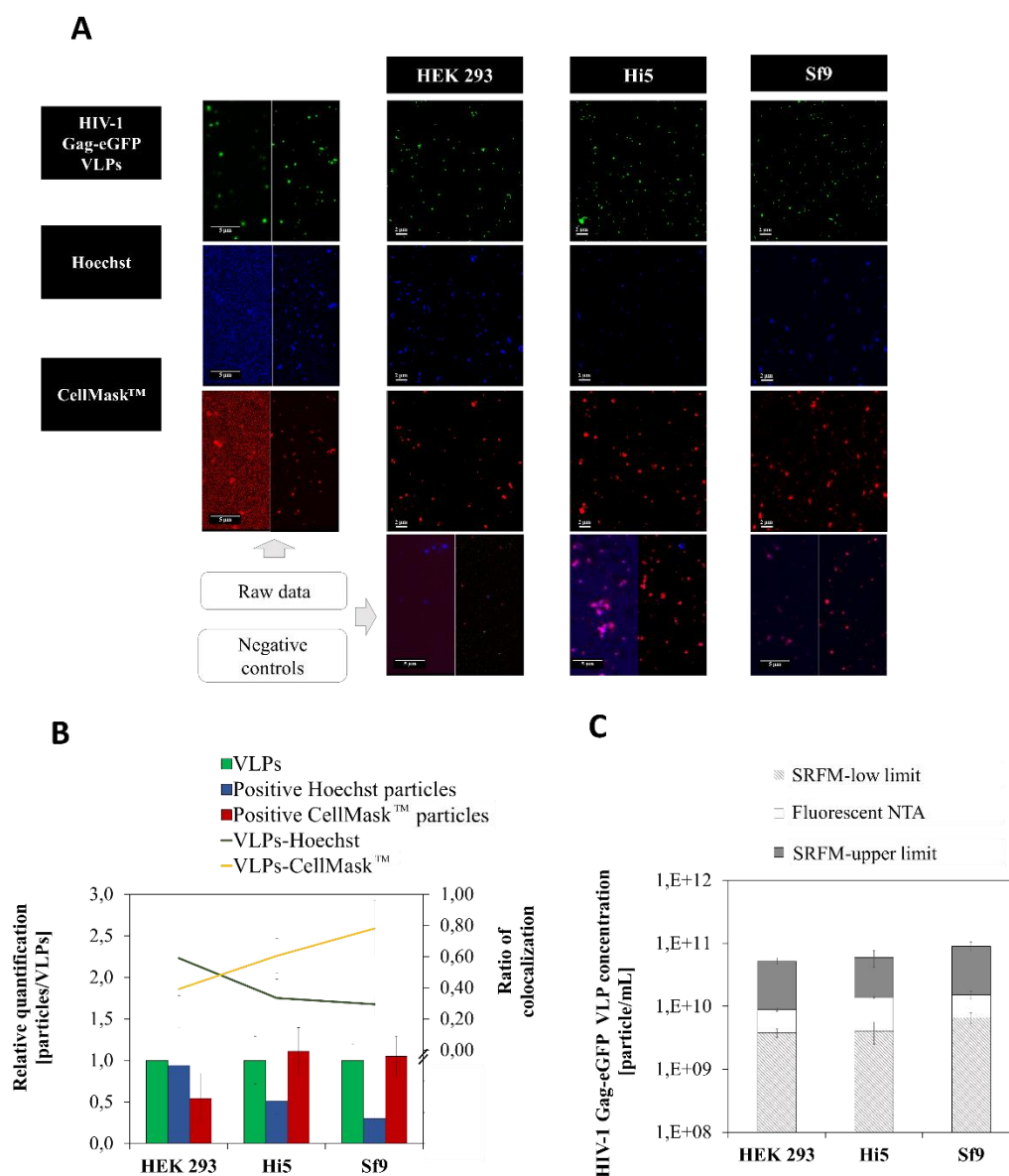


**Figure 5.** VLP quantification using HyVolution2 SRFM in transfected HEK 293 and baculovirus infected High Five (Hi5) and Sf9 cells. VLP preparations and negative controls were stained for nucleic acid (Hoechst) and cell membrane (CellMask™) detection. (A) Nanoparticle analysis diagram of the different samples. The first column shows the unprocessed images (half-left) and deconvolved and processed images (half-right) for each of the three channels, respectively. Representative 3D images of the VLPs obtained in each cell line are presented in the following columns. The same image processing procedure was used for negative controls in the last row, where the comparison of unprocessed images (half-left) and deconvolved images (half-right) is depicted, respectively. (B) Relative quantification of nucleic acid and cell membrane positive nanoparticles in comparison to VLP concentration (bar chart). Percentage of VLPs colocalizing with nucleic acid and cell membrane (line). (C) Comparison of VLP quantification by HyVolution2 SRFM and fluorescent-NTA. Upper and low VLP quantification limits by SRFM are shown. Mean values  $\pm$  standard deviation of triplicate experiments are represented.

### 3.5. VLP quantification using HyVolution2 SFRM

VLP concentrations in harvested supernatants were measured using the HyVolution2 SFRM and 3D imaging methodology. Although the visualization of HIV-1 virions with SFRM has been recently reported [28], nanoparticle quantification has been successfully achieved by light-based confocal microscopy in this work. This method is based on the quantification in a range determined by the minimum and maximum VLP concentration in the sample (Figure 5C, SFRM lower and upper limit, respectively). Results obtained showed that transiently transfected HEK 293 cells yielded  $0.4 - 4.3 \cdot 10^{10}$  VLP/mL at 72 hpt whereas baculovirus infected High Five and Sf9 cells achieved  $0.4 - 4.6 \cdot 10^{10}$  and  $0.7 - 7.5 \cdot 10^{10}$  VLP/mL at 40 hpi, respectively. A 1.6-fold increase in VLP production was attained in Sf9 cells compared to HEK 293 and High Five cells (Table 2). Refinement of the preparation protocol, such as the addition of washing steps to remove dye excess or support functionalization, could improve the precision of the method [62]. In Table 2, different methods used to quantify VLP productions are listed. Gutierrez-Granados et al. developed an approach to correlate the Gag-eGFP fluorescence signal to Gag-eGFP VLP concentration [40]. However, this technique cannot discriminate between assembled and non-assembled Gag-eGFP, which is critical as proven throughout this work. Light scattering NTA also introduces an overestimation factor since EVs, protein aggregates and other contaminant particles cannot be discriminated from VLPs [14,52]. At least 50 % of the total nanoparticles quantified in VLP productions were not VLPs and most of them fell in the same size range (Figure 4D). HPLC methods have also been applied for nanoparticle quantification [63,64]. Nevertheless, they require a labor-intensive fine-tuning depending on the type of nanoparticle to be analyzed. In the last years, flow virometry has gained increasing interest in the literature [8,52,65], with sensitivity levels comparable to PCR and 1000-fold higher than ELISA as recently reported for the detection of HIV-1 virions [66]. Although a promising approach, there is still a need for improvement since roughly a 10-fold nanoparticle underestimation compared to NTA or TEM is acknowledged [67]. Overall, the HyVolution2 SFRM offers a simple, less invasive strategy for nanoparticle

visualization in native conditions, which may complement the gold standard techniques used for nanoparticle characterization and quantification.

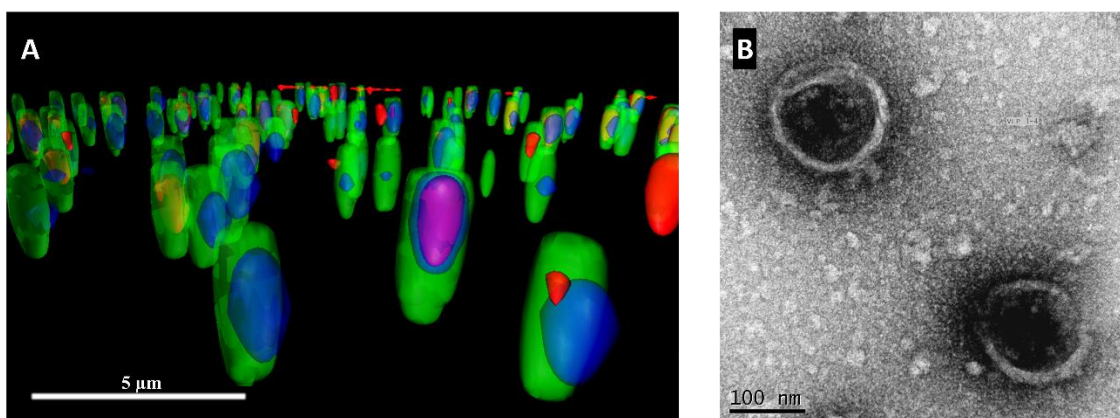


**Figure 6.** Characterization of harvested VLP supernatants from transfected HEK 293 cells. (A) Representative 3D image of VLPs stained with Hoechst and CellMask™. VLPs with triple colocalization could be detected in the sample (purple). 3D reconstructions were generated for each channel: Gag-eGFP in light-green, Hoechst in blue and CellMask™ in red, respectively. (B) Negatively stained VLP visualization by TEM.

#### 4. Conclusion

Novel tools aiming to deepen into living dynamic processes at nanometric scale are in the spotlight. In this work, the combination of HyVolution2 SRFM and 3D imaging is presented as a versatile approach to track nanoparticle production in living cells. This approach demonstrated a high sensitivity in visualizing the specific particularities of different production platforms and their associated contaminants. VLPs from harvested supernatants could be directly characterized and quantified using optical microscopy. The methodology here presented holds great potential of applicability in the field of virology and nanoparticle manufacturing toward accelerating process development and characterization.

**Table 2. Summary of VLP production quantification in clarified supernatants by different production platforms and methods.**

Type of virus or viral particle	Production system	VLP Particle Quantification ( $10^9/\text{mL}$ )	Methodology	Type of sample	Reference
<b>HIV-1 Gag-eGFP VLPs</b>	HEK 293-TGE	$5.0 \pm 0.5$	GFP Fluorescent-NTA	Supernatant	Present work
		4.0 – 43.0	HyVolution2 SRFM		
	High Five-BEVS	$9.6 \pm 0.4$	GFP Fluorescent-NTA	Supernatant	Present work
		4.1 – 45.7	HyVolution2 SRFM		
	Sf9-BEVS	$8.6 \pm 2.1$	GFP Fluorescent-NTA	Supernatant	Present work
		6.6 – 74.5	HyVolution2 SRFM		
<b>Influenza VLPs</b>	Sf9-BEVS	5.9	TEM	Supernatant analyzed after sucrose cushion	[13]
	HEK 293-BacMaM	0.2			
<b>HIV-1 Gag-eGFP VLPs</b>	HEK 293-EGE	63.6	Fluorimetry*	Supernatant	[9]
<b>HIV-1 Gag-eGFP VLPs</b>	CAP-T-TGE	58.0	Fluorimetry*	Supernatant	[43]
<b>HIV-1 Gag VLPs</b>	CHO-TGE	57.0 – 94.0	Light Scattering-NTA	0.8 $\mu\text{m}$ filtered supernatant	[14]
<b>Influenza VLPs</b>	High Five-BEVS	1.4-1.6	Light Scattering-NTA	Supernatant	[62]
		>1	Confocal Microscopy	Purified	
<b>Influenza VLPs (Gag-eGFP)</b>	HEK 293-S+TGE	0.7	Flow Cytometry	Supernatant	[8]

## **5. Acknowledgments**

The authors would like to thank Dr. Mònica Roldán for her implication in HyVolution2 SRFM analyses (Servei d'Anatomia Patològica, Hospital Sant Joan de Déu). The help of José Amable Bernabé (Institut de Ciència de Materials de Barcelona, CSIC, UAB Campus), Manuela Costa (Servei de Cultius Cel·lulars, Producció d'Anticossos i Citometria, UAB), Dr. Salvador Bartolomé (Laboratori de Luminescència i Espectroscòpia de Biomolècules, UAB), Marti de Cabo (Servei de Microscòpia, UAB), Saioa Mendizuri and Meritxell Roig (Institut of Neurociències, UAB) for the assistance with NTA, cytometry, fluorimetry, TEM and Imaris software analysis respectively, are also appreciated. Irene González-Domínguez (FPU16/02555) and Eduard Puente-Massaguer (FPU15/03577) are recipients of FPU grants from Ministerio de Educación, Cultura y Deporte of Spain. The research group is recognized as 2017 SGR 898 by Generalitat de Catalunya.

## 6. Literature

1. Charlton Hume, H.K.; Vidigal, J.; Carrondo, M.J.T.; Middelberg, A.P.J.; Roldão, A.; Lua, L.H.L. Synthetic biology for bioengineering virus-like particle vaccines. *Biotechnol. Bioeng.* **2019**, *116*, 919–935.
2. Cervera, L.; Gòdia, F.; Tarrés-Freixas, F.; Aguilar-Gurrieri, C.; Carrillo, J.; Blanco, J.; Gutiérrez-Granados, S. Production of HIV-1-based virus-like particles for vaccination: achievements and limits. *Appl. Microbiol. Biotechnol.* **2019**, *103*, 7367–7384.
3. Geeurickx, E.; Tulkens, J.; Dhondt, B.; Van Deun, J.; Lippens, L.; Vergauwen, G.; Heyrman, E.; De Sutter, D.; Gevaert, K.; Impens, F.; et al. The generation and use of recombinant extracellular vesicles as biological reference material. *Nat. Commun.* **2019**, *10*, 1–12.
4. Göttlinger, H.G. *HIV-1 Gag: a Molecular Machine Driving Viral Particle Assembly and Release*; Carla KuCarla Kuiken, BrianFoley, Thomas Leitner, Cristian Apetrei, Beatrice Hahn, Ilene Mizrachi, James Mullins, Andrew Rambaut, StevenWolinsky, and B.K. editors., Ed.; Los Alamos National Laboratory, Theoretical Biology andBiophysics: Los Alamos, New Mexico., 2001; ISBN 0269-9370.
5. Votteler, J.; Sundquist, W.I. Virus budding and the ESCRT pathway. *Cell Host Microbe* **2013**, *14*, 232–41.
6. Cervera, L.; González-Domínguez, I.; Segura, M.M.; Gòdia, F. Intracellular characterization of Gag VLP production by transient transfection of HEK 293 cells. *Biotechnol. Bioeng.* **2017**, *114*, 2507–2517.
7. Genzel, Y. Designing cell lines for viral vaccine production: Where do we stand? *Biotechnol. J.* **2015**, *10*, 728–740.
8. Venereo-Sanchez, A.; Simoneau, M.; Lanthier, S.; Chahal, P.; Bourget, L.; Ansoerge, S.; Gilbert, R.; Henry, O.; Kamen, A. Process intensification for high yield production of influenza H1N1 Gag virus-like particles using an inducible HEK-293 stable cell line.

- Vaccine* **2017**, *35*, 4220–4228.
9. Fuenmayor, J.; Cervera, L.; Gòdia, F.; Kamen, A. Extended gene expression for Gag VLP production achieved at bioreactor scale. *J. Chem. Technol. Biotechnol.* **2019**, *94*, 302–308.
  10. Cruz, P.E.; Cunha, A.; Peixoto, C.C.; Clemente, J.; Moreira, J.L.; Carrondo, M.J. Optimization of the production of virus-like particles in insect cells. *Biotechnol. Bioeng.* **1998**, *60*, 408–18.
  11. Wang, Q.; Bosch, B.-J.; Vlak, J.M.; van Oers, M.M.; Rottier, P.J.; van Lent, J.W.M. Budded baculovirus particle structure revisited. *J. Invertebr. Pathol.* **2016**, *134*, 15–22.
  12. González-Domínguez, I.; Gutiérrez-Granados, S.; Cervera, L.; Gòdia, F.; Domingo, N. Identification of HIV-1–Based Virus-like Particles by Multifrequency Atomic Force Microscopy. *Biophys. J.* **2016**, *111*, 1173–1179.
  13. Thompson, C.M.; Petiot, E.; Mullick, A.; Aucoin, M.G.; Henry, O.; Kamen, A.A. Critical assessment of influenza VLP production in Sf9 and HEK293 expression systems. *BMC Biotechnol.* **2015**, *15*, 1–12.
  14. Steppert, P.; Burgstaller, D.; Klausberger, M.; Berger, E.; Aguilar, P.P.; Schneider, T.A.; Kramberger, P.; Tover, A.; Nöbauer, K.; Razzazi-Fazeli, E.; et al. Purification of HIV-1 gag virus-like particles and separation of other extracellular particles. *J. Chromatogr. A* **2016**, *1455*, 93–101.
  15. Akers, J.C.; Gonda, D.; Kim, R.; Carter, B.S.; Chen, C.C. Biogenesis of extracellular vesicles (EV): exosomes, microvesicles, retrovirus-like vesicles, and apoptotic bodies. *J. Neurooncol.* **2013**, *113*, 1–11.
  16. Côté, J.; Garnier, A.; Massie, B.; Kamen, A. Serum-free production of recombinant proteins and adenoviral vectors by 293SF-3F6 cells. *Biotechnol. Bioeng.* **1998**, *59*, 567–575.
  17. Rhiel, M.; Mitchell-Logean, C.M.; Murhammer, D.W. Comparison of *Trichoplusia ni* BTI-Tn-5B1-4 (high five™) and *Spodoptera frugiperda* Sf-9 insect cell line metabolism in
-



- suspension cultures. *Biotechnol. Bioeng.* **1997**, *55*, 909–920.
18. Iatrou, K. Baculovirus expression vectors: A laboratory manual. *Cell* **1993**, *74*, 7–8.
  19. Cervera, L.; Gutiérrez-Granados, S.; Martínez, M.; Blanco, J.; Gòdia, F.; Segura, M.M. Generation of HIV-1 Gag VLPs by transient transfection of HEK 293 suspension cell cultures using an optimized animal-derived component free medium. *J. Biotechnol.* **2013**, *166*, 152–165.
  20. Pillay, S.; Meyers, A.; Williamson, A.L.; Rybicki, E.P. Optimization of chimeric HIV-1 virus-like particle production in a baculovirus-insect cell expression system. *Biotechnol. Prog.* **2009**, *25*, 1153–1160.
  21. Li, T.-C.; Scotti, P.D.; Miyamura, T.; Takeda, N. Latent infection of a new alphadnavirus in an insect cell line. *J. Virol.* **2007**, *81*, 10890–10896.
  22. Geisler, C.; Jarvis, D.L. Adventitious viruses in insect cell lines used for recombinant protein expression. *Protein Expr. Purif.* **2018**, *144*, 25–32.
  23. Ma, H.; Galvin, T.A.; Glasner, D.R.; Shaheduzzaman, S.; Khan, A.S. Identification of a novel rhabdovirus in *Spodoptera frugiperda* cell lines. *J. Virol.* **2014**, *88*, 6576–85.
  24. Manfredi, F.; Di Bonito, P.; Arenaccio, C.; Anticoli, S.; Federico, M. Incorporation of Heterologous Proteins in Engineered Exosomes. In *Methods in molecular biology* (Clifton, N.J.); 2016; Vol. 1448, pp. 249–260.
  25. Lua, L.H.L.; Connors, N.K.; Sainsbury, F.; Chuan, Y.P.; Wibowo, N.; Middelberg, A.P.J. Bioengineering virus-like particles as vaccines. *Biotechnol. Bioeng.* **2014**, *111*, 425–440.
  26. Jiang, W.; Tang, L. Atomic cryo-EM structures of viruses. *Curr. Opin. Struct. Biol.* **2017**, *46*, 122–129.
  27. de Pablo, P.J. Atomic force microscopy of virus shells. *Semin. Cell Dev. Biol.* **2018**, *73*, 199–208.
  28. Hanne, J.; Zila, V.; Heilemann, M.; Müller, B.; Kräusslich, H.-G. Super-resolved insights
-

- into human immunodeficiency virus biology. *FEBS Lett.* **2016**, *590*, 1858–1876.
29. Godin, A.G.; Lounis, B.; Cognet, L. Super-resolution Microscopy Approaches for Live Cell Imaging. *Biophysj* **2014**, *107*, 1777–1784.
30. Meng, B.; Lever, A.M. Wrapping up the bad news – HIV assembly and release. *Retrovirology* **2013**, *10*, 1–12.
31. Foster, T.L.; Pickering, S.; Neil, S.J.D. Inhibiting the Ins and Outs of HIV Replication: Cell-Intrinsic Antiretroviral Restrictions at the Plasma Membrane. *Front. Immunol.* **2018**, *8*, 1–20.
32. Chojnacki, J.; Eggeling, C. Super-resolution fluorescence microscopy studies of human immunodeficiency virus. *Retrovirology* **2018**, *15*, 1–16.
33. Sarder, P.; Nehorai, A. Deconvolution methods for 3-D fluorescence microscopy images. *IEEE Signal Process. Mag.* **2006**, *23*, 32–45.
34. Göttfert, F.; Wurm, C.A.; Mueller, V.; Berning, S.; Cordes, V.C.; Honigmann, A.; Hell, S.W. Coaligned Dual-Channel STED Nanoscopy and Molecular Diffusion Analysis at 20 nm Resolution. *Biophys. J.* **2013**, *105*, L01–L03.
35. Schermelleh, L.; Ferrand, A.; Huser, T.; Eggeling, C.; Sauer, M.; Biehlmaier, O.; Drummen, G.P.C. Super-resolution microscopy demystified. *Nat. Cell Biol.* **2019**, *21*, 72–84.
36. Borlinghaus, R.T.; Kappel, C. HyVolution—the smart path to confocal super-resolution. *Nat. Methods* **2016**, *13*, i–iii.
37. Hermida-Matsumoto, L.; Resh, M.D. Localization of human immunodeficiency virus type 1 Gag and Env at the plasma membrane by confocal imaging. *J. Virol.* **2000**, *74*, 8670–9.
38. Schwartz, S.; Campbell, M.; Nasioulas, G.; Harrison, J.; Felber, B.K.; Pavlakis, G.N. Mutational inactivation of an inhibitory sequence in human immunodeficiency virus type 1 results in Rev-independent gag expression. *J. Virol.* **1992**, *66*, 7176–82.

39. Segura, M.M.; Garnier, A.; Durocher, Y.; Coelho, H.; Kamen, A. Production of lentiviral vectors by large-scale transient transfection of suspension cultures and affinity chromatography purification. *Biotechnol. Bioeng.* **2007**, *98*, 789–799.
40. Gutiérrez-Granados, S.; Cervera, L.; Gòdia, F.; Carrillo, J.; Segura, M.M. Development and validation of a quantitation assay for fluorescently tagged HIV-1 virus-like particles. *J. Virol. Methods* **2013**, *193*, 85–95.
41. Puente-Massaguer, E.; Lecina, M.; Gòdia, F. Nanoscale characterization coupled to multi-parametric optimization of Hi5 cell transient gene expression. *Appl. Microbiol. Biotechnol.* **2018**, *102*, 10495–10510.
42. Longo, P.A.; Kavran, J.M.; Kim, M.-S.S.; Leahy, D.J. Transient mammalian cell transfection with polyethylenimine (PEI). *Methods Enzymol.* **2013**, *529*, 227–40.
43. Gutiérrez-Granados, S.; Cervera, L.; Segura, M. de L.M.; Wölfel, J.; Gòdia, F. Optimized production of HIV-1 virus-like particles by transient transfection in CAP-T cells. *Appl. Microbiol. Biotechnol.* **2016**, *100*, 3935–47.
44. Zhang, X.; Xu, K.; Wei, D.; Wu, W.; Yang, K.; Yuan, M. Baculovirus infection induces disruption of the nuclear lamina. *Sci. Rep.* **2017**, *7*, 1–11.
45. Mattila, P.K.; Lappalainen, P. Filopodia: Molecular architecture and cellular functions. *Nat. Rev. Mol. Cell Biol.* **2008**, *9*, 446–454.
46. Manley, S.; Gillette, J.M.; Patterson, G.H.; Shroff, H.; Hess, H.F.; Betzig, E.; Lippincott-Schwartz, J. High-density mapping of single-molecule trajectories with photoactivated localization microscopy. *Nat. Methods* **2008**, *5*, 155–157.
47. Ping-Jie Xiao, Chengwen Li, A.N. and R.J.S.; Xiao, P.J.; Li, C.; Neumann, A.; Samulski, R.J. Quantitative 3D tracing of gene-delivery viral vectors in human cells and animal tissues. *Mol. Ther.* **2012**, *20*, 317–328.
48. Xiong, Y.; Wang, T.; Wang, X.; Tong, P. Comment on “Anomalous Edge State in a Non-Hermitian Lattice.” *Annu. Rev. Biophys. Biomol. Struct.* **2016**, *36*, 107–130.

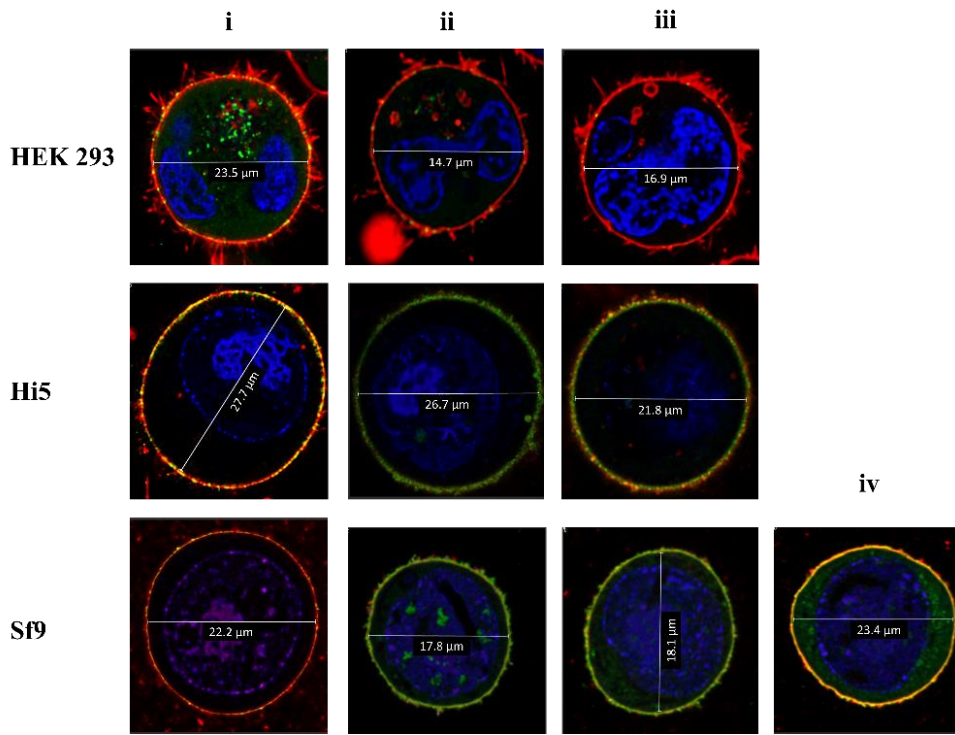
49. Michen, B.; Graule, T. Isoelectric points of viruses. *J. Appl. Microbiol.* **2010**, *109*, 388–397.
  50. Chen, Y.; Wu, B.; Musier-Forsyth, K.; Mansky, L.M.; Mueller, J.D. Fluorescence fluctuation spectroscopy on viral-like particles reveals variable Gag stoichiometry. *Biophys. J.* **2009**, *96*, 1961–1969.
  51. Puente-Massaguer, E.; Lecina, M.; Gòdia, F. Integrating nanoparticle quantification and statistical design of experiments for efficient HIV-1 virus-like particle production in High Five cells. *Appl. Microbiol. Biotechnol.* **2020**, *104*, 1569–1582.
  52. Puente-Massaguer, E.; Lecina, M.; Gòdia, F. Application of advanced quantification techniques in nanoparticle-based vaccine development with the Sf9 cell baculovirus expression system. *Vaccine* **2020**, *38*, 1849–1859.
  53. Takahashi, A.; Okada, R.; Nagao, K.; Kawamata, Y.; Hanyu, A.; Yoshimoto, S.; Takasugi, M.; Watanabe, S.; Kanemaki, M.T.; Obuse, C.; et al. Exosomes maintain cellular homeostasis by excreting harmful DNA from cells. *Nat. Commun.* **2017**, *8*, 1–14.
  54. Rulli, S.J.; Hibbert, C.S.; Mirro, J.; Pederson, T.; Biswal, S.; Rein, A. Selective and Nonselective Packaging of Cellular RNAs in Retrovirus Particles. *J. Virol.* **2007**, *81*, 6623–6631.
  55. Knezevic, I.; Stacey, G.; Petriccioni, J. WHO Study Group on cell substrates for production of biologicals, Geneva, Switzerland, 11-12 June 2007. *Biologicals* **2008**, *36*, 203–211.
  56. Eaton, L.C. Host cell contaminant protein assay development for recombinant biopharmaceuticals. *J. Chromatogr. A* **1995**, *705*, 105–114.
  57. Pato, T.P.; Souza, M.C.O.; Silva, A.N.M.R.; Pereira, R.C.; Silva, M. V.; Caride, E.; Gaspar, L.P.; Freire, M.S.; Castilho, L.R. Development of a membrane adsorber based capture step for the purification of yellow fever virus. *Vaccine* **2014**, *32*, 2789–2793.
  58. Sviben, D.; Forcic, D.; Ivancic-Jelecki, J.; Halassy, B.; Brgles, M. Recovery of infective
-

- virus particles in ion-exchange and hydrophobic interaction monolith chromatography is influenced by particle charge and total-to-infective particle ratio. *J. Chromatogr. B* **2017**, *1054*, 10–19.
59. Shiba, T.; Saigo, K. Retrovirus-like particles containing RNA homologous to the transposable element copia in *Drosophila melanogaster*. *Nature* **1983**, *302*, 119–124.
  60. Venereo-Sánchez, A.; Fulton, K.; Koczka, K.; Twine, S.; Chahal, P.; Ansorge, S.; Gilbert, R.; Henry, O.; Kamen, A. Characterization of influenza H1N1 Gag virus-like particles and extracellular vesicles co-produced in HEK-293SF. *Vaccine* **2019**, *37*, 7100–7107.
  61. Schermelleh, L.; Heintzmann, R.; Leonhardt, H. A guide to super-resolution fluorescence microscopy. *J. Cell Biol.* **2010**, *190*, 165–75.
  62. Carvalho, S.B.; Freire, J.M.; Moleirinho, M.G.; Monteiro, F.; Gaspar, D.; Castanho, M.A.R.B.; Carrondo, M.J.T.; Alves, P.M.; Bernardes, G.J.L.; Peixoto, C. Bioorthogonal Strategy for Bioprocessing of Specific-Site-Functionalized Enveloped Influenza-Virus-Like Particles. *Bioconjug. Chem.* **2016**, *27*, 2386–2399.
  63. Transfiguracion, J.; Manceur, A.P.; Petiot, E.; Thompson, C.M.; Kamen, A.A. Particle quantification of influenza viruses by high performance liquid chromatography. *Vaccine* **2015**, *33*, 78–84.
  64. Steppert, P.; Burgstaller, D.; Klausberger, M.; Tover, A.; Berger, E.; Jungbauer, A. Quantification and characterization of virus-like particles by size-exclusion chromatography and nanoparticle tracking analysis. *J. Chromatogr. A* **2017**, *1487*, 89–99.
  65. Zamora, J.L.R.; Aguilar, H.C. Flow virometry as a tool to study viruses. *Methods* **2017**, *134–135*, 87–97.
  66. Bonar, M.M.; Tilton, J.C. High sensitivity detection and sorting of infectious human immunodeficiency virus (HIV-1) particles by flow virometry. *Virology* **2017**, *505*, 80–90.
  67. van der Pol, E.; Coumans, F. a W.; Grootemaat, A.E.; Gardiner, C.; Sargent, I.L.; Harrison, P.; Sturk, A.; van Leeuwen, T.G.; Nieuwland, R. Particle size distribution of exosomes
-

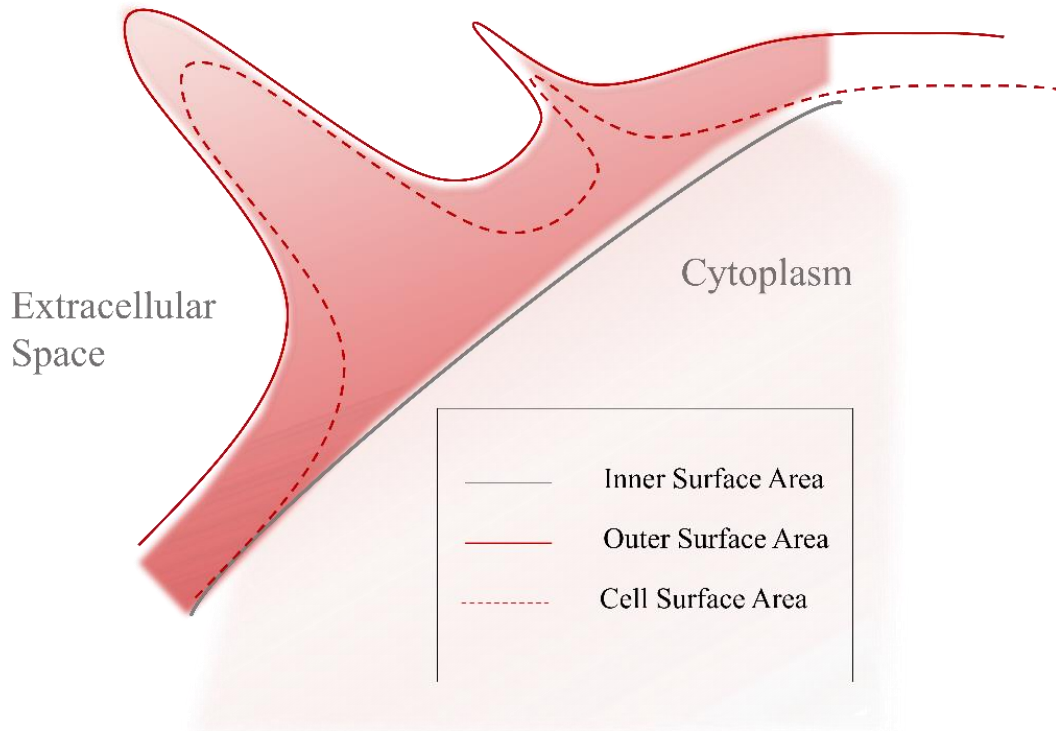
and microvesicles determined by transmission electron microscopy, flow cytometry, nanoparticle tracking analysis, and resistive pulse sensing. *J. Thromb. Haemost.* **2014**, *12*, 1182–1192.

7 Supplementary materials

A



B



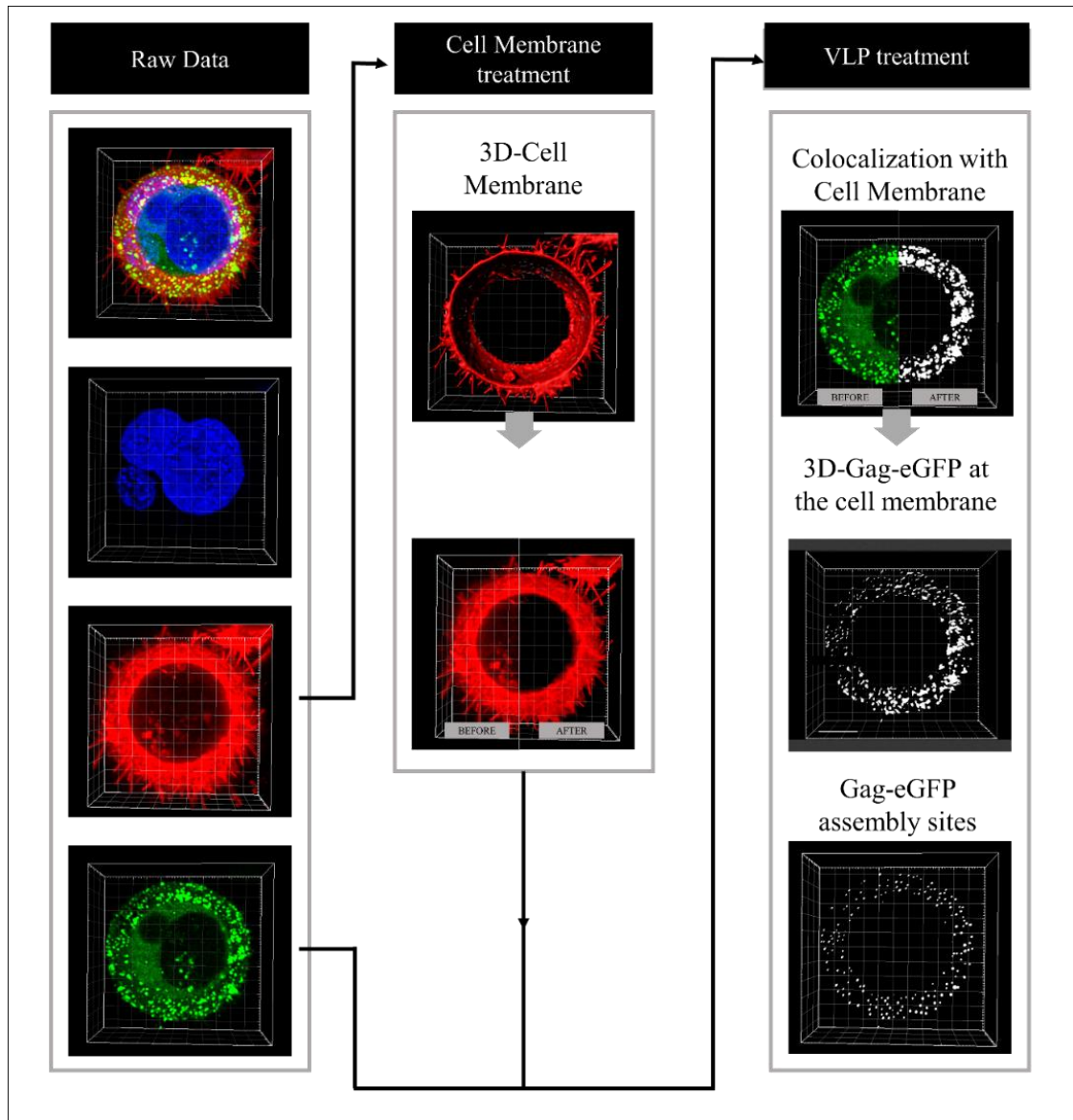
## C

	R ( $\mu\text{m}$ )	h ( $\mu\text{m}$ )	Inner Surface area ( $\mu\text{m}^2$ )	Outer Surface area ( $\mu\text{m}^2$ )	Membrane thickness Correction factor (%)	Cell Surface area ( $\mu\text{m}^2$ )
HEK 293						
i*	11,8	-	1734,9	5374,8	8	4927,1
ii	7,4	6,0	277,5	1019,3	13	885,5
iii	8,4	6,3	331,4	962,8	11	852,1
Hi5						
i	13,8	7,8	678,7	1656,8	7	1539,2
ii	13,4	3,8	314,4	607,2	7	562,5
iii	10,9	4,2	288,2	573,5	9	522,2
Sf9						
i	10,9	3,9	272,2	492,9	9	449,4
ii	8,9	1,8	167,5	333,5	11	297,1
iii	9,0	1,8	101,6	192,3	11	171,6
iv	11,7	2,7	198,3	356,1	8	326,3

\* Calculated from a whole cell by the sphere formula

**Supplementary Materials S7. Cell surface area analysis. (A) Analyzed images of transfected HEK 293 cells at 48 hpt and baculovirus infected High Five (Hi5) and Sf9 cells at 40 hpi. Biological triplicate measurements are represented. (B) Cell surface area reconstruction. Average cell surface area (dotted line) was calculated by the correction of the outer surface area (red line) using a thickness membrane factor. This factor was calculated by the difference between total surface and inner surface area (grey line). (C) Summary of raw data from cell surface area calculations in each sample with Equation 1. The inner surface area was calculated as a sphere segment with radius (R) and segment height (h) (Equation 2) and the outer surface area was obtained as the difference between total surface and inner surface areas.**





Supplementary Materials S2. Cell imaging analysis workflow to assess the VLP budding process. Raw deconvolved images acquired using HyVolution2 SRFM were treated for quantitative purposes. Cell Membrane Treatment: A new channel with cleaned membrane signal was created by 3D-cell membrane reconstruction. The comparison of raw cell membrane signal with cleaned cell membrane is shown below (before and after, respectively). VLP Treatment: Isolation of Gag-eGFP signal in the cell membrane was performed based on the colocalization between Gag-eGFP and the cleaned cell membrane channels. The comparison of total Gag-eGFP signal with colocalized Gag-eGFP is depicted (before and after, respectively). Further 3D reconstructions of 3D-Gag-eGFP at the cell membrane was conducted toward evaluating the percentage of Gag-eGFP colocalized membrane (v:v). The quantification of VLP assembly sites was also calculated using the algorithm spot in the Imaris software.

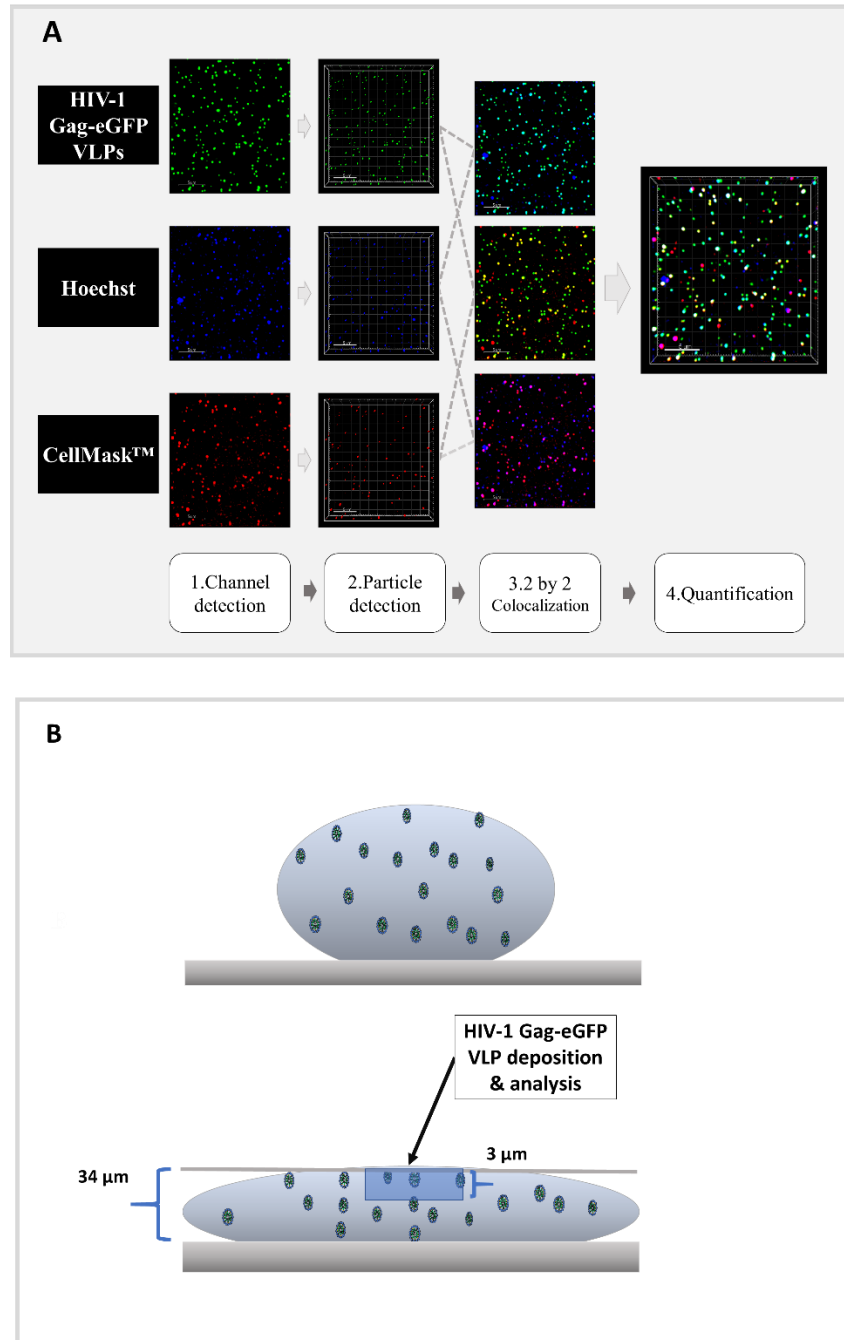
**Supplementary Materials S3. Calculation of VLP assembly sites per cell in transfected HEK 293 cells at 48 hpt and baculovirus infected High Five (Hi5) and Sf9 cells at 40 hpi.**

	HEK 293	Hi5	Sf9
Average cell diameter of negative control ( $\mu\text{m}$ )	16,4 $\pm$ 0,2	17,5 $\pm$ 0,5	15,0 $\pm$ 0,0
Average cell diameter ( $\mu\text{m}$ )	15,6 $\pm$ 0,2	28,0 $\pm$ 6,3 ‡	21,8 $\pm$ 2,8 ‡
Calculated area ( $\mu\text{m}^2$ )	764,6 $\pm$ 17,0	2589,3 $\pm$ 1115,4	1518,0 $\pm$ 390,3
Calculated volume ( $\mu\text{m}^3$ )	1988,5 $\pm$ 66,2	13262,1 $\pm$ 7941,5	5702,6 $\pm$ 2139,2
Harvest time (hpt or hpi)*	72	40	40
Concentration of viable cells at harvest time (cells/mL)*	4,08 $\pm$ 0,3 $\cdot 10^6$	3,87 $\pm$ 1,9 $\cdot 10^6$	3,42 $\pm$ 0,5 $\cdot 10^6$
Percentage of producing cells (%)*	74 $\pm$ 1	98 $\pm$ 0	99 $\pm$ 1
Specific HIV-1 Gag-eGFP VLP particle production at harvest time (HIV-1 Gag-eGFP VLPs/cell)*	1680 $\pm$ 225	3072 $\pm$ 686	2688 $\pm$ 696
Average assembly sites per surface area** (assembly sites/inner surface area $\mu\text{m}^2$ )	0,7 $\pm$ 0,2	1,1 $\pm$ 0,2	1,1 $\pm$ 0,2
Average assembly sites per cell at harvest time (assembly sites /cell)	518 $\pm$ 164	3045 $\pm$ 1733	1682 $\pm$ 716
Average assembly sites at harvest time (assembly sites/mL)	1,6 $\pm$ 0,6 $\cdot 10^9$	14,8 $\pm$ 12,3 $\cdot 10^9$	6,1 $\pm$ 3,3 $\cdot 10^9$
Ratio HIV-1 Gag-eGFP VLPs: assembly sites at harvest time	4 $\pm$ 2	2 $\pm$ 1	2 $\pm$ 1

‡ Average cell diameter calculated from Appendix 1C (out of range in NucleoCounter®NC-3000; >20 $\mu\text{m}$ )

\*Calculated from Figure 5

\*\* Calculated from Figure 3 and Appendix 1



Supplementary Materials 4: VLP quantification using HyVolution2 SFRM. VLP preparations were stained for nucleic acid (Hoechst) and cell membrane (CellMask™) detection. (A) Analysis workflow followed in VLP preparations: (1) channel detection and threshold adjustment, (2) nanoparticle detection using the spot algorithm, (3) 2-by-2 spot colocalization and (4) quantification analysis. Biological triplicates and negative controls were analyzed in each production platform. (B) Sample preparation for HyVolution2 SFRM analysis. Quantification was performed on deposited VLP samples in segments of 3 μm in height from a total volume of 50 μL and a total height of 34 μm. Samples were prepared and incubated for 30 minutes to allow for deposition and reduce nanoparticle movement in suspension.

**Chapter 5**

**Identification of Human Immunodeficiency Virus Type 1 (HIV-1)  
Based Virus-Like Particles by Multifrequency Atomic Force  
Microscopy.**

---

Published in Biophysical Journal, 2016 (111) 1173-1179

## **Abstract**

Virus-like particles (VLPs) have become a promising platform for therapeutic candidates. VLPs are formed by structural viral proteins that inherently self-assemble when expressed in a host cell. They represent a highly immunogenic and safe platform, due to the absence of the viral genome and its high protein density. One of the main important parameters in clinical development is the quality of the product. A related bottleneck in VLP-based products is the presence of extracellular vesicles as a major contaminant in the preparations. Therefore, it is highly required the set-up of techniques that allow for specific discrimination of VLPs from host vesicular bodies. In this work, novel Multifrequency Atomic Force Microscopy (MF AFM) has permitted full structural nanophysical characterization by its access to the virus capsid of the HIV-1 based VLPs. The assessment of these particles by advanced Amplitude Modulation-Frequency Modulation (AM-FM) Viscoelastic Mapping mode has enhanced the imaging resolution of their nanomechanical properties opening a new window for the study of the biophysical attributes of VLPs. Finally, the identification and differentiation of HIV-1 based VLPs from extracellular vesicles (EVs) has been performed under ambient conditions providing a novel methodology for the monitoring and quality control of VLPs.

**Keywords:** Virus-like particle (VLP), Atomic Force Microscopy (AFM), Multifrequency AFM, Bimodal AFM, AM-FM Viscoelastic Mapping Mode, Human Immunodeficiency Virus (HIV)

## 1. Introduction

Currently, more than 37 million people worldwide are living with the human immunodeficiency virus (HIV) and the epidemic still has a substantial effect on certain countries and high-risk groups [1]. Despite several efforts have been undertaken to find a proper vaccine, there is no current effective candidate against HIV infection [2]. HIV is an enveloped single-stranded RNA virus whose genome gives rise to three main polyproteins: Gag, Gag-Pol and Env. Gag gene contains the main structural proteins of HIV. Upon expression, Gag polyprotein is able to self-assemble generating non-infectious virus-like particles (VLPs) that have shown great promise as a platform for the presentation of antigens [3].

VLP-based vaccine candidates for HIV have satisfactorily been produced in mammalian and insect cells [4,5]. VLPs display a high protein density on their surface. Moreover, they represent a highly immunogenic and safe vaccine system compared to other third generation vaccines, since they do not contain the viral genome [4–6]. In this study, HIV-1 Gag-based VLPs produced by transient gene expression in mammalian cells following the previously described methodology are examined [7,8].

Similar to the native HIV virus, HIV-1 Gag VLPs are released by the cell through a budding process after the Gag polyprotein self-assembly. Thus, the final particles are enveloped by the host cell lipid membrane [3]. Additionally, the cell machinery also naturally secretes other extracellular vesicles (EVs) to the extracellular space, such as microvesicles and exosomes [9]. The presence of these EVs has been previously described in HIV and Influenza-based VLPs produced in mammalian cells [10–12] and it has also been observed in our research laboratory in all HIV-1 based VLP preparations. The need for high quality VLP-based vaccine productions is prevailing since its end-use is their human clinical application [6].

Nowadays, there are not proper techniques allowing specific discrimination of VLPs from EVs, hence the presence of vesicular bodies becomes a major bottleneck in the field of VLP-based vaccine production. For this reason, the characterization of both HIV-1 Gag VLPs and EVs is of high relevance with a view to the further development of purification methods. These particles

have been previously characterized by Electron Microscopy (EM) [7,13]. However, EM analysis requires a negative staining pre-treatment, which can lead to false positive errors, and also lacks three-dimensional (3D) structural information. Further evaluation is essential to understand the morphology and mechanical attributes of the product.

In this work, Atomic Force Microscopy (AFM) is proposed for investigating the HIV-1 Gag VLP population. AFM has been already used in virus and VLP characterization providing novel information of biological samples, such as morphology, structural data and composition in ambient conditions [14–16]. Interestingly, recent advances in multifrequency (MF) AFM modes offer a broad assessment of nanomechanical features of soft samples. The dynamic mechanical properties of an AFM cantilever are composed by a set of eigenmodes associated to different resonant frequencies. MF AFM exploits the simultaneous excitation and/or analysis of different eigenmodes and harmonics in the deflection signal to enhance the information about the tip-sample interactions. Thus, this MF AFM technique deepens into the material characteristics. Of note the application of MF AFM modes, such as amplitude modulation-frequency modulation (AM-FM) Viscoelastic Mapping, to perform the characterization of soft samples [17,18].

In this study, the application of AM-FM Viscoelastic Mapping to analyze enveloped VLPs is reported for the first time, with obtaining interesting new data of its composition and internal capsid protein structure. HIV-1 Gag VLPs were analyzed by MF AFM and its use facilitated the discrimination between VLPs and EVs present in the preparations. Nonetheless, the sample preparation based on EM protocol has important drawbacks due to the alteration of the sample and the difficulties of working with grids in AFM. For these reasons, the VLP samples were also examined under ambient conditions deposited on mica substrate. In this simple configuration, we have validated an innovative and nimble methodology for discriminating VLPs and EVs under ambient conditions.

## **2. Materials and Methods**

### **2.1. HIV-1 Gag VLP production and purification**

HIV-1 Gag-eGFP VLPs were produced and purified by transient transfection protocol, as previously described [7,13] in the human cell line: HEK 293SF-3F6 cells (NRC, Montreal, Canada) kindly provided by Dr. Amine Kamen from McGill University (Montreal, Canada). Gag gene was fused to GFP for its study, and preparations were quantified by an spectrofluorometric assay [13]. A transfection with an empty plasmid was performed as a negative control (Mock).

## **2.2. HIV-1 Gag VLP Sample preparation for AFM and EM analysis**

HIV-1 Gag-eGFP VLPs samples were prepared by two different protocols as described below.

### **2.2.1. Negative staining in carbon coated grids**

HIV-1 Gag-eGFP VLP and Mock samples were diluted 1:4 with PBS, and subsequently negatively stained at Servei de Microscopia (UAB, Bellaterra, Spain). Briefly, 5  $\mu$ L of the preparation was deposited on Quantifoil gold-coated grids (QUANTIFOIL <sup>®</sup> R2/2, Großlobbichau, Germany) and carbon-coated grids (PELCO<sup>®</sup> Center-Marked Grids, Redding, Canada) and incubated at room temperature for 5 minutes. Excess sample was carefully drained off the grid with the aid of filter paper. Then, samples were stained with 5  $\mu$ L of uranyl acetate (2%) by incubating for 1 minute at room temperature. Excess staining was dried off as explained before and grids were dried for a minimum of 50 minutes at room temperature before examination.

### **2.2.2. VLP preparation by deposition on mica substrate**

Mica substrate was prepared by defoliation prior to depositing 20  $\mu$ L of VLP preparations. Samples were incubated during 15 minutes at room temperature. Afterwards, the sample was washed with 3 mL of ultrapure water. Finally, samples were dried with a gentle flow of nitrogen gas.

## **2.3. EM analysis**

EM analysis was performed by two different microscopes. Transmission Electron Microscopy (TEM) examination was performed with JEM-1400 (JEOL USA, Pleasanton, CA, USA) transmission electron microscope equipped with ES1000W Erlangshen charge-coupled device



camera (CCD) (Model No. 785; Gatan, Pleasanton, CA, USA). Scanning electron microscopy (SEM) analyses were assessed with FE-SEM Merlin (Zeiss, Jena, Germany) scanning electron microscope.

#### **2.4. AFM analysis**

Atomic Force Microscopy imaging was performed with MFP-3D Asylum AFM (Asylum Research, Oxford Instruments, Goleta, CA, USA). In all the experiments, PPP-EFM tips (Nanosensors TM, Schaffhausen, Switzerland) with a stiffness constant  $k = 2 \text{ N/m}$  and coated with Ptlr5 were used. MF AFM is based in the use of multiple excitation modes with different characteristic frequencies. In this case, the fundamental excitation mode was used together with the second eigenmode. In simple Bimodal AFM operation mode, the tip is excited at both frequencies, with amplitudes  $A_2 < A_1$ . A remarkable benefit of multifrequency bimodal imaging is the fact that the forces between the tip and the sample are very small while allowing a clear non-destructive differentiation of composition, which makes it very convenient to investigate soft biological samples. The excitation at the fundamental mode was used to measure the topography in Amplitude Modulation AFM (AM-AFM), while changes in amplitude and phase for the second eigenmode, not affected by the feedback loop restrictions, are monitored.

On the other hand, AM-FM Viscoelastic Mapping® operation mode of Asylum Research (Oxford Instruments) was used to obtain direct contrast from mechanical properties of the samples. Similar to Bimodal AFM, two cantilever resonances are operated simultaneously; the fundamental mode was used for AM topography imaging, while a higher resonance mode is operated in FM, with an automatic gain control circuit monitoring the amplitude at the resonance frequency and adjusting the drive voltage to keep the amplitude constant, thus measuring the associated dissipation. The resonance frequency shifts describe the changes in elastic tip-sample interaction, and quantitative nanomechanical information can be obtained from analysis of the amplitude ( $A$ ) and phase ( $\Phi$ ) of the two modes, together with the frequency and the dissipation at the second eigenmode. Detailed quantitative nanomechanical analysis can be performed on the base of the application of the virial and energy transfer expressions among the multiple excited modes. Exact equations can

be found in the work by R. Garcia and R. Proksch [19,20]. The different features of each MF AFM operation mode are presented in table 1.

**Table 1: Description of the two different working modes of MF AFM used in this work.**

ModeName	Feedbackmode 1	Feedbackmode 2	Observables	Material property
<b>Bimodal AFM</b>	AM	Open	$A_1, A_2, \Phi_1, \Phi_2$	Dissipation
<b>AM-FM</b>		Frequency	$A_1, \Phi_1$	Dissipation, Stiffness,
<b>Viscoelastic</b>	AM	Modulation	Dissipation <sub>2</sub> , $\Delta f_2$	Young modulus (E)
<b>Mapping</b>				

\*  $A_n$ : Amplitude,  $\Delta f_n$ : Frequency shift,  $\Phi_n$ : Phase

### 3. Results

HIV-1 Gag-eGFP VLPs and Mock samples were produced and analyzed by EM techniques. Figure 1A shows a TEM micrograph of the HIV-1 Gag-eGFP VLP preparation. The particles are visualized as circular-like constructs of around 150 nm formed by electrodense material inside, corresponding to the Gag assembled capsid, enveloped by a lipid membrane observed as a bright corona. A second population of EVs is also detected in all VLP samples. The presence of cellular debris has also been reported in Influenza-based VLP produced in mammalian cells [12]. EVs are heterogeneous in size and present liposome-like circular structure. No electrodense contrast is spotted when its internal content is examined, which means they do not contain structured proteins as those present in VLPs. These vesicular bodies are characteristic of Mock samples (data not shown) where no HIV-1 Gag VLPs structures were recognized.

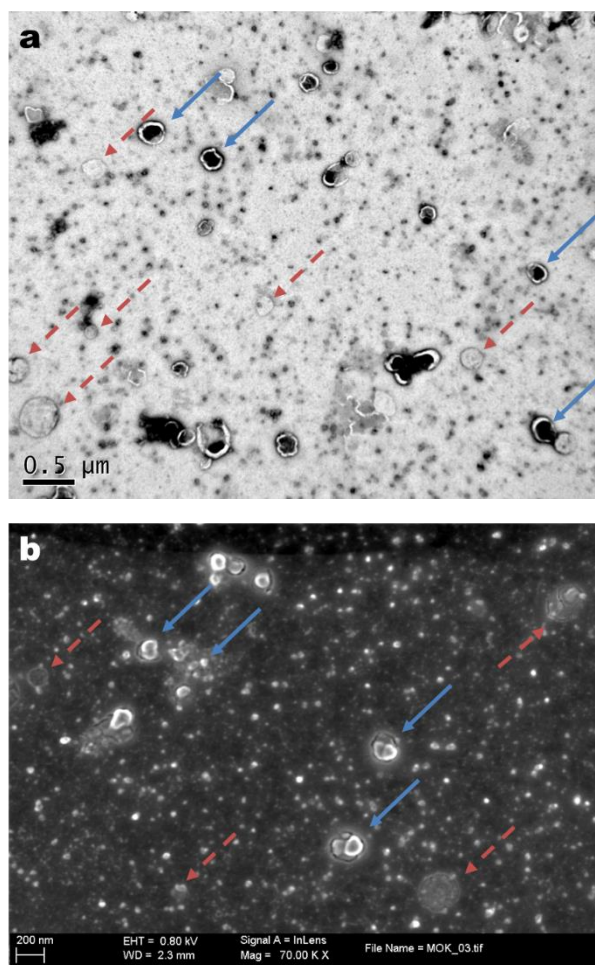


**Figure 1: Electron Microscopy Analysis of HIV-1 Gag-eGFP VLP preparations. (A)Transmission Electron Analysis of HIV-1 Gag-eGFP VLPs (B) Scanning Electron Microscopy Analysis deposited on carbon-coated grids. Straight blue arrows point to HIV-1 Gag-eGFP VLPs and red dash arrows indicate EVs structures.**

Figure 1B shows a SEM analyses of HIV-1 Gag-eGFP VLP preparation. The particles are observed as sphere-like structures of 150 nm as those obtained in Figure 1A. Interestingly, the vesicular contamination is regarded as flatten circular structures. SEM analysis allow to infer that EVs lose their morphology during the negative staining protocol while HIV-1 Gag-eGFP VLPs maintain their conformation. The different characteristics in front of negative staining can be caused by the presence of the protein capsid inside the vaccine candidate. Hence, the protein capsid offers higher mechanical resistance to these particles compared to the EVs.

The difference between the HIV-1 Gag-eGFP VLPs and the vesicular population represents a potential opportunity to develop a proper purification protocol for VLPs. However, the study of biological material by EM requires the sample to be placed in vacuum conditions. Moreover, the imaging contrast obtained by TEM depends on the electrodensity of the sample and SEM examination needs the specimen to be conductive, requiring the coating and drying of biological materials in both cases. Additionally, negative staining treatment can lead to false positive errors due to the fact that uranyl acetate deposition is not completely homogenous and VLP-like structures can be confused with a nanometric accumulation of uranyl acetate. Altogether, the application of EM techniques for regular HIV-1 Gag-eGFP VLP detection in quality control analysis is limited.

### **3.1. Identification of HIV-1 Gag VLP by AFM**

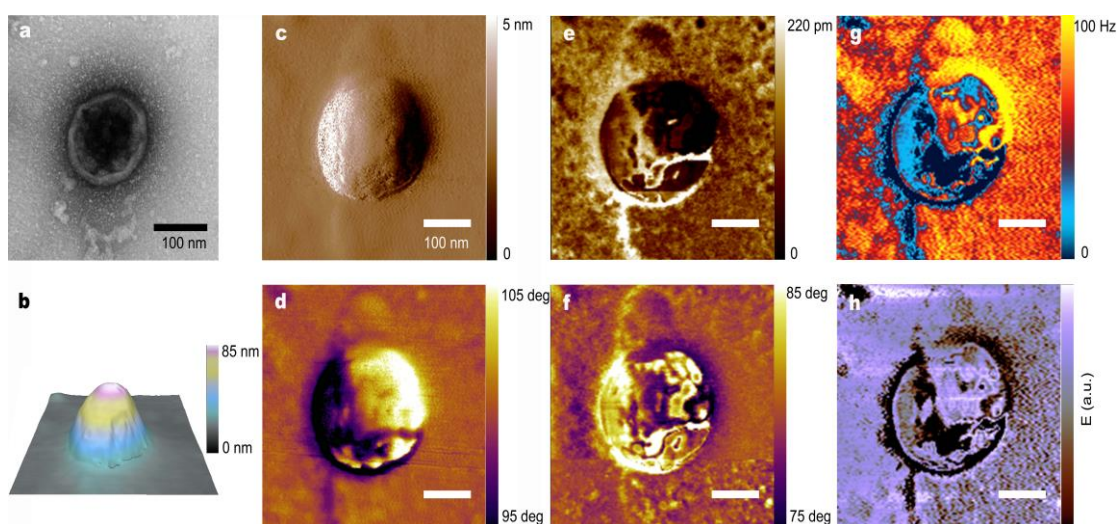
Individual HIV-1 Gag VLP identified in TEM sample was further characterized by AFM to delve into the mechanical properties of the VLPs.

Figure 2A shows the VLP examined by TEM and in Figure 2B-D the results of the Air Dry non-contact AFM investigation of the topography, amplitude ( $A_1$ ) and phase charts ( $\Phi_1$ ) are depicted, respectively. While TEM gives information about the internal content on the basis of electrodensity contrast, AFM provides detailed data of the HIV-1 Gag VLP morphology. HIV-1 Gag-eGFP VLP topography AFM analysis (Figure 2B) presents a height of around 90 nm and a diameter of around 250 nm. The higher diameter compared with TEM data can be explained due to the tip convolution effect [16]. When HIV-1 Gag-eGFP VLP diameter is calculated in the mean height as performed by Faivre-Moskalenko [15], a diameter of around 150 nm is obtained, which is in agreement with previous measurements performed with TEM. Nonetheless, the determination of the particle size for this sample is affected by the adsorption effect of VLPs into the substrate, hindering the determination of the real particle size by AFM [14].

No relevant roughness was detected in the surface HIV-1 Gag VLP structures (Figure 2B). Kuznetsov *et al.* [21] analyzed wild HIV-1 viruses by dynamic AFM and gp40 glycoprotein was identified at the surface of the virus in contrast with the observation present in this study. Even

so, the absence of surface protein is explained as the HIV-1 Gag VLPs produced in this work are only formed by the Gag gene and HIV-1 glycoproteins are contained in the Env region of the viral genome.

Of note, a significant contrast in the surface of the particle which is not related to topography data is observed in the  $\Phi_1$  image (Figure 2D). Phase contrast in AM images is related to dissipative processes hinting at the mechanic-physical properties of HIV-1 Gag-eGFP VLPs, for which advanced MF AFM modes were applied to deepen into the nanomechanical qualities of the samples.



**Figure 2: TEM and AFM imaging of an individual HIV-1 Gag VLP. A) TEM analysis B) AFM 3D Topography imaging C) AFM Amplitude and D) Phase Image of the fundamental mode; E) Second Amplitude ( $A_2$ ) and F) Phase ( $\Phi_2$ ) Images of Bimodal AFM, corresponding to the dynamics of the first excited eigenmode; and G) First excited eigenmode frequency shift ( $\Delta f_2$ ) image of AM-FM Viscoelastic mapping mode, and the corresponding calculated H) Young Modulus image**

### 3.2. Advanced characterization of HIV-1 Gag VLP by MF AFM

As previously discussed, MF AFM involves techniques where cantilever motion is driven and measured at multiple frequencies. Advanced bimodal AFM (Figure 2E-F) and AM-FM Viscoelastic Mapping (Figure 2G-H) were applied to characterize the HIV-1 Gag-eGFP VLP.

Figure 2E-F shows the amplitude ( $A_2$ ) and phase ( $\Phi_2$ ) of the second resonance frequency as measured by Bimodal AFM. These images were taken under the following parameters: initial free

oscillating amplitude of the fundamental mode  $A_{01} = 92.5$  nm, setpoint amplitude for topography image recording of  $A_{sp} = 71$  nm, and free oscillating amplitude at the second mode  $A_{02} = 5.5$  nm, corresponding to a ratio  $A_{02}/A_{01} \sim 6\%$ . The value of the first resonance frequency was  $f_1 = 80.21$  kHz and  $f_2 = 501.84$  kHz, with a relationship of  $f_2/f_1 \sim 6.25$ , which is adequate for the correct application of bimodal imaging theory for this type of tips [22]. As demonstrated by simulations by Damircheli et al., [23] phase contrast in bimodal AFM strongly depends on the relationship between the free amplitudes of the two excited modes: substantial improvement of the contrast in bimodal AFM appears when the free amplitude of the second resonant mode is minimized. Good phase contrast of the second resonant mode in both, attractive and repulsive regimes, is achieved with relationships of  $A_{02}/A_{01} < 1/10$ , being almost maximum for relationships close to  $A_{02}/A_{01} \sim 1/20$ . In our case, the origin of the strong phase contrast observed can be explained by the appropriate chosen relationship of our working amplitudes which is about  $A_{02}/A_{01} \sim 1/17$ . The enhanced contrast in bimodal AFM images of the internal structure perfectly coherent with the TEM micrograph is observed beyond the topography contrast in both images. The nature of this contrast can arise from different physical origins. Some studies refer to a strong dependence of the second mode to the Hamaker constant of the material, which should lead to an increased sensitivity of the composition of the surface for this second mode [17,24,25]. The differential composition should not significantly affect the contrast of the image since in these samples the VLPs are stained with uranyl acetate. In this case, the dynamics of the excited eigenmodes are mainly sensitive to sample stiffness and related mechanical properties [19,20]. The negative and positive phase shifts observed on the VLP structure, can be explained on the base of a respectively hardening and softening of the VLP surface with respect to the substrate taken as reference. Comparison with TEM micrograph can be used to assign the brighter area of phase 2 image with a softer surface associated with the VLP membrane, while the darker area should correspond to a hardening of the surface induced by the nuclear protein capsid embedded in the VLP. In this sense, bimodal AFM arises as a powerful tool to investigate complex biological material due to its capability of distinguishing among mechanically different structures of the biological units, with wide applicability in biophysics community [26].

To further investigate into the mechanical features, AM-FM Viscoelastic Mapping Mode was applied to analyze the HIV-1 Gag-eGFP VLPs as shown in Figure 2G-H. In this case, we used the same fundamental resonant frequency  $f_1=80,21$  kHz as in Figure 2B-D, as well as the same parameters for topography imaging in this frequency, that is  $A_{01} = 92.5$  nm and  $A_{sp} = 71$  nm, but the amplitude of the second frequency was kept constant at  $A_2 = 5.5$  nm, and the dissipation resulted from changes in drive energy to keep this amplitude constant. As the higher resonant frequency was operated in Frequency Modulation, changes in the resonant frequency values were also recorded for this higher excited mode, which are directly proportional to the sample stiffness. The structure observed in this case is again perfectly coherent with the TEM analyses but moreover, it provides specific information about the protein capsid content at the capsid of the HIV-1 Gag-eGFP VLP. Quantitative elastic modulus can be determined from frequency, amplitude, and phase of the two modes following the proper contact mechanics models [20]. Young modulus image shown in Figure 2H confirms that the strong contrast observed is in agreement with bimodal AFM image and corresponds to an enhancement of the sample stiffness, which directly correlates the material at the particle core, hence giving direct access to the intramembrane structure. Thus, MF AFM imaging allows for the mapping of the protein capsid inside the lipid membrane that conforms the particle structure, for what it is possible to unequivocally distinguish HIV-1 Gag-eGFP VLPs deposited on surfaces.

The contrast obtained by MF AFM on HIV-1 Gag-eGFP VLPs is not dependent of the substrate on which the VLPs are deposited. HIV-1 Gag VLP preparation was deposited on mica substrate and analyzed under ambient conditions by using AM-FM Viscoelastic Mapping Mode. Figure 3A shows the topography distribution over a large area of HIV-1 Gag-eGFP VLPs on mica substrate. HIV-1 Gag VLP preparations present similar topography as those observed by Faivre-Moskalenco et al. and Oropesa et al. [14,15]. Moreover, it can be highlighted the large number of VLP-like structures in the sample. Figure 3B shows the topography image and Figure 3C-D the  $\Delta f_2$  and the Young Modulus images, respectively, of a single HIV-1 Gag-eGFP VLP. By doing so, the VLP-like structure could be distinguished. This structure is characterized by spherical

shape, in agreement with previous TEM analyses (Figure 2), and specific contrast in  $\Delta f_2$  and Young modulus charts. Moreover, the strong contrast in mechanical properties also arises as a unique feature that allows to distinguish VLP from other similar contaminating topographical structures or surface roughness. In this sense, similar information is obtained without pre-treating the sample. This confirms the wide applicability of this technique even less resolution is achieved compared to TEM preparation samples.

### **3.3. Discrimination of VLPs and EVs populations in ambient conditions by AFM**

The conspicuous contrast of HIV-1 Gag-eGFP VLPs obtained by MF AFM prompts to its application as a fast and easy methodology for monitoring VLP production. MF AFM allowed to distinguish VLPs from contaminating EVs content. Therefore, it is necessary to study the EVs using the same technique. Characterization of the Mock sample was done by AFM, where isolated vesicles were visualized in EM.

Figure 4 show the AFM images obtained for Mock sample. First significant difference is that no topography evidence is obtained for vesicles, which strongly differs from HIV-1 Gag VLPs structures. The comparison between Figure 3A and Figure 4A, highlight the fact that the structures found in VLP topography chart (Figure 3A) may correspond only to HIV-1 Gag VLPs where the vesicles contamination could not be detected.

Remarkably, a significant contrast of the EVs with respect to the surroundings is obtained for the  $\Phi_1$  image (Figure 4B). This contrast is caused by the different interaction of the cantilever tip with the biological sample deposited which have different structural, compositional and/or chemical properties than the mica substrate. The images univocally confirm the observation of the cellular vesicle population present in Mock samples which are mainly composed by lipid membranes, but without the stiff protein capsid content inside the membrane at the core.



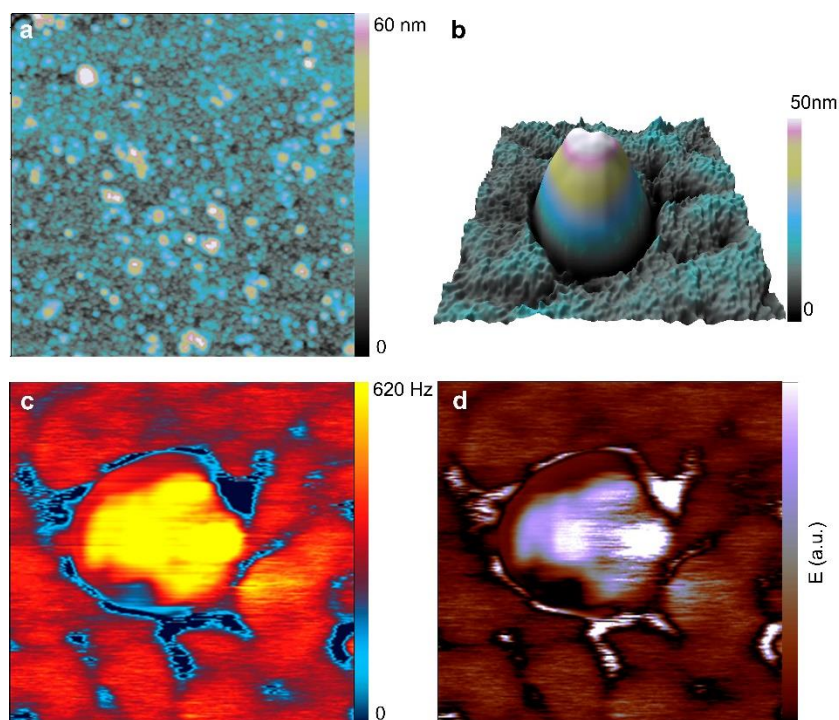


**Figure 3: Individual VLP deposited on mica substrate. A) AFM topography image of VLPs on mica substrate B) 3D topography image of a single VLP structure. C)  $\Delta f_2$  Imaging of an isolated VLP structure, as obtained by AM-FM Viscolastic mapping mode and D) the corresponding calculated Young Modulus distribution**

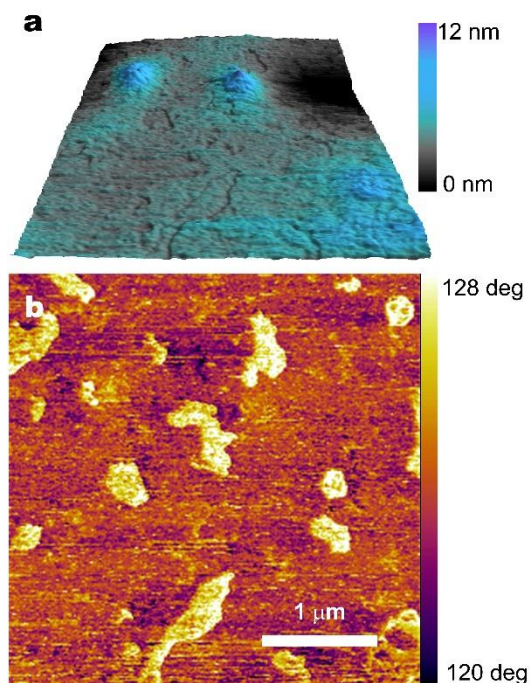


**Figure 4: Mock sample deposited on mica substrate. A) AFM Topography image of empty EVs deposited on mica substrate and B) corresponding AFM phase image, showing the contrast due to the presence of the vesicles.**

#### **4. Conclusion**

In this work, advanced characterization of enveloped HIV-1 Gag VLPs has been achieved by applying MF AFM. The analysis presents a sphere-like structure without relevant glycoproteins in its surface. Interestingly, novel information regarding the nanomechanical properties of the particle were observed by bimodal and AM-FM Viscoelastic Mapping modes. The enhanced contrast obtained in the surface of the HIV-1 Gag VLPs is related to the Gag self-assembled capsid enveloped by the host lipid membrane. Moreover, the bimodal AFM examination of HIV-1 Gag VLPs and EVs under ambient conditions enabled its identification and distinction. The application of this advanced MF AFM modes to soft samples unveils new opportunities for the study of capsid proteins composition and nanomechanical qualities of biological materials, with great impact in the biophysics community, and its further use for the development of proper and efficient strategies for the obtention of high quality VLP candidates for vaccination purposes.

#### **5. Acknowledgments**

The authors wish to thank Dr. Amine Kamen (McGill, Montreal, Canada) for providing the HEK 293 SF-3SF6. The following reagent was obtained through the NIH AIDS reagent Program, Division AIDS, NIAID, NIH: pGag-EGFP (Cat# 11468) from Dr. Marilyn Resh. We would like to thank Dr Albert Verdaguer from ICN2 (Bellaterra, Spain) for providing mica substrate and for its valuable discussions about bimodal AFM. The help of Dr. Pablo Castro from Servei de Microscòpia (UAB, Spain) in the development of electron microscopy analysis is greatly appreciated. This work was supported by the Plan Nacional de Investigación, Ministry of Science and Innovation (MINECO BIO2011-2330), and projects from the Spanish Ministerio de Economía y Competitividad FIS2013-48668-C2-1-P, and the Generalitat de Catalunya under project 2014 SGR 1216. ICN2 acknowledges support from the Severo Ochoa Program (MINECO, Grant SEV-2013-0295). N.D. wants to acknowledge the Spanish Ministerio de Ciencia e Innovación for a Ramon y Cajal research grant RYC-2010-06365.

## 6. Literature

1. Organization, W.H. World AIDS Day. *World AIDS Day 2015 Get. to zero 2015, Web 02 Feb*, <http://www.who.int/>.
2. Cohen, Y.Z.; Dolin, R. Novel HIV vaccine strategies: overview and perspective. *Ther. Adv. Vaccines* **2013**, *1*, 99–112.
3. Göttlinger, H.G. *HIV-1 Gag : a Molecular Machine Driving Viral Particle Assembly and Release*; Carla KuCarla Kuiken, BrianFoley, Thomas Leitner, Cristian Apetrei, Beatrice Hahn, Ilene Mizrachi, James Mullins, Andrew Rambaut, StevenWolinsky, and B.K. editors., Ed.; Los Alamos National Laboratory, Theoretical Biology andBiophysics: Los Alamos, New Mexico., 2001; ISBN 0269-9370.
4. Kushnir, N.; Streatfield, S.J.; Yusibov, V. Virus-like particles as a highly efficient vaccine platform: Diversity of targets and production systems and advances in clinical development. *Vaccine* **2012**, *31*, 58–83.
5. Naskalska, A.; Pyrc, K. Virus Like Particles as Immunogens and Universal Nanocarriers. *Pol. J. Microbiol.* **2015**, *64*, 3–13.
6. Noad, R.; Roy, P. Virus-like particles as immunogens. *Trends Microbiol.* **2003**, *11*, 438–444.
7. Cervera, L.; Gutiérrez-Granados, S.; Martínez, M.; Blanco, J.; Gòdia, F.; Segura, M.M. Generation of HIV-1 Gag VLPs by transient transfection of HEK 293 suspension cell cultures using an optimized animal-derived component free medium. *J. Biotechnol.* **2013**, *166*, 152–165.
8. Gutiérrez-Granados, S.; Cervera, L.; Segura, M. de L.M.; Wölfel, J.; Gòdia, F. Optimized production of HIV-1 virus-like particles by transient transfection in CAP-T cells. *Appl. Microbiol. Biotechnol.* **2016**, *100*, 3935–47.
9. Akers, J.C.; Gonda, D.; Kim, R.; Carter, B.S.; Chen, C.C. Biogenesis of extracellular vesicles (EV): exosomes, microvesicles, retrovirus-like vesicles, and apoptotic bodies. *J.*

- Neurooncol.* **2013**, *113*, 1–11.
10. Bess, J.W.; Gorelick, R.J.; Bosche, W.J.; Henderson, L.E.; Arthur, L.O. Microvesicles are a source of contaminating cellular proteins found in purified HIV-1 preparations. *Virology* **1997**, *230*, 134–44.
  11. Gluschankof, P.; Mondor, I.; Gelderblom, H.R.; Sattentau, Q.J. Cell membrane vesicles are a major contaminant of gradient-enriched human immunodeficiency virus type-1 preparations. *Virology* **1997**, *230*, 125–133.
  12. Thompson, C.M.; Petiot, E.; Mullick, A.; Aucoin, M.G.; Henry, O.; Kamen, A.A. Critical assessment of influenza VLP production in Sf9 and HEK293 expression systems. *BMC Biotechnol.* **2015**, *15*, 1–12.
  13. Gutiérrez-Granados, S.; Cervera, L.; Gòdia, F.; Carrillo, J.; Segura, M.M.; Gutierrez-Granados, S.; Cervera, L.; Godia, F.; Carrillo, J.; Segura, M.M.; et al. Development and validation of a quantitation assay for fluorescently tagged HIV-1 virus-like particles. *J. Virol. Methods* **2013**, *193*, 85–95.
  14. Oropesa, R.; Ramos, J.R.; Falcón, V.; Felipe, A. Characterization of virus-like particles by atomic force microscopy in ambient conditions. *Adv. Nat. Sci. Nanosci. Nanotechnol.* **2013**, *4*, 025007.
  15. Faivre-Moskalenko, C.; Bernaud, J.; Thomas, A.; Tartour, K.; Beck, Y.; Iazykov, M.; Danial, J.; Lourdin, M.; Muriaux, D.; Castelnovo, M. RNA control of HIV-1 particle size polydispersity. *PLoS One* **2014**, *9*, e83874.
  16. Kuznetsov, Y.G.; McPherson, A. Atomic Force Microscopy in Imaging of Viruses and Virus-Infected Cells. *Microbiol. Mol. Biol. Rev.* **2011**, *75*, 268–285.
  17. Garcia, R.; Herruzo, E.T. The emergence of multifrequency force microscopy. *Nat. Nanotechnol.* **2012**, *7*, 217–226.
  18. Lozano, J.R.; Garcia, R. Theory of Multifrequency Atomic Force Microscopy. *Phys. Rev. Lett.* **2008**, *100*, 076102.

19. Garcia, R.; Proksch, R. Nanomechanical mapping of soft matter by bimodal force microscopy. *Eur. Polym. J.* **2013**, *49*, 1897–1906.
20. Proksch, R.; Yablon, D.G. Loss tangent imaging: Theory and simulations of repulsive-mode tapping atomic force microscopy. *Appl. Phys. Lett.* **2012**, *100*, 073106.
21. Kuznetsov, Y.G.; Victoria, J.G.; Robinson, W.E.; Mcpherson, A. Atomic Force Microscopy Investigation of Human Immunodeficiency Virus ( HIV ) and HIV-Infected Lymphocytes. *J. Virol.* **2003**, *77*, 11896–909.
22. Lai, C.-Y.; Barcons, V.; Santos, S.; Chiesa, M. Periodicity in bimodal atomic force microscopy. *J. Appl. Phys.* **2015**, *118*, 044905.
23. Damircheli, M.; Payam, A.F.; Garcia, R. Optimization of phase contrast in bimodal amplitude modulation AFM. *Beilstein J. Nanotechnol.* **2015**, *6*, 1072–81.
24. Martinez, N.F.; Patil, S.; Lozano, J.R.; Garcia, R. Enhanced compositional sensitivity in atomic force microscopy by the excitation of the first two flexural modes. *Appl. Phys. Lett.* **2006**, *89*, 153115.
25. Santos, S.; Barcons, V.; Font, J.; Verdaguier, A. Unlocking higher harmonics in atomic force microscopy with gentle interactions. *Beilstein J. Nanotechnol.* **2014**, *5*, 268–77.
26. Guzman, H. V; Garcia, P.D.; Garcia, R. Dynamic force microscopy simulator (dForce): A tool for planning and understanding tapping and bimodal AFM experiments. *Beilstein J. Nanotechnol.* **2015**, *6*, 369–79

## **Chapter 6**

# **Quality assessment of virus-like particles at single particle level: a comparative study**

---

Published in *Viruses*, 2020 (12) 223

## **Abstract**

Virus-like particles (VLPs) have emerged as a powerful scaffold for antigen presentation and delivery strategies. Compared to single protein-based therapeutics, quality assessment requires a higher degree of refinement due to the structure of VLPs and their similar properties to extracellular vesicles (EVs). Advances in the field of nanotechnology with single particle and high-resolution analysis techniques provide appealing approaches to VLP characterization. In this study, six different biophysical methods have been assessed for the characterization of HIV-1-based VLPs produced in mammalian and insect cell platforms. Sample preparation and equipment set-up were optimized for the six strategies evaluated. Electron Microscopy (EM) disclosed the presence of several types of EVs within VLP preparations and cryogenic transmission electron microscopy (cryo-TEM) resulted in the best technique to resolve the VLP ultrastructure. The use of super-resolution fluorescence microscopy (SRFM), nanoparticle tracking analysis (NTA) and flow virometry enabled the high throughput quantification of VLPs. Interestingly, differences in nanoparticle concentration determination were observed between techniques. Besides, NTA and flow virometry allowed the quantification of both EVs and VLPs within the same experiment while analyzing particle size distribution (PSD), simultaneously. These results provide new insights into the use of different analytical tools to monitor the production of nanoparticle-based biologicals and their associated contaminants.

**Keywords:** VLP; Viral quantification; NTA; Flow virometry; SRFM; Cryo-TEM; SEM

## 1. Introduction

Virus-like particles (VLPs) are considered a promising platform in the field of vaccine development. Nowadays, there are several licensed VLP-based vaccines, such as Cervarix®, Gardasil®, Hecolin® or Porcilis PCV® and more than 100 candidates are undergoing clinical trials [1]. Their success as immunogens lies on their ability to mimic native viruses without containing a viral genome. Their highly organized and repetitive antigen structure has shown effective cellular and humoral immune responses [2]. Furthermore, advances in the field of bioengineering have widened their possible applications; VLP technology accepts several modifications including encapsulation, chemical conjugation or genetic engineering. By doing so, VLPs can be pseudotyped or used either as DNA or drug nanocarriers [1,3].

VLP quality assessment is of major importance, since both, the physicochemical and biological properties are responsible of their clinical efficacy. The preservation of their structural integrity during all the stages of vaccine manufacturing, storage and administration is critical to ensure their success [4]. The study of particle size distribution (PSD) or particle concentration are some of the critical quality attributes (CQA) that could be monitored in this regard [5]. Overall, the specific detection and quantification of VLPs entails several difficulties, especially for enveloped VLPs, which are composed of a protein capsid surrounded by the host-cell lipid membrane. VLPs must be distinguished from other similar nanovesicle structures; extracellular vesicles (EVs) [6], adventitious viruses, or baculoviruses (BV) in insect cell systems [7], which are important process-related impurities. In this sense, traditional quantification methods such as TCID<sub>50</sub> or PCR could not be applied due to the non-infective nature of VLPs

Comprehensive studies on VLP-based vaccine candidates have been conducted by multiple approaches, including biochemical, biological and biophysical methods [3]. Biochemical protein gels, biological enzyme-linked immunosorbent assay (ELISA) or immunoblot are normally used [8–11]. Nonetheless, these assays cannot distinguish assembled from non-assembled structures [12]. Among biophysical methods, analytical ultracentrifugation, dynamic light scattering (DLS) and transmission electron microscopy (TEM) were primarily used to assess VLP physical



properties [3]. Recently, technical progress in the field of microscopy, as well as the application of nanotechnology to virology, have given rise to several single nanoparticle analytical technologies. These techniques represent the most advanced methods to evaluate VLP size, polydispersity, purity and even nanoparticle composition simultaneously [3,12].

Among them, electron microscopy (EM) has traditionally been the preferred technique since resolution at the nanometric or even atomic level is achieved [13]. Within EM methods, transmission (TEM), scanning (SEM) and cryogenic (cryo-TEM) methodologies are frequently used. TEM is the gold standard technique for the characterization of virus-like structures, as reported in a myriad of studies [3,14]. This methodology requires a contrast medium for sample visualization, typically a heavy metal solution containing a cationic or anionic salt, being negative staining the most extended strategy [15]. In TEM-Negative staining, a thin layer of biological material is covered by a dried non-crystalline amorphous layer of uranyl acetate. Differential electron scattering between the biological material and the surrounding staining layer enabled the generation of the electron micrographs. The application of SEM in the characterization of different materials has been demonstrated in several works [16]. However, few studies address its use as a tool for VLP characterization. The addition of Alcian Blue solution to the grid before sample deposition results in the activation of the grid with a net positive charge, with positive results reported for the visualization of other negatively charged specimens such as nucleic acids [17]. Since viral structures and EVs are known to have an overall negative charge at physiological pH [18,19], this strategy could improve their adsorption and reduce nanoparticle loss during the sample preparation process. Cryo-TEM has also gained increasing interest as a tool for nanoparticle visualization over the last years [13]. Essentially, this technique enables the visualization of viruses and VLPs in their native conformation at nanometric and even atomic scale [3], and the addition of a contrast solution is not required. A key point of this technique is the rapid freezing process which reduces sample damage. The selection of an adequate grid and support film is of utmost importance since the correct formation of a thin ice film is pivotal for an adequate sample visualization. Perforated carbon films are generally the preferred option since

they allow the biological material to be imaged in the ice generated between the holes in the carbon support film [20,21].

The study of viral vectors and nanoparticles by confocal microscopy has been traditionally restricted by the Abbe diffraction limit. However, the appearance of super-resolution fluorescence microscopy (SRFM) enabling to surpass this constraint has opened a breadth of opportunities to apply confocal microscopy to the nanoscale [22]. Despite SRFM has been mainly used to study cellular processes, its application to appraise individual viral structures is becoming more popular [23]. In previous works, a method for VLP quantification by HyVolution2 SRFM has been described by González-Domínguez and co-workers [24,25]. This method combines sub-Airy confocal microscopy with mathematical deconvolution, which has been described to achieve resolutions up to 140 nm [26]. Finally, light scatter-based technologies, such as nanoparticle tracking analysis (NTA) and flow virometry are also gaining attention for viral particle and EV quantification [5,12,27,28]. NTA is a method to characterize and quantify nanoparticles in solution that relates the rate of Brownian motion to nanoparticle size. Its use in the assessment of nanoparticles has been reported for viruses, VLPs and other nanoparticles [5,29–31]. This technique is theoretically able to detect nanoparticles with a size comprised between 30 and 1000 nm, while keeping the nanoparticle concentration around  $10^8$  particles/mL and 20 – 60 particles/frame [29]. The latter indicates that the range of possible nanoparticle concentrations is narrow, and it is often required to dilute the sample to meet this criterion, which is generally attained by trial and error. Flow virometry has recently emerged as a technique to specifically detect viruses similarly to conventional cell-based flow cytometry [27]. Labeling studies at single particle level, particle quantification or virus sorting are some of the applications that can be performed with this technology [27]. Considering the high difference in volume between a cell and a nanoparticle, which can be one million-fold [32], the acquisition settings need to be adjusted to detect the scattered or fluorescence signal from nanoparticles. Still, a significant loss of scattered light that fall in the range of the background noise of the instrument is normally observed, presenting different sensitivities depending on the equipment [33]. To address this

issue, the implementation of the violet (405 nm) side scatter (V-SSC) has been reported to improve the sensitivity but also the resolution of the method [34]. Owing to the specific features of each analytical method, characterization results, such as particle concentration obtained by different techniques are often difficult to compare.

The aim of this work is the characterization of VLPs using several advanced nanoparticle analytical methods, and to discuss the technological limitations that may affect their use, including sample preparation or equipment set-up. The study of PSD, ultrastructural analysis, VLP quantification and differentiation from other nanoparticle subpopulations has been performed. The studied VLPs are those from HIV-1 Gag, since they are proposed as a platform for the development of a vaccine candidate against HIV, but also as a scaffold for chimeric or multivalent vaccine development [2,35]. Upon expression in the host cell, the Gag polyprotein travels to the cell membrane and after an oligomerization process, HIV-1 Gag VLPs are released from the cell through a budding process [36,37]. Thus, the final nanoparticles are enveloped by the host cell lipid membrane [38], with sizes comprised between 100 – 200 nm. In previous works, the Gag polyprotein has been fused to GFP to track the VLP production process [36]. By doing so, VLPs could be easily quantified and distinguished from other contaminant particles. Besides, product characteristics are known to be affected by the expression system selected for VLP production [39]. Here, the two most relevant systems for the generation of HIV-1 Gag-based VLPs have been used [40]. VLPs obtained by transient gene expression in HEK 293 cells and baculovirus (BV) infected Sf9 cells have been characterized in parallel. This study provides relevant data on the use of different analytical methods to evaluate the production of VLPs and their associated contaminants in animal cell-based bioprocesses.

## **2. Materials and Methods**

### **2.1. HEK 293 mammalian cell line, culture conditions and transient transfection**

The mammalian cell line used in this work is a serum-free suspension-adapted HEK 293 cell line (HEK 293SF-3F6 from NRC, Montreal, Canada) kindly provided by Dr. Amine Kamen from McGill University (Montreal, Canada). Cells were cultured as previously described [1]. HIV-1

Gag-eGFP VLP production was achieved by transient transfection. Briefly, the pGag-eGFP plasmid encoding for the Gag-eGFP polyprotein, is diluted with FreeStyle 293 medium (Invitrogen, Carlsbad, CA, USA) and vortexed for 10 seconds, then polyethylenimine (PEI) is added at 1:2 DNA:PEI ratio (w/w) and vortexed three times, the mixture is incubated for 15 min at RT and is added to the cell culture, where a medium exchange has been already performed. HIV-1 Gag-eGFP VLPs were harvested at 72 hours post transfection (hpt) by centrifugation at 1000 xg during 15 min. Supernatants were stored at 4 °C until analysis. Non-transfected negative controls reproducing cell growth conditions were also produced, for comparison.

## **2.2. Sf9 insect cell line, culture conditions and baculovirus infection**

The suspension-adapted lepidopteran insect cell line used in this work is the *Spodoptera frugiperda* (Sf9, cat. num. 71104, Merck, Darmstadt, Germany) gently provided by Dr. Nick Berrow (Institute of Biomedical Research, Barcelona, Spain). Sf9 cells were cultured in Sf900III medium (Thermo Fisher Scientific, Grand Island, NY, USA) in 125-mL disposable polycarbonate Erlenmeyer flasks. Cell cultures were shaken at 130 rpm using an orbital shaker (Stuart, Stone, United Kingdom) and maintained at 27 °C. HIV-1 Gag-eGFP VLP production was achieved through infection with the recombinant baculovirus *Autographa californica* multiple nucleopolyhedrovirus (AcMNPV) encoding for the Gag-eGFP protein (BD Biosciences, San José, CA, USA). Shortly, Sf9 cells were grown to  $2 - 3 \cdot 10^6$  cells/mL and were infected at a multiplicity of infection (MOI) of 1. HIV-1 Gag-eGFP VLPs were harvested at 40 or 72 hours post infection (hpi) by centrifugation at 1000 xg during 15 min, and supernatants were kept at 4 °C until analysis. Non-infected negative controls reproducing cell growth conditions were also produced, for comparison.

Biophysical analyses were performed on HIV-1 Gag-eGFP VLP supernatants obtained as previously described. The study of FreeStyle cell culture medium (Invitrogen), Sf900III cell culture medium (Thermo Fisher Scientific) and conditioned cell culture media obtained from

HEK 293 and Sf9 non-transfected/infected conditions using the same protocols was also included in each analysis.

### **2.3. Electron microscopy (EM)**

EM analyses were performed at Servei de Microscòpia at Universitat Autònoma de Barcelona (UAB, Barcelona, Spain). Particle size distribution (PSD) analyses were performed with ImageJ Fiji (ImageJ, NIH, WI, USA) and SigmaPlot 12.0 (Systat Software Inc., San Jose, CA, USA).

#### **2.3.1. Transmission electron microscopy (TEM)-Negative Staining**

Prior to negative staining, HIV-1 Gag-eGFP VLPs were concentrated by double sucrose cushion 25 % - 45 % (w:v) at 31.000 rpm and centrifuged for 2.5 h at 4°C using a SW32 rotor in a Beckman Optima L100XP centrifuge (Beckman Coulter Inc., Brea, CA, USA). The 25 % - 45 % interphase was recovered and stored at 4 °C until analysis [2]. TEM micrographs were analyzed after air-dried negative staining. The protocol used is summarized in Figure 1A. Briefly, VLP samples were deposited onto carbon-coated copper or Holey carbon 200 mesh grids (Micro to Nano, Wateringweg, the Netherlands). Grids were glow discharged in a PELCO easiGlow glow discharger unit (PELCO, Fresno, CA, USA). Thereafter, 8 µL of the sample were loaded onto the grid and incubated at RT for 1 min. Excess sample was carefully drained off the grid with the aid of filter paper. Samples were negatively stained with 8 µL of uranyl acetate (2 %) by incubation for 1 min at RT. Excess stain was drained off as previously indicated, and grids were dried. TEM examinations were performed with a Jeol JEM-1400 (JEOL USA, Pleasanton, CA, USA) transmission electron microscope equipped with an ES1000W Erlangshen charge-coupled device camera (CCD) (Model No. 785; Gatan, Pleasanton, CA, USA).

#### **2.3.2. Scanning electron microscopy (SEM)-Alcian Blue staining**

HIV-1 Gag-eGFP VLP visualization by SEM was performed by staining VLP-containing supernatants with Alcian Blue solution, adapted from Gállego [3]. The protocol used is shown in Figure 2A. Briefly, Alcian Blue solution 1% in 3% acetic acid (Sigma Aldrich, St Louis, MO, USA) was diluted in ultrapure water achieving a final concentration of 1µg/mL. Carbon-coated

copper or Holey carbon 200 mesh grids were placed in this solution for 5 min, then the excess of Alcian Blue solution was removed by washing the grid in ultrapure water. Grids were dried with filter paper. Thereafter, 8  $\mu$ L of the sample were placed on the grid and incubated at RT for 5 min. Excess sample was carefully drained off the grid with the aid of filter paper. Negative staining, was applied to the samples when required, using the protocol described in section 2.3.1. SEM images were assessed in a FE-SEM Merlin scanning electron microscope (Zeiss, Jena, Germany). Micrographs were taken with the lens mode with secondary electron detector with an electron high tension (EHT) comprised between 1 - 2 eV, with 2.9 - 7.5 mm of working distance using a protocol adapted from González-Domínguez et al. [4].

### **2.3.3. Cryogenic transmission electron microscopy (cryo-TEM)**

Cryo-TEM analyses on HIV-1 Gag-eGFP VLPs were also carried out from harvested supernatants. In Figure 3A, the sample preparation procedure for VLP visualization is presented. A 2 - 3  $\mu$ L of sample were blotted onto 200 or 400 mesh Holey carbon grids (Micro to Nano, Wateringweg, the Netherlands) previously glow discharged in a PELCO easiGlow glow discharger unit. Samples were subsequently plunged into liquid ethane at  $-180$  °C using a Leica EM GP cryo workstation and observed in a Jeol JEM-2011 TEM electron microscope operating at 200 kV. During imaging, samples were maintained at  $-173$  °C, and pictures were taken using a CCD multiscan camera (Model No. 895, Gatan).

### **2.4. Super-resolution fluorescence microscopy (SRFM)**

SRFM was performed with a TCS SP8 confocal microscope equipped with Huygens deconvolution suite, communication software and GPU arrays (Leica Microsystems, Wetzlar, Germany), at Servei d'Anatomia Patològica from Hospital Sant Joan de Déu (Esplugues de Llobregat, Barcelona, Spain), as previously described [5]. A summary of the protocol is depicted in Figure 4A. Briefly, harvested VLPs were directly loaded onto the microscope slide and adsorbed to the surface of the cover glass after an incubation time of 30 min at RT (Figure 4A). HIV-1 Gag-eGFP VLP preparations were analyzed with 100 X magnification (zoom 5), 3 of line average and 496 x 496 with HC PL APO CS2 100 X/1.40 OIL objective with the HyVolution2

mode (Leica). 5 fields of 13 sections per each biological triplicate were studied in harvested HIV-1 Gag-eGFP VLPs. HyVolution2 deconvolution was performed with the SVI Huygens Professional program with the *best resolution* strategy (Scientific Volume Imaging B.V., Hilversum, the Netherlands). HIV-1 Gag-eGFP VLP concentration was calculated based on the division of particle number by 3D image volume as previously described [5]. Briefly, direct quantification was performed on deposited HIV-1 Gag-eGFP VLP samples with 23 x 23 x 3  $\mu\text{m}$  in *xyz* 3D image from a total loaded volume of 50  $\mu\text{L}$  distributed in 24 x 60 mm under the cover glass with a total height of 34  $\mu\text{m}$ . Assuming complete sample deposition, minimum concentration of Gag-eGFP VLPs was also calculated. PSD analyses were performed using SigmaPlot 12.0 software (Systat Software Inc.)

### **2.5. Nanoparticle tracking analysis (NTA)**

HIV-1 Gag-eGFP VLPs and total particle content were analyzed by NTA. A NanoSight® NS300 device (Malvern Panalytical, Malvern, United Kingdom) equipped with a blue filter module (488 nm) and a neutral filter was used to quantify GFP-fluorescent nanoparticles and total particle by light diffraction, respectively. The measurements were performed at the Service of Preparation and Characterization of Soft Materials located at Institut de Ciència de Materials de Barcelona (ICMAB, CSIC, Campus UAB). The workflow used for HIV-1 Gag-eGFP VLP quantification is summarized in Figure 5A. Prior to injection into the device chamber, each sample was diluted to obtain 1 mL sample with a concentration around  $10^8$  particles/mL. Sample injection into the chamber was continuously added using a pump to improve the robustness of the measurement and minimize the photobleaching effect due to fluorescence depletion over time (Figure 5B) [6]. The videos recorded were then analyzed with the NTA 3.2 software (Malvern Panalytical) by tracking the individual particle movement, where camera level and detection threshold were adjusted manually for each sample (Table 1). Three independent analyses were carried out. Videos of 60 s were recorded at RT and particles were identified and tracked by their Brownian motion. HIV-1 Gag-eGFP VLP concentrations were calculated as the total fluorescent particles and the concentration of EVs was calculated as the difference between light scattering particles

and fluorescent particles. PSD analyses were performed with NTA 3.2 software (Malvern Panalytical) & SigmaPlot 12.0 software (Systat Software Inc.).

**Table 1. NTA analysis settings.**

	VLPs		Total nanoparticles	
	Camera Level	Threshold	Camera Level	Threshold
HEK 293 supernatants	16	4	10	4
Sf9 supernatants	16	3	8	3
HEK 293 conditioned medium	-	-	10	4
Sf9 conditioned medium	-	-	14	3
FreeStyle culture medium	-	-	13	5
Sf900III culture medium	-	-	13	4

## 2.6. Flow virometry

Flow virometry experiments were performed with a CytoFLEX LX (Beckman Coulter Inc.) with violet side scatter (V-SSC) 405 nm filter configuration at Servei de Cultius Cel·lulars, Producció d'Anticossos i Citometria (UAB, Barcelona, Spain). The different steps required in the analysis are described in Figure 6A. Measurements from different experiments were standardized using a mixture of Megamix-Plus Side Scatter and Forward Scatter (FSC) fluorescent polystyrene beads (0.1, 0.16, 0.20, 0.24, and 0.5  $\mu\text{m}$ ; Biocytex, Marseille, France). Threshold of height trigger signal in Violet Side Scatter (V-SSC) was manually adjusted to 1200 and laser gains were set as 72, 9 and 106 for FSC, V-SSC and B525-FITC lasers, respectively. Samples were diluted with PBS 1 X until the abort rate value was below the 2 %. 300.000 events per sample were analyzed at a flow rate of 10  $\mu\text{L}/\text{min}$ . V-SSC vs B525-FITC density plots were used to gate the different particle populations (i.e. small EVs, large EVs and VLPs). Gating was manually adjusted for each channel. The results were analyzed with the CytExpert software (Beckman Coulter). Nanoparticle concentrations were calculated with equation (1):



$$Particle\ concentration\ \left(\frac{Events}{mL}\right) = (Events) \cdot \frac{\mu l}{mL} \cdot Dilution \quad (1)$$

Particle size diameters based on the median violet side scatter were calculated by Mie correlation [7] using FCM Scatter-Diameter software [8]. Megamix-Plus SSC and FCC fluorescent polystyrene beads were used as the reference material with a refractive index (RI) of 1.633 with a 405 nm illumination wavelength [7]. The following RI were used for Mie correlation: 1.374 (vesicle cytosol), 1.394 (vesicle upper cytosol), 1.354 (vesicle lower cytosol), 1.474 (vesicle membrane) and 1.345 (vesicle surrounding medium) all adjusted to 405 nm as illumination wavelength. The vesicle membrane thickness was defined as 10 nm [7]. The half angle parameter was defined as circular aperture geometry. The maximum diameter was fixed as 3000 nm, the triggering threshold as 60 arbitrary units (a.u.) and the log decade number parameter comprised between 0 - 6. Thereafter, HIV-1 Gag-eGFP VLP and EV mean sizes were exported with the FlowJo software (BD Biosciences).

### 3. Results

#### 3.1. Transmission electron microscopy (TEM)-Negative Staining

VLP characterization by TEM with uranyl acetate as the negative staining solution is shown in Figure 1. VLPs were concentrated by ultracentrifugation according to previous studies [1]. VLPs produced in HEK 293 (Figure 1B & 1D) and Sf9 animal cell lines (Figure 1C & 1E) were examined in order to identify differences arising from the expression of these nanoparticles in each specific cell platform. Uranium strongly reacts with phosphate and amino groups and typically stains protein, nucleic acid and lipid membranes [9]. Thus, VLPs were observed as spherical electrodense structures surrounded by a bright corona (white arrows) that might correspond to structured Gag monomers surrounded by the lipid membrane [1,10]. Less electrodense nanoparticles were also observed throughout the sample, pointed as EVs elsewhere (dashed grey arrows), as also observed in conditioned medium (Supplementary materials S1) [11]. The presence of BV was detected in Sf9 cell concentrated samples (black arrows) along with VLPs (white arrows). Interestingly, differences between VLPs and EVs were less evident in Sf9

micrographs compared to HEK 293 ones. A mean population diameter of  $165 \pm 54$  nm ( $n = 71$ ) and  $146 \pm 33$  nm ( $n = 69$ ) was quantified in HEK 293 and Sf9 samples, respectively (Figure 1F - G). Indeed, TEM characterizations revealed that only the  $52 \pm 6$  % and  $55 \pm 14$  % of the nanoparticles analyzed were VLPs in HEK 293 and Sf9 concentrated samples. Negative staining hindered a more detailed characterization of the structure of the different specimens due to the presence of artifacts and background noise in all samples (Figure 1B - E) [12].

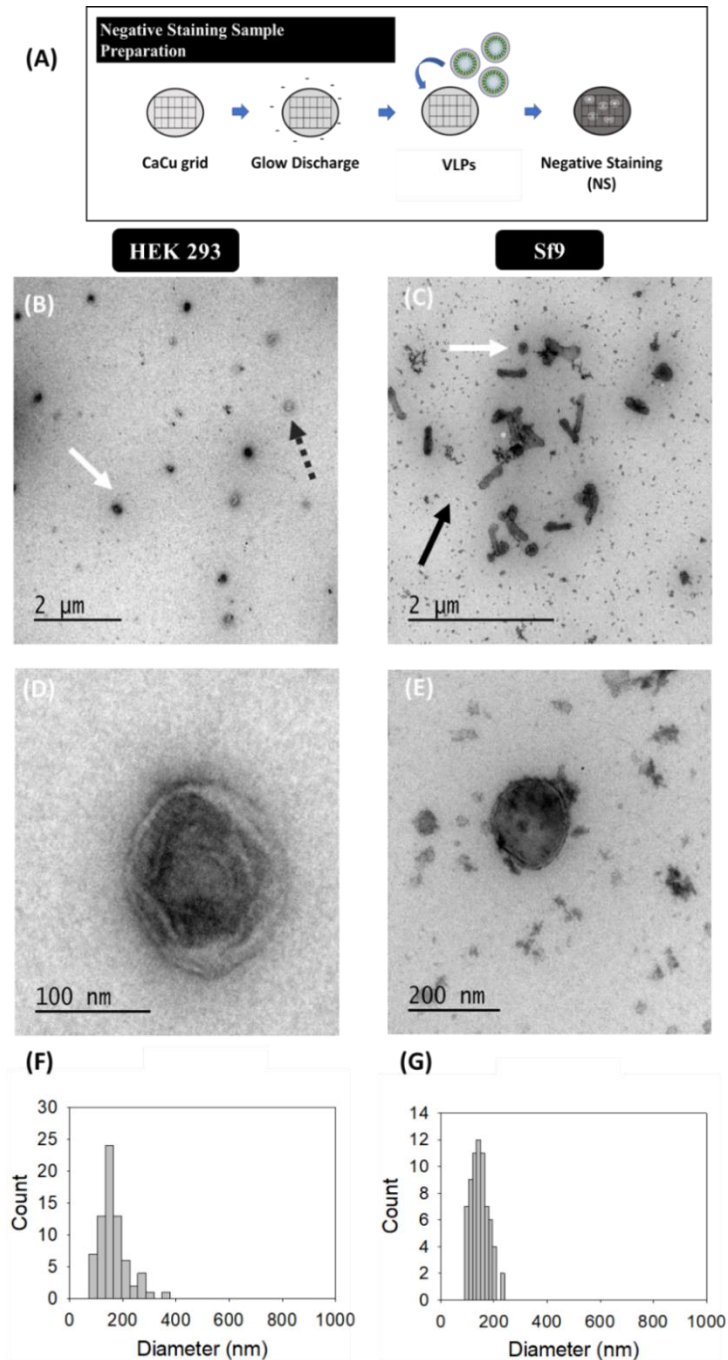


**Figure 1.** Transmission electron microscopy with negative staining analysis of HIV-1 Gag-eGFP VLPs produced in HEK 293 and Sf9 cell lines harvested at 72 hpt and 72 hpi, respectively. (A) Sample preparation protocol; (B - E) Samples corresponding to the 25 - 45 % ultracentrifugation fraction from HEK 293 supernatants (B, D) and Sf9 supernatants (C, E). All samples were stained with uranyl acetate in Ca-Cu grids. (F - G) PSD analysis of HEK 293 and Sf9 cell concentrated samples, respectively. White arrows indicate the presence of virus-like particle in HEK 293 and Sf9 cell productions and black arrows indicate the presence of baculovirus (BV) in Sf9 samples. Negative controls were performed using the same conditions (Supplementary Materials S1).

### 3.2. Scanning electron microscopy (SEM)-Alcian Blue Staining

SEM analyses were directly performed on harvested VLP supernatants from transfected HEK 293 (Figure 2B-D & 2F) and baculovirus infected Sf9 cells (Figure 2E & 2G). Initial analyses using standard sample preparation protocols resulted in the loss of a high portion of the nanoparticles prior to visualization (data not shown). Thus, the combination of SEM with Alcian Blue solution was investigated (Figure 2). Uranyl acetate staining was also assessed as the reference methodology. The comparison between sample negative staining, Alcian Blue grid pre-treatment followed by sample negative staining, and only Alcian Blue grid pre-treatment is shown in Figure 2B - E, respectively. Samples stained with uranyl acetate presented an important background regardless the grid treatment with Alcian Blue solution (Figure 2B - C & S1). When including uranyl acetate for sample staining, a significant background signal could be detected forming large and irregular salt stacks deposited on the sample grid probably related to the interaction with phosphate salts and amino acids from the cell culture media. This background was similar to the one observed in TEM micrographs (Figure 1). Contrarily, nanoparticles could be individually resolved as 3D sphere-like structures by only introducing the Alcian Blue grid treatment without negative staining (white arrows). Despite the improvement in nanoparticle resolution achieved by the Alcian Blue grid pre-treatment, VLPs and EVs could not be distinguished in these analyses. Thus, the calculation of particle size distribution (PSD) was performed considering all nanoparticles as a single population, resulting in  $296 \pm 88$  nm ( $n = 94$ ) for HEK 293 and  $162 \pm 60$  nm ( $n = 57$ ) for Sf9 cell supernatants. The presence of EVs in conditioned cell supernatants could also be observed by SEM- Alcian Blue Staining (Supplementary Materials, S1), as well as the typical rod-shape capsids of BV (black arrows) in baculovirus infected Sf9 cell supernatants (Figure 2E).

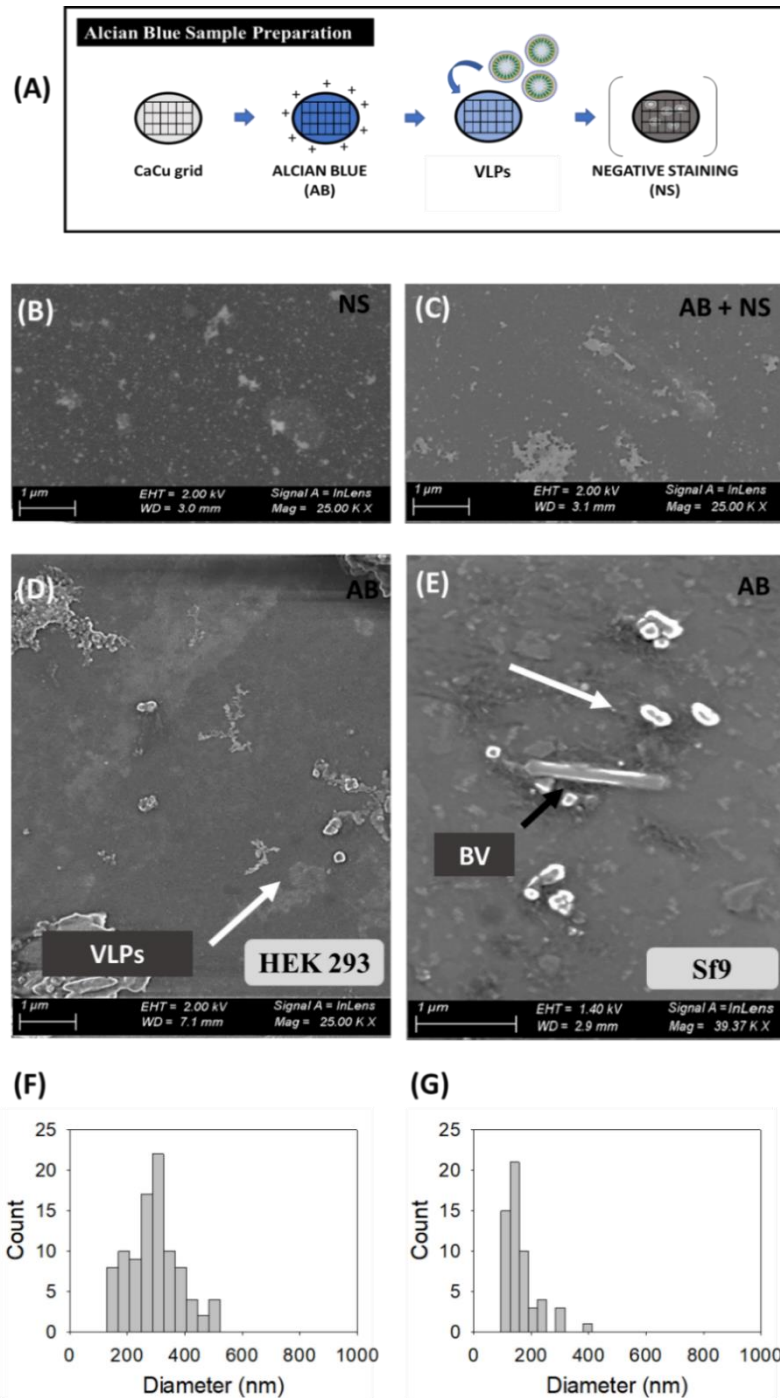


**Figure 2.** Scanning electron microscopy analysis of HIV-1 Gag-eGFP VLPs produced in HEK 293 and Sf9 cell lines harvested at 72 hpt and 72 hpi, respectively. (A) Sample preparation protocol; (B – E) Comparison of different sample preparation methods: (B) negative staining (NS), (C) Alcian Blue solution and negative staining (AB + NS) on HEK 293 supernatants; (D) Supernatant from HEK 293 cells & (E) supernatant from Sf9 cells treated with only Alcian Blue (AB) during 1 min in a Holey carbon 200 mesh grid. (F – G) PSD analysis of HEK 293 and Sf9 cell supernatants, respectively. White arrows indicate the presence of nanoparticles in HEK 293 and Sf9 supernatants and black arrows indicate the presence of baculoviruses (BV). Negative controls were performed using the same conditions (Supplementary Materials S1).

### 3.3. Cryogenic transmission electron microscopy (cryo-TEM)

Ultrastructural analysis of VLP, EV and BV populations could be performed without previous sample concentration using cryo-TEM (Figure 3B-F). Gag-eGFP VLPs were observed as an electron-dense nanoparticle surrounded by a lipid envelope with a granular-like heterogeneous internal structure (Figure 3B – C, white arrows). Gag-eGFP VLPs produced in both platforms displayed an average size of  $202 \pm 68$  nm ( $n = 59$ ) for HEK 293 and  $146 \pm 42$  nm ( $n = 188$ ) for Sf9 cells (Figure 3G & H, respectively). In parallel, different EV subpopulations could be detected, encompassing exosomes (30 – 100 nm), microvesicles (50 – 2000 nm) and multivesicular bodies (MVB) (Figure 3D - F)[13]. Similar structures were detected in conditioned media from both cell lines (Supplementary Materials S1), suggesting that a basal expression of these EV is continuously produced by the cell lines. As for Sf9 cell-derived supernatants, a large concentration of BV was detected (black arrows), including different phenotypes of the BV: occlusion-derived BV (ODV), relaxed BV (rBV) or infective BV (Figure 3F). ODV presented several rod-shaped nucleocapsids arranged in parallel disposition inside vesicular bodies (light blue arrow), while rBV capsid organization in spiral structure could be clearly distinguished (mid-blue arrow) [14]. Budded BVs present ovoid-like structures containing one nucleocapsid, as depicted by dark blue arrow, where the DNA is highly compacted in super coil structures. Baculovirus-containing vesicles or protein structures other than the nucleocapsid could also be identified (cBV). The apical spikes from the infective BV phenotype and the BV lateral pocket, which is the space between the lipid bilayer and the nucleocapsid, could be resolved using this technique (Figure 3G) [14]. Differences in Gag-eGFP (green) VLPs (Figure 3I) and Gag (brown) VLPs (Figure 3J) were also evaluated by cryo-TEM. Gag VLPs evidenced a higher internal degree of organization in comparison to Gag-eGFP VLPs, since a structured Gag-lipid membrane interaction was observed similar to that of immature HIV-1 virions [15].

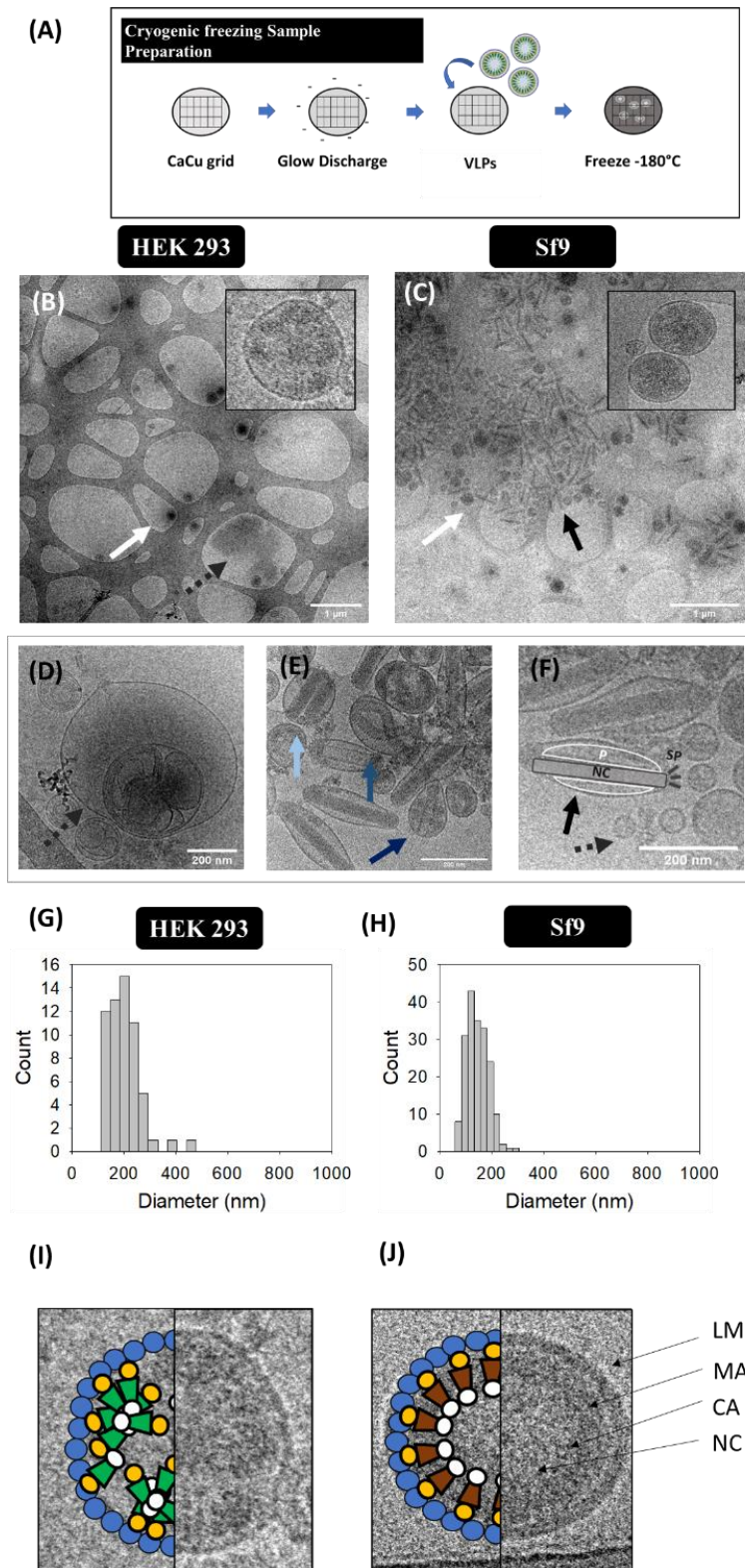


Figure 3. Cryo-TEM analysis of HIV-1 Gag-eGFP VLPs produced in HEK 293 and Sf9 cell lines harvested at 72 hpt and 72 hpi, respectively. (A) Sample preparation protocol. Supernatant from HEK 293 (B) and Sf9 cells (C). Both samples were prepared and visualized in Holey carbon grids. (D – F) Morphological characterization of contaminant particles including multivesicular bodies (MVB) (D), occlusion-derived BV (ODV, light blue), relaxed-form BV (rBV, mid-blue) or BV-containing vesicles or protein structures (cBV, dark blue) (E). Analysis

of the infective BV structure: nucleocapsid (NC), lateral pocket side (P) and apical spikes (SP) (F). (G – H) PSD analysis of HEK 293 and Sf9 cell supernatants, respectively. White arrows indicate the presence of virus-like particles, dashed grey arrows point extracellular vesicles (EVs) and infective baculoviruses are shown in black arrows. (I – J) Ultrastructural organization of an HIV-1 Gag-eGFP (I) and an HIV-1 Gag VLP (brown) produced in Sf9 cells by recombinant baculovirus infection. LM: lipid membrane, MA: matrix; CA: capsid, NC: nucleocapsid. Negative controls were performed using the same conditions (Supplementary Materials S1).

### 3.4. Super-resolution fluorescence microscopy (SRFM)

HyVolution2 SRFM analyses were applied to HEK 293 and Sf9 supernatants. A simple preparation method like those used for studies at cellular level by confocal microscopy was applied. Confocal microscopy images were acquired at 100 X magnification as depicted in Figure 4B, where VLPs correspond to green dots. Zoom in on 3D VLP structure presented an elongated structure in the Z plane while a smaller diameter was observed in the XY axis due to the convolution effect of light. A mean VLP diameter of  $268 \pm 77$  nm ( $n = 371$ ) was obtained in HEK 293 samples, whereas an average of  $261 \pm 104$  nm ( $n = 794$ ) was measured for Sf9 cell supernatants (Figure 4C - D). VLP concentrations were comprised in the range of  $10^9 - 10^{10}$  VLPs/mL in both platforms, representing a 1.7-fold difference for Sf9 over HEK 293-derived VLPs (Table 2). Same acquisition was performed on conditioned medium from both cell lines, where no GFP signal was obtained in the 3D images (Supplementary Materials, S1).



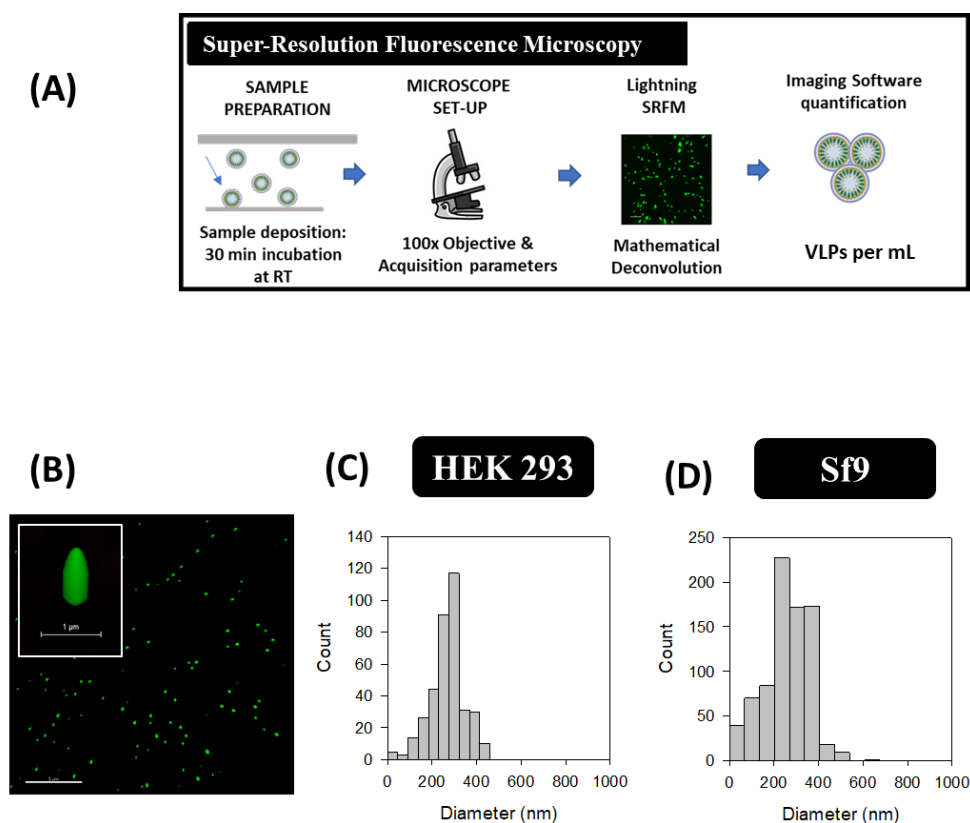


**Figure 4.** Super-resolution fluorescence microscopy analysis of HIV-1 Gag-eGFP VLPs produced in HEK 293 and Sf9 cell lines harvested at 72 hpt and 40 hpi, respectively. (A) Sample preparation and analysis workflow and (B) Gag-eGFP VLP imaging. (C - D) PSD analysis of HEK 293 supernatants and Sf9 cell supernatants, respectively. HEK 293 and Sf9 supernatants were directly quantified after its addition to the microscope slide. Negative controls were performed using the same conditions (Supplementary Materials S1).

### 3.5. Nanoparticle tracking analysis (NTA)

The total amount of nanoparticles produced in each platform was evaluated with the light scattering NTA mode, whereas VLPs were analyzed with the fluorescent filter module (Figure 5A). The PSD and the concentration of VLPs and other nanoparticle populations was performed with the combination of both analyses. An average diameter of  $143 \pm 39$  nm for VLPs and  $161 \pm 66$  nm considering all nanoparticles as a single population was measured in HEK 293 samples. In the case of Sf9 cell supernatants, an average diameter of  $213 \pm 95$  nm was measured for VLPs and  $194 \pm 75$  nm for total nanoparticles. Comparison of VLP concentration in both platforms resulted in a 1.7-fold increase in Sf9 compared to HEK 293 samples (Figure 5C - D). On the contrary, a higher EV content was found in HEK 293 samples (Table 2). Analysis with light

scattering mode of FreeStyle and Sf900III cell culture media gave a concentration of  $0.6 \pm 0.1 \cdot 10^9$  and  $24.4 \pm 1.1 \cdot 10^9$  diffracting particles/mL, respectively with a mean size diameter of  $174 \pm 39$  nm,  $92.7 \pm 74.6$  nm, respectively. Thus, a 2-fold particle concentration is obtained in Sf900III compared to FreeStyle media that directly interferes with total particle quantification. Finally, conditioned media presented a concentration of  $17.6 \pm 0.9 \cdot 10^9$  and  $27.3 \pm 1.5 \cdot 10^9$  diffracting particles/ml, with a mean diameter of  $174 \pm 65$  nm and  $101 \pm 47$  nm in HEK 293 and Sf9 conditioned medium respectively, as those obtained in the supernatants (Table 2).

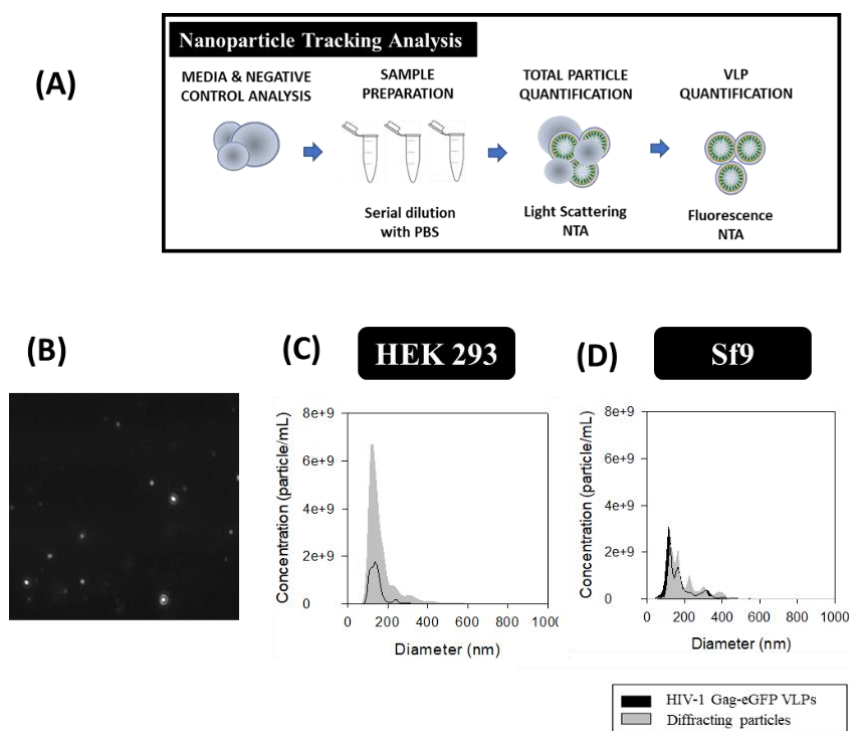


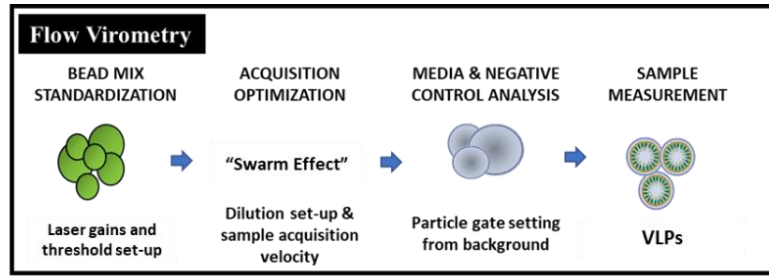
**Figure 5.** Nanoparticle tracking analysis of HIV-1 Gag-eGFP VLPs produced in HEK 293 and Sf9 cells harvested at 72 hpt and 40 hpi, respectively. (A) Sample preparation and analysis workflow. (B) Image of nanoparticles tracked by NTA. (C - D) PSD analysis of HEK 293 and Sf9 cell supernatants, respectively. HEK 293 and Sf9 supernatants were diluted with filtered PBS for the analysis. Negative controls were performed using the same protocol (Supplementary Materials S1).

### 3.6. Flow virometry

Flow virometry has been applied in combination with slow nanoparticle flow speed sample injection ( $10 \mu\text{L}/\text{min}$ ) and the assessment of the most appropriate sample dilution range for analysis. Negative controls were also included for comparison to the VLP producing conditions

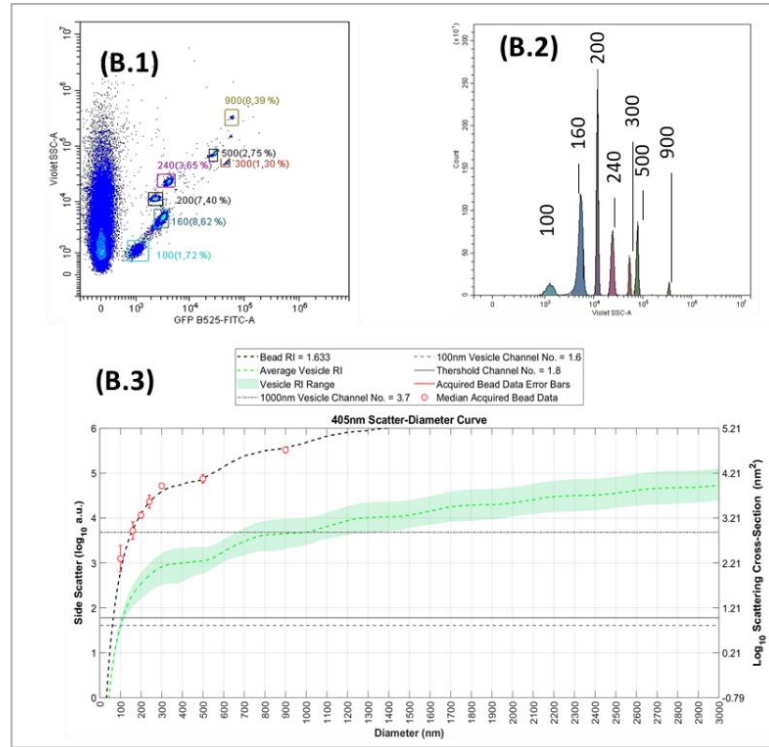
(Supplementary Materials, S1). Equipment calibration for VLP analysis was performed using commercial beads with a known diameter of 100, 160, 200, 240, 300, 500 and 900 nm in order to minimize inter-equipment variability (Figure 6B.1 - 2). Mie scatter modelling allowed to convert the V-SSC intensities of VLPs and EVs to their corresponding size with the FCMPass software developed by Welsh and co-authors (Figure 6 3B.3 & Supplementary Materials, S2) [8]. By doing so, the detection of nanoparticles with diameters down to 100 nm could be achieved.

After equipment set-up, different nanoparticle populations could be assessed in one single analysis. Three main populations were detected in transfected HEK 293 and baculovirus infected Sf9 samples (Figure 6G). Two of these populations corresponded to EVs, subdivided as small and large EVs, whereas the third one was related to VLPs (fluorescent particles). EVs displayed a high level of heterogeneity in the V-SSC, with values ranging from  $10^2$  to  $10^5$  a.u. Interestingly, a second subpopulation of VLPs was detected in baculovirus infected Sf9 samples with a higher V-SSC intensity probably associated to the aggregation of VLPs or the interaction of VLPs with other cellular compounds released to the medium. This second VLP subpopulation generated a more pronounced right-skewed V-SSC distribution compared to the homogeneous VLP population observed in HEK 293 samples (data not shown). By using this methodology, VLP concentrations in the range of  $10^8$  particles/mL were quantified, with a 1.5-fold increase in VLP concentration achieved in Sf9 over HEK 293 cell supernatants (Table 2). Similar level of EVs were quantified in conditioned medium with both cell lines (Supplementary Materials, S1). Mean size analysis of the VLPs and EVs using the Mie correlation resulted in  $114 \pm 26$  nm for VLPs and  $115 \pm 26$  nm for EVs in HEK 293 cell supernatants (Figure 6D & 6F), while a mean diameter of  $117 \pm 22$  nm and  $115 \pm 24$  nm was measured for VLPs and EVs, respectively in Sf9 cell supernatants (Figure 6E & G).

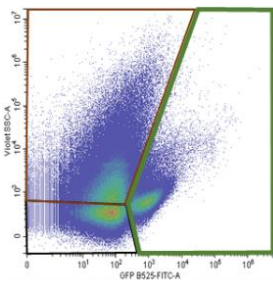


(A)

(B)

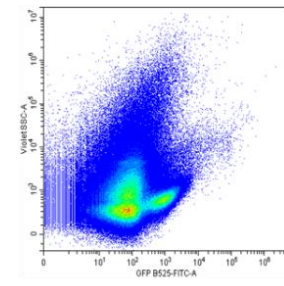


(C)



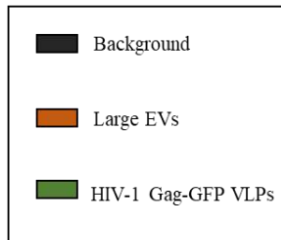
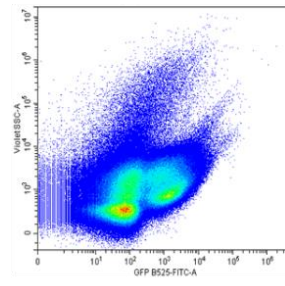
(D)

**HEK 293**

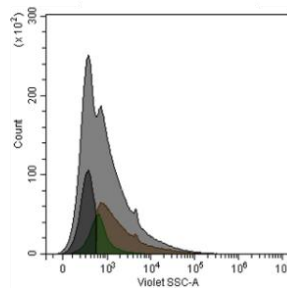


(E)

**Sf9**



(F)



(G)

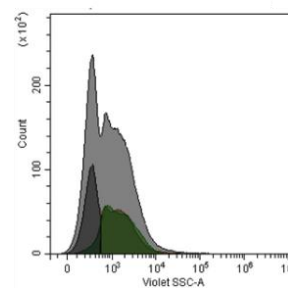


**Figure 6. Flow virometry analysis of HIV-1 Gag-eGFP VLPs produced in HEK 293 and Sf9 cells harvested at 72 hpt and 40 hpi, respectively. (A) Sample preparation and analysis workflow and (B) Equipment calibration using beads with a known diameter. Megamix-Plus fluorescent beads of 100, 160, 200, 240, 300, 500 and 900 nm were used. (B.1) Density plot of nanobeads in GFP B525-FITC-A vs. V-SSC, (B.2) GFP B525-FITC-A histogram of the nanobeads and (B.3) Mie correlation of the nanobeads with FCMPass® software [8]. (C) Gating of the different nanoparticle populations in a density plot. Background signal, EVs and HIV-1 Gag-eGFP VLPs were identified. (D - G) Density and histogram plots of nanoparticles produced in HEK 293 (D, F) and Sf9 cell supernatants (E, G), respectively. HEK 293 and Sf9 supernatants were diluted with filtered PBS for the analysis, respectively. Negative controls were performed using the same conditions (Supplementary Materials S1).**

## **4. Discussion**

### **4.1. Sample preparation and equipment set-up**

Among the different techniques used, the cost, technical requirements and the time needed for sample analysis are practical issues that have to be considered to select an adequate analytical technique for nanoparticle characterization (Table 3) [16]. Regarding sample preparation, purified VLPs were loaded and stained by the addition of uranyl acetate in TEM-Negative staining. Altogether, sample preparation time required less than 10 min per sample, without considering the previous ultracentrifugation step, which required one day of experimentation. Compared to negative staining protocol (Figure 1A), SEM-Alcian Blue grids were not treated by glow discharge before the addition of Alcian Blue solution. The VLP-containing supernatant was directly loaded, representing an overall process duration of 15 min. As for cryo-TEM, sample preparation required an approximate time of 10 min; however, the equipment set-up required a longer time of pre-conditioning compared to TEM and SEM, since a temperature of  $-170^{\circ}\text{C}$  and vacuum was needed in the system prior to analysis. In SRFM, acquisition of VLP 3D images took about 10 min per field and data analysis with the Imaris Software required 15 - 20 min to process the different channels and construct the final image. Finally, the time needed to conduct a complete NTA analysis required 1 h due to sample preparation and software analysis (Figure 5A), while in flow virometry the different nanoparticle populations could be analyzed in one single analysis (Table 3).

In most cases, the sample preparation and equipment set-up are based on trial-and-error, which can introduce a certain degree variability in the characterization of the results. In the case of TEM, the low electron density present in biological samples in combination to working under vacuum conditions entails the use of staining methodologies, as for the negative staining with uranyl acetate, for a better resolution of the specimens under evaluation. Uranium strongly reacts with phosphate and amino groups [9], which confers a higher level of electron density to biological samples with VLPs observed as nanoparticles surrounded by a bright corona. Despite the simplicity of negative staining, the presence of artifacts and background due to the composition of the staining solution are observed (Figure 1B - D), as reported in the literature [17,18]. Depending on the sample origin, this can have a major impact, as observed in Sf9 cell micrographs (Figure 1), where a higher background was detected compared to HEK 293 samples and EVs could not be distinguished from VLPs (Figure 1C). This background is probably caused by the interaction between uranyl acetate and insect cell culture medium compounds, including protein hydrolysates [19]. Of note, new chemically defined insect cell culture media might also reduce this problem [20]. Different approaches have been investigated to overcome the drawbacks of negative staining [12]. SEM-Alcian Blue has been studied here as a possible alternative. On the one hand, TEM has been traditionally used for viral intraparticle characterization, while SEM is generally applied for a broader screening of biological populations [21,22]. Novel preparation methods, such as ionic liquid infiltration [22] or virus quantification by Prep/g [23] have been reported to assess bacterial and viral preparations with SEM in the recent years. In the same line, the use of Alcian Blue as a solution for grid pre-treatment was shown to increase the adsorption of nanoparticles in this work, thus allowing to improve the detection of these particles without negative staining (Figure 2). However, the differentiation of VLPs from EVs was not possible due to their similar morphology. This new label-free preparation method is an interesting approach to use in combination with X-ray spectroscopy [4], SRFM [24], or “wet” SEM [22] to deepen into nanoparticle characterization. Alternatively, the low contrast present in biological samples can also be overcome in EM using cryo-TEM (Figure 3). However, this technique requires an adjustment of the cryogenic freezing protocol for each sample depending on its

physicochemical properties [25], and longer times are needed per analysis. Overall, all EM techniques demand a high expertise from the user and often entail long sample analysis times (Table 3). Then, the development of more automatic and high throughput complementary methods is required to monitor the VLP manufacturing process in a faster manner.

SRFM, NTA and flow virometry can be implemented to this purpose since they allow mass quantification of nanoparticles. However, sample standardization and technical expertise is still critical for an adequate nanoparticle assessment (Table 3). A microscope equipped with advanced capture and image processing modules, the optimization of acquisition conditions together with different imaging software are required for SRFM. Additional process automatization should be developed to widen its application since the time required for sample analysis is still high and operator-dependent. In NTA, relevant parameters to be considered are the camera level and the detection threshold during nanoparticle analysis [26]. These settings should be manually adjusted for both light scattering and fluorescence lasers in order to record the video and perform the automatic quantification. NTA measurements depend on the refractive index (RI) of each particle and the nanoparticle containing solution. Thus, different specific settings were applied to measure HEK 293 and Sf9 cell supernatants (Table 1). Another important feature affecting the final output with NTA is size heterogeneity of nanoparticle populations in the sample, which hinder the quantification of the small subpopulations due to the screening effect of higher particles, as reported by van der Pol et al. [26]. Regarding flow virometry, differences in the measurements due to inter-equipment variability have been pointed as one of the major challenges of this technique. Nevertheless, the use of commercial beads as standard nanoparticles and the implementation of Mie correlations have contributed to solve this problem [27–29]. Similarly, tunable resistive pulse sensing (TRPS), Atomic Force Microscopy (AFM) and field-flow fractionation coupled to multiangle light scattering (FFF-MALS) are single particle analysis methods that can be implemented for nanoparticle characterization [16].

#### 4.2. Ultrastructural analysis

Single particle analysis conducted by SRFM, NTA and flow virometry is an interesting option for characterization analyses since specific labeling can be applied to study different nanoparticle populations [30,31]. The use of the fluorescently tagged Gag polyprotein enabled the differentiation of VLPs from the other co-produced nanoparticle populations in this work. These analytical methods have also been successfully used in combination with immunolabeling to quantitatively assess viral populations [31]. A step further has been recently achieved in SRFM with the possibility to detect nucleic acids and the lipid membrane in VLPs [32]. The commercially available ViroCyt® flow cytometer has been similarly used to quantify different viral isolates, including the Ebola virus [33]. Still, the detection of VLPs with ViroCyt® has not been reported so far [23]. Nevertheless, none of these techniques achieve the levels of nanoparticle resolution as compared to EM methods (Table 3).

Among the different EM methods evaluated, cryo-TEM showed a higher benefit compared to TEM and SEM since the native conformation of the different nanoparticles could be assessed. The ultrastructural analysis of the different VLP, EV and BV subpopulations could be described in detail, with remarkable differences between Gag-eGFP and Gag VLPs. The Gag polyprotein is known to travel to the vicinity of the plasma membrane, aggregate with other Gag monomers, and bud to the extracellular space as an immature HIV-1 particle (Figure 3J) [15,34]. Interestingly, Gag-eGFP VLPs do not achieve the expected organized structure as Gag VLPs probably due to the eGFP fusion that alters the native budding process [35]. These differences could not be detected by TEM owing to the interference of negative staining with the samples [1,36,37]. To the best of our knowledge, this is the first time where the intraparticle protein organization of a Gag-eGFP VLP was observed. Therefore, it is shown that fusion proteins can introduce morphological alterations in the structure of the nanoparticles produced and cryo-TEM is an interesting method to identify them.



### 4.3. Particle size distribution

The PSD of VLPs has been studied with the six methods evaluated in this work. Typically, the VLP mean diameter is comprised between 100 and 200 nm, as observed by TEM, cryo-TEM, NTA and flow virometry [38]. Non-symmetric right-skewed distributions were observed for VLPs measured with the different techniques. Similar PSDs of HIV-1 Gag VLPs produced in CAP-T and CHO cells were shown by Gutierrez-Granados et al. and Steppert et al., respectively [39,40]. Bigger fluorescent particles, specially found in Sf9 samples when measured by NTA and flow virometry, could be related to the aggregation of VLPs or the interaction of VLPs with other cellular compounds released to the medium. SEM and SRFM presented higher PSD in comparison to the rest of analytical technologies. SEM analysis of HEK 293 samples resulted in a PSD of  $296 \pm 88$  nm, which could indicate that several EVs were quantified instead of VLPs, since microvesicles can reach up to 2000 nm [13]. HyVolution2 SRFM yielded the highest VLP PSD values in both cell platforms ( $> 250$  nm), which has also been observed by Xiao and co-workers when analyzing Cy5-labeled adeno-associated viruses [41], and could be attributed to the convolution effect of light. In this case, the fluorochrome individual intensity does not necessarily correlate with the real particle size and might result in particle size diameter overestimation [42]. The use of more resolutive SRFM technologies, such as stimulated emission depletion (STED) or stochastic optical reconstruction microscopy (STORM) could reduce this effect [43]. However, STED and STORM require specific fluorophores that tolerate the high laser intensities applied and also a higher level of expertise and equipment infrastructure in comparison to HyVolution2 SRFM.

The PSD of EVs was assessed by NTA and flow virometry (Figure 5 & 6). In both cases, EVs presented an average diameter comprised between 100 and 200 nm, similar to that of VLPs. Nonetheless, a right-skewed distribution with vesicles diameters from 45 to 500 nm was observed, especially in Sf9 samples. These results correlate with the existence of several types of EVs, encompassing exosomes and microvesicles, and BVs as visualized in cryo-TEM micrographs (Figure 3). Of note, the PSD of rod-shape baculoviruses could not be accurately characterized by

any of these methods due to the fact they assume all nanoparticles are spherical. Van der Pol and coworkers also observed the size heterogeneity of EVs, with diameters ranging between 70 and 800 nm. They report a minimum detection limit for EVs of 70 - 90 nm with NTA and 150 - 190 nm by flow virometry [26]. Lower EV detection limits of 45 nm with NTA and 100 nm by flow virometry were reported in this work. The sample composition and also the implementation of the V-SSC instead of the 488 nm SSC in flow virometry could contribute to explain these differences [44]. Still, a higher level of accuracy is possible by using National Institute of Standards and Technology (NIST)-traceable beads in the Mie correlation for the measurements performed with flow virometry.

#### **4.4. Particle concentration**

SRFM, NTA and flow virometry were compared for the quantification of nanoparticles in HEK 293 and Sf9 cell samples (Figure 4 - 6 and Table 2). Compared to SRFM and NTA, flow virometry yielded a lower concentration of nanoparticles being around 30-fold lower for VLPs and > 60-fold lower for EVs (Table 2). Similar differences in quantification by flow virometry have also been reported by van der Pol and co-authors in the analysis of urinary vesicles [26]. Differences in nanoparticle quantification between techniques could be related to the swarm effect, which is based in the fact that more than one particle passes through the detector simultaneously. However, the analysis of the same sample dilutions by flow virometry and NTA resulted in a linear correlation between both methods (fluorescent particles,  $R^2 > 0.99$ ; total particles  $R^2 > 0.91$ ), indicating that the swarm effect could not be the main reason behind these results (Supplementary Materials, S3). On the other hand, it is also possible that the detection of small particles fell in the range of the background signal of the cytometer, thus contributing to reduce the final titers. Even though the average particle size of EVs and VLPs was above the minimum detection diameter of flow virometry, additional refinement of the Mie correlation could still be required to adequately explain these data.

Analysis of the different nanoparticle populations in each platform revealed that at least 50 % of the total particles produced did not correspond to VLPs (Table 2). The possibility to discriminate

but also simultaneously quantify VLPs and the rest of specimens by NTA and flow virometry represents a remarkable advantage for nanoparticle-based bioprocesses. However, further refinement of these light scattered-based methodologies is required, since background levels of particles in the same range as EVs have been quantified in cell culture media analyses (Supplementary Materials, S1).

## 5. Conclusion

The selection of an adequate analytical method is essential in the VLP characterization process. Among the six methodologies studied in this work, cryo-TEM was shown as the best method to evaluate the nanoparticle structure in its native conformation with the highest resolution. Detailed characterizations of the different EV and BV subpopulations, concomitantly expressed with VLPs, were observed in HEK293 and Sf9 cell-derived productions. Alternatively, the high-throughput analysis of VLPs and their differentiation from other contaminant particles was achieved by SRFM, NTA and flow virometry. From these analytical technologies, flow virometry showed to be the most rapid method to quantify the concentration and PSD of the different nanoparticle subpopulations simultaneously. However, further improvements are needed to reduce the differences between quantification results. Taken together, these results highlight the combined use of cryogenic electron microscopy with high throughput techniques to improve vaccine development and nanoparticle-based processes.

**Table 2. Quantification of VLP and EV concentrations from transfected HEK 293 and baculovirus infected Sf9 cell supernatants using different analytical methods.**

Technique	VLPs ( $10^9$ /mL)			EVs ( $10^9$ /mL)	
	FV	NTA	SRFM	FV	NTA
<b>HEK 293</b>	$0.2 \pm 0.0$	$5.0 \pm 0.5^*$	$4.0 - 43.0^*$	$0.2 \pm 0.0$	$16.6 \pm 2.9^{**}$
<b>Sf9</b>	$0.2 \pm 0.0$	$8.6 \pm 2.1^*$	$6.6 - 74.5^*$	$0.3 \pm 0.0$	$9.7 \pm 1.6^{**}$
<b>Fold difference (Sf9:HEK 293)</b>	1.5	1.7	1.7	1.2	0.6

\*From González-Domínguez 2019 [5]; \*\*EVs from only diffracting particles (see Materials and Methods)

Table 3. Comparison of the different analytical technologies assessed in this work.

Parameter	TEM	SEM	Cryo-TEM	HyVolution2 SRFM	NTA	Flow virometry
Complexity	+++	+++	+++++	+++	++	++
Time of measurement	++++	++++	+++++	+++	++	+
Small detected EV, virus or viral-structure	Nanometric (<10 nm) [45]	Nanometric (<10 nm) [21]	Atomic [46]	Nanometric (140 nm) [47]	Nanometric (30 nm) [48] <sup>e</sup>	Nanometric (100-200 nm) [26]
Pros	Widely used, ultrastructural analysis	Surface analysis of viral populations	Ultrastructural analysis in its native form	Direct visualization, compatible with fluorescence	Easy handling, compatible with fluorescence	Simultaneous analysis of different light scatter and fluorescence labeling
Cons	Staining required, working under vacuum conditions	Working under vacuum conditions	Time consuming, working at cryogenic temperatures	Data analysis, convolution effect of light	Screening effect, acquisition settings variability	Sensitivity, inter-equipment variability

## 6. Acknowledgments

The help of Manuela Costa (Servei de Cultius Cel·lulars, Producció d'Anticossos i Citometria, UAB) and Ángel Calvache and Jorge Fomaro (Beckman Coulter) for facilitating access to the Cytotflex XL equipment and the Megamix-Plus beads is very appreciated. The authors would like to acknowledge the help of Marti de Cabo and Emma Rossinyol (Servei de Microscòpia, UAB, Barcelona, Spain) for the assistance with EM methodologies, Dr Mònica Roldan for the support with SRFM (Servei d'Anatomia Patològica, Hospital Sant Joan de Déu, Barcelona, Spain) and Dr Joshua Welsh (NIH, Maryland, USA) for the help with FCMPass Software.

## 7. Literature

1. Cervera, L.; Gutiérrez-Granados, S.; Martínez, M.; Blanco, J.; Gòdia, F.; Segura, M.M. Generation of HIV-1 Gag VLPs by transient transfection of HEK 293 suspension cell cultures using an optimized animal-derived component free medium. *J. Biotechnol.* **2013**, *166*, 152–165.
2. Puente-Massaguer, E.; Lecina, M.; Gòdia, F. Integrating nanoparticle quantification and statistical design of experiments for efficient HIV-1 virus-like particle production in High Five cells. *Appl. Microbiol. Biotechnol.* **2020**, *104*, 1569–1582.
3. Gállego Ossul, I. Estructura y propiedades de las placas de cromatina de los cromosomas metafásicos: Estudio mediante técnicas de microscopía TEM, AFM y Espectroscopia de Fuerza Atómica, Universitat Autònoma de Barcelona, 2010.
4. González-Domínguez, I.; Grimaldi, N.; Cervera, L.; Ventosa, N.; Gòdia, F. Impact of physicochemical properties of DNA/PEI complexes on transient transfection of mammalian cells. *N. Biotechnol.* **2019**, *49*, 88–97.
5. González-Domínguez, I.; Puente-Massaguer, E.; Cervera, L.; Gòdia, F. Quantification of the HIV-1 virus-like particle production process by super-resolution imaging: From VLP budding to nanoparticle analysis. *Biotechnol. Bioeng.* **2020**, bit.27345.
6. Malvern Instruments Limited *Determining fluorescence Limit of Detection with Nanoparticle Tracking Analysis (NTA)*; 2015;
7. de Rond, L.; Coumans, F.A.W.; Nieuwland, R.; van Leeuwen, T.G.; van der Pol, E. Deriving Extracellular Vesicle Size From Scatter Intensities Measured by Flow Cytometry. *Curr. Protoc. Cytom.* **2018**, *86*, 1–14.
8. Welsh, J.A.; Horak, P.; Wilkinson, J.S.; Ford, V.J.; Jones, J.C.; Smith, D.; Holloway, J.A.; Englyst, N.A. FCM PASS Software Aids Extracellular Vesicle Light Scatter Standardization. *Cytom. Part A* **2019**, cyto.a.23782.
9. Ellis, E.A. Staining Sectioned Biological Specimens for Transmission Electron

- Microscopy: Conventional and En Bloc Stains. In *Electron Microscopy: Methods and Protocols, Methods in Molecular Biology ( Methods and Protocols)*, vol 1117; Kuo, J., Ed.; Humana Press: Totowa, NJ, USA, 2014; pp. 57–72 ISBN 978-1-62703-776-1.
10. Cervera, L.; Fuenmayor, J.; González-Domínguez, I.; Gutiérrez-Granados, S.; Segura, M.M.; Gòdia, F. Selection and optimization of transfection enhancer additives for increased virus-like particle production in HEK293 suspension cell cultures. *Appl. Microbiol. Biotechnol.* **2015**, *99*, 9935–9949.
  11. González-Domínguez, I.; Gutiérrez-Granados, S.; Cervera, L.; Gòdia, F.; Domingo, N. Identification of HIV-1–Based Virus-like Particles by Multifrequency Atomic Force Microscopy. *Biophys. J.* **2016**, *111*, 1173–1179.
  12. Charlton Hume, H.K.; Vidigal, J.; Carrondo, M.J.T.; Middelberg, A.P.J.; Roldão, A.; Lua, L.H.L. Synthetic biology for bioengineering virus-like particle vaccines. *Biotechnol. Bioeng.* **2019**, *116*, 919–935.
  13. Akers, J.C.; Gonda, D.; Kim, R.; Carter, B.S.; Chen, C.C. Biogenesis of extracellular vesicles (EV): exosomes, microvesicles, retrovirus-like vesicles, and apoptotic bodies. *J. Neurooncol.* **2013**, *113*, 1–11.
  14. Wang, Q.; Bosch, B.-J.; Vlak, J.M.; van Oers, M.M.; Rottier, P.J.; van Lent, J.W.M. Budded baculovirus particle structure revisited. *J. Invertebr. Pathol.* **2016**, *134*, 15–22.
  15. Göttlinger, H.G. *HIV-1 Gag : a Molecular Machine Driving Viral Particle Assembly and Release*; Carla KuCarla Kuiken, BrianFoley, Thomas Leitner, Cristian Apetrei, Beatrice Hahn, Ilene Mizrachi, James Mullins, Andrew Rambaut, StevenWolinsky, and B.K. editors., Ed.; Los Alamos National Laboratory, Theoretical Biology andBiophysics: Los Alamos, New Mexico., 2001; ISBN 0269-9370.
  16. Heider, S.; Metzner, C. Quantitative real-time single particle analysis of virions. *Virology* **2014**, *462–463*, 199–206.
  17. De Carlo, S.; Harris, J.R. Negative staining and cryo-negative staining of macromolecules

- and viruses for TEM. *Micron* **2011**, *42*, 117–131.
18. Lua, L.H.L.; Connors, N.K.; Sainsbury, F.; Chuan, Y.P.; Wibowo, N.; Middelberg, A.P.J. Bioengineering virus-like particles as vaccines. *Biotechnol. Bioeng.* **2014**, *111*, 425–440.
  19. Palomares, L.A.; Realpe, M.; Ramírez, O.T. An Overview of Cell Culture Engineering for the Insect Cell-Baculovirus Expression Vector System (BEVS). In *Methods in Molecular Biology*; 2015; Vol. 5, pp. 501–519 ISBN 978-3-319-10319-8.
  20. Thermo Fisher Scientific *ExpiSf™ Expression System*; 2020;
  21. Gencer, D.; Bayramoglu, Z.; Nalcacioglu, R.; Kleespies, R.G.; Demirbag, Z.; Demir, I. Characterisation of three Alphabaculovirus isolates from the gypsy moth, *Lymantria dispar dispar* (Lepidoptera: Erebidae), in Turkey. *Biocontrol Sci. Technol.* **2018**, *28*, 107–121.
  22. Golding, C.G.; Lamboo, L.L.; Beniac, D.R.; Booth, T.F. The scanning electron microscope in microbiology and diagnosis of infectious disease. *Sci. Rep.* **2016**, *6*, 26516.
  23. Blancett, C.D.; Fetterer, D.P.; Koistinen, K.A.; Morazzani, E.M.; Monninger, M.K.; Piper, A.E.; Kuehl, K.A.; Kearney, B.J.; Norris, S.L.; Rossi, C.A.; et al. Accurate virus quantitation using a Scanning Transmission Electron Microscopy (STEM) detector in a scanning electron microscope. *J. Virol. Methods* **2017**, *248*, 136–144.
  24. Pedersen, M.; Jamali, S.; Saha, I.; Daum, R.; Bendjennat, M.; Saffarian, S. Correlative iPALM and SEM resolves virus cavity and Gag lattice defects in HIV virions. *Eur. Biophys. J.* **2019**, *48*, 15–23.
  25. Thompson, R.F.; Walker, M.; Siebert, C.A.; Muench, S.P.; Ranson, N.A. An introduction to sample preparation and imaging by cryo-electron microscopy for structural biology. *Methods* **2016**, *100*, 3–15.
  26. van der Pol, E.; Coumans, F. a W.; Grootemaat, A.E.; Gardiner, C.; Sargent, I.L.; Harrison, P.; Sturk, A.; van Leeuwen, T.G.; Nieuwland, R. Particle size distribution of exosomes and microvesicles determined by transmission electron microscopy, flow cytometry,

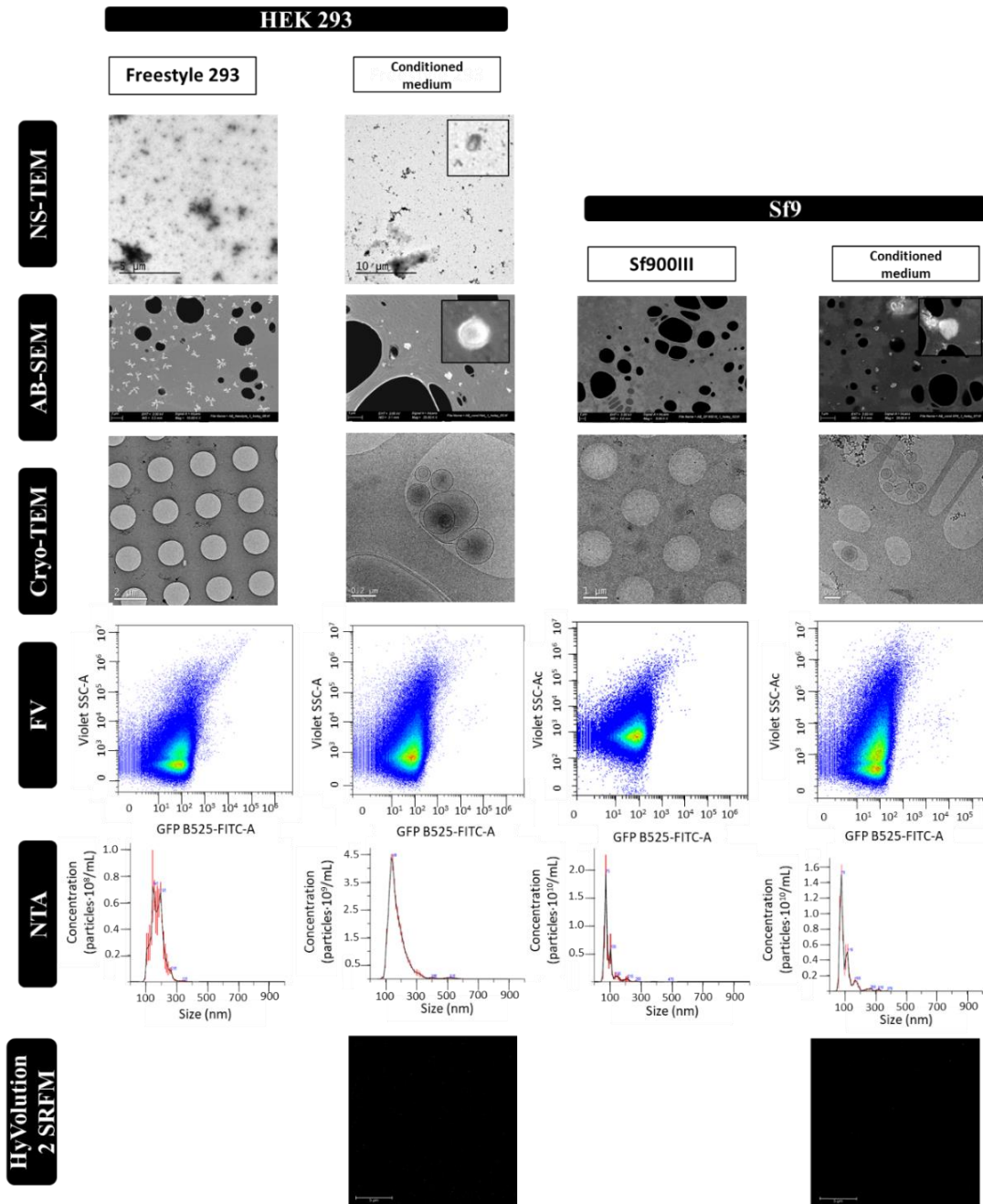
- nanoparticle tracking analysis, and resistive pulse sensing. *J. Thromb. Haemost.* **2014**, *12*, 1182–1192.
27. Welsh, J.A.; Holloway, J.A.; Wilkinson, J.S.; Englyst, N.A. Extracellular Vesicle Flow Cytometry Analysis and Standardization. *Front. Cell Dev. Biol.* **2017**, *5*, 1–7.
28. Van Der Pol, E.; Hoekstra, A.G.; Sturk, A.; Otto, C.; Van Leeuwen, T.G.; Nieuwland, R. Optical and non-optical methods for detection and characterization of microparticles and exosomes. *J. Thromb. Haemost.* **2010**, *8*, 2596–2607.
29. Welsh, J.A.; Horak, P.; Wilkinson, J.S.; Ford, V.J.; Jones, J.C.; Smith, D.; Holloway, J.A.; Englyst, N.A. FCM<sub>PASS</sub> Software Aids Extracellular Vesicle Light Scatter Standardization. *Cytom. Part A* **2019**.
30. Yang, Z.; Sharma, A.; Qi, J.; Peng, X.; Lee, D.Y.; Hu, R.; Lin, D.; Qu, J.; Kim, J.S. Super-resolution fluorescent materials: an insight into design and bioimaging applications. *Chem. Soc. Rev.* **2016**, *45*, 4651–4667.
31. Zamora, J.L.R.; Aguilar, H.C. Flow virometry as a tool to study viruses. *Methods* **2017**, *134–135*, 87–97.
32. Puente-Massaguer, E.; Lecina, M.; Gòdia, F. Application of advanced quantification techniques in nanoparticle-based vaccine development with the Sf9 cell baculovirus expression system. *Vaccine* **2020**, *38*, 1849–1859.
33. Rossi, C.; Kearney, B.; Olschner, S.; Williams, P.; Robinson, C.; Heinrich, M.; Zovanyi, A.; Ingram, M.; Norwood, D.; Schoepp, R. Evaluation of ViroCyt® Virus Counter for Rapid Filovirus Quantitation. *Viruses* **2015**, *7*, 857–872.
34. Strauss, J.D.; Hammonds, J.E.; Yi, H.; Ding, L.; Spearman, P.; Wright, E.R. Three-Dimensional Structural Characterization of HIV-1 Tethered to Human Cells. *J. Virol.* **2016**, *90*, 1507–1521.
35. Pornillos, O.; Higginson, D.S.; Stray, K.M.; Fisher, R.D.; Garrus, J.E.; Payne, M.; He, G.P.; Wang, H.E.; Morham, S.G.; Sundquist, W.I. HIV Gag mimics the Tsg101-recruiting



- activity of the human Hrs protein. *J. Cell Biol.* **2003**, *162*, 425–434.
36. Chen, Y.; Wu, B.; Musier-Forsyth, K.; Mansky, L.M.; Mueller, J.D. Fluorescence fluctuation spectroscopy on viral-like particles reveals variable Gag stoichiometry. *Biophys. J.* **2009**, *96*, 1961–1969.
37. Venereo-Sanchez, A.; Gilbert, R.; Simoneau, M.; Caron, A.; Chahal, P.; Chen, W.; Ansorge, S.; Li, X.; Henry, O.; Kamen, A. Hemagglutinin and neuraminidase containing virus-like particles produced in HEK-293 suspension culture: An effective influenza vaccine candidate. *Vaccine* **2016**, *34*, 3371–3380.
38. Inamdar, K.; Floderer, C.; Favard, C.; Muriaux, D. Monitoring HIV-1 Assembly in Living Cells: Insights from Dynamic and Single Molecule Microscopy. *Viruses* **2019**, *11*, 72.
39. Steppert, P.; Burgstaller, D.; Klausberger, M.; Berger, E.; Aguilar, P.P.; Schneider, T.A.; Kramberger, P.; Tover, A.; Nöbauer, K.; Razzazi-Fazeli, E.; et al. Purification of HIV-1 gag virus-like particles and separation of other extracellular particles. *J. Chromatogr. A* **2016**, *1455*, 93–101.
40. Gutiérrez-Granados, S.; Cervera, L.; Segura, M. de L.M.; Wölfel, J.; Gòdia, F. Optimized production of HIV-1 virus-like particles by transient transfection in CAP-T cells. *Appl. Microbiol. Biotechnol.* **2016**, *100*, 3935–47.
41. Ping-Jie Xiao, Chengwen Li, A.N. and R.J.S.; Xiao, P.J.; Li, C.; Neumann, A.; Samulski, R.J. Quantitative 3D tracing of gene-delivery viral vectors in human cells and animal tissues. *Mol. Ther.* **2012**, *20*, 317–328.
42. Sarder, P.; Nehorai, A. Deconvolution methods for 3-D fluorescence microscopy images. *IEEE Signal Process. Mag.* **2006**, *23*, 32–45.
43. Schermelleh, L.; Ferrand, A.; Huser, T.; Eggeling, C.; Sauer, M.; Biehlmaier, O.; Drummen, G.P.C. Super-resolution microscopy demystified. *Nat. Cell Biol.* **2019**, *21*, 72–84.
44. McVey, M.J.; Spring, C.M.; Kuebler, W.M. Improved resolution in extracellular vesicle
-

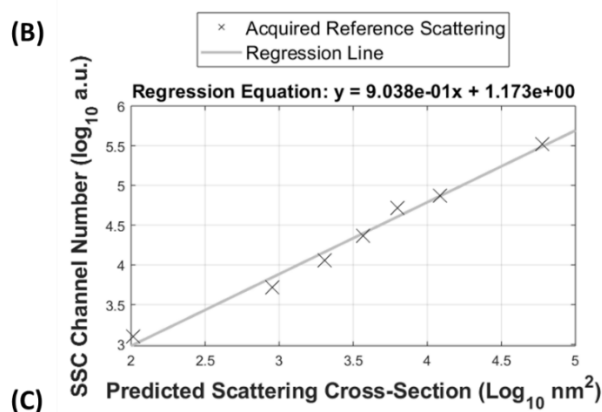
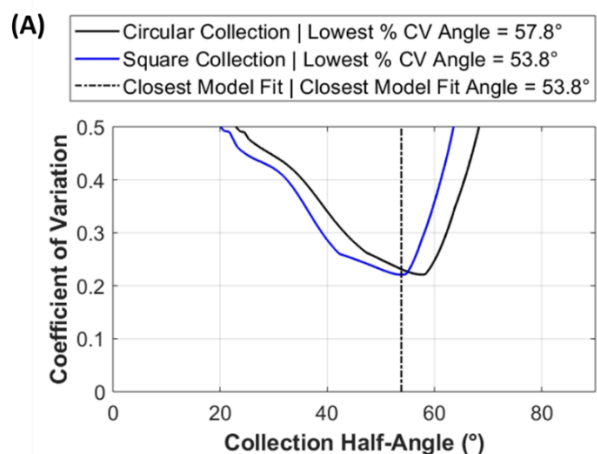
- populations using 405 instead of 488 nm side scatter. *J. Extracell. Vesicles* **2018**, *7*, 1–11.
45. Popov, V.L.; Tesh, R.B.; Weaver, S.C.; Vasilakis, N.; Popov, V.L.; Tesh, R.B.; Weaver, S.C.; Vasilakis, N. Electron Microscopy in Discovery of Novel and Emerging Viruses from the Collection of the World Reference Center for Emerging Viruses and Arboviruses (WRCEVA). *Viruses* **2019**, *11*, 477.
46. Jiang, W.; Tang, L. Atomic cryo-EM structures of viruses. *Curr. Opin. Struct. Biol.* **2017**, *46*, 122–129.
47. Borlinghaus, R.T.; Kappel, C. HyVolution—the smart path to confocal super-resolution. *Nat. Methods* **2016**, *13*, i–iii.
48. Kramberger, P.; Ciringir, M.; Štrancar, A.; Peterka, M. Evaluation of nanoparticle tracking analysis for total virus particle determination. *Viol. J.* **2012**, *9*, 265.

## 8. Supplementary materials



Supplementary Materials S1. Negative control analyses: cell culture and conditioned media controls. FreeStyle 293 and Sf900III media for HEK 293 and Sf9 cells were analyzed by NS-TEM, AB-SEM and cryo-TEM, NTA, flow virometry and SRFM, respectively. Analyses were performed applying the same sample preparation and equipment set up than in the VLP analyses. In NS-TEM, AB-SEM and cryo-TEM analyses of FreeStyle, the presence of salts was detected while low electrodense aggregates were observed in cryo-TEM images of Sf900III cell culture media. In EM micrographs of both conditioned media, the presence of EVs was depicted. NTA analyses of FreeStyle medium, conditioned HEK 293 medium, Sf900III and Sf9 conditioned media had a mean hydrodynamic diameter of  $174 \pm 39$  nm,  $174 \pm 65$  nm,  $92.7 \pm 74.6$  nm,  $101 \pm 47$  nm with a concentration of  $0.6 \pm 0.1 \text{ E}+9$ ,  $17.6 \pm 0.9 \text{ E}+9$ ,  $24.4 \pm 1.1 \text{ E}+9$ ,  $27.3 \pm 1.5 \text{ E}+9$  diffracting particles/ml, respectively adapted from [1,2]. Flow virometry analyses of FreeStyle

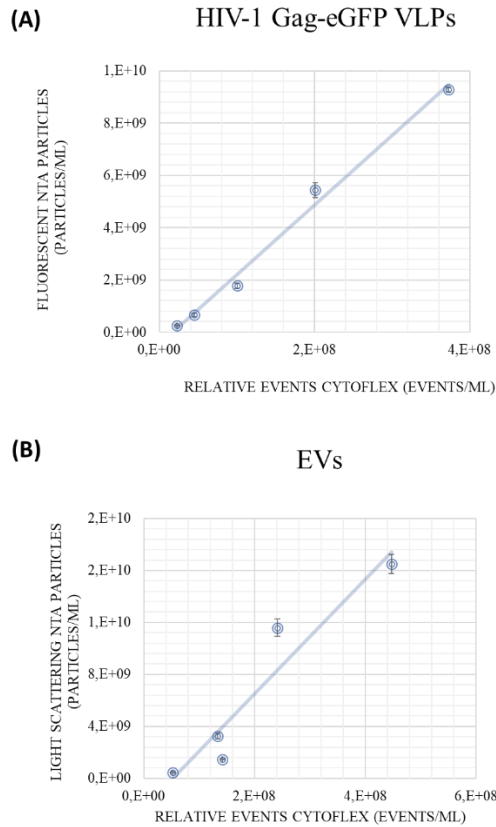
medium, conditioned HEK 293 medium, Sf900III and Sf9 conditioned had a concentration of  $0.08 \text{ E}+9$ ,  $0.17 \text{ E}+9$ ,  $0.07 \text{ E}+9$ ,  $0.77 \text{ E}+9$  of EV particles respectively when same settings were applied. HyVolution2 SRFM analyses of conditioned media adapted from [2] using the same conditions showed no signal due to the absence of HIV-1 Gag-eGFP VLPs, as expected.



(C)

Bead Diameter (nm)	Median V-SSC (a.u.)	rCV (%)
100	1246.4	18.9
160	5248.8	10.34
200	11542.3	3.53
240	23266.4	6.52
300	51993.8	2.61
500	75025.8	3.83
900	328552.7	2.42

Supplementary Materials S2. MIE correlation for EV analysis with FCMPass Software. (A) Collection half-angle (B) Lineal regression SSC vs. predicted scattering cross-section (C) Acquired reference Megamix bead information used.



**Supplementary Materials S3. Nanoparticle correlation between flow virometry and NTA (A) HIV-1 Gag-eGFP VLPs measured with NTA using the fluorescence filter and the population corresponding to fluorescent particles in flow virometry are represented: (Fluorescent particles/mL) = 26,67 ( events /mL) - 5E+08;  $R^2 = 0,9909$ ; (B) EVs measured with light scattering in NTA and the population corresponding to EVs in flow virometry are represented: (Light Scattering particles/mL) = 44,18 ( events /mL) - 2E+09;  $R^2 = 0,9082$ .**

## **Chapter 7**

### **A four-step purification process for HIV-1 Gag VLPs: from cell culture supernatant to lyophilization**

---

### **Abstract**

HIV-1 Gag-based virus-like particles (VLPs) have high potential as scaffold for the development of chimeric vaccines and delivery strategies. The obtention of preparations that can be preserved independently from cold chain is highly desirable to facilitate distribution and access worldwide. In this work, a nimble purification process has been developed facilitating the production of HIV-1 Gag VLPs. Suspension-adapted HEK 293 cells cultured in chemically defined cell culture media were used to produce the VLPs by transient gene expression (TGE). A four-step down-stream process (DSP) consisting of membrane filtration, ion exchange chromatography, desalting column and lyophilization was performed. Membrane and resin capacity were optimized for each step and the total amount of protein, dsDNA, VLPs and EVs content was analyzed for the different stages. A concentration of  $2.2 \pm 0.8 \cdot 10^9$  VLPs/mL in the lyophilized samples was obtained after its storage at room temperature for two months. The morphology and structural integrity were assessed by cryo-TEM. Remarkably, the EV content was reduced by almost 100%. Besides, these first results in enveloped VLP lyophilization offer great promise to overcome the difficulty to distribute vaccines in poorly served remote areas thanks to increased vaccine stability until final administration.

**Keywords:** HIV-1 VLPs, purification, lyophilization, EVs, nanoparticle quantification.

## 1. Introduction

Virus-like particles (VLPs) are recognized as one of most promising strategies in recombinant vaccine development due to their ability to mimic native viruses with the lack of viral genome. Their highly organized and repetitive antigen-presenting structure has shown to stimulate both cellular and humoral immune responses [1,2]. Furthermore, VLPs represent also an interesting platform to be used in DNA and drug delivery applications [1,3,4]. Among the different candidates, HIV-1 Gag VLPs offer great promise since they have been used for the development of HIV-1 vaccine candidates in preclinical studies [5], but also as scaffold for chimeric candidates against other diseases [1]. The production of HIV-1 Gag VLPs needs for the expression of the Gag polyprotein in a producer cell line. Upon expression, Gag travels to the cell membrane and after an oligomerization process, VLPs bud to the cell culture supernatant. Thus, the final nanoparticles are enveloped by a host cell lipid membrane [6], with an expected size between 100 – 200 nm. Due to their enveloped structure, HIV-1 Gag VLPs are more sensitive to shear stress forces, osmotic pressure and extreme pH [5,7]. Owing to these particularities, the obtention of these VLPs has been a challenge during the last decades.

Purification of HIV-1 Gag VLPs was initially performed by centrifugation followed by ultracentrifugation to separate the cell culture supernatant from cells and to further concentrate the VLPs up to 1000-fold, respectively [5]. These methods are non-scalable and labor-intensive, which may cause inter-experimental variabilities. To overcome these problems, efforts are being undertaken towards the development of cost-effective scalable processes [5,8,9]. New matrices have been developed to maximize purification yields of viral structures by reducing the mechanical stress, increasing the pore size and using more inherent materials [7,9]; polymer-grafted beads, monoliths, membrane adsorbers, gigapore or mixed mode resins in chromatographic steps have been successfully applied to VLPs and viral vectors [8–13]. Membrane-based unit operations, like filtration or ultrafiltration have been also successfully reported for influenza VLPs; the use of tangential flow filtration (TFF) with large pore sizes, and hollow fibers or membrane cassettes has been reported [14–16]. Alternative operation units, such



as two-phase extraction or flocculation have been also described in VLP purification strategies [17,18]. With views to polish the VLPs from process-related impurities and prepare them for formulation, diafiltration or size exclusion chromatography (SEC) are mainly used [18]. Polishing steps aim to remove dsDNA, host-cell proteins (HCP) and other contaminant particles that might co-elute with VLPs, such as EVs. Finally, the preservation of purified HIV-1 Gag VLPs is another general concern in the field. While cold chain storage is still the classical approach, the instability associated to this step prior to administration can affect the efficiency of the candidate [19]. Engineering VLPs at protein level [1] or the optimization of formulation buffer by the addition of sugars [20] are some reported solutions. Nonetheless, less information is available about the thermostability of HIV-1 Gag VLPs and more appealing strategies such as freeze-drying have not been tested, to date [21].

In addition to the reported challenges in HIV-1 Gag VLP purification, the separation of these enveloped structures from EVs is highly difficult since they share similar physicochemical and biochemical properties [5]. In this regard, no complete separation process has been reported in the literature. Nonetheless, an enrichment of HIV-1 Gag VLPs over total particles has been described by TFF, IEX chromatography or heparin affinity chromatography, giving hope for progress in this matter [15,22,23]. Limitations at analytical level for the specific quantification of VLPs and EVs strongly contribute to this fact.

The use of appropriate analytical methods is pivotal to ensure the structural integrity of the VLPs, as well as its separation from other nanoparticles during process development [14]. In previous works, Gag polyprotein has been fused to the enhanced green fluorescence protein (eGFP). By doing so, nanoparticle particle analysis (NTA) and flow virometry methods coupled to fluorescence have allowed the simultaneous quantification of VLPs and EVs within the same samples. Compared to other biological and biochemical methods [3], these biophysical assays are not only able to distinguish between VLPs and EVs, but also to specifically quantify assembled VLP structures from free Gag monomer released during cell culture death [5,24,25].

In this work, the stability, purification and preservation of HIV-1 Gag VLPs have been studied. The combination of membrane-based and chromatographic methods together with lyophilization is proposed here. Concretely, a purification process consisting of flocculation and depth filtration to obtain the clarified supernatant, IEX chromatography to concentrate the VLPs and SEC to polish and prepare the purified material for lyophilization has been developed. VLP, EV, dsDNA and total protein concentration was quantified during the different unit operations, as well as, the capacity, yield and operation time. The obtained data on HIV-1 Gag VLP purification and preservation will contribute to define strategies that will facilitate their manufacturing and distribution worldwide [21].

## **2. Materials and Methods**

### **2.1. Mammalian cell line, culture conditions and transient gene expression**

The mammalian line used in this work is a serum-free suspension-adapted HEK 293 cell line (HEK 293SF-3F6, NRC, Montreal, Canada) kindly provided by Dr. Amine Kamen (McGill University, Montreal, Canada). Cells were cultured in disposable PETG Flask (Thermo Fisher, San Jose, CA, USA) at 37 °C, 5% CO<sub>2</sub>, 80% RH at 110 rpm in Multitron shakers (INFORS HT, New York, NY, USA) with HyCell™ TransFx-H medium from HyClone™ (GE HealthCare, Chicago, IL, USA). HyCell™ culture medium was supplemented with 0.1% Kolliphor188 (Sigma Aldrich, St Louis, IL, USA) and 4 mM GlutaMax (Gibco, Life Technologies, Thermo Fisher). Cell density and viability was routinely assessed with Vi-Cell XR (Beckman Coulter, Brea, CA, USA).

HIV-1 Gag-eGFP VLPs were obtained using transient gene expression with a pGag-eGFP plasmid, which codes for a Rev independent HIV-1 Gag protein fused in frame to the enhanced GFP [26]. Shortly, the HIV-1 (HBX2) Gag DNA with the Kozak consensus sequence was synthesized by TOPGene Technologies (Sant-Laurent, Canada) and cloned PmeI/NheI in pAdCMV5-GFPq to give rise the plasmid pAdCMV5-GagGFP.

HEK 293 cells were transfected using 25-kDa linear polyethylenimine (PEI) (PolySciences, Warrington, PA, USA) at  $2 \cdot 10^6$  cells/mL and VLP containing supernatants were harvested at 72 hours post transfection (hpt) by centrifugation at 1000 *xg* during 15 min. A final DNA concentration of 1  $\mu$ g/mL and a DNA to PEI mass ratio of 1:2. DNA/PEI complexes were formed by adding PEI to plasmid DNA diluted in fresh culture media (10 % of the total volume of the culture to be transfected). The mixture was incubated for 15 min to allow DNA/PEI complex formation. HIV-1 Gag-eGFP VLPs were harvested at 72 hours post transfection (hpt), ensuring cell culture viabilities higher than 90 % [24]. Supernatants were stored at 4 °C or -80 °C and cell pellets at -20 °C until analysis. Non-transfected negative controls reproducing cell growth conditions were also analyzed, for comparison.

## **2.2. Flow Cytometry**

The percentage of Gag-eGFP producing cells (GFP-positive cells) was assessed using a BD FACS Canto II flow cytometer (BD Biosciences, San Jose, CA, USA). The 488 nm laser was used for GFP-measurement in the FITC-A detector. A total of 20.000 events were analyzed in every sample. In first place, SSC-H vs FSC-A density plot and FSC-A vs FSC-H density plot were used to gate individual cell population. Then, positive GFP populations were assessed with GFP FITC-A vs APC-A density plot and the individual histogram for each fluorochrome. Gating was adjusted manually for each channel with an intensity comprised between 0.5 and  $1 \cdot 10^3$  multiple fluorescence units. The results were analyzed with the FACS DIVA software (BD Biosciences, San Jose, CA, USA).

## **2.3. Spectrofluorometry**

Quantification of Gag-eGFP in sample supernatants and pelleted cells was assessed using an in-house developed and validated spectrofluorometry assay [27]. Green fluorescence was measured at room temperature (RT) using a Cary Eclipse Fluorescence Spectrophotometer (Agilent Technologies, Santa Clara, CA, USA) with the following settings:  $\lambda_{ex}$ = 488 nm (slit 5 nm),  $\lambda_{em}$ = 510 nm (slit 10 nm). Relative fluorescence units (RFU) were calculated by subtracting fluorescence units (FU) values from non-transfected/infected samples. There is a linear

correlation between fluorescence intensity and p24 values determined using the HIV INNOTEST ELISA (Innogenetics NV, Gent, Belgium). RFU values can be converted to Gag-eGFP concentration values using the following equation (1):

$$Gag - GFP \left( \frac{ng}{mL} \right) = (3,245 \cdot RFU - 1,6833) \cdot 36 \quad (1)$$

where Gag-eGFP is the estimated concentration of polyprotein and RFU is the measured GFP fluorescence intensity in the samples. RFU values from different days were normalized with a 0.1 mg/mL quinine sulfate solution as internal control. To further convert Gag-GFP concentration to VLP concentration, it was assumed that one VLP contains 2500 Gag-GFP monomers with a molecular weight of 84-kDa per monomer [28].

#### **2.4. Flow Virometry**

Flow virometry experiments were performed with a CytoFLEX (Beckman Coulter Inc., Brea, CA, USA) with violet side scatter (V-SSC) 405 nm filter configuration. In all cases, samples were diluted with PBS 1 X until the abort rate value was below the 2 %. 300.000 events per sample were analyzed at a flow rate of 10  $\mu$ L/min. V-SSC vs B525-FITC density plots were used to gate the different particle populations. Gating was manually adjusted for each channel. The results were analyzed with the CytExpert software (Beckman Coulter). Nanoparticle concentrations were calculated with equation (2):

$$\frac{VLPs \text{ or } EVs}{mL} = \frac{events}{uL} \cdot \frac{uL}{mL} \cdot Dilution \quad (2)$$

#### **2.5. Total protein and double stranded DNA (dsDNA) quantification**

Total protein concentration was determined using RC/DC assay (Bio-Rad Laboratories, Hercules, CA, USA). The calibration curve was obtained using bovine serum albumin (BSA) standards (Thermo Fisher) diluted in distilled water with a concentration range of 50 – 250  $\mu$ g/mL. Double stranded DNA (dsDNA) quantification was performed with the Quant-iT™ PicoGreen® dsDNA kit (Life Technologies, Waltham, MA, USA). Protein and dsDNA assays were performed

---

according to the instructions from the manufacturer in a 96-well plate format respectively. The 96-well plates were read and analyzed with Synergy HTX multi-mode reader and Gen5 software, respectively (BioTek Instruments, Inc., Winooski, VT, USA). Since Gag-GFP VLPs emit at the same range as the Quant-iT™ PicoGreen® reagent, the native fluorescence was measured prior to the reagent addition and later subtracted to the fluorescence after the reaction.

## **2.6. Dynamic Light Scattering (DLS)**

Dynamic light scattering (DLS) experiments were performed using a Zetasizer Nano ZS instrument (Malvern instruments, Malvern, UK) with a He/Ne 633 nm laser at 173°. The hydrodynamic diameter and polydispersity index (PDI) were calculated with cumulative fit correlation at 25°C and 0.8872 cP. Briefly, HIV-1 Gag-eGFP VLPs were prepared in 60 µL final volume, and placed in disposable plastic cuvettes (Scharlab S.L., Barcelona, Spain) followed by automated experimental data collection where 11 scans were performed in each independent measurement.

## **2.7. Nanoparticle Tracking Analysis (NTA)**

HIV-1 Gag-eGFP VLPs and total particle content were analyzed by NTA. A NanoSight® NS300 device (Malvern Panalytical, Malvern, United Kingdom) equipped with a blue laser module (488 nm) and a neutral density filter was used to quantify GFP-fluorescent nanoparticles and total particle by light diffraction, respectively. Data were analyzed with the NanoSight® NTA 3.2 software (Malvern Panalytical), where camera level and detection threshold were adjusted manually for each sample. Prior to injection into the device chamber, each sample was diluted to obtain 1 mL sample with a concentration around  $10^8$  particles/mL. Three independent analyses were carried out. Videos of 60 s were recorded at RT and particles were identified and tracked by their Brownian motion. HIV-1 Gag-eGFP VLP concentrations were calculated as the total fluorescent particles and the concentration of EVs was calculated as the difference between light scattering particles and fluorescent particles.

## **2.8. Cryo-TEM**

Cryo-TEM analyses were performed at Servei de Microscòpia at Universitat Autònoma de Barcelona (UAB, Barcelona, Spain). A 2 - 3  $\mu\text{L}$  of sample were blotted onto 200 or 400 mesh Holey carbon grids (Micro to Nano, Wateringweg, the Netherlands) previously glow discharged in a PELCO easiGlow glow discharger unit (PELCO, Fresno, CA, USA). Samples were subsequently plunged into liquid ethane at  $-180\text{ }^{\circ}\text{C}$  using a Leica EM GP cryo workstation and observed in a Jeol JEM-2011 TEM electron microscope operating at 200 kV (JEOL USA, Pleasanton, CA, USA). During imaging, samples were maintained at  $-173\text{ }^{\circ}\text{C}$ , and pictures were taken using a CCD multiscan camera (Model No. 895, Gatan, Pleasanton, CA, USA).

## **2.9. Sodium dodecyl sulfate-polyacrylamide gel (SDS-PAGE) electrophoresis and Western blot analysis**

Precast TGX 4-15 % Midi Gel (Bio-Rad Laboratories, Hercules, CA, USA) were used in a Tris-Glycine buffer system. The protocol was adapted from Aguilar et al. and Joshi et al.[29,30]. Briefly, 45  $\mu\text{L}$  of sample were mixed with 20  $\mu\text{L}$  of 4x Laemili Buffer and 1.4 M DTT to a final concentration of 1% v/v. Each sample was incubated at  $95\text{ }^{\circ}\text{C}$  for 20 min. Precision Plus Protein™ Standards All Blue (Bio-Rad) was used as protein marker. Samples were diluted 1:4 with distilled water before its addition to the gel. The gel was run at 200 V(400 mA). Coomassie staining solution was used to stain the total protein in the SDS-PAGE. For the western blot analysis, proteins were blotted using Trans-Blot® turbo system (Bio-Rad) with 0.2  $\mu\text{m}$  nitrocellulose membranes and blocked with 5 % (w:v) skimmed milk overnight at  $4\text{ }^{\circ}\text{C}$ . Detection of HIV-1 Gag-GFP protein was performed by incubation with primary mouse monoclonal antibody against HIV- 1 p24 (ab9071, abcam, Cambridge, UK), diluted 1:1000 in PBS-T for 2 h. Anti-mouse IgG conjugated with horse radish peroxidase (HRP) (abcam), diluted 1:1000 in PBS-T was used as secondary antibody. Finally, the membrane was incubated with enhanced chemiluminescence (ECL) reagent (Bio-Rad), and visualized using a ChemiDoc imager (Bio-Rad).

### **2.10. Thermostability studies of HIV-1 Gag-eGFP VLPs**

Preliminary thermostability studies of HIV-1 Gag-eGFP VLPs at different temperatures were performed prior to DSP development. HIV-1 Gag-eGFP VLPs were produced as previously described [31]. Thermostability studies were performed during 90 days at four different conditions: 37 °C, 4 °C, -20 °C and -80 °C.

### **2.11. Preliminary serial filtration experiments**

Serial filtration experiments were performed with SartoScale PP3 polypropylene filter membrane of 25 mm and 4.5 cm<sup>2</sup> effective surface area (Sartorius AG, Göttingen, Germany). Filters with 5 µm, 3 µm, 1.2 µm, 0.65 µm, 0.45 µm nominal pore size were used. A total volume of 40 mL of cell culture supernatant containing HIV-1 Gag-eGFP VLPs were sequentially filtered at 266 LMH (liter per meter hour) corresponding to a flow rate of 2 mL/min at RT in sterile conditions with the different filters. MasterFlex® pump with MasterFlex® 96410-13 silicon tubes (Cole-Parmer, Montreal, Canada) and pressure gauge (WIKA Alexander Wiegand SE & Co. KG, Klingenberg, Germany) connected to the filter inlet were used in the filtration experiments. 2 mL of sample was taken between serial filtration for further analysis. Same experiment was run for negative control, for comparison.

### **2.12. Preparative clarification experiments**

Preparative primary clarification of HIV-1 Gag-eGFP VLPs from HEK 293 cell cultures were carried out at 72 hpt. 1L of cell culture was incubated for 1.5 hours (h) at RT were flocculation of cells was obtained, followed by dead end filtration with MilliStak®+ D0HC µpod filter with 23 cm<sup>2</sup> effective surface area (Merck, Kenilworth, NJ, USA), adapted from [16]. Filtration was performed at average LMH of 135.5 ± 34.3 in sterile conditions. Secondary filtration prior to chromatographic runs was performed with 0.45 µm SartoScale PP3 polypropylene filter membrane of 25 mm and 4.5 cm<sup>2</sup> effective surface area (Sartorius AG, Göttingen, Germany) at an average flux off 171.1 ± 60.7 LMH. Filters were flushed and conditioned with 50 mL of 50 mM HEPES, pH 7.4, 300 mM NaCl buffer. MasterFlex® pump with MasterFlex® 96410-13

silicon tubes (Cole-Parmer) and pressure gauge (WIKA Alexander Wiegand SE & Co. KG) connected to the filter inlet were used for the filtration experiments.

Flocculation of cells was monitored through optical density at 600 nm, and filtration process was monitored by measuring the eGFP fluorescence in the clarified material with Synergy HTX multi-mode reader and Gen5 software, respectively (BioTek Instruments, Inc.). Load capacity ( $L \cdot m^{-2}$ ) of primary and secondary filters in the screening experiments was evaluated until feed pressure reached a maximum of 14.5 psi (1 bar) according to Carvalho et al. [16].

### **2.13. Ion-Exchange Chromatography (IEX)**

Clarified cell culture supernatant containing HIV-1 Gag-eGFP VLPs was loaded into a 0.86 mL XT Acrodisc® Mustang® QXT membrane adsorber (Mustang Q, PALL Corporation, New York, NY, USA). Before loading, the column was equilibrated with 50 mM HEPES, 100 mM NaCl, pH 7.2 (5 % buffer B). After the loading phase, the column was washed with equilibration buffer (5 % buffer B) for 5 membrane volumes. In the linear gradient purification, a salt linear gradient from 100 to 1000 mM NaCl (5 to 50 % buffer B) in 20 membrane volumes was used. For the step gradient chromatography experiments, a final optimized method of 300, 700, 900 and 1200 mM (15%, 35%, 45% and 60% buffer B) of 10 membrane volumes each was used. In both purification strategies, the column was regenerated with 100 % buffer B for 10 membrane volumes. After regeneration, the membrane was sanitized using 10 membrane volumes of 1 M NaOH. UV absorbance at 280, 260 and 488 nm and pH were measured online in AKTA Explorer (GE Healthcare). All the preparative purification runs were performed using a flow rate from 1 to 5 mL/min in the flow through and of 1 mL/min in the elution. Fractions were collected and pooled according to the chromatograms.

### **2.14. SEC Chromatography & Lyophilization**

Desalting step after IEX at bench scale was performed with pD10 desalting column according to manufacturer's instructions (GE Healthcare). HIV-1 Gag-eGFP VLPs were eluted in PBS (Hyclone). Preparative chromatography was performed with 43-mL sepharose 4 Fast Flow (4FF) packed column at a constant flow rate of 1 or 2 mL/min. Briefly, SEC column was equilibrated



with 20 mM NaH<sub>2</sub>PO<sub>4</sub>, 50 mM NaCl, 2 mM MgCl<sub>2</sub>, 2% Sucrose pH 7.5. Then, 4-6.4 mL of HIV-1 Gag-eGFP VLPs were loaded and eluted with the equilibration buffer in the void volume. UV absorbance at 280, 260 and 488 nm and pH were measured online in AKTA Explorer (GE Healthcare). The different fractions obtained were pooled and analyzed according to the chromatogram. Purified HIV-1 Gag-eGFP VLPs after SEC were frozen at -80 °C and subsequently lyophilized at -60 °C at 100 μbar for 24 hours (h) in a VirTis BenchTop 6K (SP Industries, Warminster, PA, USA). 1 mL aliquots in 1.8 mL vials (Thermo Fisher) were used to this purpose. Lyophilized material was stored at RT until analysis.

### **3. Results**

#### **3.1. Stability studies on HIV-1 Gag VLPs**

##### **3.1.1. Thermostability of HIV-1 Gag VLPs**

Thermostability studies of HIV-1 Gag-eGFP VLPs were performed to assess their resistance to different storage conditions. Cell culture temperature (37 °C), standard cold chain (4 °C), and freezing temperatures (-20 and -80 °C) were tested. Two different techniques were combined to analyze VLP stability over time: spectrofluorometry and fluorescent nanoparticle tracking analysis (NTA) (Figure 1A). Spectrofluorometry enables the quantification of Gag-eGFP polyprotein that could be indirectly related to VLP concentrations [27], while NTA tracks individual GFP fluorescent nanoparticles [32], thus the specific quantification of assembled VLP from free Gag monomer and the particle size distribution (PSD) of the VLP population could be assessed, simultaneously.

Initial concentration of  $2.4 \pm 0.5 \cdot 10^{10}$  VLPs/mL was obtained in crude harvested supernatants by both techniques (Figure 1A). Along storage, a constant VLP concentration of  $2.4 \pm 0.5 \cdot 10^{10}$  and  $2.2 \pm 0.6 \cdot 10^{10}$  VLPs/mL at 4 °C or -80 °C was observed by NTA over three months, respectively. Contrarily, a loss in VLP titer of  $26 \pm 11$  % and  $52 \pm 13$  % at 37 °C was measured by spectrofluorometry and NTA, after ten days, respectively. Thus, a degradation of the VLP structure and the Gag-eGFP polyprotein might be taking place in this condition. For -20 °C

storage, a mean concentration of  $2.2 \pm 0.2 \cdot 10^{10}$  VLPs/mL (0% loss) was obtained in regard to Gag-eGFP quantification, while a loss of  $47 \pm 16$  % was quantified by NTA after 10 days of storage. The PSD analysis of  $-20$  °C condition showed a loss of nanoparticles in the range of 100 to 200 nm, and the appearance of larger aggregates with time (Figure 1A). Since Gag-eGFP by fluorescence quantification is maintained, a particle disruption might be the main cause of instability at  $-20$  °C due an heterogenous freezing process and the appearance of larger ice crystals.

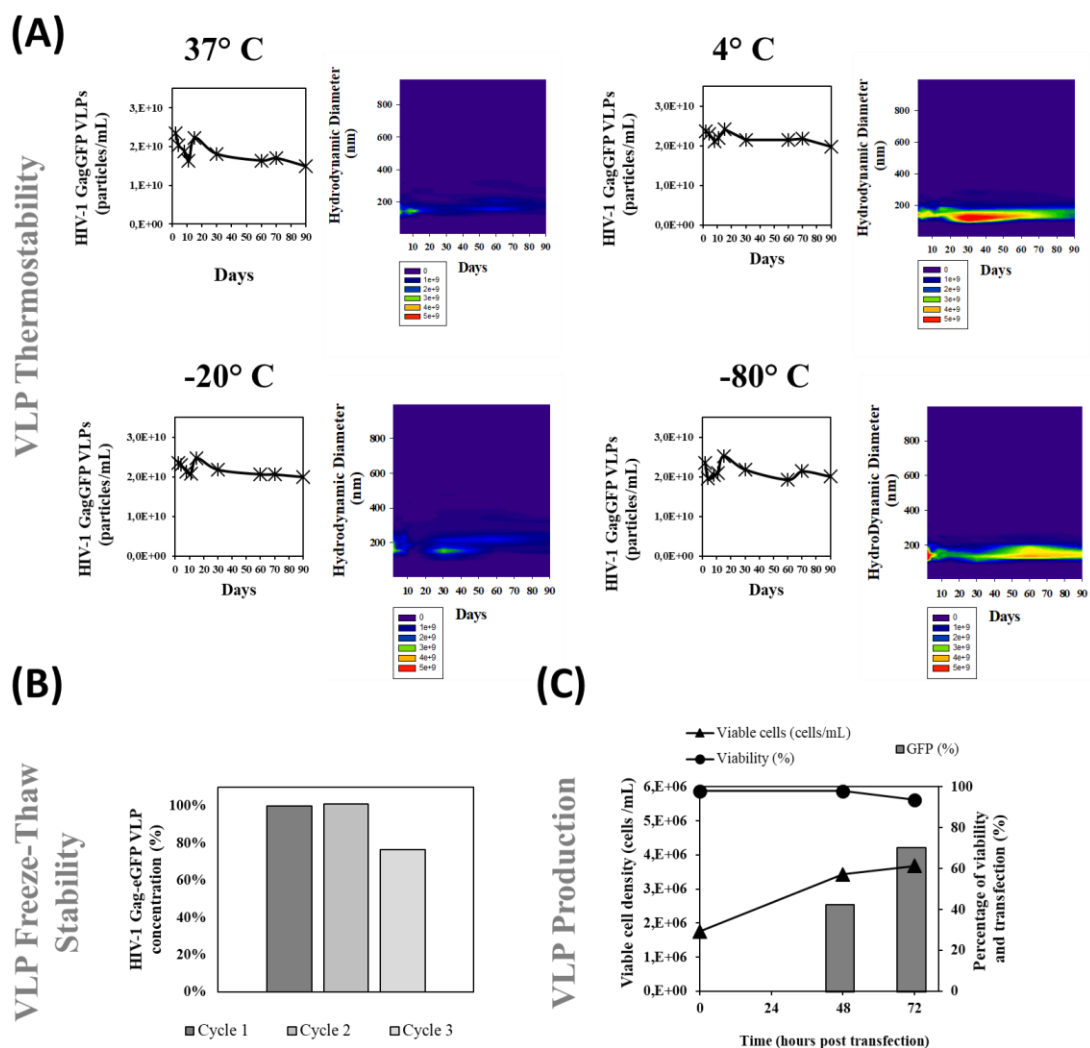


**Figure 1:** HIV-1 Gag-eGFP VLP thermostability studies. (A) HIV-1 Gag-eGFP VLPs were stored at different temperatures: 37 °C, 4 °C,  $-20$  °C and  $-80$  °C, respectively. Concentration of HIV-1 Gag-eGFP VLPs was quantified by spectrofluorometry-based assay [27] (line chart) and the particle size distribution (PSD) was analyzed with NTA (contour chart) for the four conditions with time. (B) Further long-term freeze and thaw cycles at  $-80$  °C were analyzed by flow virometry. (C) HIV-1 Gag-eGFP VLPs were produced in HEK 293 cells and harvested at 72 hpt, as previously described [31].

In summary, the best choice to store HIV-1 Gag-eGFP VLPs supernatants up to a three-month period would be 4 °C, while freezing at -80 °C would be the best option for longer periods. Further analyses of freeze and thaw cycles at -80 °C presented a good stability when no more than two cycles are performed on HIV-1 Gag-eGFP VLPs (Figure 1B). Due to the good long-term results depicted at -80 °C, conditioned supernatant composition could be taken as a reference material for the development of new formulation buffers for enveloped HIV-1 Gag-eGFP VLPs in terms of ion concentration, pH, viscosity or protein concentration.

### **3.1.2. Aggregation of HIV-1 VLPs**

To prevent aggregation problems at clarification stage, sequential filtration experiments were performed in harvested HIV-1 Gag-eGFP VLPs. A total of five membrane filters with 5, 3, 1.2, 0.65 and 0.45 µm pore size were tested. The same experiments were performed with conditioned cell culture medium as well from non-transfected supernatants. A total of 40 mL were filtered, and samples were taken between each step. Total protein and dsDNA were quantified to assess the levels of process-derived impurities, whereas VLP content was monitored by flow virometry and relative fluorescence units (RFU). Analyses performed on VLP containing supernatant (Figure 2A & 2B) or conditioned cell culture medium (Figure 2C) showed no significant loss of total protein, dsDNA or VLP content. Thus, it was concluded that HIV-1 Gag-eGFP VLPs do not suffer from aggregation in cell culture supernatants.

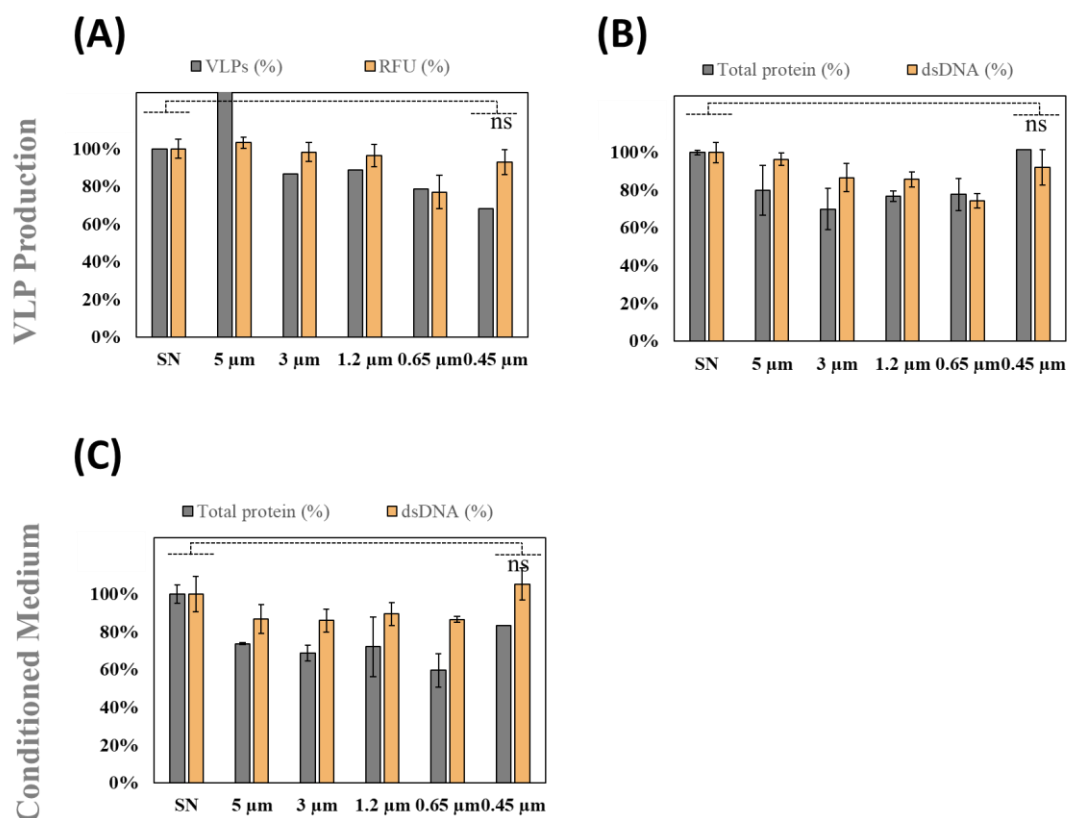


**Figure 2: Sequential filtration experiments of HIV-1 Gag-eGFP VLPs. (A-B) Analysis of HIV-1 Gag-eGFP VLP productions: (A) VLP nanoparticle concentration measured by flow virometry (VLPs) and relative fluorescent units (RFU) and (B) total protein and dsDNA content after the different filters. (C) Analysis of conditioned cell culture medium in regard to total protein and dsDNA content after the different filters. Statistical analyses of technical replicates were performed with ANOVA or T Student test. Ns: non-significant.**

### 3.2. Four steps down-stream process of HIV-1 Gag VLPs

#### 3.2.1. Clarification

The proposed four-step DSP process for HIV-1 Gag-eGFP VLPs was tested and characterized. Concretely, a purification train consisting of filter-based clarification, IEX chromatography to concentrate the VLPs, and SEC to polish and prepare the purified material for lyophilization was developed.

Clarification aimed to separate cells from cell culture supernatant, where HIV-1 Gag-eGFP VLPs have been secreted during the production phase. To do so, a combined strategy encompassing

flocculation and depth filtration was proposed. One liter of cell culture supernatant was incubated in 1L-Erlenmeyer flask for 1.5 h at RT, where cells settled to the bottom of the flask and liquid phase was subsequently filtered. Due to the mean size diameter of these cells, which is around 15-20  $\mu\text{m}$  [33], the Stokes law describes a very low gravity sedimentation velocity ( $v$ ) calculated as follows:

$$v = \frac{d^2 (\rho_p - \rho_m) \times g}{18 \eta} \quad (3)$$

where  $g$  is the acceleration of gravity ( $9.807 \text{ m/s}^2$ ),  $\rho_p$  is the particle density,  $\rho_m$  is the medium density,  $d$  is the particle diameter, and  $\eta$  is the medium viscosity. Assuming a similar  $\rho_p$ , as those calculated for CHO cells, of  $1051 \text{ kg/m}^3$  [34], a  $\rho_m$  of  $1000 \text{ kg/m}^3$ , and a  $\eta$  of  $0.001 \text{ kg/(m s)}$  at  $20^\circ\text{C}$ , a settling velocity of  $1 \text{ cm/h}$  is obtained [35]. Thus, the cell broth sedimentation in 1L Erlenmeyer is expected to occur in several hours. Nonetheless, a settled bed was obtained after 1.5 h, pointing then spontaneous flocculation, as the main driving force in the settling process. After that time, depth filtration with MilliStak@D0HC was performed. Feed pressure and fluorescence in the clarified volume was monitored during the experiment (Figure 3A). A total time of 3.5 h was needed to filtrate all the liquid phase, with no feed pressure observed during the process ( $\sim 0 \text{ psi}$ ). Purification yield and contaminant removal were compared when only flocculation, flocculation and depth filtration and centrifugation, as the reference protocol were assessed (Figure 3C-D). A concentration of  $8.2 \cdot 10^9$ ,  $7.4 \cdot 10^9$  and  $7.1 \cdot 10^9 \text{ VLPs/mL}$  was calculated for the three processes, respectively (Figure 3C), while the dsDNA content and total protein was higher in the filtered sample compared to the centrifuged one (Figure 3D,  $p.\text{value} < 0.01$ ). The clarified material was further characterized by cryo-TEM where the presence of VLPs (black arrows), but also the naturally co-produced EVs of different sizes were identified (white dashed arrows, Figure 3B). Despite containing more impurities, the clarified material showed a total filter capacity of  $43.5 \text{ mL/cm}^2$ . As a proof of concept, settled cells were resuspended with the addition of 50 mL of PBS (Hyclone) and loaded to the filter. The entrance of concentrated cells to the depth-filter immediately increased the feed pressure to 16 psi (1.1 bar), over the defined limit of

1 bar. Thus, the settling of cells prior to depth filtration allowed to increase the filter capacity in a limitless way, since feed pressure only increased when cells were loaded. Similar improvements in terms of filter capacity were reported by Westoby and co-workers when CHO cells flocculation at acidic pH was performed before microfiltration [35].

Since the depth filter has a pore size of 0.55  $\mu\text{m}$ , the clarified material could be directly loaded onto a chromatographic column. Alternatively, long-term storage at  $-80\text{ }^{\circ}\text{C}$  after clarification is often required in large scale processes; thus, a secondary clarification was also evaluated (Figure 3E-G) to be used after thawing were precipitates can appear. The 0.45  $\mu\text{m}$  PP3 pore size filter was selected based on the previously presented sequential filtration results (Figure 2). Filtration was performed under the same conditions and the process was stopped when feed pressure reached 12 psi. At-line monitoring of the process was performed, where a total volume of 350 mL was processed per filter representing a 77.8 mL/cm<sup>2</sup> load capacity. A concentration of  $7.5 \cdot 10^9$  and  $8.1 \cdot 10^9$  VLPs/mL and non-significant (ns) differences in RFU (Figure 3F) was quantified before and after filtration, while same total protein and reduced dsDNA was found (Figure 3G), supporting the use of this filtration step prior to chromatographic experiments if required.

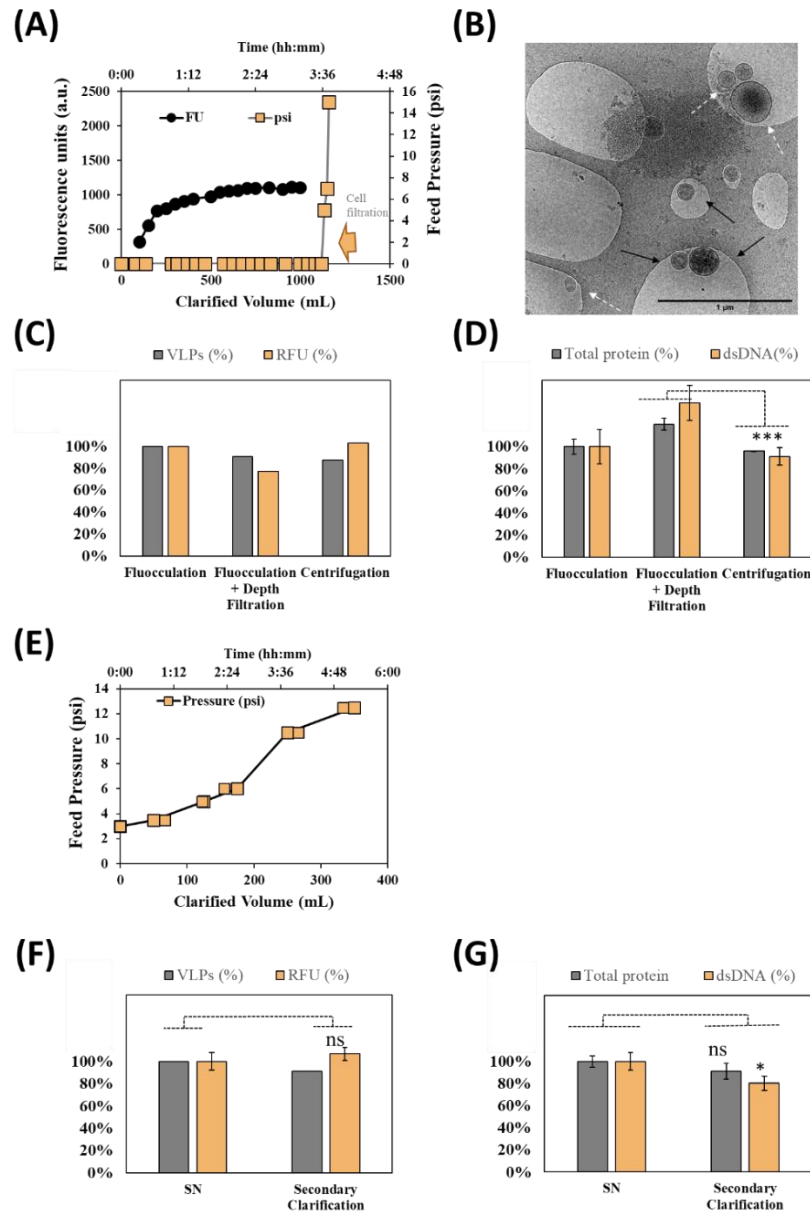


**Figure 3: Primary and secondary clarification of HIV-1 Gag-eGFP VLPs.** (A) At-line monitoring of depth filtration process, fluorescence units (FU) in the clarified volume and feed pressure (psi) were measured with time. (B) Cryo-TEM micrographs of clarified material after dead end filtration. Black arrows indicate the presence of VLPs while white dashed arrows point the EVs. Three different processes were compared: flocculation, flocculation and depth filtration and centrifugation as the reference protocol. The VLP nanoparticle concentration measured by flow virometry (VLPs) and relative fluorescent units (RFU) (C), and total protein and dsDNA content (D) were compared between primary clarification strategies. (E) At-line monitoring of secondary filtration process, feed pressure (psi) were measured with time. The recovery of VLP nanoparticle concentration measured by flow virometry (VLPs) and relative fluorescent units (RFU) (F) and total protein and dsDNA content (G) were compared before and after the secondary clarification. Statistical analyses of technical replicates were performed with T Student test. Ns: non-significant.

### 3.2.2. IEX Chromatography

The concentration and purification of HIV-1 Gag-GFP VLPs was assessed by means of IEX Chromatography. Initial linear gradient experiments were performed on clarified supernatant to evaluate the suitability of Mustang Q membrane to purify these nanoparticles. 20 mL of cell culture conditioned medium, as negative control and HIV-1 Gag-eGFP VLP-containing supernatant were loaded into a 0.86 mL Mustang Q in two separate experiments (Figure 4A and 4C, respectively). Elution was assessed with salt linear gradient from 100 to 1000 mM NaCl [30]. Three different absorbances were monitored online: UV260, UV280 and UV488 to monitor nucleic acid, protein and Gag-eGFP content, respectively. The purification of HIV-1 Gag-eGFP VLPs from process-related impurities was clearly observed in these analyses, where a unique peak in UV488 absorbance (E2) was observed in the VLP run compared to the negative control. This VLP peak could be separated from two other peaks detected in the UV260 and UV280 chromatograms, named as E1 and E3, respectively. The VLP peak had an area of 496.1 mL·mAU measured with the UV488 absorbance that corresponds to 22.5 - 43.3 % of B Buffer and 26.7 - 61.5 mS/cm of conductivity (Figure 4C). The presence of HIV-1 Gag-eGFP VLPs was confirmed by flow virometry (VLPs) and RFU quantifications, where a 26 % of total VLP content was recovered in the peak E2 (Figure 4D). The VLP peak presented a protein concentration of 0.19  $\mu\text{g}/\mu\text{L}$  and dsDNA below limit of detection (LOD).

From the total protein loaded, a  $37 \pm 5\%$  and  $14 \pm 0\%$  were collected in the flow through (FT) and wash (W) fractions, respectively, while the rest was distributed in the other two peaks (E1 and E3). In the case of dsDNA,  $52 \pm 10\%$  was recovered in the third peak (E3), meanwhile it was below LOD in the other pooled fractions (Figure 4E). The same behavior was observed when only conditioned medium was loaded (Figure 4B). Thus, the purification of HIV-1 Gag-eGFP VLPs is demonstrated by IEX NaCl salt gradient, where free protein is collected in the FT and in the low-salt concentrations peak (E1), while the dsDNA is strongly bound to the membrane and is eluted at higher salt concentrations (E3).



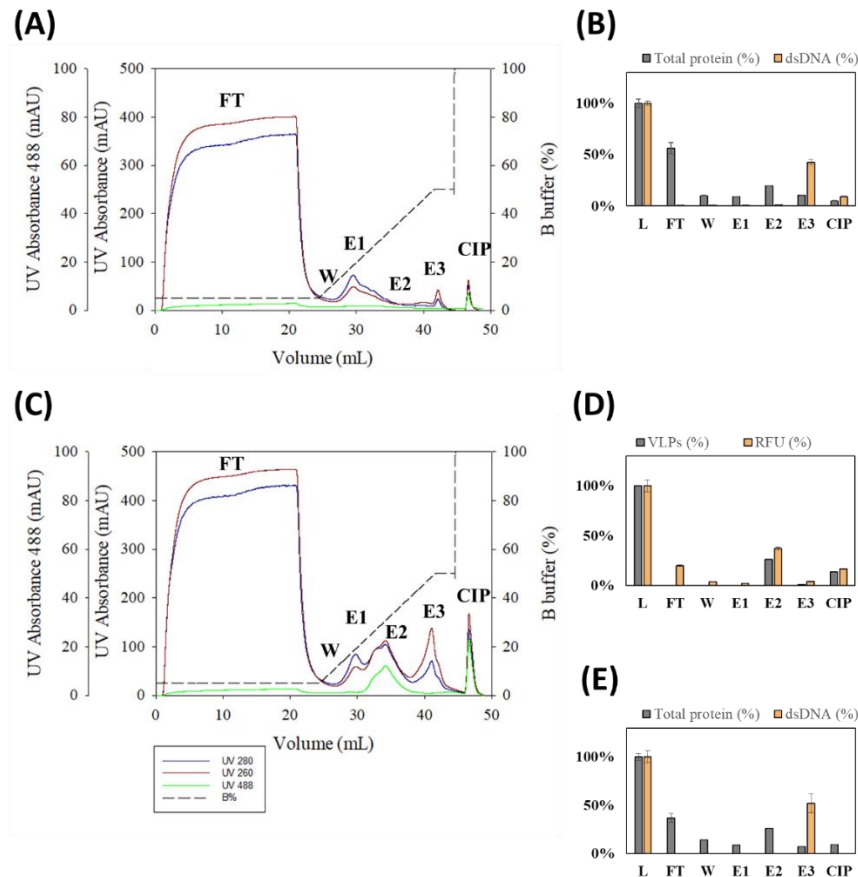


**Figure 4: Ion Exchange Chromatography (IEX) purification of HIV-1 Gag-eGFP VLPs. (A-B) IEX Chromatography analysis of conditioned cell culture medium and (C-E) HIV-1 Gag-eGFP VLP supernatant. Equilibration buffer was 50 mM HEPES, 100 mM NaCl with pH 7.2 and linear gradient elution was performed from 100 to 1000 mM NaCl (5 to 50 % buffer B) in 20 membrane volumes at 1 mL/min. (A and C) Chromatogram of the linear gradient purification of conditioned medium or HIV-1 Gag-eGFP VLP supernatant using a Mustang® QXT, respectively. The recovery of VLP nanoparticle concentration measured by flow virometry (VLPs) and relative fluorescent units (RFU) (D) and total protein and dsDNA content in the conditioned cell culture medium run (B) and in the HIV-1 Gag-eGFP VLP run (E) were also assessed. The loading material was 20 mL of harvested HEK 293 cell culture by centrifugation. L: load material; FT: flow-through; W: wash; E1-E3: pooled fractions for peaks 1-3 and CIP: cleaning in place with 2M NaCl.**

Optimization of the IEX chromatography step was performed focusing on two main aspects: studying the dynamic binding capacity (DBC) and optimizing the elution by applying a step gradient to concentrate the HIV-1 Gag-eGFP VLPs in the elution phase. A total volume of 150 mL representing 7.5 times more supernatant than in the previous run was loaded to study the DBC. Thereafter, an initial three-step gradient of 15 %, 45 % and 60 % of buffer B was tested,

based on the results observed in the linear gradient (Figure 4C E1-E3, respectively). The results are presented in Figure 5A-C. Absence of HIV-1 Gag-eGFP VLPs was observed in the FT (Figure 5B), when a total amount of  $6.6 \cdot 10^{11}$  VLPs was loaded, according to flow virometry results. A second run was then performed, with a total volume of 413 mL of supernatant loaded (Figure 5E-G). In this case, the presence of HIV-1 Gag-eGFP VLPs was neither observed in the FT from a total load of  $3.33 \cdot 10^{12}$  VLPs. Thus, a maximum load of  $3.84 \cdot 10^{12}$  VLPs/mL of Mustang Q membrane and 480 mL per mL of membrane volume was achieved.

Regarding the elution, two peaks were found in the 45% step corresponding to HIV-1 Gag-eGFP VLPs and a second corresponding to dsDNA in the first step run (Figure 5A-C E2.1 and E2.2, respectively). Therefore, an alteration of the VLP purification profile was observed when higher amounts of supernatant are loaded. To separate this double peak obtained in the 45% fraction, a four-step elution profile was then assessed encompassing 15 %, 35 %, 45 % and 60 % of B buffer (Figure 5E-G). With this new profile, HIV-1 Gag-eGFP VLPs were concentrated in the 35 % fraction with a concentration of  $1.7 \cdot 10^{11}$  VLPs/mL and a total recovery of 38% of the VLPs. Moreover, the presence of HIV-1 Gag-eGFP VLP was also observed in 15 % and 60 % salt steps representing the 8% and the 26 % of the load material, respectively. Thus, several HIV-1 Gag-eGFP VLP subpopulations were recovered when higher loads were used representing a total 72% of recovery. Like in previously runs, free protein was recovered in the flow through (FT) or eluted at low salt concentrations, whereas dsDNA eluted in the 45 % peak representing more than the 50 % of the loaded dsDNA.

To assess the quality of the different VLP subpopulations, E1, E2.1 and E4 peaks from the four-step run were loaded to a pd10 desalting column and were analyzed by DLS (Figure 5G). In all four cases, a unique population of nanoparticles with a mean hydrodynamic diameter between 100 and 200 nm, like in the loaded supernatant (S). Finally, biochemical analyses of the purified fraction were assessed by means of SDS-PAGE and Western Blot anti-p24 (Figure 5H and 5I, respectively). In these analyses, Gag-eGFP polyprotein (~87 kDa) was the protein present in higher concentrations and other proteins showed to be below the LOD in the SDS-PAGE gel.

Again, the presence of HIV-1 Gag-eGFP VLPs was observed in the four peaks, meanwhile it was not detected in the FT or W fractions. Although HIV-1 Gag-eGFP VLPs appeared in more than one peak, in E2 fraction VLPs were concentrated 56-fold and volume was reduced 55 times compared to crude supernatants.

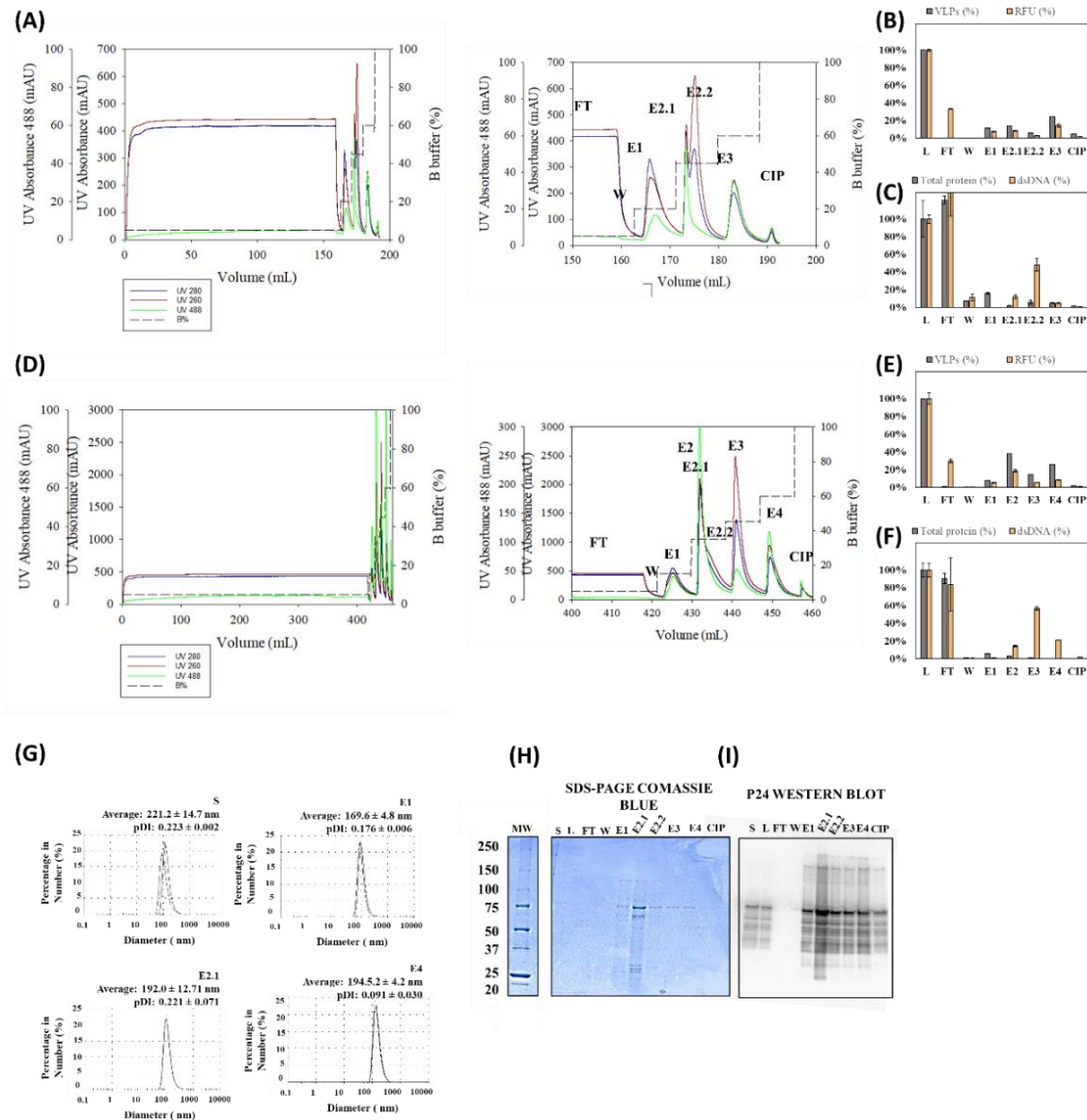


**Figure 5: Optimization of IEX Chromatography.** (A and D) Chromatogram of the step gradient purification of HIV-1 Gag-eGFP VLP supernatant using a Mustang® QXT. The loading material was produced in HEK 293 cell culture and harvested at 72 hpt by centrifugation and filtered with 0.45  $\mu\text{m}$  PP3 filter. The membrane was equilibrated with 50 mM HEPES, 100 mM NaCl with pH 7.2. A total load of 150 mL was eluted in a step gradient of 15-45-60% of B buffer (A) or a total load of 413 mL was eluted in a step gradient of 15-35-45-60% of B buffer (B), respectively. The recovery of VLP nanoparticle concentration measured by flow virometry (VLPs) and relative fluorescent units (RFU) (B and E) and total protein and dsDNA content (C and F) were also assessed, respectively. From chromatogram (D), peaks E1, E2.1 and E3 were

loaded onto a pd10 desalting column and HIV-1 Gag-eGFP VLPs contained in the void volume were recovered in PBS (HyClone) and further analyzed by DLS, where three independent measurements were performed per sample (G); Average: mean hydrodynamic diameter; pDI: polydispersity index. SDS-PAGE Comassie Blue (H) and p24 Western Blot (I) were also performed from the different fractions obtained in this run. S: supernatant; L: load material; FT: flow-through; W: wash; E1-E4: pooled fractions for peaks 1-4 and CIP: cleaning in place with 2M NaCl.

### 3.2.3. SEC and lyophilization of HIV-1 Gag-eGFP VLPs

IEX fractions (Figure 6A, E1-E4) were loaded into a 43-mL SEC column, where VLPs were collected in the void volume diluted in lyophilization buffer (Figure 6B, SEC1-SEC4). Lyophilization buffer was composed of 20 mM NaH<sub>2</sub>PO<sub>4</sub>, 50 mM NaCl, 2 mM MgCl<sub>2</sub>, 2% Sucrose (w:v) and pH 7.5 to prevent from sample damage during storage. The removal of NaCl coming from IEX was tracked with conductimetry sensor (dotted line, Figure 6B). A huge peak was observed in the elution volume, after the recovery of HIV-1 Gag-eGFP VLPs in SEC1 to SEC4 fractions, respectively. An average removal of  $96 \pm 7\%$  and  $88 \pm 1\%$  in terms of total protein and dsDNA was obtained after SEC (Figure 6E and F, respectively). As expected, HIV-1 Gag-eGFP VLPs were mainly eluted from 35% salt step in IEX (E2), as shown by the presence of a huge peak of 1.126 mL·mAU in SEC2 pooled fraction. This peak corresponded to  $1.08 \cdot 10^{11}$  VLPs and represented the 75% of the Gag-eGFP polyprotein loaded material (Figure 6D). Lower VLP concentrations of  $0.12 \cdot 10^9$ ,  $0.03 \cdot 10^9$  and  $0.11 \cdot 10^9$  VLPs/mL were obtained in SEC1, SEC3 and SEC4 fractions, respectively. The complete mass balance of the purification train is depicted in Table 1.

First attempts in the lyophilization of HIV-1 Gag-eGFP VLPs were then performed in views to optimize its storage and transportation. HIV-1 Gag-eGFP VLPs were lyophilized in 1 mL vials and stored at RT for two months. Alternatively, purified HIV-1 Gag-eGFP VLPs were frozen at -80 °C, in the same buffer, as control. Lyophilized samples were resuspended in distilled water, prior to analysis. Cryo-TEM, DLS, flow virometry (FV) and NTA were used to evaluate particle integrity in purified samples. Concentrated and purified HIV-1 Gag-eGFP VLPs are clearly observed in Cryo-TEM micrographs (Figure 7), compared to initial clarified material depicted in

Figure 3B. HIV-1 Gag-eGFP VLPs are detected as spherical electron-dense nanoparticles surrounded by a lipid membrane in both frozen and lyophilized and reconstituted samples. The particle size distribution (PSD) analyses showed a mean hydrodynamic diameter of  $172.1 \pm 1.1$  nm and  $215.2 \pm 11.9$  nm measured by fluorescent NTA or DLS in the frozen sample, respectively, while nanoparticle aggregation was observed after lyophilization with a PSD of  $343.3 \pm 15.3$  and  $593.1 \pm 23.8$  nm measured with NTA and DLS, respectively. Nanoparticle concentration of VLPs and EVs presented a decrease in VLP concentration after lyophilization, likely to the aggregation phenomenon, since similar apparent concentrations are depicted in Cryo-TEM analyses. Of note, a VLP/EV ratio of  $1.99 \pm 0.97$  was obtained in SEC samples, pointing a notable enrichment of HIV-1 Gag-eGFP VLPs over EVs. Compared to crude clarified material (Figure 2E), the presence of EVs was very low in Cryo-TEM micrographs and represented the 2% of the initial material after SEC and was below LOD in lyophilized samples (Table 2). Overall, total protein and dsDNA were removed in almost 100% from the crude supernatant, presenting a final concentration of  $26.0 \pm 6.3$   $\mu\text{g/mL}$  and  $49.6 \pm 28.2$   $\text{ng/mL}$  of total protein and dsDNA (Table 1). The percentage of Gag-eGFP polyprotein from total protein was 94% compared to the 4% quantified in initial material.

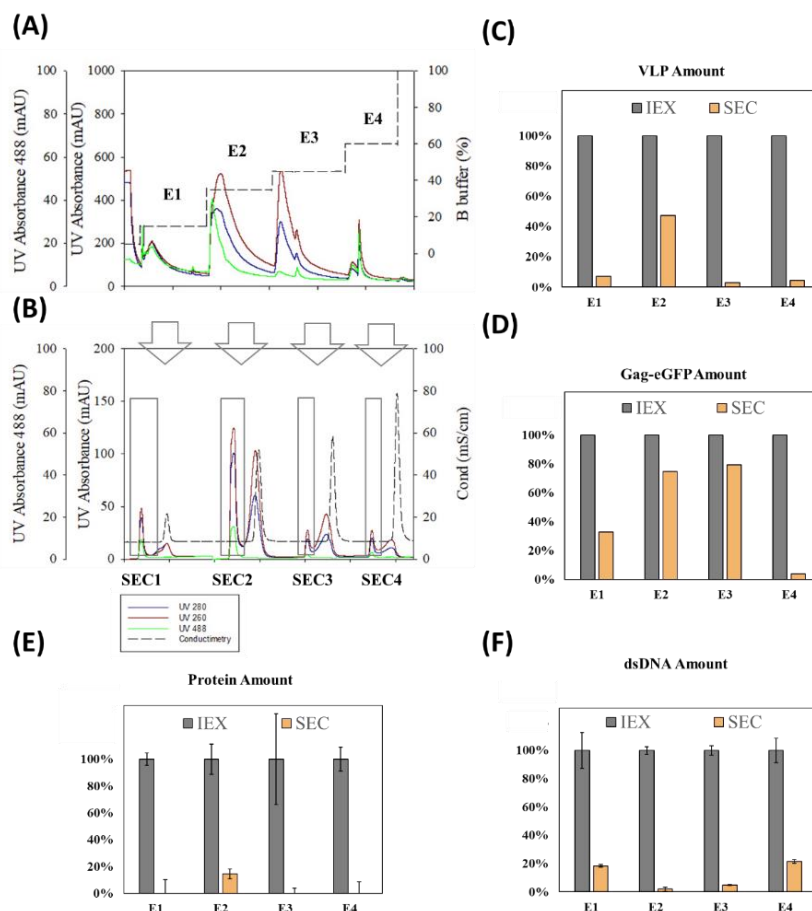


**Figure 6: SEC of HIV-1 Gag-eGFP VLPs.** (A) Chromatogram of IEX chromatography based on previous optimization protocol using a Mustang® QXT (Figure 5). HIV-1 Gag-eGFP VLP supernatant produced in HEK 293 cell culture, clarified by flocculation and depth filtration was used as initial material (Figure 3). Equilibration buffer was 50 mM HEPES, 100 mM NaCl with pH 7.2 and step gradient of a total load of 283 mL eluted in step gradient of 15-35-45-60% of B buffer corresponding to E1-E2-E3-E4 peaks. (B) Chromatogram of SEC from the four peaks obtained in IEX. A 43 mL Sepharose 4 Fast Flow (4FF) packed column was used. SEC column was equilibrated with 20 mM NaH<sub>2</sub>PO<sub>4</sub>, 50 mM NaCl, 2 mM MgCl<sub>2</sub>, 2% Sucrose pH 7.5. The recovery of VLPs (C), Gag-eGFP polyprotein (D), total protein (E) and dsDNA (F) was assessed for each peak.

**Table 1: Mass balance of total protein, dsDNA and Gag-eGFP polyprotein. CI: clarified material; IEX: E2 peak from IEX chromatography; SEC: SEC2 peak from SEC.**

Sample	Volume	Total protein ( $\mu\text{g/mL}$ )	Total protein (%)	dsDNA ( $\text{ng/mL}$ )	dsDNA (%)	Gag-eGFP ( $\mu\text{g/mL}$ )	Gag-eGFP (%)	Gag-eGFP / Total protein (%)
CI	282	$503.9 \pm 1.5$	$100 \pm 0$	$3103.9 \pm 179.2$	$100 \pm 6$	22.0	100	4
IEX	15	$306.6 \pm 34.6$	$3 \pm 1$	$545.4 \pm 87.7$	$1 \pm 0$	56.7	13	18
SEC	18	$26.0 \pm 6.3$	$0 \pm 0^*$	$49.6 \pm 28.2$	$0 \pm 0$	24.3	$10^*$	94

**Table 2: Nanoparticle mass balance of VLPs and EVs based on FV and NTA quantification. CI: clarified material; IEX: E2 peak from IEX chromatography; SEC: SEC2 peak from SEC; FV: Flow virometry.**

Sample	Volume (mL)	FV (events $\cdot 10^9/\text{mL}$ )		NTA (particles $\cdot 10^9/\text{mL}$ )		VLPs/ Total Particles (%)	VLPs (%)
		VLPs	EVs	VLPs	EVs		
CI	282	7.4	28.9	$4.7 \pm 0.2$	$9.7 \pm 0.9$	$27 \pm 9$	$100 \pm 4$
IEX	15	21.6	20.1	-	-	52	18
SEC	18	6.0	4.6	$12.6 \pm 0.7$	$9.9 \pm 0.4$	$65 \pm 11$	$14 \pm 1$
Lyophilization	18	$2.1 \pm 0.7$	$1.6 \pm 0.7$	$2.2 \pm 0.8$	LOD	$80 \pm 32$	$3 \pm 1$

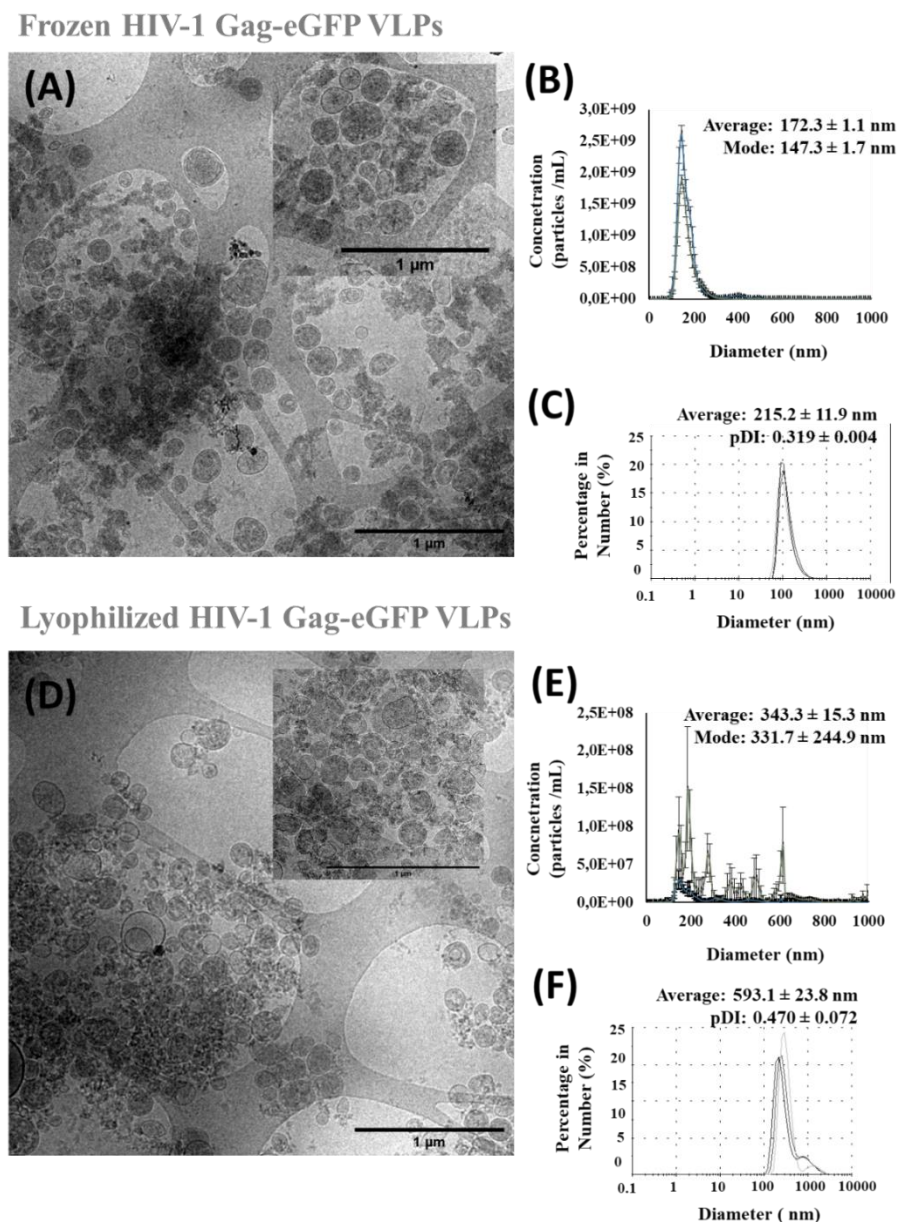


**Figure 7: Characterization of purified HIV-1 Gag-eGFP VLPs.** The purified nanoparticles were stored under different conditions for two months after SEC. (A-C) Frozen HIV-1 Gag-eGFP VLPs (D-F) Lyophilized HIV-1 Gag-eGFP VLPs. (A, D) Cryo-TEM micrographs of the purified material, respectively. (B,E) PSD analysis by NTA of total nanoparticles (blue line) measured by light scattering or VLPs (green line) measured with the fluorescence filter. (C, F) PSD analysis with DLS. Three independent measurements were performed. Average: mean hydrodynamic diameter; PDI: polydispersity index.



## 4. Discussion

### 4.1. Purification train and unit capacity

A four-step process has been developed for HIV-1 Gag-eGFP VLPs. Load capacities and flux rates are summarized in Table 3. Load capacities between 400 and more than 800 L/m<sup>2</sup> were achieved in membrane-based processes. Carvalho et al. analyzed different filters for primary and secondary clarification for influenza VLPs produced with baculovirus expression vector system (BEVS), where a maximum load of 150 L/m<sup>2</sup> reported for primary clarification with MilliStak®+ D0HC. Here, the addition of a flocculation step before filtration allowed for the clarification of the whole cell culture in one single run. Feed pressure was maintained at 0 psi, preventing from possible VLP mechanical stress during clarification. About secondary clarification, even higher load capacities and flux rates were observed without affecting recovery yields (Table 3). This secondary clarification could be dispensed provided that clarified material is subsequently loaded onto the chromatographic column. However, a continuous DSP process is not always feasible, hence this filtration aims to remove large precipitates that might appear in the freeze and thaw process for long-term storage.

IEX Chromatography was performed with a Mustang Q composed by 16 layers of Mustang Q membrane with a bed volume of 0.86 mL and a surface area of 4.9 cm<sup>2</sup>. From the different optimizations performed, a maximum load capacity of 842.9 L/m<sup>2</sup> was achieved (Figure 5D) corresponding to 480.2 mL per mL of bed volume. Of note, DBC was not achieved in any of the experiments tested. Thus, a VLP load higher than  $3.84 \cdot 10^{12}$  VLPs is still possible although maximum column pressure provided by the manufacturer or operation time might then be the limiting factor. High DBC of  $4.70 \cdot 10^{10}$  virus particles (vp) per square centimeter of adenoviruses, more than  $8.7 \cdot 10^{10}$  transduction units (TU) of lentiviral vectors and  $1.27 \cdot 10^8$  infective units (ifu) of  $\gamma$ -retroviruses per mL of bed volume have been reported with membrane adsorbers [36–38]. Similarly, Steppert and co-workers reported a DBC of  $8.6 \cdot 10^{12}$  of total particles per mL in QA monolith in the purification of HIV-1 Gag VLPs [11]. These data support the use of strong quaternary amine ion exchangers to concentrate and purify enveloped viruses and viral particles,

---

as those used in the present work. In addition, these novel materials work at faster flux rates by allowing convective flux inside the matrix [39]. On the other hand, due to the strong binding obtained with Q ligand, high salt concentrations are required for the elution and a direct competition with dsDNA is observed. With views to overcome this fact, alternative weak ligands have been also proposed [39].

SEC chromatography has been used as desalting column after IEX Chromatography to perform a buffer exchange. A maximum 6.4 mL load is allowed in a 43-mL SEC column. Thus, several rounds are required to purify higher volumes, as for the E2 fraction here. Despite the simplicity of the method, a dilution factor of 1.71 and a larger operation times are needed. Alternative membrane-based ultrafiltration and diafiltration has been described in the literature to overcome such limitations. Specifically, Tangential Flow Filtration (TFF) with 300-kDa and 1000-kDa cutoff membranes has been used for the concentration of influenza VLPs with recoveries of 44 % and more than 80 % by Venereo et al. and Carvalho et al., respectively [14,15]. Moreover, the use of hollow fibers has been highlighted in virus purification due to their open-channels and lot-to-lot consistency [7,39].

Lyophilization has been explored for the preservation of purified HIV-1 Gag-eGFP VLPs. Despite the obvious advantages of lyophilized materials compared to cold chain, the process of freeze-drying is still a challenge in viral-based vaccines, especially for enveloped viruses. Lipid damage, protein damage, changes in the pH or osmolarity or aggregation are some of the reported drawbacks [21]. Here, HIV-1 Gag-eGFP VLPs were lyophilized in a tailored lyophilization buffer, where the maintenance of particle integrity was confirmed by Cryo-TEM. Nonetheless, particle aggregation was observed by means of particle tracking techniques. Together with the 2 % (w:v) sucrose used in this work, the addition of sorbitol or gelatin as cryoprotectants might prevent from membrane damage and aggregation. On the other hand, process parameters, such as freezing rate, have been also pointed as critical to control ice formation during lyophilization [21]. Thus, further optimization of the formulation buffer and process parameters might improve the present results.

Table 3: Summary of process parameters

Process	Maximum Volume (mL)	Effective Surface Area   Volume		Load Capacity		Concentration factor	Flux rate	
		Area (cm <sup>2</sup> )	Volume (mL)	(L/m <sup>2</sup> )	(mL/mL)		LMH	mL/min
Primary Filtration	1000	23	-	434.8	-	1	135.5	-
Secondary Filtration	350	4.5	-	777.8	-	1	171.1	-
IEX Chromatography	413	4.9	0.86	842.9	480.2	50	-	1-5
SEC Chromatography	6.4	2.01	43	-	0.2	0.58	-	1-2

#### 4.2. VLP quality and purification yield

Lyophilized HIV-1 Gag-eGFP VLP vials containing  $2.2 \cdot 10^9$  VLPs have been purified from HEK 293 clarified supernatants. Purified samples contained 24  $\mu$ g of Gag-eGFP polyprotein per vial, which represent the 94% of the total protein quantified by means of RCDC assay has been reported. Of note, no nuclease treatment was added before IEX Chromatography and dsDNA was removed by almost 100 %, with a concentration of only  $49.6 \pm 28.2$  ng/mL before lyophilization. Furthermore, quantification of EVs in the final preparation was  $1.6 \cdot 10^9$ , according to flow virometry analyses whereas, their quantification was below LOD by NTA. The presence of EVs over VLPs was also almost neglectable in Cryo-TEM micrographs. Although, the enrichment of HIV-1 Gag VLPs over total particles has been reported previously [15,22], further analyses are required to confirm these results since indirect quantification methods have been used [5]. In the present work, the presence of eGFP fluorochrome in fusion with the Gag polyprotein has facilitated the specific quantification of assembled VLPs from total nanoparticles during the purification process. The combined use of two different nanoparticle quantification methods (i.e. flow virometry and NTA), together with Cryo-TEM [25] has been applied here to confirm the enrichment of HIV-1 Gag-eGFP VLPs over EVs.

A recovery  $14 \pm 1\%$  of VLPs from the crude supernatant was achieved before lyophilization (Table 2). While primary and secondary clarification showed no significant loss of HIV-1 Gag-

eGFP VLPs, the elution of more than one peak containing HIV-1 Gag-eGFP VLPs was observed after IEX Chromatography. The presence of different subpopulations within HIV-1 Gag VLPs has been described by Steppert et al. and Aguilar et al. [12,22]. IEX chromatography allowed a selective purification of HIV-1 Gag-eGFP VLPs homogenous populations [21], which might be desirable for clinical use.

## **5. Conclusion**

HIV-1 Gag VLPs are a very promising platform for antigen and drug delivery strategies. A complete purification train from crude supernatants to purified HIV-1 Gag VLP preparations has been developed in this work. Thermostability and particle aggregation studies of harvested HIV-1 Gag-eGFP VLPs showed these particles to be stable at 4 °C for up to three months and recommended -80°C as an optimal freezing temperature for their long-term storage. A nimble DSP consisting of clarification, IEX chromatography, SEC and lyophilization was developed. The separation of HIV-1 Gag-eGFP VLPs from EVs was observed in the final purified samples, where Gag-eGFP polyprotein represented more than the 95% of total protein. In summary, lyophilized vials containing  $2.2 \cdot 10^9$  VLPs and 24 µg of Gag polyprotein were obtained and stored at RT for up to two months. These first results in enveloped VLP lyophilization open the window for developing new formulations increasing nanoparticle stability for its use and transportation worldwide.

## **6. Acknowledgments**

The authors would like to acknowledge the help of Marti de Cabo (Servei de Microscòpia, UAB, Barcelona, Spain) for the assistance with Cryo-TEM. DLS and NTA measurements were performed at NanoQAM service located at Département de Chimie Université du Québec à Montréal (UQAM, Montreal, Canada) and at the Service of Preparation and Characterization of Soft Materials located at Institut de Ciència de Materials de Barcelona (ICMAB, CSIC, Campus UAB), where the help of Jose Amable Bernabé is appreciated. Flow virometry experiments were performed with CytoFLEX (Beckman Coulter) at the Immunophenotyping Service from The Research Institute of the McGill University Health Centre (RI-MUHC, Montreal, Canada) and at

Banc de Sang i Teixits (BST, Barcelona, Spain), where the assistance of Immunophenotyping Service and BST staff is kindly appreciated. The help of Xingge Xu, Michelle Tran, Aline Do Minh, Hanan Chaabane, Pranav Joshi, Dr Alina Venereo and Dr Omar Farnos and the rest of the Viral Vectors and Vaccines Bioprocessing Group (Department of Bioengineering, McGill University, Montreal, Canada) is kindly appreciated.

## 7. Literature

1. Charlton Hume, H.K.; Vidigal, J.; Carrondo, M.J.T.; Middelberg, A.P.J.; Roldão, A.; Lua, L.H.L. Synthetic biology for bioengineering virus-like particle vaccines. *Biotechnol. Bioeng.* **2019**, *116*, 919–935.
2. Donaldson, B.; Lateef, Z.; Walker, G.F.; Young, S.L.; Ward, V.K. Virus-like particle vaccines: immunology and formulation for clinical translation. *Expert Rev. Vaccines* **2018**, *17*, 833–849.
3. Lua, L.H.L.; Connors, N.K.; Sainsbury, F.; Chuan, Y.P.; Wibowo, N.; Middelberg, A.P.J. Bioengineering virus-like particles as vaccines. *Biotechnol. Bioeng.* **2014**, *111*, 425–440.
4. Hill, B.D.; Zak, A.; Khera, E.; Wen, F. Engineering Virus-like Particles for Antigen and Drug Delivery. *Curr. Protein Pept. Sci.* **2017**, *19*, 112–127.
5. Cervera, L.; Gòdia, F.; Tarrés-Freixas, F.; Aguilar-Gurrieri, C.; Carrillo, J.; Blanco, J.; Gutiérrez-Granados, S. Production of HIV-1-based virus-like particles for vaccination: achievements and limits. *Appl. Microbiol. Biotechnol.* **2019**, *103*, 7367–7384.
6. Göttlinger, H.G. *HIV-1 Gag: a Molecular Machine Driving Viral Particle Assembly and Release*; Carla KuCarla Kuiken, BrianFoley, Thomas Leitner, Cristian Apetrei, Beatrice Hahn, Ilene Mizrahi, James Mullins, Andrew Rambaut, StevenWolinsky, and B.K. editors., Ed.; Los Alamos National Laboratory, Theoretical Biology andBiophysics: Los Alamos, New Mexico., 2001; ISBN 0269-9370.
7. Besnard, L.; Fabre, V.; Fettig, M.; Gousseinov, E.; Kawakami, Y.; Laroudie, N.; Scanlan, C.; Pattnaik, P. Clarification of vaccines: An overview of filter based technology trends and best practices. *Biotechnol. Adv.* **2016**, *34*, 1–13.
8. Effio, C.L.; Hubbuch, J. Next generation vaccines and vectors: Designing downstream processes for recombinant protein-based virus-like particles. *Biotechnol. J.* **2015**, *10*, 715–27.

9. Moleirinho, M.G.; Silva, R.J.S.; Alves, P.M.; Carrondo, M.J.T.; Peixoto, C. Current challenges in biotherapeutic particles manufacturing. *Expert Opin. Biol. Ther.* **2020**, *20*, 451–465.
10. Pato, T.P.; Souza, M.C.O.; Silva, A.N.M.R.; Pereira, R.C.; Silva, M. V.; Caride, E.; Gaspar, L.P.; Freire, M.S.; Castilho, L.R. Development of a membrane adsorber based capture step for the purification of yellow fever virus. *Vaccine* **2014**, *32*, 2789–2793.
11. Steppert, P.; Burgstaller, D.; Klausberger, M.; Berger, E.; Aguilar, P.P.; Schneider, T.A.; Kramberger, P.; Tover, A.; Nöbauer, K.; Razzazi-Fazeli, E.; et al. Purification of HIV-1 gag virus-like particles and separation of other extracellular particles. *J. Chromatogr. A* **2016**, *1455*, 93–101.
12. Pereira Aguilar, P.; Schneider, T.A.; Wetter, V.; Maresch, D.; Ling, W.L.; Tover, A.; Steppert, P.; Jungbauer, A. Polymer-grafted chromatography media for the purification of enveloped virus-like particles, exemplified with HIV-1 gag VLP. *Vaccine* **2019**, *37*, 7070–7080.
13. Tzeng, T.-T.; Lai, C.-C.; Weng, T.-C.; Cyue, M.-H.; Tsai, S.-Y.; Tseng, Y.-F.; Sung, W.-C.; Lee, M.-S.; Hu, A.Y.-C. The stability and immunogenicity of inactivated MDCK cell-derived influenza H7N9 viruses. *Vaccine* **2019**, *37*, 7117–7122.
14. Carvalho, S.B.; Silva, R.J.S.; Moleirinho, M.G.; Cunha, B.; Moreira, A.S.; Xenopoulos, A.; Alves, P.M.; Carrondo, M.J.T.; Peixoto, C. Membrane-Based Approach for the Downstream Processing of Influenza Virus-Like Particles. *Biotechnol. J.* **2019**, *14*, 1–12.
15. Venereo-Sanchez, A.; Simoneau, M.; Lanthier, S.; Chahal, P.; Bourget, L.; Ansoerge, S.; Gilbert, R.; Henry, O.; Kamen, A. Process intensification for high yield production of influenza H1N1 Gag virus-like particles using an inducible HEK-293 stable cell line. *Vaccine* **2017**, *35*, 4220–4228.
16. Carvalho, S.B.; Silva, R.J.S.; Moreira, A.S.; Cunha, B.; Clemente, J.J.; Alves, P.M.; Carrondo, M.J.T.; Xenopoulos, A.; Peixoto, C. Efficient filtration strategies for the

- clarification of influenza virus-like particles derived from insect cells. *Sep. Purif. Technol.* **2019**, *218*, 81–88.
17. Gencoglu, M.F.; Heldt, C.L. Enveloped virus flocculation and removal in osmolyte solutions. *J. Biotechnol.* **2015**, *206*, 8–11.
  18. Ladd Effio, C.; Wenger, L.; Ötes, O.; Oelmeier, S.A.; Kneusel, R.; Hubbuch, J. Downstream processing of virus-like particles: Single-stage and multi-stage aqueous two-phase extraction. *J. Chromatogr. A* **2015**, *1383*, 35–46.
  19. Kumru, O.S.; Joshi, S.B.; Smith, D.E.; Middaugh, C.R.; Prusik, T.; Volkin, D.B. Vaccine instability in the cold chain: Mechanisms, analysis and formulation strategies. *Biologicals* **2014**, *42*, 237–259.
  20. Lynch, A.; Meyers, A.E.; Williamson, A.-L.; Rybicki, E.P. Stability studies of HIV-1 Pr55gag virus-like particles made in insect cells after storage in various formulation media. *Viol. J.* **2012**, *9*, 210.
  21. Hansen, L.J.J.; Daoussi, R.; Vervaeet, C.; Remon, J.P.; De Beer, T.R.M. Freeze-drying of live virus vaccines: A review. *Vaccine* **2015**, *33*, 5507–5519.
  22. Steppert, P.; Burgstaller, D.; Klausberger, M.; Kramberger, P.; Tover, A.; Berger, E.; Nöbauer, K.; Razzazi-Fazeli, E.; Jungbauer, A. Separation of HIV-1 gag virus-like particles from vesicular particles impurities by hydroxyl-functionalized monoliths. *J. Sep. Sci.* **2017**, *40*, 979–990.
  23. Reiter, K.; Aguilar, P.P.; Wetter, V.; Steppert, P.; Tover, A.; Jungbauer, A. Separation of virus-like particles and extracellular vesicles by flow-through and heparin affinity chromatography. *J. Chromatogr. A* **2019**, *1588*, 77–84.
  24. Cervera, L.; González-Domínguez, I.; Segura, M.M.; Gòdia, F. Intracellular characterization of Gag VLP production by transient transfection of HEK 293 cells. *Biotechnol. Bioeng.* **2017**, *114*, 2507–2517.



25. González-Domínguez, I.; Puente-Massaguer, E.; Cervera, L.; Gòdia, F. Quality Assessment of Virus-Like Particles at Single Particle Level: A Comparative Study. *Viruses* **2020**, *12*, 223.
26. Venereo-Sanchez, A.; Gilbert, R.; Simoneau, M.; Caron, A.; Chahal, P.; Chen, W.; Ansorge, S.; Li, X.; Henry, O.; Kamen, A. Hemagglutinin and neuraminidase containing virus-like particles produced in HEK-293 suspension culture: An effective influenza vaccine candidate. *Vaccine* **2016**, *34*, 3371–3380.
27. Gutiérrez-Granados, S.; Cervera, L.; Gòdia, F.; Carrillo, J.; Segura, M.M. Development and validation of a quantitation assay for fluorescently tagged HIV-1 virus-like particles. *J. Virol. Methods* **2013**, *193*, 85–95.
28. Chen, Y.; Wu, B.; Musier-Forsyth, K.; Mansky, L.M.; Mueller, J.D. Fluorescence fluctuation spectroscopy on viral-like particles reveals variable Gag stoichiometry. *Biophys. J.* **2009**, *96*, 1961–1969.
29. Joshi, P.R.H.; Cervera, L.; Ahmed, I.; Kondratov, O.; Zolotukhin, S.; Schrag, J.; Chahal, P.S.; Kamen, A.A. Achieving High-Yield Production of Functional AAV5 Gene Delivery Vectors via Fedbatch in an Insect Cell-One Baculovirus System. *Mol. Ther. Methods Clin. Dev.* **2019**, *13*, 279–289.
30. Pereira Aguilar, P.; González-Domínguez, I.; Schneider, T.A.; Gòdia, F.; Cervera, L.; Jungbauer, A. At-line multi-angle light scattering detector for faster process development in enveloped virus-like particle purification. *J. Sep. Sci.* **2019**, *42*, 2640–2648.
31. Cervera, L.; Fuenmayor, J.; González-Domínguez, I.; Gutiérrez-Granados, S.; Segura, M.M.; Gòdia, F. Selection and optimization of transfection enhancer additives for increased virus-like particle production in HEK293 suspension cell cultures. *Appl. Microbiol. Biotechnol.* **2015**, *99*, 9935–9949.
32. Malvern Instruments Limited *Determining fluorescence Limit of Detection with Nanoparticle Tracking Analysis (NTA)*; 2015;

33. González-Domínguez, I.; Puente-Massaguer, E.; Cervera, L.; Gòdia, F. Quantification of the HIV-1 virus-like particle production process by super-resolution imaging: From VLP budding to nanoparticle analysis. *Biotechnol. Bioeng.* **2020**, bit.27345.
34. Anderson, E.C.; Petersen, D.F.; Tobey, R.A. Density Invariance of Cultured Chinese Hamster Cells with Stage of the Mitotic Cycle. *Biophys. J.* **1970**, *10*, 630–645.
35. Westoby, M.; Chrostowski, J.; Vilmorin, P. De; Smelko, J.P.; Romero, J.K.; Carolina, N. Effects of Solution Environment on Mammalian Cell Fermentation Broth Properties : Enhanced Impurity Removal and Clarification Performance. **2011**, *108*, 50–58.
36. Nestola, P.; Villain, L.; Peixoto, C.; Martins, D.L.; Alves, P.M.; Carrondo, M.J.T.; Mota, J.P.B. Impact of grafting on the design of new membrane adsorbers for adenovirus purification. *J. Biotechnol.* **2014**, *181*, 1–11.
37. McNally, D.J.J.; Darling, D.; Farzaneh, F.; Levison, P.R.R.; Slater, N.K.H.K.H. Optimised concentration and purification of retroviruses using membrane chromatography. *J. Chromatogr. A* **2014**, *1340*, 24–32.
38. Kutner, R.H.; Puthli, S.; Marino, M.P.; Reiser, J. Simplified production and concentration of HIV-1-based lentiviral vectors using HYPERFlask vessels and anion exchange membrane chromatography. **2009**, *7*, 1–7.
39. Nestola, P.; Peixoto, C.; Silva, R.R.J.S.; Alves, P.M.; Mota, J.P.B.; Carrondo, M.J.T. Improved virus purification processes for vaccines and gene therapy. *Biotechnol. Bioeng.* **2015**, *112*, 843–857.



## General Discussion

---

HIV-1 Gag VLPs are on the spotlight as a scaffold for antigen presentation against different diseases [1,2], but also for other biomedical applications, such as delivery purposes [3–5], and even as reference material for extracellular vesicles (EVs) [6]. In this work, an advanced production platform for the obtention of HIV-1 Gag VLPs in the GMP-compliant suspension-adapted HEK 293 cell line was used to perform a deep characterization of the parameters governing the production process, and of the critical quality attributes (CQA) required to develop an efficient purification process. The use of animal-derived component free and chemically defined media was used in this thesis to speed up the transition from laboratory to large-scale manufacturing of these particles [7]. Several work have focused on the optimization of HIV-1 Gag VLP production in animal cell cultures [8–15]. Current research activities encompass the development of novel optimization strategies through metabolic engineering, the development of stable cell lines for the production of HIV-1 Gag VLPs and the generation of novel chimeric candidates. Great efforts have been also undertaken in their production by means of PEI-mediated transient gene expression (TGE) in large-scale, including the HEK 293 platform used here [16,17].

Advancements in nanotechnology and microscopy techniques offer great promise to revisit already established biotechnological processes and discover new parameters influencing them. In this thesis, we took advantage of those technologies to study the PEI-mediated TGE in HEK 293 cells. The application of cryogenic Electron Microscopy (cryo-EM) in combination to Nanoparticle Tracking Analysis (NTA) and Dynamic Light Scattering (DLS) enabled to describe the DNA/PEI complex formation in a physicochemical manner. Upon the addition of PEI to DNA, complexes of around 300 nm were immediately formed and during their incubation in cell culture medium, an heterogenous aggregation process was observed. Furthermore, the use of X-ray spectroscopy directly pointed the contribution of Na and Cl ions into the complex formation process. Although it is conventionally accepted that DNA/PEI complexes should have a size in

the range of nanometers [18], the presence of large aggregates had a positive impact on transfection yields of HEK 293 cells in the present strategy.

To deepen into the physicochemical process-parameters that drive this phenomenon, a rational-design study on the DNA/PEI complexation process was performed. By means of Design of Experiments (DoE), the physicochemical factors: pH, NaCl concentration and incubation time of the DNA/PEI complexation media were optimized. The use of DoE benefits from the analysis of more than one variable at a time, while also learning about their interactions by dramatically reducing the number of experiments. Cytostatic and cytotoxic effects, transfection efficiency, in terms of percentage of producing cells, and final production titers were assessed and optimized in HEK 293 cells. This holistic view provided an optimal condition, corresponding to NaCl concentration of 125 mM, and a DNA/PEI incubation time of 11 minutes, whereas the pH was shown to be non-significant. Interestingly, the physicochemical characterization of these optimal DNA/PEI complexes presented again a high mean hydrodynamic diameter, where the presence of micrometric DNA/PEI aggregates was also identified by cryo-EM.

Similar conclusions in regards to the positive effect of micrometric DNA/PEI complexes in the transfection of other mammalian cell lines [19–21], primary cell lines [20] and tumor models [21] have been reported in the literature. Pezzoli et al. observed a higher sedimentation of these large DNA/PEI complexes as the main cause of their success in the transfection of adherent cell cultures, compared to nanometric ones [20]. However, it is not clear if this process may also lead the efficiency of transfection on suspension cells, as for the HEK 293 cells evaluated in this work. Furthermore, pre-complexation of DNA/PEI complexes is generally performed with ionic solutions at large-scale processes of mammalian cell cultures [22]. Thus, similar physicochemical behaviors might be taking place in those protocols. Additional characterization of DNA/PEI complexes used on large-scale approaches could bring light to this matter.

Nevertheless, not only simple variables, like NaCl concentrations or incubation time take a role in PEI-mediated processes. PEI charge density, structure and chemical modifications, nitrogen / phosphate (N/P) ratio, DNA and PEI concentrations or complex preparation and addition process

have also a major impact [22–26]. Furthermore, cell culture-related parameters such as the cell line used, cell culture medium composition, cell concentration, time of contact of DNA/PEI complexes with cells, or the addition or replacement of medium in the transfection protocol have also a huge influence [22,27,28]. Van Gaal et al. reviewed the myriad of DNA delivery protocols present in literature [27]. This heterogeneity hampers the direct comparison between works, making impossible to estimate the contribution to improvement on the DNA delivery field. The effect of the different variables on DNA/PEI physicochemical properties might be behind these unsolved questions. For instance, Bono and co-authors studied the volume of DNA/PEI complex formation and the order of addition in its mixture, showing a difference in the physicochemical properties of those complexes that eventually correlated with their transfection efficiency [26]. Broader analyses, where more variables are taken into consideration, should be performed to gain insight into process-parameters interactions that affect TGE processes from a physicochemical point of view.

Although the physicochemical properties have been characterized in the pre-complexation medium, the final features of DNA/PEI complexes responsible of their efficiency are those present upon their addition to the cell culture [20,25]. In this regard, the endocytosis of micrometric DNA/PEI complexes through macropinocytosis uptake has been confirmed by drug inhibition endocytosis assays. The macropinocytosis pathway endocytoses particles in the micrometric range into early endosomes that are lately transferred to late endosomes converted to lysosomes [29]. From that point, the most extended hypothesis is proton-sponge effect releasing the complexes to the cytoplasm, where the DNA is then transported to the cell nucleus. Though, these intracellular mechanisms remain unclear [24]; in fact, alternative explanations to the proton-sponge effect have been described, such as a pore formation in the endosomal membrane, fusion in the endosomal membrane, or photochemical disruption [18]. In regard to the nuclear DNA delivery, two theories have been proposed: the entry through cell division or an active transport through the nuclear pores [18]. The quantitative study of DNA/PEI complex disassembly at intracellular level showed the presence of micrometric DNA/PEI complexes in the vicinity of the

nuclear envelope at 24 hours post transfection. Thus, corroborating its cellular uptake and release from late endosomes. Furthermore, assembled DNA/PEI complexes were not detected inside the cell nucleus, thus supporting the hypothesis of an active transport through nuclear pores. The use of super-resolved images with the combination of Confocal Laser Scanning Microscopy (CLSM) images coupled with deconvolution demonstrated to be very useful for the analysis of nanometric structures at intracellular level with Manders' Overlap coefficient. Nonetheless, the combination of these novel mathematical methods with colocalization methods, as the ones assessed in this work, should be carefully evaluated, as expertise in deconvolution software is required for a proper use of these technologies.

Advancements in confocal microscopy methodologies were also applied to the study of the HIV-1 Gag VLP budding process in living cells. The use of SRFM HyVolution2 mode (Leica Microsystems) was used to this purpose. HyVolution2 allows an optimized image acquisition, while directly applying deconvolution into the same software. The direct communication between the confocal microscope and the deconvolution software reduces the risk to obtain unbiased results since physical and optical parameters like excitation/emission wavelengths or specifications of the objective lens are directly uploaded in the same software. Of note, HyVolution2 has been recently updated to Lightning, which has reported resolutions down to 120 nm [30]. This user-friendly method combined with 3D multicolor imaging analysis allowed the quantitative study of HIV-1 Gag VLPs budding not only in HEK 293 cells, but also in Sf9 and Hi5 insect cell lines. From these studies a different assembly capacity depending on the production platform was observed. According to these results,  $518 \pm 164$ ,  $3045 \pm 1733$  and  $1682 \pm 716$  VLP assembly sites per cell were theoretically calculated for transfected HEK 293 cells and baculovirus infected High Five cells and Sf9, respectively.

In addition, SRFM could be also applied to the characterization and quantification of HIV-1 Gag VLPs present in crude supernatants. The lipid membrane of VLPs and the presence of nucleic acids alongside these nanoparticles could also be detected using common staining procedures. Results obtained showed that transiently transfected HEK 293 cells yielded  $0.4 - 4.3 \cdot 10^{10}$



VLP/mL at 72 hpt, whereas baculovirus infected High Five and Sf9 cells achieved  $0.4 - 4.6 \cdot 10^{10}$  and  $0.7 - 7.5 \cdot 10^{10}$  VLP/mL at 40 hpi, respectively. These HyVolution 2 quantifications were in the same range as fluorescent based NTA measurements, highlighting the great potential of this method, as an alternative particle counting technique.

Although the evident improvement in resolution achieved by HyVolution2, HIV-1 Gag VLP budding characterization would benefit from the application of even more resolute SRFM techniques. Pioneer techniques achieving down to 20 nm resolutions have been recently reported and applied to the characterization of HIV-1 biology [31]. Furthermore, the combination of SRFM with electron microscopy also offers great promise [32]. Also, 3D imaging software methods developed here could be largely improved by the development of automated tools that will facilitate its analysis, shortening data analysis times. Nonetheless, the use of more sophisticated methods, present also clear limitations, like the need for certain fluorophores, access to equipment infrastructure and higher expertise. Additionally, the study of living cells must deal with live cell compatibility, acquisition speed and multicolor imaging. Hence, the use of highly resolute SRFM strategies might not be feasible in some of these studies [33].

The appearance of novel particle quantification methods is essential to properly study complex biomacromolecules, as the HIV-1 Gag VLPs studied here. First, Atomic Force Microscopy (AFM) was used to assess the nanomechanical properties of an individual HIV-1 Gag VLP with advanced amplitude modulation-frequency modulation (AM-FM) viscoelastic mapping mode. The application of AFM in viral-based product characterization can provide relevant information in the study of its composition and structure. Different studies have been performed on virus characterization using AFM, where the external and internal structure or its nucleic acid content has been observed [34]. Furthermore, the ease and compatibility with liquid solutions has enabled mass viral populations studies and the study of these viruses in the surface of the host cells, while being produced [35]. Additional studies on VLPs would be of much interest to deepen into the physical properties of these structures for understanding the intraparticle interactions and to highlight differences from other adventitious viral structures or EVs, like those reported in this

work. Secondly, the use of Transmission Electron Microscopy (TEM), Scanning Electron Microscopy (SEM), cryo-TEM, HyVolution2 SRFM, NTA and flow virometry were compared in this thesis. Among the three microscopic methods used, cryo-TEM was identified as the most resolute method to analyze the ultrastructure of HIV-1 Gag VLPs in its native conditions. On the other hand, HyVolution2 SRFM, NTA and flow virometry allowed the high-throughput quantification of HIV-1 Gag VLPs. Due to the presence of Gag-eGFP fusion protein, not only the specific quantification of HIV-1 Gag VLPs was achieved, but also the rest of contaminant particles were quantified by NTA and flow virometry by light scattering modes. These results represent a step forward in the characterization of biological nanoparticles, since the presence of several subtypes EVs, and different baculoviruses-derived conformations in BEVS systems were observed, which could account for false positive particles provided that only light-based methods are applied. Furthermore, biochemical methods like ELISA, which can specifically quantify a certain protein, cannot distinguish the presence of assembled from non-assembled structures pointed also as a source of contamination specially in BEVS systems. This fact has been evidenced throughout this thesis with the comparison of indirect fluorescence-based Gag polyprotein quantification versus particle counting methods in different chapters.

The advances obtained in terms of product characterization and quantification were applied in the development of a cost-effective and scalable purification process for HIV-1 Gag VLPs. Novel membrane-based strategies, like the use of depth filter and membrane adsorbers were used. A four-step purification process consisting on clarification by flocculation and depth filtration, Ion Exchange Chromatography (IEX), buffer exchange by Size Exclusion Chromatography (SEC) and lyophilization was defined to purify HIV-1 Gag VLPs. Purified and lyophilized HIV-1 Gag-eGFP VLP vials containing  $2.2 \cdot 10^9$  VLPs, which corresponds to 24  $\mu$ g of Gag-eGFP per vial were obtained. Gag-eGFP represented the 94 % of total protein quantified, whereas, dsDNA was reduced almost a 100 % with a final concentration of  $49.6 \pm 28.2$  ng/mL. Furthermore, the percentage of EVs was also reduced in respect to VLPs: from the initial  $27 \pm 9$  % of VLPs from

total particles this percentage was considerably enriched having a removal of almost 100 % of EVs in the final preparations, as also confirmed by cryo-TEM analyses.

Purification methods for VLPs and viral-based products are widely reported in literature [36,37]. However, this is the first time, to our knowledge, where a complete purification train has been developed for HIV-1 Gag VLPs and their separation from EVs has been quantified. Nonetheless, a clear limit of this process is the purification yield, which went down to 3% after lyophilization. Two main reasons contribute to this fact: the low yield achieved in IEX Chromatography likely due to the presence of HIV-1 Gag VLP subpopulations that elute at different salt concentrations, as also reported by Steppert et al., and Aguilar et. al, [38,39], and a remarkable aggregation after lyophilization, quantified by NTA and DLS, which may underestimate particle quantification in the reconstituted preparation. Advanced filtration-based unit operations for nanoparticles, like ultrafiltration and diafiltration with Tangential Flow Filtration (TFF) could strongly improve the present results obtained by IEX, as recently reported for HIV-1 Gag VLPs [40] and influenza VLPs [11,41]. Novel formulations for HIV-1 Gag VLPs with optimized cryoprotectant and excipient composition or alternative use of spray-drying methods may contribute to disaggregate the VLPs [42,43]. Also, a rational-design approach using DoE techniques could aid to accelerate the process development of novel powder formulations [44]. Of note, the nanoparticle characterization methods presented in this thesis can be of help to ensure the maintenance of the biophysical properties upon drying and to specifically quantify HIV-1 Gag VLPs in the purified samples in a high-throughput manner.

Despite the advantages that nanoparticle fluorescent-based methods have provided in this work, it would be necessary to adapt the quantification methods for pre-clinical and clinical preparations, where the product would not have a fluorescent reporter. In this regard, Carvalho and co-authors developed a functionalized influenza VLP through alkyne-azide cycloaddition reaction, which allows the specific incorporation of a reporter for process development, while ensuring the translation of non-tagged candidates for manufacturing purposes [45]. In the same line, Geurickx et al., used a PEGylation to make HIV-1 Gag-eGFP VLPs compatible with

biofluids containing EVs. The addition of PEGylated HIV-1 Gag-eGFP VLPs to biofluids was used as tracker for down-stream development and data normalization, whereas the further segregation of HIV-1 Gag-eGFP VLPs from EVs was performed with anti-PEG magnetic beads [6]. These tag-on tag-off methods could be very interesting for process development purposes, by keeping the fluorescent-based nanoparticle methods reported here. Finally, for final product characterization, classical methods, like cryo-TEM, can be used in the absence of a fluorescent reporter despite being more time-consuming.

HIV-1 Gag VLPs have a great potential to be combined with other immunogens, proteins, enzymes or DNA for a wide range of applications. The co-production of the immunogen with the Gag polyprotein, but also the genetic fusion of proteins through Gag [4] or complementary proteins like Vpx [46] have been proposed for antigen presentation and delivery strategies. *In vitro* modifications by conjugation or non-covalent interactions, could be also approached without affecting the VLP assembly process, but including additional steps in the DSP part [47]. The present platform based on PEI-mediated transfection allows the rapid test of several candidates obtaining enough amounts for preclinical and early clinical studies. In addition, the findings on product characterization and purification could be further combined with other optimized platforms, for the obtention of purified HIV-1 Gag VLPs or chimeric candidates, but also for other similar biomacromolecules, like enveloped viruses or EVs.

## Literature

1. Cervera, L.; Gòdia, F.; Tarrés-Freixas, F.; Aguilar-Gurrieri, C.; Carrillo, J.; Blanco, J.; Gutiérrez-Granados, S. Production of HIV-1-based virus-like particles for vaccination: achievements and limits. *Appl. Microbiol. Biotechnol.* **2019**, *103*, 7367–7384.
2. Charlton Hume, H.K.; Vidigal, J.; Carrondo, M.J.T.; Middelberg, A.P.J.; Roldão, A.; Lua, L.H.L. Synthetic biology for bioengineering virus-like particle vaccines. *Biotechnol. Bioeng.* **2019**, *116*, 919–935.
3. Voráčková, I.; Ulbrich, P.; Diehl, W.E.; Ruml, T. Engineered retroviral virus-like particles for receptor targeting. *Arch. Virol.* **2014**, *159*, 677–688.
4. Kaczmarczyk, S.J.; Sitaraman, K.; Young, H. a; Hughes, S.H.; Chatterjee, D.K. Protein delivery using engineered virus-like particles. *Proc. Natl. Acad. Sci.* **2011**, *108*, 16998–17003.
5. Deo, V.K.; Kato, T.; Park, E.Y. Chimeric Virus-Like Particles Made Using GAG and M1 Capsid Proteins Providing Dual Drug Delivery and Vaccination Platform. *Mol. Pharm.* **2015**, *12*, 839–845.
6. Geurickx, E.; Tulkens, J.; Dhondt, B.; Van Deun, J.; Lippens, L.; Vergauwen, G.; Heyrman, E.; De Sutter, D.; Gevaert, K.; Impens, F.; et al. The generation and use of recombinant extracellular vesicles as biological reference material. *Nat. Commun.* **2019**, *10*, 1–12.
7. Cervera, L.; Gutiérrez-Granados, S.; Martínez, M.; Blanco, J.; Gòdia, F.; Segura, M.M. Generation of HIV-1 Gag VLPs by transient transfection of HEK 293 suspension cell cultures using an optimized animal-derived component free medium. *J. Biotechnol.* **2013**, *166*, 152–165.
8. Cervera, L.; Fuenmayor, J.; González-Domínguez, I.; Gutiérrez-Granados, S.; Segura, M.M.; Gòdia, F. Selection and optimization of transfection enhancer additives for increased virus-like particle production in HEK293 suspension cell cultures. *Appl. Microbiol. Biotechnol.* **2015**, *99*, 9935–9949.
9. Fuenmayor, J.; Cervera, L.; Gutiérrez-Granados, S.; Gòdia, F. Transient gene expression optimization and expression vector comparison to improve HIV-1 VLP production in HEK293 cell lines. *Appl. Microbiol. Biotechnol.* **2018**, *102*, 165–174.
10. Fuenmayor, J.; Cervera, L.; Rigau, C.; Gòdia, F. Enhancement of HIV-1 VLP production using gene inhibition strategies. *Appl. Microbiol. Biotechnol.* **2018**, *102*, 4477–4487.

11. Venereo-Sanchez, A.; Simoneau, M.; Lanthier, S.; Chahal, P.; Bourget, L.; Ansorge, S.; Gilbert, R.; Henry, O.; Kamen, A. Process intensification for high yield production of influenza H1N1 Gag virus-like particles using an inducible HEK-293 stable cell line. *Vaccine* **2017**, *35*, 4220–4228.
12. Puente-Massaguer, E.; Lecina, M.; Gòdia, F. Integrating nanoparticle quantification and statistical design of experiments for efficient HIV-1 virus-like particle production in High Five cells. *Appl. Microbiol. Biotechnol.* **2020**, *104*, 1569–1582.
13. Puente-Massaguer, E.; Lecina, M.; Gòdia, F. Application of advanced quantification techniques in nanoparticle-based vaccine development with the Sf9 cell baculovirus expression system. *Vaccine* **2020**, *38*, 1849–1859.
14. Fernandes, B.; Vidigal, J.; Correia, R.; Carrondo, M.J.T.; Alves, P.M.; Teixeira, A.P.; Roldão, A. Adaptive laboratory evolution of stable insect cell lines for improved HIV-Gag VLPs production. *J. Biotechnol.* **2020**, *307*, 139–147.
15. Gutiérrez-Granados, S.; Cervera, L.; Segura, M. de L.M.; Wölfel, J.; Gòdia, F. Optimized production of HIV-1 virus-like particles by transient transfection in CAP-T cells. *Appl. Microbiol. Biotechnol.* **2016**, *100*, 3935–47.
16. Fuenmayor, J.; Cervera, L.; Gòdia, F.; Kamen, A. Extended gene expression for Gag VLP production achieved at bioreactor scale. *J. Chem. Technol. Biotechnol.* **2019**, *94*, 302–308.
17. Gutiérrez-Granados, S.; Farràs, Q.; Hein, K.; Fuenmayor, J.; Félez, P.; Segura, M.; Gòdia, F. Production of HIV virus-like particles by transient transfection of CAP-T cells at bioreactor scale avoiding medium replacement. *J. Biotechnol.* **2017**, *263*, 11–20.
18. Shi, B.; Zheng, M.; Tao, W.; Chung, R.; Jin, D.; Ghaffari, D.; Farokhzad, O.C. Challenges in DNA Delivery and Recent Advances in Multifunctional Polymeric DNA Delivery Systems. *Biomacromolecules* **2017**, *18*, 2231–2246.
19. Sang, Y.; Xie, K.; Mu, Y.; Lei, Y.; Zhang, B.; Xiong, S.; Chen, Y.; Qi, N. Salt ions and related parameters affect PEI-DNA particle size and transfection efficiency in Chinese hamster ovary cells. *Cytotechnology* **2015**, *67*, 67–74.
20. Pezzoli, D.; Giupponi, E.; Mantovani, D.; Candiani, G. Size matters for in vitro gene delivery: investigating the relationships among complexation protocol, transfection medium, size and sedimentation. *Sci. Rep.* **2017**, *7*, 44134.
21. Zhang, W.; Kang, X.; Yuan, B.; Wang, H.; Zhang, T.; Shi, M.; Zheng, Z.; Zhang, Y.; Peng, C.; Fan, X.; et al. Nano-structural effects on gene transfection: Large, botryoid-shaped nanoparticles enhance DNA delivery via macropinocytosis and effective

- dissociation. *Theranostics* **2019**, *9*, 1580–1598.
22. Gutiérrez-Granados, S.; Cervera, L.; Kamen, A.A.; Gòdia, F. Advancements in mammalian cell transient gene expression (TGE) technology for accelerated production of biologics. *Crit. Rev. Biotechnol.* **2018**, *38*, 1–23.
  23. Blakney, A.K.; Yilmaz, G.; McKay, P.F.; Becer, C.R.; Shattock, R.J. One Size Does Not Fit All: The Effect of Chain Length and Charge Density of Poly(ethylene imine) Based Copolymers on Delivery of pDNA, mRNA, and RepRNA Polyplexes. *Biomacromolecules* **2018**, *19*, 2870–2879.
  24. Yue, Y.; Wu, C. Progress and perspectives in developing polymeric vectors for in vitro gene delivery. *Biomater. Sci.* **2013**, *1*, 152–170.
  25. Raup, A.; Wang, H.; Synatschke, C. V.; Jérôme, V.; Agarwal, S.; Pergushov, D. V.; Müller, A.H.E.; Freitag, R. Compaction and Transmembrane Delivery of pDNA: Differences between 1-PEI and Two Types of Amphiphilic Block Copolymers. *Biomacromolecules* **2017**, *18*, 808–818.
  26. Bono, N.; Ponti, F.; Mantovani, D.; Candiani, G. Non-Viral in Vitro Gene Delivery: It is Now Time to Set the Bar! *Pharmaceutics* **2020**, *12*, 1–23.
  27. van Gaal, E.V.B.; Van Eijk, R.; Oosting, R.S.; Kok, R.J.; Hennink, W.E.; Crommelin, D.J.A.; Mastrobattista, E. How to screen non-viral gene delivery systems in vitro? *J. Control. Release* **2011**, *154*, 218–232.
  28. Ulasov, A. V; Khramtsov, Y. V; Trusov, G.A.; Rosenkranz, A.A.; Sverdlov, E.D.; Sobolev, A.S. Properties of PEI-based polyplex nanoparticles that correlate with their transfection efficacy. *Mol. Ther.* **2011**, *19*, 103–12.
  29. Rewatkar, P. V.; Parton, R.G.; Parekh, H.S.; Parat, M.-O. Are caveolae a cellular entry route for non-viral therapeutic delivery systems? *Adv. Drug Deliv. Rev.* **2015**, *91*, 92–108.
  30. Microsystems Leica *LIGHTNING. Image information extraction by adaptative deconvolution*; 2018;
  31. Chojnacki, J.; Eggeling, C. Super-resolution fluorescence microscopy studies of human immunodeficiency virus. *Retrovirology* **2018**, *15*, 1–16.
  32. Chojnacki, J.; Müller, B. Investigation of HIV-1 Assembly and Release Using Modern Fluorescence Imaging Techniques. *Traffic* **2013**, *14*, 15–24.
  33. Schermelleh, L.; Ferrand, A.; Huser, T.; Eggeling, C.; Sauer, M.; Biehlmaier, O.; Drummen, G.P.C. Super-resolution microscopy demystified. *Nat. Cell Biol.* **2019**, *21*, 72–

- 84.
34. de Pablo, P.J. Atomic force microscopy of virus shells. *Semin. Cell Dev. Biol.* **2018**, *73*, 199–208.
35. Kuznetsov, Y.G.; McPherson, A. Atomic Force Microscopy in Imaging of Viruses and Virus-Infected Cells. *Microbiol. Mol. Biol. Rev.* **2011**, *75*, 268–285.
36. Effio, C.L.; Hubbuch, J. Next generation vaccines and vectors: Designing downstream processes for recombinant protein-based virus-like particles. *Biotechnol. J.* **2015**, *10*, 715–27.
37. Moleirinho, M.G.; Silva, R.J.S.; Alves, P.M.; Carrondo, M.J.T.; Peixoto, C. Current challenges in biotherapeutic particles manufacturing. *Expert Opin. Biol. Ther.* **2020**, *20*, 451–465.
38. Reiter, K.; Aguilar, P.P.; Wetter, V.; Steppert, P.; Tover, A.; Jungbauer, A. Separation of virus-like particles and extracellular vesicles by flow-through and heparin affinity chromatography. *J. Chromatogr. A* **2019**, *1588*, 77–84.
39. Pereira Aguilar, P.; Schneider, T.A.; Wetter, V.; Maresch, D.; Ling, W.L.; Tover, A.; Steppert, P.; Jungbauer, A. Polymer-grafted chromatography media for the purification of enveloped virus-like particles, exemplified with HIV-1 gag VLP. *Vaccine* **2019**, *37*, 7070–7080.
40. Negrete, A.; Pai, A.; Shiloach, J. Use of hollow fiber tangential flow filtration for the recovery and concentration of HIV virus-like particles produced in insect cells. *J. Virol. Methods* **2014**, *195*, 240–246.
41. Carvalho, S.B.; Silva, R.J.S.; Moleirinho, M.G.; Cunha, B.; Moreira, A.S.; Xenopoulos, A.; Alves, P.M.; Carrondo, M.J.T.; Peixoto, C. Membrane-Based Approach for the Downstream Processing of Influenza Virus-Like Particles. *Biotechnol. J.* **2019**, *14*, 1–12.
42. Hansen, L.J.J.; Daoussi, R.; Vervaet, C.; Remon, J.P.; De Beer, T.R.M. Freeze-drying of live virus vaccines: A review. *Vaccine* **2015**, *33*, 5507–5519.
43. Kanojia, G.; Soema, P.C.; Frijlink, H.; Amorij, J.; Kersten, G. Developments in the formulation and delivery of spray dried vaccines. **2017**, *13*, 2364–2378.
44. Jain, N.K.; Sahni, N.; Kumru, O.S.; Joshi, S.B.; Volkin, D.B.; Russell Middaugh, C. Formulation and stabilization of recombinant protein based virus-like particle vaccines. *Adv. Drug Deliv. Rev.* **2015**, *93*, 42–55.
45. Carvalho, S.B.; Freire, J.M.; Moleirinho, M.G.; Monteiro, F.; Gaspar, D.; Castanho,



- M.A.R.B.; Carrondo, M.J.T.; Alves, P.M.; Bernardes, G.J.L.; Peixoto, C. Bioorthogonal Strategy for Bioprocessing of Specific-Site-Functionalized Enveloped Influenza-Virus-Like Particles. *Bioconjug. Chem.* **2016**, *27*, 2386–2399.
46. Wu, X.; Liu, H.; Xiao, H.; Kim, J.; Sessaiah, P.; Natsoulis, G.; Boeke, J.E.F.D.; Hahn, B.H. Targeting Foreign Proteins to Human Immunodeficiency Virus Particles via Fusion with Vpr and Vpx. **1995**, *69*, 3389–3398.
47. Hill, B.D.; Zak, A.; Khera, E.; Wen, F. Engineering Virus-like Particles for Antigen and Drug Delivery. *Curr. Protein Pept. Sci.* **2017**, *19*, 112–127.

## Conclusions

---

From the results obtained in this thesis, the following conclusions can be highlighted:

1. DNA/PEI complex formation and incubation in cell culture medium impacts the transfection of HEK 293 cells due to the aggregation of DNA/PEI complexes. An heterogeneous aggregation, where the presence of ~300 nm DNA/PEI complexes and large aggregates after 15 minutes of incubation was observed. Furthermore, the transfection capacity of the complexes with different size was studied by drug inhibition endocytosis, where the positive contribution of DNA/PEI aggregates in the final transfection efficiency is concluded.
2. The physicochemical factors governing the DNA/PEI complexation process was studied using a Design of Experiments (DoE) approach. An optimal DNA/PEI complexation condition with 125 mM NaCl solution, as complexation medium, and a total incubation of 11 minutes was determined and validated. The physicochemical characterization of these complexes showed the presence of branched-like complex aggregates in the optimum condition. Micrometric DNA/PEI complexes was shown to be the key physicochemical property ensuring the highest transient gene expression (TGE) yields. The present model can bring light to large-scale TGE processes, where similar DNA/PEI complexations in ionic solutions are performed.
3. The tracking of DNA/PEI complex disassembly at intracellular level was quantitatively studied in super-resolved images by deconvolution. This mathematical treatment was shown to improve the colocalization results, and the Manders' Overlap coefficient was highlighted as the best quantitative coefficient to evaluate the colocalization of nanoparticles. A heterogeneous behavior of DNA/PEI complex population was found during their disassembly at intracellular level. DNA/PEI complexes were strongly interacting at the time of transfection and their disassembly was progressively observed between the 2 to 10 hours post transfection (hpt). However, some micrometric complexes

- were still present in the nucleus surroundings 24 hpt, while no DNA/PEI complex was observed inside the cell nucleus.
4. HIV-1 Gag-eGFP VLP assembly and budding process was characterized with HyVolution2Super-Resolution Fluorescence Microscopy (SRFM). Identification and quantification of individual HIV-1 Gag-eGFP VLP assembly sites in the cell membrane of living cells was achieved by means of 3D imaging analyses. Furthermore, the comparison of TGE-HEK 293 platform with the Baculovirus Expression Vector System (BEVS) in Sf9 and Hi5 insect cells was performed. By doing so, different budding capacities, from 500 to 3000 assembly sites per cell, were described at intracellular level. The presence of EVs concomitantly produced with HIV-1 Gag-eGFP VLPs, as contaminant particles, and a different percentage of assembled HIV-1 Gag-eGFP VLPs versus Gag monomer was described for each platform. HEK 293 was concluded the best platform regarding HIV-1 Gag-eGFP VLP assembly, whereas, BEVS-Sf9 presented the best balance of productivity and contaminating particles levels.
  5. A novel method for the quantification of HIV-1 Gag-eGFP VLPs with HyVolution2 SRFM was developed. Quantifications in the range of  $10^9$ - $10^{10}$  VLPs/mL were obtained, similarly to the reference technique (fluorescent NTA). Moreover, the lipid membrane of HIV-1 Gag-eGFP VLPs and the presence of nucleic acids in these nanoparticles could be detected using common staining procedures.
  6. Individual characterization of an HIV-1 Gag-eGFP VLP was achieved by Atomic Force Microscopy (AFM). The nanomechanical properties of an individual HIV-1 Gag-eGFP VLP was measured by bimodal and amplitude modulation-frequency modulation (AM-FM) viscoelastic mapping mode. The enhanced contrast obtained in the surface of the HIV-1 Gag VLPs was related to the Gag underneath the host-cell lipid membrane. Moreover, the AFM examination of HIV-1 Gag-eGFP VLPs and extracellular vesicles

- (EVs) under ambient conditions enabled their differentiation due to topological differences.
7. Characterization and quantification of HIV-1 Gag-eGFP VLPs was performed by Transmission, Scanning and cryogenic Electron Microscopy (TEM, SEM and cryo-TEM), HyVolution2 SRFM, Nanoparticle Tracking Analysis (NTA) and flow virometry. EM methods revealed the presence of several types of EVs within HIV-1 Gag-eGFP VLP preparations and cryo-TEM resulted in the best technique to resolve the HIV-1 Gag-eGFP VLP ultrastructure. HyVolution2 SRFM, NTA and flow virometry enabled the high throughput quantification of VLPs, where differences in nanoparticle concentration were observed between techniques. Moreover, NTA and flow virometry allowed the quantification of both EVs and HIV-1 Gag-eGFP VLPs within the same experiment, while analyzing particle size distribution (PSD), simultaneously.
  8. A four-step down-stream process combining flocculation with membrane filtration, ion exchange chromatography, desalting column and lyophilization was performed. Membrane and resin capacity were optimized for each step and the total amount of protein, dsDNA, HIV-1 Gag-eGFP VLPs and EVs content was analyzed for the different steps. A concentration of  $2.2 \cdot 10^9$  VLPs/mL in purified and lyophilized preparations was obtained after its storage at room temperature for two months. Good morphology and structural integrity were confirmed by cryo-TEM analyses. Remarkably, the EV content was reduced by almost a 100% in the reconstituted sample and Gag polyprotein represented a 94% of total protein quantified with a concentration of 24  $\mu\text{g/mL}$ .

## Curriculum Vitae

---

## EDUCATION AND TRAINING

---

- 2016-2020**      **PhD in Biotechnology**  
Universitat Autònoma de Barcelona. Escola d'Enginyeria.
- 2018-2020**      **Teaching assistant & laboratory teaching assistant**  
Universitat Autònoma de Barcelona. Facultat de Biociències.  
Biotechnology degree | Bioreactors
- 2018-2019**      **Higher Education Teacher-Training Program.**  
Universitat Autònoma de Barcelona | 175 h.
- 2019**            **Research Stay at Professor Amine Kamen group.**  
McGill University, Montreal. Department of Bioengineering | 4 months.
- 2017**            **Research Stay at Professor Alois Jungbauer group.**  
University of Natural Resources and Life Sciences (BOKU), Vienna.  
Department of Biotechnology | 1 month.
- 2014-2015**      **MSc in Nanoscience and Advanced Nanotechnology**  
**Qualification:** 9.0/10  
**Range:** 3<sup>rd</sup> of the promotion (3<sup>rd</sup> on 10 graduated students in 2015)  
Universitat Autònoma de Barcelona. Facultat de Biociències.
- 2010-2014**      **BSc in Biotechnology**  
**Qualification:** 8.5/10  
**Range:** 7<sup>th</sup> of the promotion (7<sup>th</sup> on 68 graduated students in 2014)  
Universitat Politècnica de València. Escuela Técnica Superior de Ingeniería Agronómica y del Medio Natural (ETSIAMN).
- SICUE Exchange program in 4<sup>th</sup> course
  - Ara Group ( High Performance Group)
  - Extracurricular Practices with Dr. Diego Orzáez. (Instituto de Biología Molecular y Celular de Plantas (IBMCP |2012)

## PROJECTS & COLLABORATIONS

---

- 2019-2020**      **Rational design of novel quatsomes for the DNA delivery approaches**  
| Diego Valdospinos, MSc student.  
Supervision, Prof. Francesc Gòdia in partnership with Dr. Nora Ventosa, ICMAB, Barcelona.
- 2019-2020**      **Microscopia Confocal Espectral y superresolución.**  
Invited speaker | 1.5 h. Hospital Sant Joan de Déu, Barcelona.
- 2019**            **Development of Scalable Downstream Processing Platform for HEK-293 Cell-based Influenza Vaccine Production.** | 2 months.  
Research fellowship, Prof. Amine Kamen, McGill University, Montreal.
- 2017**            **Optimización de la producción de vectores AAV9-CAG-hSulfamidasa en un sistema con células en suspensión.**  
Research assistant, Prof. Francesc Gòdia, UAB, Barcelona.

### Publications

**González-Domínguez I, Puente-Massaguer E, Cervera L, Gòdia F.** Quantification of the HIV-1 virus-like particle production process by super-resolution imaging: From VLP budding to nanoparticle analysis. *Biotechnology and Bioengineering*, 2020.

**González-Domínguez I, Puente-Massaguer E, Cervera L, Gòdia F.** Quality assessment of virus-like particles at single particle level: a comparative study. *Viruses*, 2020.

**Aguilar PP, González-Domínguez I, Schneider TA, Gòdia F, Cervera L, Jungbauer A.** At-line multi-angle light scattering detector for faster process development in enveloped virus-like particle purification. *Journal of Separation Science*, 2019.

**González-Domínguez I, Cervera L, Gòdia F, & Roldán M.** Quantitative colocalization analysis of DNA delivery by PEI-mediated cationic polymers in mammalian cells. *Journal of Microscopy*, 2019.

**González-Domínguez I, Grimaldi N, Cervera L, Ventosa N, & Gòdia F.** Impact of physicochemical properties of DNA/PEI complexes on transient transfection of mammalian cells. *New Biotechnology*, 2019.

**Cervera L, González-Domínguez I, Segura MM, Gòdia F.** Intracellular characterization of Gag VLP production by transient transfection of HEK 293 cells. *Biotechnology and Bioengineering*, 2017.

**González-Domínguez I, Gutiérrez-Granados S, Cervera L, Gòdia F, Domingo N.** Identification of HIV-1-Based Virus-like Particles by Multifrequency Atomic Force Microscopy. *Biophysical Journal*, 2016.

**Cervera L, Fuenmayor J, González-Domínguez I, Gutiérrez-Granados S, Segura MM, Gòdia F.** Selection and optimization of transfection enhancer additives for increased virus-like particle production in HEK293 suspension cell cultures *Applied Microbiology and Biotechnology*, 2015.

### Conferences

**González-Domínguez I, Puente-Massaguer E, González-Domínguez I, Cervera L, Gòdia F.** European Congress in Animal Cell Technology (ESACT) Meeting (May 2019 | **oral communication**)

**González-Domínguez I, Schneider T, Aguilar A, Cervera L, Jungbauer A, Gòdia F.** 2nd ESACT Frontiers Retreat, Zagreb 2018. (October 2018 | poster communication)

**Puente-Massaguer E, González-Domínguez I, Cervera L, Gòdia F.** European Congress on Biotechnology (July 2018 | **oral communication**)

**Cervera L, Fuenmayor J, González-Domínguez I, Gòdia F.** Vaccine Technology VII (June 2018 | **oral communication**)

**González-Domínguez I, Cervera L, Grimaldi N, Domingo N, Ventosa N, Gòdia F.** 13th Protein Expression in Animal Cells (PEACE) Conference, Valencia, Spain (September 2017 | **oral communication & best poster prize**)

**González-Domínguez I, Cervera L, Grimaldi N, Domingo N, Ventosa N, Gòdia F.** 25th European Congress in Animal Cell Technology (ESACT) Meeting (May 2017, poster communication)



González-Domínguez I, **Gòdia F**, Cervera L. 29th Japanese Association of Animal Cell Technology (JAACT) (November 2016 | **oral communication**)

González-Domínguez I, **Gòdia F**, Cervera L. Cell Culture Engineering XV (May 2016 | **oral communication**)

**González-Domínguez I**, Cervera L, Segura MM, Gòdia F. 24th European Congress in Animal Cell Technology (ESACT) Meeting (May 2015 | poster communication)

---

#### SPECIALIZED COURSES

---

**Advanced Course in Downstream Processing.** Delft University of Technology (July 2018 | 42h).

**Research Papers for Sciences.** Universitat Autònoma de Barcelona. (February 2018 | 30h).

**English Pronunciation for Teachers.** Universitat Autònoma de Barcelona. (January 2018 | 30h).

**1<sup>st</sup> Edition Cells for Viral Vaccine production.** European Society of Animal and Cell Technology (ESACT) (September 2016 | 20h).

**Iniciativa Emprendedora Universitaria: Proceso de Creación de Empresas.** Industrial Organization School (EOI) in collaboration with the Spanish Industry Energy and Tourism Ministry and the Spanish Education, Culture and Sports Ministry (October 2015 | 36h).

**2<sup>th</sup> Edition Cell for Cell Screening.** European Society of Animal and Cell Technology (ESACT) (September 2015 | 20h).

**4<sup>th</sup> Edition Animal Cell Technology Course.** European Society of Animal and Cell Technology (ESACT) (September 2014 | 20h).

---

#### HONORS AND FUNDING

---

**2019** FPU EEBB Grant. Spanish Education, Culture and Sports Ministry

**2016** FPU PhD Grant. Spanish Education, Culture and Sports Ministry

**2015** Beca de Colaboración. Spanish Education, Culture and Sports Ministry